Investigation on Halide Perovskite Nanostructures and Thin Films for Optoelectronic and Solar Cell Applications

A Thesis Submitted to
Indian Institute of Technology Guwahati
For the Degree of

Doctor of Philosophy

By
JOYDIP GHOSH

Department of Physics
Indian Institute of Technology Guwahati
Guwahati-781039, India

AUGUST 2020

Dedicated to

…..My beloved **Grandmother**

Department of Physics
Indian Institute of Technology Guwahati
Guwahati-781039, India

STATEMENT

The work contained in the thesis entitled "**Investigation on Halide Perovskite Nanostructures and Thin Films for Optoelectronic and Solar Cell Applications**" has been carried out by me at Indian Institute of Technology Guwahati under the supervision of **Prof. P. K. Giri**, Professor, Department of Physics, Indian Institute of Technology Guwahati. This work has not been submitted elsewhere for the award of any degree.

Joydip Ghosh

Roll No. - **156121015**

Senior Research Fellow
Department of Physics
Indian Institute of Technology Guwahati
Guwahati-781039, India

Prof. P. K. Giri
Professor
Department of Physics
Indian Institute of Technology Guwahati
Guwahati-781039, India
Phone: ***+91 361 2582703****, Fax:* ***+91 361 2690762***
Email: ***giri@iitg.ac.in***

CERTIFICATE

This is to certify that the work contained in the thesis entitled "**Investigation on Halide Perovskite Nanostructures and Thin Films for Optoelectronic and Solar Cell Applications**" has been carried out by **Mr. Joydip Ghosh** at Indian Institute of Technology Guwahati under my supervision. This work has not been submitted elsewhere for the award of any degree.

Prof. P. K. Giri
Thesis supervisor

ACKNOWLEDGEMENT

This thesis becomes a reality with the kind support and encouragement from numerous people. Now, it is my pleasure to express my gratitude to those persons for their assistance, support, and inspiration.

First of all, I would like to express my sincere gratitude to my thesis supervisor, Prof. P. K. Giri, for his inspiring guidance, valuable discussion, kind support, constant encouragement, and useful suggestions. I owe my sincerest gratitude to him for giving me the opportunity to work under his guidance. His fruitful discussion, kind support, constant encouragement, and useful suggestions made the completion of my Ph.D. possible. His vast knowledge and immense passion for science has greatly inspired me and shaped my perception of scientific research. I am thankful for giving me the complete freedom in my research work and providing the essential arrangements, laboratory facilities, and moral support throughout my Ph.D. work to achieve the goal.

I express my sincere gratitude to my Doctoral Committee members, Prof. Seenipandian Ravi, Prof. Girish Sampath Setlur, and Prof. Gopal Das, for their regular review of my work, constructive criticism, and valuable suggestions.

I am thankful to our Head of the Department of Physics, other faculty members of Physics, members of the Central Instruments Facilities, and Centre for Nanotechnology for providing me a research-friendly environment with up-to-date research facilities. I am immensely grateful to the Indian Institute of Technology Guwahati for providing the fellowship, good accommodation in this beautiful campus, and having a pleasant working environment. A special thanks to the scientific/technical officers/staffs, Dr. Sidananda Sarma, Dr. Gayatri Natu, Indrajit Talukdar, Kaustubh Acharya, Dr. Kula K. Senapati, Sandhan Sarma, Ashim Malakar, Tenison Basumatary, Dr. Nayan Mani Das, Sujit Deb, Milan Mahadani, Emlin Elsa Abraham and Reena Dey for their help and co-operation to complete my work. I am also thankful to the Central Workshop, Department of Mechanical Engineering, for the fabrication of essential components used in my experimental setup. I would like to thank especially Prof. Minoru Fujii, Dr. Sugimoto from Kobe University, Japan, Dr. Wolfgang Theis from the University of Birmingham, UK, for providing the opportunity to use some of their laboratory facilities. I would like to acknowledge Dr. Sudip Chakraborty from IIT Indore for theoretical calculations.

I would like to express my appreciation and thanks to my friends and lab-mates for their help and good company. I should not forget to mention a few of them. I express my sincere

gratitude to my seniors Dr. Ramesh Ghosh, Dr. Biswajit Choudhury, Dr. Sk. Md. Obaidullah, Dr. Rajender Gone, Dr. Jitendra Kumar, Dr. Kamal Kumar Paul, Larionette P. L. Mawlong, and Somorjit Singh for their help in research and their good company. Thanks to my labmates, Dr. Sumana, Ruma, Sumaiya, Abhilasha, Neda, Tarik, Ravinder, Koushik, Tadasha, and Abdul for their support and help to bring the thesis in reality. I should not forget to mention Anirban, Rishav, Dr. Krishnakanta, Sumit, Sunil, Dr. Partha, Dr. Sanjib, Dr. Biswajit and Milan from other LAB for their cheerful and enjoyable company through my ups and downs during my Ph.D. journey. I would like to thank my close friends Ashis, Santu, Sarif, Sofi, Bandhan, Bhutu, Chotu, Reetwik, Sayam, Supriya, Kaustav, Sudeb, Subhendu, Bheku, Sahelye, Shekhar and Sourav for their cheerful support.

I am very much thankful to my father and mother for their love, blessing, and constant encouragement to pursue higher study. I am highly grateful to Pramila Das Vairagya (Dida), Madan Ghosh (mama), Subrata Ghosh (Kaku), and Basanti Ghosh (Kakima) for constant motivation. I am immensely thankful to Pradip (dada) and Shilpa (boudi) for their constant support and encouragement. I am fortunate to have Susmita in my life for support and love through my ups and downs during my Ph.D. journey. Finally, I wish to express my deep sense of gratitude to my grandmother (thakuma) for her love, blessing, and constant encouragement. I spent my childhood days under her guidance, and she was instrumental to build my character, morality, and personality. I am dedicating this thesis to my grandmother.

Joydip Ghosh

IIT Guwahati

CONTENTS

SYNOPSIS

Over the past few years, halide perovskites with formula ABX_3 (where A is a large cation, B is a metal cation, and X is halide anion (Cl, Br or I)), have emerged as a promising class of semiconductors due to their extraordinary performance in solar cells with the advantages of high light absorption coefficients, tunable optical band gap, high carrier mobility, long electron-hole diffusion lengths, and low-cost and low-temperature processing. Recently, perovskite solar cells have achieved power conversion efficiencies over 23%. Low cost and solution-processable fabrication techniques make perovskite as a potential candidate in the field of photovoltaics, though there are several challenges yet to overcome. Based on their unique optical and electrical properties, hybrid perovskites have also shown great promises in other optoelectronic devices, such as light-emitting diodes (LEDs), laser, and photodetectors (PDs), etc.

Perovskite nanoparticles (NPs) and quantum dots (QDs) show much superior optoelectronic properties than their bulk counterpart due to the size reduction and quantum confinement effect. There are several chemical processes for the synthesis of perovskite NPs and QDs, which often show the very high efficiency of light emission. For device applications, NPs are required in a solid or thin-film form, though the emission intensity decreases when NPs are deposited as thin films due to spontaneous aggregation. To overcome this issue, an alternative approach is a growth of perovskite NPs/nanocrystals (NCs) confined in porous inorganic templates such as porous aluminum oxide (Al_2O_3) and silica (SiO_2), etc. Thus, the confinement of perovskite NPs in the alternative porous template, such as mesoporous silicon nanowire array (Si NW) is very interesting for different optoelectronic applications. The ambient stability is one of the major challenges for perovskite optoelectronic devices. Due to the encapsulation by the porous inorganic matrix, the ambient stability of NPs confined in the mesoporous template is expected to be much superior.

The most explored synthesis process for $CsPbX_3$ perovskite NCs/QDs is the hot injection method. This is rather a tedious multistep process to dissolve different raw reagents, either polar solvents, or organic surfactants/ligands, by heating at high temperature. There is a need to look for alternative processes, which may be less tedious. One of the alternative processes of synthesis of $CsPbX_3$ NCs can be solvent-free, solid-state process by mechanochemical milling, which results in perovskite NCs with superior optoelectronic properties and better stability. The partial substitution of Pb^{2+} in Pb-based perovskite by other impurity ions, such

as Mn, and other main group metal cations, transition metal cations, and rare earth metal cations, are also explored to improve the optoelectronic properties of the perovskite NCs. Mn-doped $CsPbCl_3$ NCs show unusual dual-color emission, which can be tunable by varying Mn doping content, measurement temperature, and excitation intensity.

Due to the high absorption coefficient and long carrier diffusion lengths, halide perovskite is very promising for high-performance photodetection. The heterojunction of perovskite material with different types of semiconductors, including 2D materials, can be very interesting for high-performance PDs. A suitable heterostructure of perovskite with other semiconductors can increase the photogenerated carrier separation and transport form perovskite, which may result in superior photodetection. The plasmonic NPs can also improve the performance of perovskite PDs due to localized surface plasmon resonance (LSPR). Plasmonic metal NPs on perovskites can increase optical absorption, photogenerated charge separation, and transport, which may collectively result in the superior performance of the perovskite PDs.

Most of the studies on perovskite solar cells are based on the fabrication of perovskite films by a spin coating method. Fabrication of large-area pinhole-free perovskite films for solar cells by novel alternative methods is still very challenging. We find that a two-step vacuum-solution deposition technique, in which inorganic PbI_2 layer is first deposited by vapor deposition and subsequently dipped in CH_3NH_3I solution, results in a highly compact pinhole-free $CH_3NH_3PbI_3$ layer with superior photovoltaic performance.

This thesis presents a systematic study on the controlled growth of perovskite nanostructures and films with superior optoelectronic properties and stability for their applications in high-performance photodetectors, LEDs, and solar cells. We believe that these studies are very significant in addressing the current challenges of energy and environmental issues and multifunctional optoelectronic applications. The complete thesis work has been organized into eight chapters, as detailed below:

Chapter 1 presents an introduction on the key properties, growth strategies of halide perovskite with formula ABX_3 (where A= CH_3NH_3 or Cs, B= Pb and X= Cl, Br, I) and their potential utilization in different technological applications, such as solar cells, photodetectors (PDs), light-emitting diodes (LEDs), etc. Recent progress on the fabrication of halide perovskite-based nanostructure/heterostructure and thin films for high-performance solar cells, LED, PD, etc. are presented. The problems and challenges of utilizing perovskite in the device

applications and the key parameters to improve the performances of the device are discussed. The chapter ends with the motivation and focus of the present work.

Chapter 2 presents a detailed investigation of the controlled fabrication of $CH_3NH_3PbI_3$ perovskite NPs on a mesoporous silicon nanowire template and study the mechanism of its high photoluminescence (PL) quantum yield. The PL quantum yield of the embedded perovskite NPs was measured to be 9.82% as compared to the low yield (0.69%) of the perovskite film. Depending on the size of the perovskite NPs, the center of the PL peak of the of NPs shows a large blue-shift as compared to that of the perovskite film. A detailed systematic study reveals that a decrease in particle size and the quantum confinement in perovskite NPs are primarily responsible for the enhanced yield as well as the blue-shift of PL. This study demonstrates an easy and cost-effective fabrication of perovskite NPs on a novel mesoporous Si NWs template, which is a versatile platform, and it unravels the mechanism behind its superior photophysical properties.

Chapter 3 presents a comprehensive study of the strong cathodoluminescence (CL), bright PL, and photoresponse characteristics of $CH_3NH_3PbBr_3$ NPs embedded in a mesoporous Si NW template with superior ambient stability. The perovskite NPs confined in the mesopores show blue-shifted and enhanced CL emission as compared to the bare perovskite film, while the PL intensity of perovskite NPs is exceptionally high compared to its bulk counterpart. A systematic analysis of the CL/PL spectra reveals that the quantum confinement effect and ultralow density of defects in the perovskite NPs are mainly responsible for the enhanced CL and PL emissions. The room temperature PL quantum yield of the $CH_3NH_3PbBr_3$ NPs film on the NW template was found to be 40.5%, while that of perovskite film was 2.8%. Interestingly, the Si NWs/ $CH_3NH_3PbBr_3$ NPs junction shows superior visible light photodetection, and the prototype photodetector shows a high responsivity (0.223 A/W) with response speeds of 0.32 s and 0.28 s of growth and decay in photocurrent, respectively, at 2 V. This work demonstrates a low-cost fabrication of $CH_3NH_3PbBr_3$ NPs on a novel porous NW template, which shows excellent photophysical and optoelectronic properties with superior ambient stability.

Chapter 4 presents a facile solvent-free, room-temperature bulk scale solid-state synthesis of highly luminescent color-tunable $CsPbX_3$ perovskite NCs with superior optoelectronic performance and exceptional ambient stability. The composition tuned all-inorganic perovskite NCs exhibit high PL quantum yield (up to 95%) with adjustable emission color in the range 416 to 691 nm and high color purity (linewidth ~14 nm). The highly

luminescent perovskite NCs were utilized for the demonstration of color-tunable down-converting light-emitting diodes with high luminous efficiency (~42 lm/W for $CsPbBr_3$). We further integrate the $CsPbBr_3$ NCs on a direct CVD grown large-area monolayer MoS_2 on Si/SiO_2 substrates and fabricate a vertical heterojunction PD. The heterojunction PD shows very high responsivity (24.3 A/W at 405 nm) and extremely fast photo-response with photocurrent growth and decay times of 5.5 μs and 24.0 μs, respectively. The improved performance of the type-II heterojunction PD is attributed to the fast transfer of photogenerated electrons from $CsPbBr_3$ NCs to monolayer MoS_2 and the resulting n-doping of the MoS_2, which are fully supported by density functional theory based electronic structure calculations and Kelvin probe force microscopy measurement. Our results pave the way for the large-scale synthesis of highly stable and color-tunable $CsPbX_3$ NCs and their application in bright LEDs and high-performance photodetector with a swift response.

In Chapter 5, we present a facile, bulk scale room temperature solid-state synthesis of highly stable and luminescent Mn-doped $CsPbCl_3$ perovskite NCs with high Mn substitution, and investigate the origin and tunability of its dual-color emission. The Mn-doped $CsPbCl_3$ NCs exhibit distinct excitonic PL emission at ~412 nm and Mn related emission at ~590 nm with high PL quantum yield (up to 35%). Low-temperature PL measurement and excitation intensity-dependent PL, along with time-resolved PL studies, revealed valuable insights into the origin and tunability of Mn related orange-red PL in the dual color emitting Mn-doped $CsPbCl_3$ NCs. The PL line shape analysis revealed a new PL peak in the range ~634–666 nm, which grows stronger with higher doping concentration, and it is attributed to structural defects in the NCs. Finally, white light-emitting diodes (LEDs) were fabricated by employing blue-emitting $CsPbCl_{1.5}Br_{1.5}$ NCs, green-emitting $CsPbBr_3$ NCs, and orange-red emitting 10% Mn-doped $CsPbCl_3$ NCs all grown by the same method. Our work demonstrates a low-cost synthesis strategy for high Mn doping in $CsPbCl_3$ NCs with superior ambient stability and highly tunable emission.

In Chapter 6, we discuss an air-processed high-performance self-powered photodetector based on $CH_3NH_3PbI_3$ perovskite with plasmonic silver nanoparticle (Ag NP) embedded hole-transport-layer (HTL), without the use of any electron-transporting layer (ETL). It is demonstrated that in the absence of ETL in the device, the Ag NPs embedded PEDOT:PSS HTL improves the photodetection performance significantly. A novel N_2 gas-assisted fast crystallization method was used for the deposition of perovskite film in ambient

conditions to form a uniform perovskite layer. At zero bias, the ETL-free Ag NPs-perovskite hybrid device shows ~45% enhanced responsivity and ~3 times faster photoresponse compared to the pristine device. The enhancements in the performance of hybrid photodetector are attributed to plasmon-enhanced optical absorption and hot electron generation, as well as improvement in charge extraction and transport by Ag NPs, which are corroborated by steady-state, time-resolved PL measurements and Kelvin probe force microscopy-based work function analysis. Our results are significant for the development of high-performance, low-cost, ETL free plasmonic perovskite photodetectors for futuristic applications.

Chapter 7 presents the effect of substrate temperatures on the growth of vapor-deposited lead iodide film and its conversion into high-quality $CH_3NH_3PbI_3$ perovskite film using a two-step vacuum-solution deposition process for a large-area perovskite solar cells. With the increase in substrate temperatures for PbI_2 deposition, the films become more compact and pinhole-free with high crystallinity. Subsequently, the PbI_2 films were dipped into CH_3NH_3I solution and annealed for its transformation into $CH_3NH_3PbI_3$ perovskite film. Perovskite films using PbI_2 films deposited with higher substrate temperatures (150 ºC) possess large grain size and pinhole-free morphology, and these films show very high absorption coefficient in the UV-visible region and low radiative recombination compared to the film deposited at room temperature, which is beneficial for improving its performance in solar cells. We fabricated FTO/PEDOT:PSS/$CH_3NH_3PbI_3$/PCBM/Al planar perovskite solar cell with a device area of 5 mm × 5 mm using PbI_2 layers deposited at different substrate temperatures, while keeping the fabrication process identical for all the solar cells. Interestingly, the power conversion efficiency (PCE) improved by ~66% for the elevated temperature deposition of PbI_2 layer owing to the improved structural and optical properties of the perovskite film. The PCE was observed to be 13.1% for solar cells using PbI_2 layers deposited at 150 ºC, while PCE of the cell using PbI_2 layers deposited near room temperature (30 ºC) was found to be only 7.9%. In addition, the devices made using the PbI_2 layer deposited at 150 ºC show improved ambient stability as compared to the case of the PbI_2 layer deposited at 30 ºC. Thus, pinhole-free compact perovskite film helps in improved stability of the device due to the slowdown of diffusion of oxygen and water molecules into the compact perovskite layer. These results demonstrate that the spin-coating free two-step vapor-solution deposition technique is suitable for large-area perovskite solar cells with improved efficiency. Our results may stimulate further investigations for the vapor-solution process technique for high-efficiency perovskite solar cells.

Chapter 8 presents a summary of the work and highlights of the main contributions of the present thesis. Future scope of work on halide perovskite-based optoelectronic devices and solar cells are presented at the end.

LIST OF PUBLICATIONS:

A. In Peer-Reviewed Journals:

1. Joydip Ghosh, Ramesh Ghosh, and P. K. Giri, "Mesoporous Si Nanowire Templated Controlled Fabrication of Organometal Halide Perovskite Nanoparticles with High Photoluminescence Quantum Yield for Light-Emitting Applications." ***ACS Appl. Nano Mater.,*** 1, 1551-1562 (2018).

2. Joydip Ghosh, Ramesh Ghosh, and P. K. Giri, "Strong Cathodoluminescence and Fast Photoresponse from Embedded $CH_3NH_3PbBr_3$ Nanoparticles Exhibiting High Ambient Stability" ***ACS Appl. Mater. Interfaces,*** 11, 16, 14917-14931, (2019).

3. Joydip Ghosh, Gayatri Natu, and P. K. Giri, "Plasmonic hole-transport-layer enabled self-powered hybrid perovskite photodetector using a modified perovskite deposition method in ambient air" ***Org. Electron.,*** 71, 175-84, (2019).

4. Joydip Ghosh, Modasser Hossain, and P. K. Giri, "Origin and tunability of dual color emission in highly stable Mn doped $CsPbCl_3$ nanocrystals grown by a solid-state process" ***J. Colloids & Interface Sci.,*** 564, 357-370, (2020).

5. Joydip Ghosh, L. P. L. Mawlong, Manasa G. B, A. J. Pattison, W. Theis, S. Chakraborty and P. K. Giri "Solid-state synthesis of stable and color tunable cesium lead halide perovskite nanocrystals and the mechanism of high-performance photodetection in a monolayer $MoS_2/CsPbBr_3$ vertical heterojunction" ***J. Mater. Chem. C***, 8, 8917-8934, (2020).

6. Joydip Ghosh, Ramesh Ghosh, and P. K. Giri "Tuning the visible photoluminescence in Al doped ZnO thin film and its application in label-free glucose detection" ***Sens. Actuator B Chem.,*** 254, 681-689, (2018).

7. Ramesh Ghosh, Joydip Ghosh, Ruma Das, L. P. L. Mawlong, K. K. Paul, and P. K. Giri, "Multifunctional Ag nanoparticle decorated Si nanowires for sensing, photocatalysis and light emission applications" ***J. Colloid Interface Sci. ,*** 532, 464-473465 (2018).

B. Conference Proceeding

1. Joydip Ghosh, and P. K. Giri, "Effect of plasmonic metal nanoparticles on the performance of air processed inverted perovskite solar cells" ***AIP Conf. Proc.*** 20192082, 050004.1 (2019).

C. Manuscripts under Review/Communication:

1. Joydip Ghosh, and P. K. Giri, "Vacuum Deposited PbI_2 Film Grown at Elevated Temperatures for Improved Efficiency of Large-Area $CH_3NH_3PbI_3$ Based Planar Perovskite Solar cells" **(under revision)**.

2. Joydip Ghosh, and P. K. Giri "Recent advances in Perovskite/2D materials Hybrid Photodetectors" (invited review article) **(under review)**.

D. Conference Papers Presented:

1. Joydip Ghosh, Ramesh Ghosh, and P. K. Giri, "Fluorescence Quenching Based Glucose Sensing by Al Doped ZnO Thin Films", **NCRANNT-2016**, NEHU, Shillong, 8-9 September, 2016.

2. Joydip Ghosh, Ramesh Ghosh, and P. K. Giri, "Quantum Confinement Induced Photoluminescence Enhancement in Organo-Metal Halide Perovskite Nanoparticles Grown on a Mesoporous Nanowire Template", **ICC-2017**, Bikaner, Nov 24-25, 2017.

3. Joydip Ghosh, and P. K. Giri, "Effect of plasmonic metal NPs on inverted perovskite solar cell", **HyPe - 2017**, S.N. Bose National Centre for Basic Sciences, Kolkata, 14th -15th December, 2017.

4. Joydip Ghosh, and P. K. Giri, "Effect of plasmonic metal nanoparticles on the performance of air processed inverted perovskite solar cells", **ICONMAT-2019**, CUSAT, Kochi, Kerala, January 3-5, 2019.

5. Joydip Ghosh, L. P. L. Mawlong, and P. K. Giri , "Low cost, Solvent-free Mechanochemical-Synthesis of Color Tunable Cesium Lead Halide Perovskite Nanocrystals for High Performance Photodetection with CVD Grown Large Area Monolayer MoS_2", **PSCO-2019**, Lausanne, Switzerland, 30th September- 2nd October, 2019.

6. Joydip Ghosh, Gayatri Natu, and P. K. Giri, "Plasmonic hole-transport-layer enabled self-powered hybrid perovskite photodetector using a modified perovskite deposition method in ambient air", **ICANN-2019**, IIT Guwahati, 18-21st December 2019.

7. Joydip Ghosh, Larionette P. L. Mawlong, Manasa G. B, A. J. Pattison, W. Theis, S. Chakraborty, and P. K. Giri, "Solid-state Synthesis of Color Tunable Cesium Lead Halide Nanocrystals with High Stability and Mechanism of High-Performance Photodetection in Monolayer MoS_2/$CsPbBr_3$ Heterojunction", **ICONSAT-2020**, S.N. Bose National Centre for Basic Sciences, Kolkata, 5-7th march, 2020.

8. Joydip Ghosh, and P. K. Giri, "Solid-State Synthesis of Stable and Color Tunable Cesium Lead Halide Perovskite Nanocrystals and Mechanism of High-Performance Photodetection in a Monolayer MoS_2/$CsPbBr_3$ Vertical Heterojunction" **VCAN-2020**, Vellore Institute of Technology, Vellore, 17-19th June, 2020. ***(Best Oral Presentation Award Sponsored by "Royal Society of Chemistry")***

E. Workshops Attended:

1. "National Workshop on Advanced Probing Techniques in TEM", February 15-16th, 2016, IIT Guwahati, India.

2. "Workshop on advanced coating technology: opportunity for Indian industries (WACT-2016)", February 25-26th, 2016, IMMT Bhubaneswar.

3. "2nd National Workshop on MEMS/NEMS and Theranostic devices (NWNTD-2016)", March 21-22nd ,2016, IIT Guwahati, India.

4. "3rd National Workshop on MEMS/NEMS and Theranostic devices (NWNTD-2017)", March 21-23rd, 2017, IIT Guwahati, India.

5. "5th National Workshop on MEMS/NEMS and Theranostic devices (NWNTD-2019)", February 21-23rd, 2019, IIT Guwahati, India.

LIST OF ABBREVIATIONS

Abbreviation	***Description***
1-L	Monolayer
2D	Two Dimensional
CVD	Chemical Vapor Deposition
CL	Cathodoluminescence
DRS	Diffuse Reflectance Spectroscopy
EDS	Energy Dispersive X-ray Spectroscopy
ETL	Electron Transport Layer
EQE	External Quantum Efficiency
FESEM	Field Emission Scanning Electron Microscopy
FETEM	Field Emission Transmission Electron Microscopy
FWHM	Full Width at Half Maxima
HRTEM	High Resolution Transmission Electron Microscopy
HTL	Hole Transport Layer
KPFM	Kelvin Probe Force Microscopy
LED	Light Emitting Diode
MACE	Metal-assisted Chemical Etching
NC	Nanocrystal
NIR	Near Infrared
NP	Nanoparticle
NW	Nanowire
PD	Photodetector
PCE	Power Conversion Efficiency
PL	Photoluminescence
QC	Quantum Confinement
QD	Quantum Dot
QY	Quantum Yield
STEM	Scanning Transmission Electron Microscopy
TEM	Transmission Electron Microscopy
TRPL	Time Resolved Photoluminescence

UV-Vis	Ultraviolet Visible
XPS	X-ray Photoelectron Spectroscopy
XRD	X-ray Diffraction

Chapter 1

Introduction

Over the past decades, significant advances have been made in the synthesis, processing, and characterization of semiconductor nanostructures and thin films for potential technological applications in diverse areas, such as, energy conversion and storage devices, integrated optoelectronic and photonic devices, biosensors, etc. Since 2009, metal halide perovskites have emerged as a promising class of semiconductors due to their extraordinary performance in solar cells and other optoelectronic devices with the advantages of high light absorption coefficients, long electron-hole diffusion lengths, high carrier mobility, tunable optical band gap, and low-cost and low-temperature processing. The unique optical and electrical properties of halide perovskites have also shown great promises in other optoelectronic devices, such as light-emitting diodes (LEDs), laser, and photodetectors, etc. Perovskite nanostructures show interesting optical and electrical properties that significantly differ from their bulk counterpart such as strong anisotropic absorption and emission, high photoluminescence quantum yields (PL QY), large exciton binding energies and widely tunable bandgaps. Thus, perovskite nanostructures can offer many exciting and potentially unique opportunities for different optoelectronics.

In this chapter, we briefly present the important features of halide perovskite semiconductors. Structure, defects, and photophysical properties of perovskite nanostructures and thin films are presented systematically. Methodologies for the growth of various types of perovskite nanostructures and thin films and fundamental issues related to the growth process are discussed. The recent advances in halide perovskites for different optoelectronic applications, such as solar cells, photodetectors, light-emitting diodes, etc. are presented. The existing challenges and shortcomings of perovskite-based optoelectronic devices, such as toxicity of lead, ion migration, and poor stability in the presence of oxygen and water molecules are discussed in brief. The motivation and the focus of the present thesis are presented at the end of the chapter.

1.1. Halide Perovskite Semiconductors

The term ‘perovskite’ refers to the mineral form of calcium titanate ($CaTiO_3$), which was discovered in 1839 by the German mineralogist Gustav Rose and was named after the Russian mineralogist Lev Perovski. Since then, the term ‘perovskite’ is generally used to describe a group

of compounds having the crystalline structure of calcium titanium oxide. In 2009, Kojima et al. first demonstrated the application of organometal halide perovskite in solar cells.[1] Since then, these halide perovskite materials with the general formula of ABX_3 (where A and B are cations, and X is halide anion) have drawn extensive research attention for solar cells and other optoelectronic applications. By the combination of 'A', 'B' and 'X' ions, a large family of perovskite materials can be fabricated.[2-4] 'A' may be monovalent organic cation such as methylammonium ($CH_3NH_3^+$) and formamidinium ($HC(NH_2)_2^+$) or metal cation like Cs^+ while 'B' corresponds to divalent metal ions such as Pb^{2+} or Sn^{2+}.[5] These cations have been combined with halide anions (X), including Cl^-, Br^-, and I^-. Among the large group of halide perovskite materials, organic-inorganic methylammonium lead halide ($CH_3NH_3PbX_3$) and all-inorganic cesium lead halide ($CsPbX_3$) have shown great promises in solar cells and other optoelectronic applications. Thus, we focus on these two types of halide perovskites.

1.2. Crystal Structure of Halide Perovskite

Typically, the ABX_3 structure of perovskite consists of a three-dimensional (3D) network of corner-sharing $[BX_6]^{4-}$ octahedra, in which B^{2+} ions are located at the center of the octahedra, while the large cavity between adjacent octahedra is occupied by A^+ ions. The most widely studied perovskite material system is methylammonium lead halide. **Fig. 1.1** illustrates the crystal structure of organic-inorganic methylammonium lead halide perovskite.

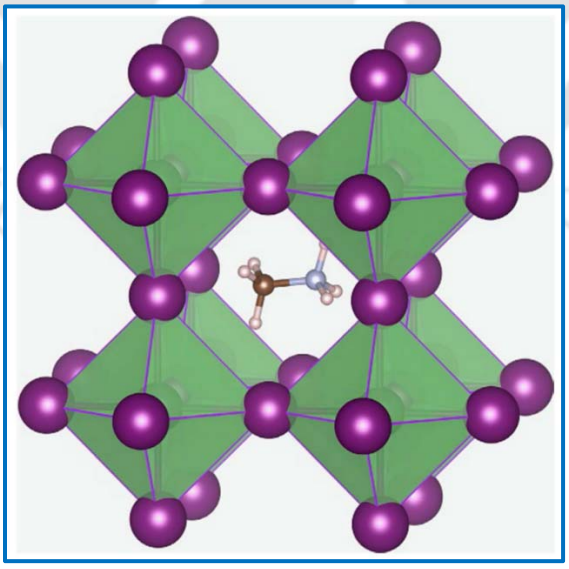

Fig. 1.1: Crystal structure of organometal halide $CH_3NH_3PbX_3$ (X= Cl^-, Br^- or I^-) perovskite. Methylammonium cation ($CH_3NH_3^+$) occupies the central A site surrounded by 12 nearest-neighbour halide ions in corner-sharing PbX_6 octahedra. Adopted from Ref. [6].

The crystal structure is comprised of an extended framework of corner-sharing PbI_6 octahedra with the methylammonium cation ($CH_3NH_3^+$) occupying the central A site and surrounded by 12 nearest-neighbour iodide ions.[6, 7] The all-inorganic cesium lead halide perovskites have the same crystal structure, as illustrated in **Fig. 1.1,** where A site methylammonium cation is replaced by cesium cation. For the formation of mixed composition halide perovskite or doping in perovskite, A, B, and/or X-sites can be substituted partially or completely with alternative elements/molecules of similar size.

Depending upon the temperature, perovskites exhibit different phases. In the temperature region 160 to 330 K, $CH_3NH_3PbI_3$ perovskite shows the tetragonal phase (space group I4/mcm). Above 330 K, the tetragonal phase transfers to the cubic phase (space group Pmm), and bellow 160 K tetragonal phase of $CH_3NH_3PbI_3$ converts to the orthorhombic phase (space group Pnma). **Fig. 1.2** illustrates the crystal structure of $CH_3NH_3PbI_3$ with different phases.[8]

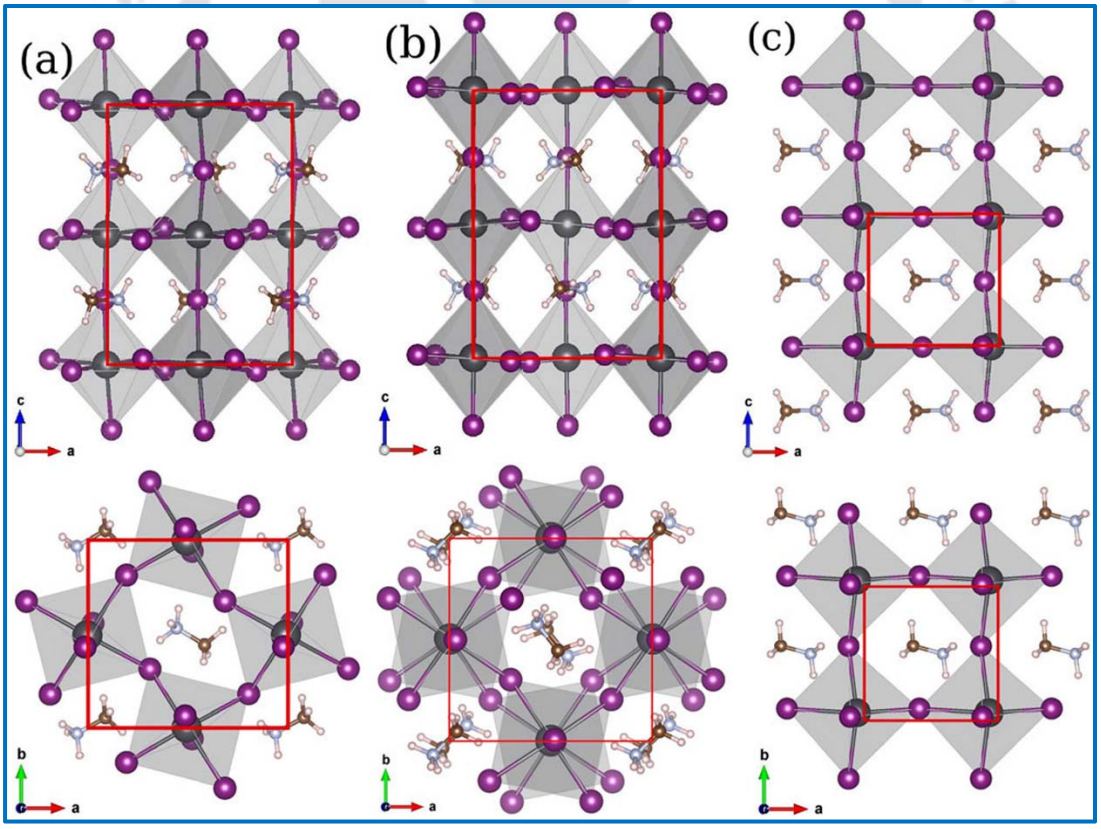

Fig. 1.2: Comparison of the crystal structure of $CH_3NH_3PbI_3$ with (a) orthorhombic, (b) tetragonal, and (c) cubic phases. Top row: ac-plane, bottom row: ab-plane. Adopted from Ref. [8].

Fig. 1.2(a-c) depicts the orthorhombic, tetragonal, and cubic phases $CH_3NH_3PbI_3$, respectively, along a-c (top row) and a-b (bottom row) plane. $CH_3NH_3PbBr_3$ crystals show three different phases, orthorhombic (<145 K), tetragonal (145-237 K), and cubic (>237 K).[9] Note that at room temperature, $CH_3NH_3PbI_3$ shows tetragonal phase while $CH_3NH_3PbBr_3$ perovskite exhibits cubic phase.

For all-inorganic $CsPbX_3$ perovskite, the cubic phase is stable at higher temperatures. At room temperature, the $CsPbX_3$ possesses a thermodynamically preferred orthorhombic structure with the space group Pnma.[10] Note that different polymorphs of perovskite have a strong influence on their optoelectronic properties. For example, $CsPbI_3$ with cubic polymorph (black phase) shows excellent performance in solar cells, while the orthorhombic polymorph (yellow phase) of $CsPbI_3$ exhibits poor device performance.

1.3. Band Structure of Halide Perovskite

Investigation of the electronic band structure of a material is one of the fundamental interest in order to predict its suitability for different optoelectronic and other applications. Generally, perovskite material has a well-defined conduction band, valance band, large dielectric constants, and small effective mass.[11] **Fig. 1.3** illustrates the band structure of $CH_3NH_3PbX_3$ (X = I, Br, Cl) perovskite calculated using the approximate quasiparticle density functional theory (DFT)-1/2 method.[12] The thick solid lines correspond to the conduction band (CB) and valance band (VB) of $CH_3NH_3PbI_3$, $CH_3NH_3PbBr_3$, and $CH_3NH_3PbCl_3$. The bandgap increases by substitution of halide ions from I to Cl, as shown in **Fig. 1.3,** which is in good agreement with the experimental data. The substitution of halide ions (I, Br or Cl) has little influence on the band dispersion of the CB (consisting mainly of Pb 6p states) but leads to substantial changes in the VB (consisting mainly of halide np states and to some extent of Pb 6 s states) of perovskite, as shown in **Fig. 1.3**. More dispersion in the VB is observed when substituting I by Br and Cl, shown by the downshifting of the bands at the Γ point (see **Fig. 1.3**).[12] Note that the bandgap of perovskite can be tuned over the entire UV-visible range by changing the halide content.

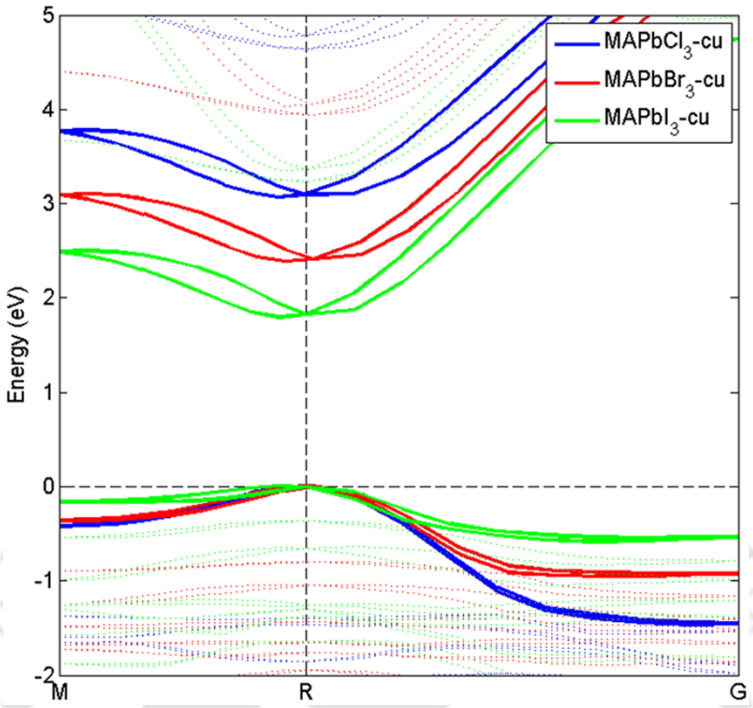

Fig. 1.3: Calculated DFT-1/2 band structure of $CH_3NH_3PbCl_3$, $CH_3NH_3PbBr_3$, and $CH_3NH_3PbI_3$. The solid lines correspond to the conduction and valance band of each system. Adopted from Ref. [12]

1.4. Key Properties of Halide Perovskite

Here, we summarize the different properties of halide perovskite relevant for different optoelectronic applications.

1.4.1. Tunable Light Absorption and Emission

One of the most fascinating properties of halide perovskites is that they are direct-bandgap semiconductors with very large absorption coefficients of up to ~10^5 cm^{-1} in the UV-visible range.[13, 14] The optical-absorption coefficient of perovskite material is closely related to its electronic structure. Due to the strong light absorption, a very thin layer of perovskite is effective for different optoelectronic applications. Interestingly, the bandgap of halide perovskites can be tuned by chemical substitution without significant changes in the fundamental electronic properties. Generally, the bandgap and transport properties of halide perovskite can be tunable by changing A site cation, metal cation, and halide anion, though the easiest way to tune the bandgap of perovskite over the entire UV-visible region is the substitution of halide content from Cl to Br to I. For example, the bandgap of $CH_3NH_3PbCl_3$, $CH_3NH_3PbBr_3$ and $CH_3NH_3PbI_3$ are observed to be ~3.1 eV, 2.2 eV, and 1.6 eV, respectively.[15] For other mixed halide perovskites, bandgap was

found to lie in between 1.6 eV and 3.1 eV depending upon the halide ions. Change of A site cation also slightly affects the bandgap. For instance, by replacing methylammonium by formamidinium cation, which is a slightly larger molecule, bandgap changes from 1.6 to ~1.48 eV. As perovskite is a direct bandgap semiconductor, it shows strong photoluminescence (PL) emission due to the band edge excitonic recombination. Typically, the photogenerated carrier generation and exciton recombination efficiency vary for different halide perovskites. For example, iodine based perovskites ($CH_3NH_3PbI_3$ or $CsPbI_3$) exhibit very high photogenerated carrier generation with low radiative recombination, which is suitable for solar cell and photodetection applications. On the other hand, bromine-based perovskites ($CH_3NH_3PbBr_3$ or $CsPbBr_3$) show high radiative recombination with high photoluminescence quantum yield (PL QY) suitable for LED applications. However, carrier generation and recombination of halide perovskite depend on several other factors, such as defects, grain boundaries, etc.

Interestingly, perovskite nanostructures have shown interesting size-dependent optical and electronic properties that differ significantly from their bulk counterparts.[16-18] Bulk perovskite possesses low PL QY, which is attributed to two key limiting factors: (a) a low exciton binding energy, which results in low electron-hole radiative recombination rate, and (b) the presence of mobile ionic defects, which are characterized by low formation energy. On the other hand, very high radiative recombination with high PL QY is observed in perovskite nanostructures due to quantum confinement effect and ultra-low defects. The bandgap and emission properties can also be tunable depending on size and shapes of different perovskite nanostructures, such as nanocrystals (NCs), quantum dots (QDs), nanoplatelets (NPLs), nanosheets (NSs), nanowires (NWs), etc.[19] Note that, the sizes of these perovskite nanostructures can be precisely controlled down to a single perovskite layer, and, consequently, significantly below the exciton Bohr radius.[17, 20] Thus absorption and PL emission vary strongly with a small change in the size of the nanostructures in the strong quantum confinement regime.

1.4.2. Superior Charge Transport

Carrier transport is an important parameter in any optoelectronic device. Charge-carrier transport in semiconductors is directly related to the electronic band structure. In halide perovskites, photoinduced charge carriers quickly relax to band edges due to the electron-phonon coupling.[21] The electron-phonon coupling in perovskite has a substantial impact on its charge carrier dynamics, leading to high intrinsic mobility.[22] Due to the long drift lengths, as estimated from their

mobilities and carrier lifetimes, halide perovskites are suitable for high-performance solar cells and photodetectors. Free photogenerated carriers are usually associated with diffusion lengths. The diffusion lengths of polycrystalline $CH_3NH_3PbI_3$ film were measured to be >1 μm, while for $CH_3NH_3PbI_3$ single crystal it was observed to be >175 μm.[23, 24] Note that diffusion lengths are strongly correlated with film composition and morphology and grain size being sensitive to deposition methods as well as processing conditions. For polycrystalline perovskites film, diffusion coefficients and mobilities have been reported up to 0.05-0.2 $cm^2 s^{-1}$ and 1–30 $cm^2 V^{-1} s^{-1}$, respectively, while for single crystal perovskites the carrier mobility was observed to be > 200 $cm^2 V^{-1} s^{-1}$.[25, 26] The carrier lifetimes of perovskite also vary from few ns to μs depending upon the composition, morphology, grain size, defects, etc. Thus, due to high carrier mobility, long diffusion length, and long carrier lifetime, halide perovskites have emerged as a potential candidate for photodetection and solar cell applications.

1.4.3. Defects and Traps

In semiconductors, there are mainly two types of carrier trap states: (a) deep traps, and (b) shallow traps.[27] Note that the trap states are mostly generated at the surfaces and interfaces of perovskites due to a higher possibility of crystal-structure deformation. The electron-phonon coupling also creates trap state in perovskite.[28] Stranks et al. demonstrated that trap states are intrinsic to the perovskite, and the trap density can vary with temperature due to thermally activated atomic vacancies, which are the common form of the shallow defects in halide perovskites.[29] The shallow defects strongly affect the charge-transport properties of perovskite. For polycrystalline perovskite films, bulk trap density was calculated to be in the range 5×10^{14} - 7.5×10^{17} cm^{-3}, while the surface trap density was measured to be ~10^{17} cm^{-3}.[30] However, for perovskite single-crystals, the trap density was found to be as low as 10^{10} cm^{-3}.[31] Note that defects and trap density in perovskite depend on synthesis procedure, composition, morphology, grain boundaries, etc. The defect and trap states are detrimental to the performance of different perovskite optoelectronic devices. Different strategies have been explored to control/ minimize the defects and charge traps in perovskite, and enhanced performances were observed. Ion migration can hinder the long-term stability of perovskite optoelectronic devices. Due to chemical or structural changes caused by ion migration, the trap density in halide perovskites can increase, which result in poor device performance.

1.5. Fabrication of Perovskite Films and Nanostructures

Over the past decades, numerous chemical and physical techniques have been developed for the fabrication of high-quality perovskite thin films and shape tailored perovskite nanostructures, aimed at dedicated advanced applications.

1.5.1. Fabrication of Perovskite Films

The morphology of the perovskite active layer has a significant impact on the final device performances. The uniform crystalline films with high coverage and large grains are beneficial to achieve higher power conversion efficiencies (PCE) of solar cells. Small grain sizes increase the volume of grain boundaries within the perovskite layer, which can act as charge traps and facilitate trap assistant recombination, thereby limiting device efficiency. Generally, morphology is influenced by the deposition method, solvent, composition, and any subsequent post-treatments of the perovskite layer. Fabrication of perovskite films by solution processing is well established for solar cells and other optoelectronic applications due to simple, low cost and low-energy manufacturing process. A number of different solution deposition techniques have been developed. Usually, for the deposition of perovskite active layer, single-step spin coating, or sequential two-step spin coating methods are used. In the 'one-step' deposition processes, the perovskite precursors are dissolved in a common solution before they are casted into a film.[2] In the two-step deposition method, one precursor (usually a metal halide, e.g., PbI_2) is first casted onto a substrate, and then the other precursor (usually the organic component CH_3NH_3I) is deposited on top of it for conversion into perovskite structure.[32]

Zhou et al. fabricated mixed halide organic-inorganic perovskite films by a single-step spin coating method for solar cells.[33] A 1:3 ratio of $PbCl_2$:CH_3NH_3I was mixed in dimethylformamide (DMF), with a concentration of 0.73M and 2.2M, respectively. The mixture solution was stirred at room temperature overnight and spin-coated on the substrates without pre-heating at 2000 rpm for 30 seconds, and then annealing at 90 °C for 1 h and 100 °C for 25 minutes results in perovskite film.

Nie et al. prepared solution-processed perovskite films with millimeter-scale grains for high-efficiency solar cells.[34] They fabricated a perovskite film by a single step hot casting method, as shown schematically in **Fig. 1.4**. Their approach involves casting a hot (~70°C) precursor solution of PbI_2 and CH_3NH_3Cl onto a substrate maintained at a temperature of up to 180°C and subsequently spin coated (15 s) to obtain a uniform perovskite film. A precursor solution PbI_2 and

CH_3NH_3Cl with a molar ratio of 1:1 results in mixed halide perovskite films with the best morphology and device performance. They observed large, millimeter-scale crystalline grains with a unique leaf-like pattern radiating from the center of the grain.

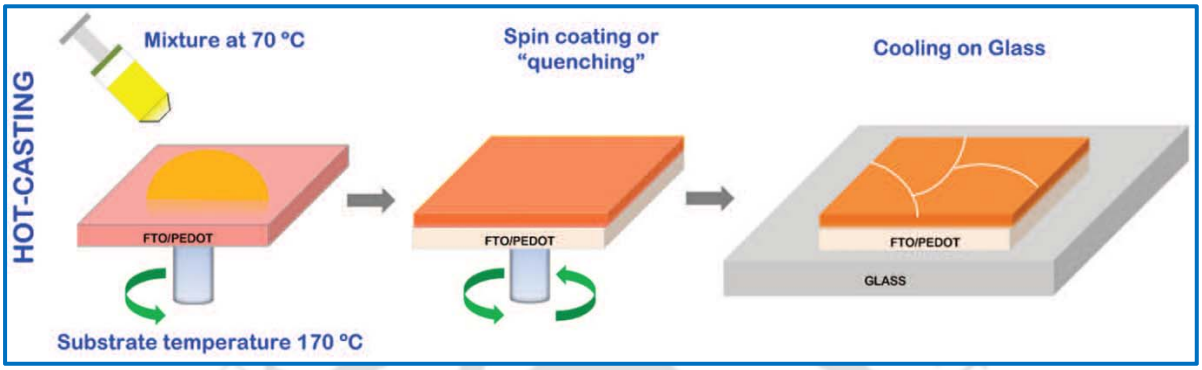

Fig. 1.4: Processing scheme for perovskite thin film deposited by single-step hot-casting methods. Adopted from Ref. [34].

Xiao et al. demonstrated a method of forming a continuous and compact $CH_3NH_3PbI_3$ perovskite film by two-step interdiffusion of spin-coated stacking layers of PbI_2 and CH_3NH_3I through annealing, as depicted in **Fig. 1.5**.[35]

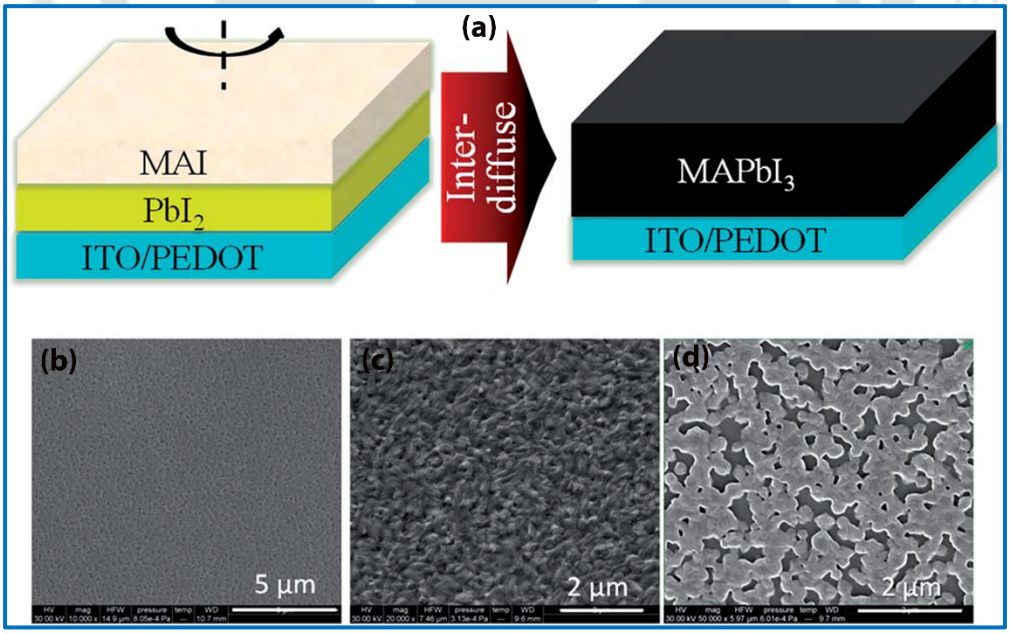

Fig. 1.5: Schematics of spin coating of PbI_2 and CH_3NH_3I and the conversion of the stacking layer into a perovskite layer upon annealing. The SEM image of (b) the PbI_2 film, (c) the annealed perovskite layer formed by an interdiffusion process, and (d) the annealed perovskite film spun from the premixed PbI_2 and CH_3NH_3I solution. Adopted from Ref. [35].

First, PbI_2 and CH_3NH_3I were dissolved in DMF and 2-propanol, respectively, as precursor solutions. A supersaturated hot solution of PbI_2 was used for quick drying to obtain a pin-hole free and compact PbI_2 layer, as shown in **Fig. 1.5(b)**. Further CH_3NH_3I solution in propanol was spin coated on top of the PbI_2 layer. Next, the bilayer films were annealed at a temperature of 100 °C for the formation of the perovskite layer. The morphology of perovskite is shown in **Fig. 1.5(c).** For comparison, they also fabricated perovskite film by a single-step spin coating method using premixed PbI_2 and CH_3NH_3I and observed non-uniform films with discontinuous microstructures on the surface, as shown in **Fig. 1.5(d).**

Li et al. used a vacuum flash-assisted solution process for the deposition of high-quality perovskite film with large grains.[36] The perovskite precursor solution was first spin coated on top of the substrates. Next, the film was placed for a few seconds into a vacuum chamber to boost the rapid crystallization of the perovskite. The pressure applied during the vacuum flash process influences the formation of perovskite film with superior quality. They obtained optimal results with an applied pressure of 20 Pa.

Different organic solvents have different evaporation rates and can solubilize perovskite precursors with different efficiency. Various solvents and solvent additives can be used to modify the structural uniformity and crystallinity within a perovskite film. Perovskite films deposited from a DMF solvent do not usually completely cover a surface, but instead, contain voids and pinholes present at the surface or in the bulk of the active layer. Higher boiling point solvents (e.g., dimethylsulfoxide (DMSO) or γ-butyrolactone (GBL)) are usually able to produce more uniform crystal domains and smoother film surfaces. Different types of modified spin coating methods have also been explored for the deposition of perovskite layer, such as solvent engineering, anti-solvent assisted crystallization, gas-assisted nucleation, etc. to form homogenous perovskite films directly from the perovskite precursor solution. Xiao et al. reported a one-step anti-solvent-induced fast crystallization method for the fabrication of uniform perovskite films with large grains.[37] $CH_3NH_3PbI_3$ perovskite precursor solution (45 wt%) in DMF was then spin-coated on the substrates at 5000 rpm. After a specific delay time (e.g., 6 s), a bad solvent/anti-solvent (chlorobenzene) was quickly added to the substrate, as illustrated in **Fig. 1.6**. The role of the anti-solvent is to rapidly decrease the solubility of $CH_3NH_3PbI_3$ in the mixed solvent and thereby promoting fast nucleation and growth of uniform and compact perovskite film. In the conventional

spin-coating process, in contrast, more rough and non-uniform perovskite film with poor coverage was observed, as illustrated in **Fig. 1.6**.

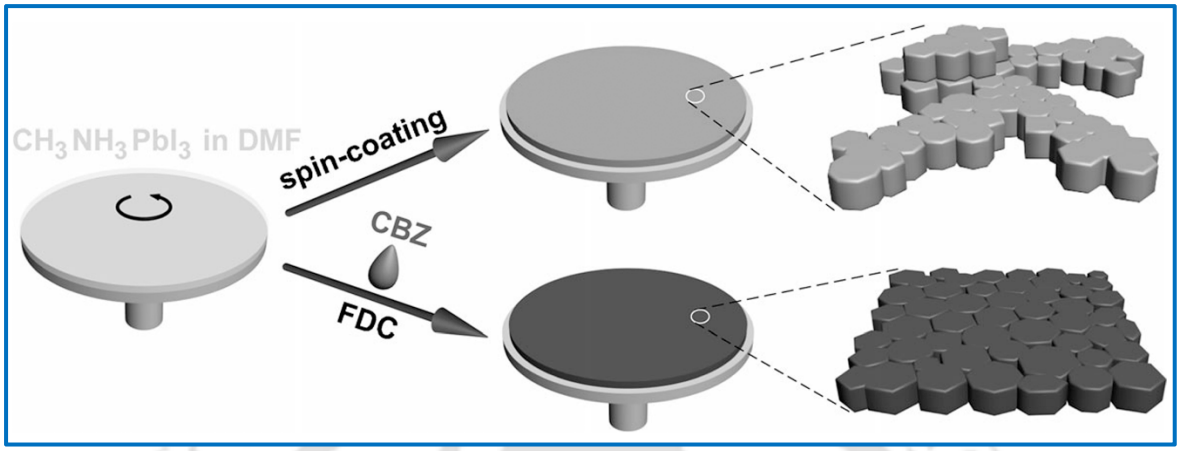

Fig. 1.6: Schematic illustration of the anti-solvent assisted fast crystallization process and conventional spin-coating process for fabricating perovskite films. Conventional spin-coating (top) results in non-uniform poor perovskite film. In the fast crystallization process (bottom), the second solvent (chlorobenzene) results in uniform perovskite film. Adopted from Ref. [37].

Though significant progress has been achieved in solution-processed high-quality perovskite film for high-efficiency solar cells, the deposition of large-area perovskite film for commercial applications by the spin coating method is quite challenging due to the complexity of the processing and reproducibility of the devices.[38] In the spin coating method, different toxic and volatile organic solvents, such as DMF, DMSO are also used. Thus, it is important to explore alternative green methods for the deposition of large-area perovskite film without toxic solvents. Interestingly, spin coating free deposition techniques have also been explored for perovskite films.

Liu reported the fabrication of homogeneous perovskite films by using the dual-source co-evaporation technique.[14] They placed approximately 500 mg of CH_3NH_3I and100 mg of $PbCl_2$ into separate crucibles for dual-source vapour deposition. The base pressure of the deposition chamber was maintained at ~10^{-5} mbar. CH_3NH_3I was heated to ~120 ºC, and $PbCl_2$ was heated to ~ 325ºC. **Fig. 1.7(a)** depicts the schematic illustration of the deposition of perovskite films by the dual-source vapour deposition process. The vapour-deposited films are extremely uniform, with grain size of scale of hundreds of nanometers, as shown in **Fig. 1.7(b)**. The optimum device performance was observed with a 330 nm thick active perovskite film. However, it is very difficult to control the deposition of the organic part (CH_3NH_3I) in the dual-source co-evaporation technique.

Fan and co-workers fabricated perovskite film by a single-source vapour deposition process.[39] $CH_3NH_3PbI_3$ single crystals were fabricated by the reaction of CH_3NH_3I and PbI_2. Next, these single crystals are grind to form fine powder, and this perovskite powder was used for vacuum deposition. The thickness of the perovskite active film was about 400 nm.

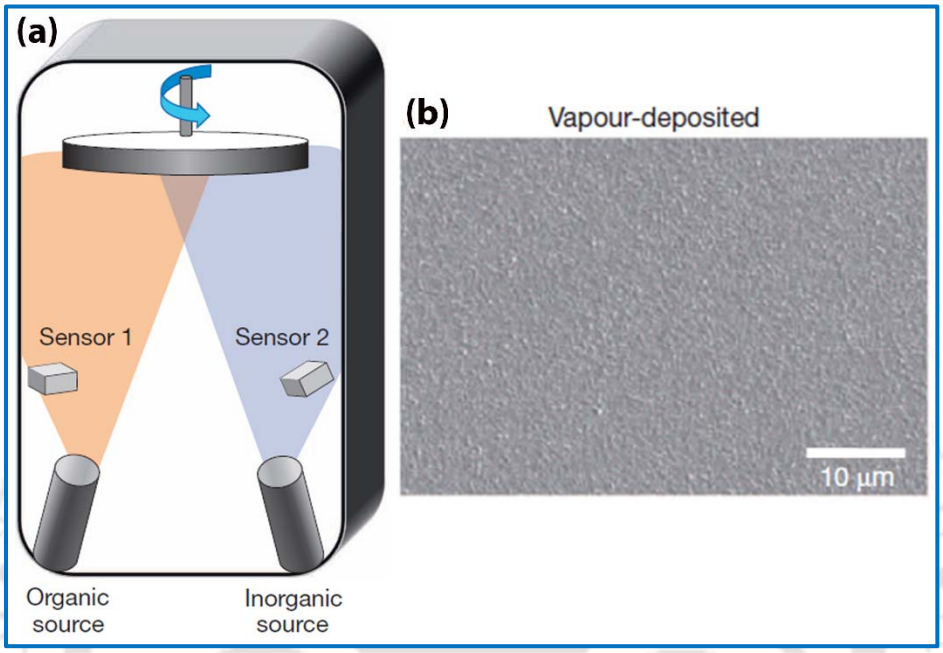

Fig. 1.7: (a) Schematic illustration of dual-source thermal evaporation technique for deposition of perovskite film. (b) FESEM image of vapour deposited perovskite film. Adopted from Ref. [14].

Chen et al. reported a sequential deposition of PbI_2 and CH_3NH_3I for the fabrication of perovskite film.[40] Longo et al. reported flash evaporation for the deposition of perovskite film.[41] Fu et al. reported a hybrid sequential deposition method in which PbI_2 was deposited by vapor deposition, while the CH_3NH_3I was deposited by spin coating technique.[42] Though significant advances have achieved in the deposition of perovskite films, it is still interesting to study alternative methods for the deposition of perovskite films at ambient conditions.

1.5.2. Fabrication of Perovskite Nanostructures

Interestingly, despite being counterintuitive, metal halide perovskites were demonstrated to be good not only for separating charges efficiently in high-performance photovoltaics but also for bringing charges together to create light.[16, 18, 43] Unfortunately, bulk perovskite possesses very low PL QY, while the nanostructure perovskites exhibit very high PL QY. Significant advancement has been made in the fabrication of perovskite nanostructures by several methods. Fabrication of

nanostructures can be classified either as “top-down” or as “bottom-up” method. Top-down strategies involve a fragmentation and structuring of macroscopic solids, either chemically or mechanically, whereas the bottom-up routes start with molecules and ions and proceed for nucleation and growth of nanostructures. Liquid-phase chemical reactions, such as the hot-injection method, and ligand assisted reprecipitation (LARP) method are the most explored synthesis methods for the fabrication of different shape-tailored perovskite nanostructures.

The hot injection is involved in the rapid injection of a precursor into a hot solution of the remaining precursors, ligands, and a high boiling solvent.[44] The key parameters to control the size and shape of colloidal NCs/QDs in hot injection technique are : (i) ratio of the surfactants to the precursors; (ii) injection temperature of the cation or anion precursor; (iii) reaction time; and (iv) concentration of the precursors. Protesescu et al. first demonstrated the colloidal synthesis of all-inorganic $CsPbX_3$ (X = Cl, Br, and I) NCs by hot injection method.[45] Composition tunable $CsPbX_3$ NCs were synthesized by injecting Cs-oleate precursor solution into a hot solution (140−200 °C) of PbX_2 (X= Cl, Br, I) salts, dissolved in octadecene (ODE), carboxylic acids, and primary amines.[45] They observed monodispersed perovskite NCs, as shown in the TEM image **(Fig. 1.8(a))**. By simply adjusting the ratio of lead halide salts, they also synthesized mixed-halide perovskite NCs.

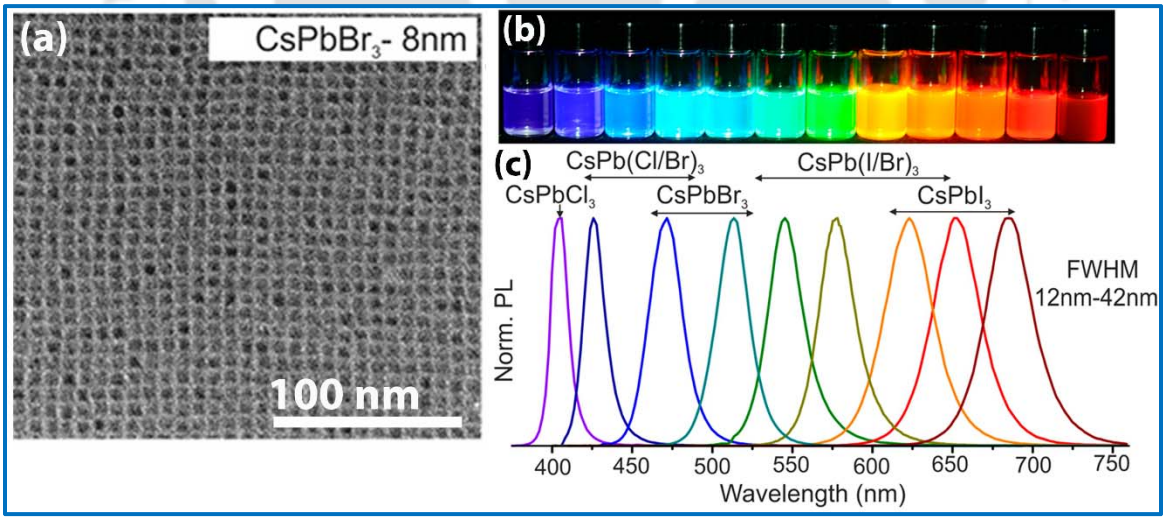

Fig. 1.8: (a) TEM image of monodispersed $CsPbBr_3$ NCs. (b) Photograph of a colloidal dispersion of different perovskite NCs under UV light showing the bright emissions of different colors. (c) Normalized PL spectra of perovskite NCs showing emission over the entire visible region. Adopted from Ref. [45].

Fig. 1.8(b) depicts the emission of different colors from the NCs under UV light excitation. The PL emission of the perovskite NCs could be finely tuned across the entire visible spectrum

(410−700 nm) by varying the halide composition, as shown in **Fig. 1.8(c).** These NCs exhibit very high PL QY (50−90%).

Vybornyi et al. synthesized organic-inorganic hybrid $CH_3NH_3PbX_3$ perovskite NCs by hot injection method using high-boiling nonpolar solvent (1-octadecene) in the presence of oleylamine and oleic acid as coordinating ligands.[46] These NCs show PL QY in the range of 15-50%.

Bekenstein et al. reported colloidal quasi-two-dimensional $CsPbBr_3$ nanoplates (NPLs) with PL QY of 84%.[47] Zhang and co-workers demonstrated $CsPbBr_3$ NWs by hot injection method using high reaction temperatures and long reaction times.[48]

Doping in perovskite NCs with Mn, and other main group metal cations, transition metal cations, and rare earth metal cations are also explored to improve the optoelectronic properties. By making simple modifications to the standard hot-injection approach, lead halide based NCs systems were successfully doped with different impurity ions.[49-52] Parobek et al. synthesized Mn^{2+} doped $CsPbCl_3$ NCs using hot injection method by simply employing $MnCl_2$, in addition to $PbCl_2$.[53] These NCs show dual-color PL emission: (a) emission in the UV region is attributed to the band edge excitonic recombination, (b) emission in the orange-red region is observed due to the energy transfer to Mn^{2+} state and followed by radiative recombination. **Fig. 1.9(a)** depicts the TEM image of Mn-doped $CsPbCl_3$ NCs and **Fig. 1.9(b)** shows a comparison of the PL spectra of undoped $CsPbCl_3$ and Mn-doped $CsPbCl_3$ NCs. The emissions of undoped and Mn-doped $CsPbCl_3$ NCs under UV light are shown in **Fig. 1.9(c)**.

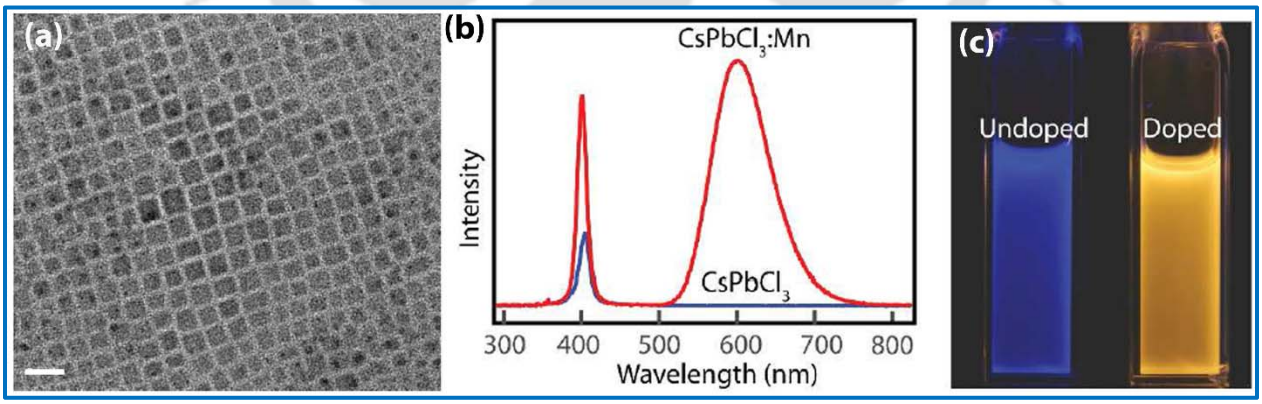

Fig. 1.9: (a) TEM images of Mn-doped $CsPbCl_3$ NCs. (b) Comparison of PL spectra of undoped and Mn-doped $CsPbCl_3$ NCs. (c) Photograph of colloidal dispersion of undoped and Mn-doped $CsPbCl_3$ NCs under UV showing the corresponding emission. Adopted from Ref. [53].

For the synthesis of perovskite NCs by the LARP process, first, a supersaturated perovskite precursor solution is prepared. Next, a solvent is added in which the solubility of the ions is very

low. Under such conditions, spontaneous crystallization and precipitation reactions occur, which result in perovskite NCs. Zhang et al. reported color-tunable colloidal $CH_3NH_3PbX_3$ QDs with PL QY up to 70% using the LARP method.[54] Li and co-workers synthesized all inorganic $CsPbX_3$ QDs by room temperature LARP method.[55]

Though these colloidal NCs show very high light emission efficiency, the emission intensity tends to substantially reduce when NCs are processed as thin films due to spontaneous aggregation. Note that the luminescent NPs are often necessary in solid or thin-film form for practical device applications. Interestingly, the growth of perovskite NCs inside an ordered inorganic mesoporous host matrix is an alternative, ligand-free route to study the effects on the optical properties due to size reduction. Interestingly, the growth of perovskite NPs using porous aluminum oxide (Al_2O_3) and silica (SiO_2) templates have been reported, which show very interesting optical properties due to quantum size effect.[56-59] Another advantage of this perovskite NPs/NCs embedded in the porous template is its enhanced air stability due to the encapsulation from the surrounding atmosphere by the stable inorganic host matrix.[58] Demchyshyn et al. reported nanoporous Si and Al_2O_3 thin films as templates for the growth of perovskite nanocrystallites directly within device-relevant architectures without the use of colloidal stabilization, as illustrated in **Fig.1.10(a)**.[58] They observed blue-shifted PL with high PL QY and enhanced stability in the perovskite NCs confined in the mesoporous template. **Fig. 1.10(b)** depicts the TEM image of $CH_3NH_3PbI_3$ NCs embedded in mesoporous Si template. **Fig. 1.10(c)** shows a comparison of PL spectra of bulk and perovskite NCs showing the blue shift in PL peak for NPs.

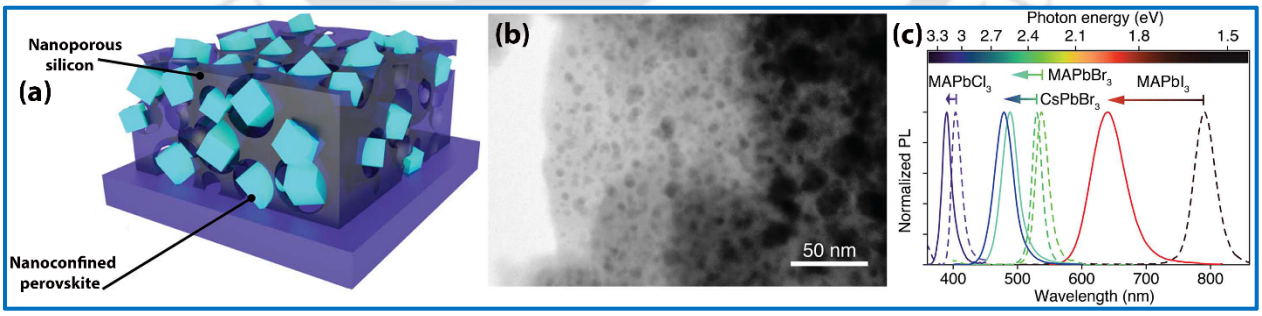

Fig. 1.10: (a) Schematic of perovskite NCs embedded in porous Si template. (b) TEM image of perovskite NCs embedded in mesoporous Si template. (c) Comparison PL of different perovskite NCs showing tunable PL emission over the entire visible region. Dashed lines indicate PL spectra of bulk perovskite films. Adopted from Ref. [58].

1.6. Applications of Metal Halide Perovskite

Halide perovskites have emerged as a class of most promising and cost-effective semiconductor materials for next-generation optoelectronic devices.[60] Some of the potential applications of perovskites are elaborated below.

1.6.1. Perovskite Solar cells

For the first time, in 2009, Kojima *et al.* used organic-inorganic hybrid perovskite in a solar cell with the architecture of a dye-sensitized solar cell with a PCE of 3.8%.[1] In 2012, Kim *et al.* reported an evolutionary jump in PCE (9.7%) using spiro-MeOTAD and mesoporous TiO_2 as the hole transport and electron transport materials, respectively, for the first reported perovskite-based solid-state mesoscopic heterojunction solar cell.[61] Since then, perovskite solar cells using a solution-processed photoactive layer have reached PCEs over 23% using compositional or interfacial engineering.[62, 63] For efficient perovskite solar cells, the quality of the perovskite layer and a defect-free interfacial structure are very important.

A perovskite solar cell has a structure that usually comprises a substrate, electrodes, a perovskite photoactive layer, together with necessary charge transport layers (i.e., a hole transport layer (HTL) and an electron transport layer (ETL). The HTL and ETL are used to separate and transport of photogenerated holes and electrons, respectively, while the perovskite layer acts as a light-absorbing active material. Due to the low exciton binding energy and the ambipolar charge carrier mobility of perovskites, charge carriers can be extracted even without any HTL or ETL. However, HTL and ETL are necessary to achieve high-efficiency solar cells, as the open-circuit voltage (V_{OC}), short circuit current density (J_{SC}), and fill factor (FF) in a solar cell are determined by these transport layers. **Fig. 1.11** illustrates a typical device structure of a perovskite solar cell on a fluorine-doped tin oxide (FTO) or ITO glass substrate. Depending on the position/sequence of the ETL and HTL, the device structure is defined. Generally, the n-i-p device is called as normal structure, and p-i-n structure is called as inverted device structure.[64]

Depending on the structure, perovskite solar cells are mainly of two types: meso-superstructured perovskite solar cells that incorporate a mesoporous layer, and planar perovskite solar cell in which all layers are planar.[65] First demonstrated highly efficient perovskite solar cells were typical mesoporous n-i-p structured.[66] In mesostructured solar cells, a compact ETL (e.g., compact TiO_2) is usually deposited onto a transparent conducting oxide layer (e.g., FTO), which is used to extract electrons and block holes. The compact TiO_2 layer is usually deposited by spin

coating and typically requires sintering or calcination at high temperature.[67] Next, a mesoporous layer (such as TiO_2, Al_2O_3, ZnO, ZrO_2, NiO) is deposited on top of the compact layer.[68-70] Next, the perovskite active material is deposited on top of mesoporous layer.[71]

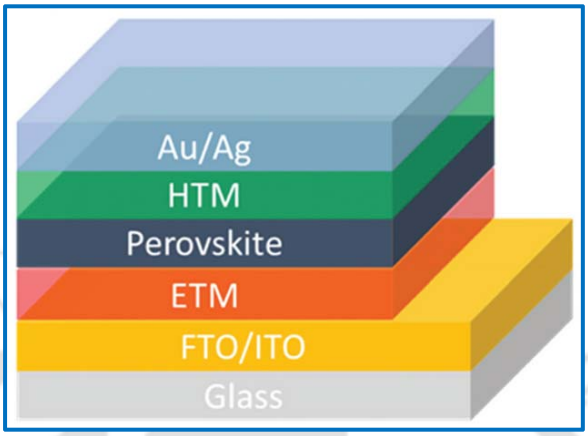

Fig. 1.11: Device architecture of a perovskite solar cell. Adopted from Ref. [60].

Finally, HTL (e.g., spiro-MeOTAD) and electrode are deposited to complete the device. You and co-workers demonstrated FTO/TiO_2/$CH_3NH_3PbI_3$/spiro-OMeTAD/Au solar cells with an efficiency of 20.1%.[72] Note that due to high-temperature sintering/calcination process involved in mesostructured devices, it is difficult to fabricate it on flexible substrates.

The configuration of planar perovskite solar cells can be either a normal structure or an inverted structure. Typically, the normal structure is similar to that of mesostructured devices, except that it does not utilize mesoporous materials. In inverted structure devices, generally different organic-semiconductors are used as HTL (e.g., PEDOT:PSS) and ETL (e.g., PCBM, C60-SAM or PFN).[73] Li et al. fabricated an inverted structure consisting of ITO/PEDOT:PSS/ $CH_3NH_3PbI_{3-x}Clx$/PCBM/PFN/Al in ambient air with humidity and achieved a PCE of 17.1%.[74] The organic-semiconductors have the advantage of relatively simple compatibility with the low-temperature deposition processes. Thus, inverted structure planar configuration is very useful for the fabrication of devices in flexible substrates.[75]

A large number of organic and inorganic materials have been used as ETM and HTM in perovskite solar cells.[7] One can design an efficient device by selecting perovskites, HTM, and ETM by referring to the energy states and bandgaps, as shown in **Fig. 1.12**.[60] Due to photoexcitation, electrons and hole pairs are generated in perovskite active layers, which further transport to ETL and HTL, as shown in **Fig. 1.12.**

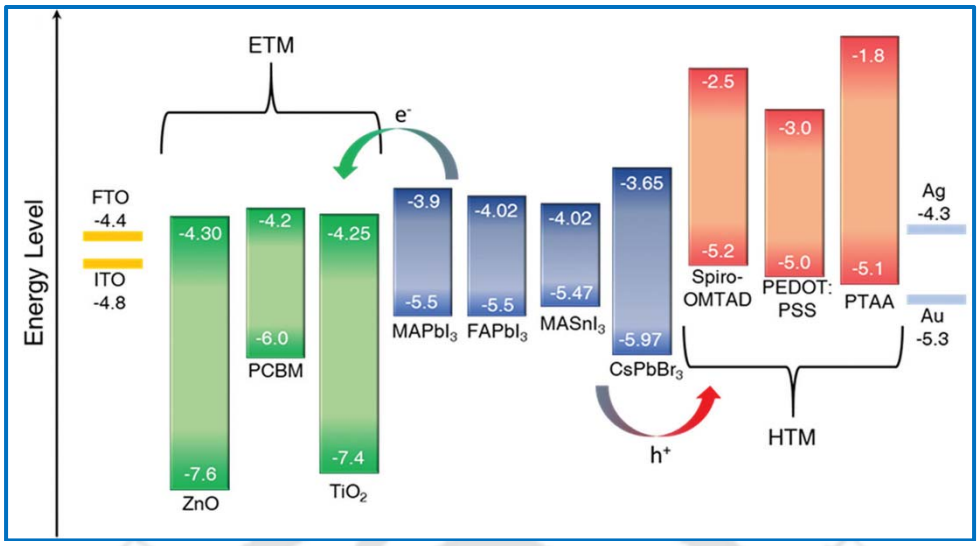

Fig. 1.12: Energy levels of various ETM, HTM, perovskite, and electrode materials. Adopted from Ref. [60].

Flexible photovoltaics have been attracting more attention due to their unique properties, including lightweight, high flexibility, and the ability to be reshaped easily.[75] Polymeric materials such as PEN or PET are widely used as a substrate for flexible perovskite solar cells.[76] Liu et al. reported flexible solar cells with PCE of 17.3% and structure of PEN/ITO/SnO_2/Perovskite/Spiro-OMeTAD/Au.[77] Li et al. fabricated perovskite solar cells on a flexible substrate with PCE of 18.3% and structure of PEN/ITO/SnO_2-CPTA/Perovskite/SpiroOMeTAD /Au.[74]

The morphology and microstructure of the polycrystalline perovskite thin-film have a significant effect on the performance and stability of the solar cell. In the polycrystalline film, grain boundaries are formed due to break in the crystal structure of the material. Generally, grains are relatively free from defects or traps, while the accumulation of defects is observed at the grain boundaries.[78] Due to defects present at the grain boundaries, the recombination of photogenerated carriers is also higher at the grain boundaries, which finally results in lower photovoltaic performance. Note that film morphology and grain size are strongly dependent on the perovskite deposition process. By controlling the dynamics of crystallization of perovskite using solvent or temperature control, compact perovskite films with micron-size grains can be fabricated, which results in superior solar cell performances.[31, 34, 37]

Though significant advances have been achieved on perovskite photovoltaics, long term stability is one of the important issues in this technology towards commercialization.[79] [80]Ambient stable halide perovskites and lead-free perovskites for solar cells still needs to be investigated.[81]

1.6.2. Photodetectors

Photodetectors are representative optoelectronic devices that can convert optical signals into electrical ones based on the photoelectric effect, which are one of the key components in contemporary multifunctional technologies.[82-84] The effective and ultrasensitive photodetection is very important in a wide range of fields, such as optical communication, spectroscopy, biomedical imaging, environmental monitoring, biological/chemical sensing, security, fire detection, night-vision, motion detection, video imaging, etc.[85] In the high-performance photodetector, typically a semiconductor material efficiently absorbs incident photons and produce electron-hole pairs upon photoexcitation and built-in electric field or external bias is used to separate photogenerated carriers effectively to generate an electrical output.[86] Currently, the photodetectors in the entire UV-NIR spectrum are dominated by detectors made from inorganic semiconductors, such as Si, Ge, and InGaAs.[15] However, there are certain limitations of these photodetectors due to their complicated manufacturing technologies, high-quality crystals, high power consumption, high cost, and bulkiness of the photodetectors. Therefore, low-cost photodetectors with broad light detection, high sensitivity, and fast response are highly desirable.

Recently, low-cost, solution-processable perovskite high-performance photodetectors have been revealed with high responsivity and fast photoresponse, which makes them promising candidates for different light-detection devices.[87, 88] The responsivity (R) and detectivity (D*) of perovskite photodetectors have achieved over 10^9 AW^{-1} and 10^{16} Jones, respectively while the response speed up to <1 ns, which is significant compared to other photodetectors.[88, 89] However, the device with high responsivity often shows slower response and vice versa depending on the device architecture. Photodetectors have different architectures according to the demand of a particular application. In general, there are two types of architectures of perovskite photodetector: (a) lateral structure device and (b) vertical structure device. Note in both lateral and vertical structure devices, perovskite act as a light-absorbing active material. **Fig. 1.13(a)** depicts a simple schematic of vertical structure photodetector, while **Fig. 1.13(b)** shows a schematic illustration of a photodetector with a lateral structure.[90] Lateral structure-based photodetectors include photoconductors and phototransistors, while vertical structure photodetectors include photodiodes, heterojunction photodetectors, solar cell structure (p-i-n or n-i-p) devices. Except for phototransistors, all the other photodetectors are two-terminal devices; one electrode is the

cathode, and another is the anode. In contrast, phototransistors are device with three terminals; source, drain, and gate electrodes.[91]

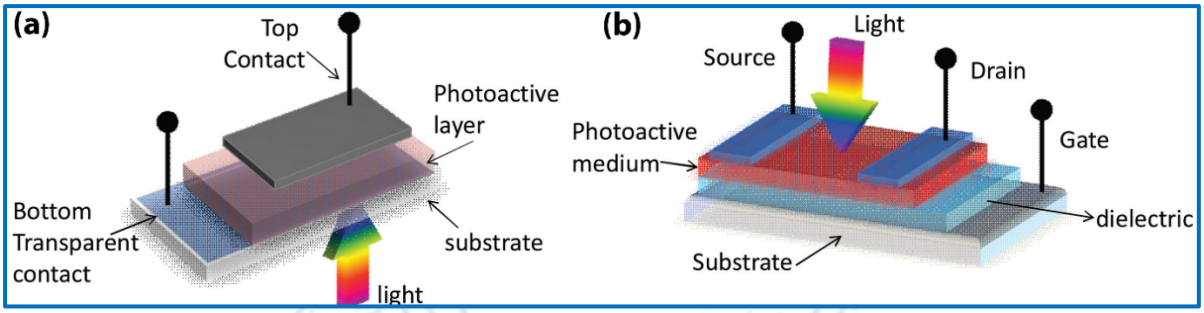

Fig. 1.13: (a) Schematic illustration of the device configurations of (a) vertical structure and (b) lateral structure photodetectors. Adopted from Ref. [[90]].

Most of the reported high-performance perovskite photodetectors with high responsivity and fast response time are planar or mesoporous "solar cell structure." In these types of p-i-n or n-i-p photodetectors, one HTL and another ETL are used to separate and transport of photogenerated electrons and holes, while the perovskite layer acts as a light-absorbing active material. Dou et al. have reported a vertically designed perovskite photodetector similar to a solar cell configuration of ITO/PEDOT:PSS/$CH_3NH_3PbI_{3-x}Cl_x$/PCBM/PFN/Al.[92] This photodetector showed a broad band photoresponse in the wavelength region from 300 to 800 nm, while the detectivity was observed to be 10^{14} Jones, which is almost one order of magnitude higher compared to the detectivity of a commercial Si-based photodetector. Bao et al. presented highly flexible self-powered perovskite photodetectors with the configuration of PEN/Au NW/$CH_3NH_3PbI_3$/PCBM/Al with responsivity 321 mA/W, and response speed of 4 µs.[93] Sutherland et al. reported a self-powered perovskite photodetector with the structure of FTO/TiO_2/Al_2O_3/PCBM/$CH_3NH_3PbI_3$/spiro OMeTAD/Au by exploiting interface engineering of the device with the response speed of 1µs and responsivity of 0.4 AW^{-1}.[94] Zhang et al. reported perovskite photodetectors with a controllable photoconductive gain by designing a trapped-electron-induced hole injection structure of ITO/PEDOT:PSS/ $CH_3NH_3PbI_3$/PCBM:F4-TCNQ/BCP/Au.[95] The high-performance of the perovskite photodetector was attributed to the excellent intrinsic optical and electronic properties of the solution-processed hybrid perovskites, as well as the judicious interface engineering. These photodetectors with solar cell architecture can operate without any applied bias. However, self-powered perovskite photodetectors exhibit high dark current, low gain, and slower photoresponse.

Perovskite photodetectors with 2D materials (e.g., graphene, transition metal dichalcogenides) and without the ETL-HTL layer have also been reported, which shows high photoresponsivity with the fast response time.[96] Spina et al. reported $CH_3NH_3PbI_3$ NW/graphene photo field-effect transistor (FET) with photoresponsivity of 2.6 × 10^6 A/W and photocurrent growth and decay times of 55/75 S.[97] Xie and co-workers demonstrated $CH_3NH_3PbI_{3-x}Cl_x$ film/ P_3HT/graphene photo FET with photoresponsivity of 4.3 × 10^9 A/W.[98] Kwak et al. demonstrated $CsPbBr_{3-x}I_x$ NCs/graphene photo FET with a responsivity of 8.2 ×10^8 A/W and response speed of 0.81/3.65 S.[99] In these perovskite/graphene photo FETs, graphene serves as a carrier-transporting channel material while perovskite act as a light-harvesting active material.

Due to the high carrier mobility, unique optical properties, monolayer and few-layer transition metal dichalcogenides (TMDs), such as MoS_2, $MoSe_2$, WS_2, and WSe_2 have been widely applied in photodetectors, which shows very fast response speed along with high photoresponsivity.[100] However, the performances of these 2D TMD based photodetectors are limited by the low light absorbance. Thus, the integration of 2D TMD materials with high light-harvesting perovskite NCs/QDs, can lead to substantial enhancement in the light absorption resulting in high photoresponsivity along with fast response.[101-104] Lin et al. reported $CsPbBr_3$ QDs/ MoS_2 photo FET with a responsivity of 4.68×10^4 A/W and response speed of 0.0075 s/0.0080 s.[105] Wang et al. reported $CH_3NHH_3PbI_3/MoS_2$ heterostructure photodetectors, which exhibit responsivity of 3.3×10^5 A/W and photoresponse speed of <0.025 s /0.05 s.[105] Song et al. reported monolayer $MoS_2/CsPbBr_3$ hybrid type-II heterostructure photodetector.[100] The schematic illustration of the $MoS_2/CsPbBr_3$ hybrid photodetector is presented in **Fig. 1.14(a)**. $MoS_2/CsPbBr_3$ forms a type-II heterojunction, as shown in the energy band diagram of **Fig. 1.14(b)**.

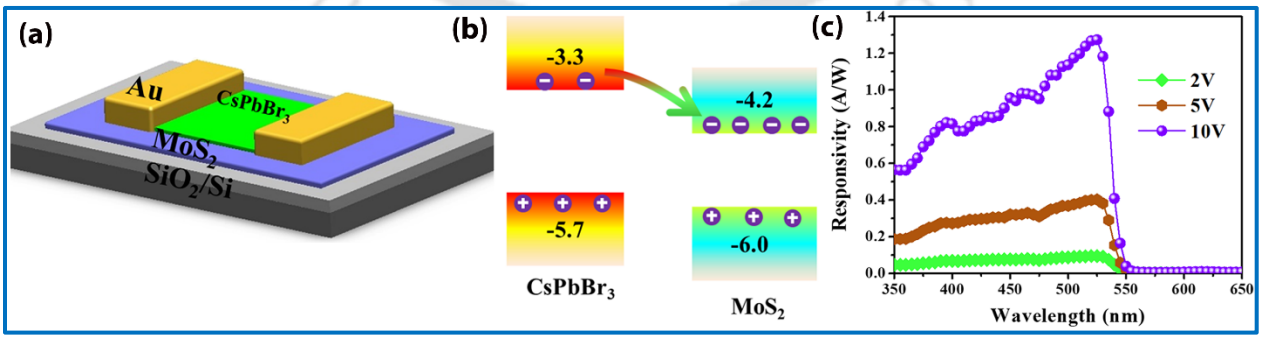

Fig. 1.14: (a) Schematic illustration of the hybrid $MoS_2/CsPbBr_3$ photodetector. (b) Energy band structure of MoS_2 and $CsPbBr_3$ showing charge transfer. (c) The spectral responsivity of the hybrid photodetector at different applied biases. Adopted from Ref. [100].

Under illumination, photogenerated electrons transfer from $CsPbBr_3$ perovskite to monolayer MoS_2, which results in higher photocurrent in the hybrid device, as shown in **Fig. 1.14(b).** The responsivity of the hybrid device increases with the increase in applied bias due to the enhanced photogenerated carrier separation (see **Fig. 1.14(c)**). Li et al. fabricated $CH_3NH_3PbI_3/WS_2$ hybrid photodetector which exhibits photoresponsivity of 76.7 mA/W.[106]

Despite the remarkable progress in this field perovskite photodetectors, there are still challenges concerning stability, reproducibility, and commercialization. Fabrication of charge transport layer free self-powered photodetector with low dark current and ultra-fast response photodetector needs further investigation.

1.6.3. Light-Emitting Devices

The high PL QY (close to 100%) and tunable PL of perovskites have attracted major attention for the fabrication of multicolor high-performance perovskite LEDs.[107] The ambipolar carrier migration and low defect density in halide perovskites enable efficient injection of charges across the interfaces, ameliorating the device performance.[108] Moreover, the emission color of perovskite LED can be easily turned from blue to green or red by simply changing the halide anion from Cl to Br, or I. Recently, external quantum efficiencies (EQEs) of green and red-emitting perovskite LEDs have been achieved over 20%.[109, 110]

Due to the excellent emission property and low defects, perovskite NCs/QDs are widely used in high-performance perovskite LEDs. Ling et al. demonstrated green-emitting perovskite LED using solution-processed $CH_3NH_3PbBr_3$ nanoplatelets.[111] A schematic of the device configuration of the LED is presented in **Fig. 1.15(a),** while EL emission spectra of the LED at different applied biases is shown in **Fig. 1.15(b).** Inset of **Fig. 1.15(b)** depicts the digital photograph of the LED showing bright green emission. Lin et al. reported high performance LED with EQE of 20.3% using compositionally graded quasi-core/shell $CsPbBr_3/CH_3NH_3Br$ perovskite layer.[110]

White light LED (WLED) is another kind of LEDs, which has served as an alternative to the traditional incandescent light. Halide perovskites have widely been used in the fabrication of WLEDs.[112] Typically, WLED consists of UV/blue-emitting chips with a coating of either two or three layers of blue, green, or red-emitting materials, which finally produce white light.[113] Zhou et al. employed $CsPbBrI_2$ perovskite NCs as a red-emitting component in YAG-based WLEDs.[114]

However, the EQE of these devices is relatively low. Further investigation is required for the fabrication of perovskite LEDs with high EQE.

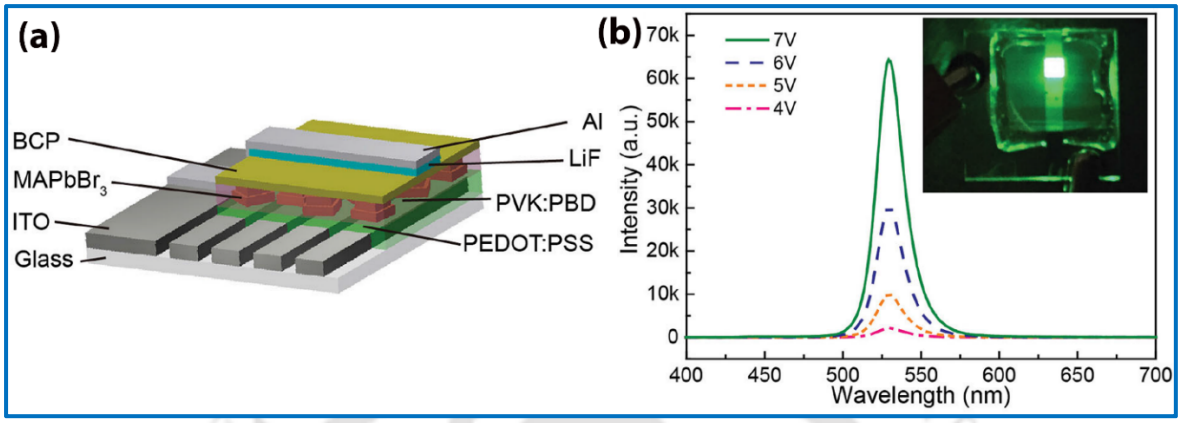

Fig. 1.15: (a) Device architecture of perovskite LED with perovskite nanoplatelets as emitter. (b) Electroluminescence spectra of the LED at different applied bias voltage. The inset shows a photograph of a working device. Adopted from Ref. [111].

1.7. Challenges in the Fabrication and Applications of Halide Perovskites

In the last decade, halide perovskites have been extensively explored for a diverse range of applications. Still, there are many unresolved issues and challenges that need to be addressed, and there are plenty of room for further improvement towards commercial applications of perovskite optoelectronic devices. Extensive research progress has been achieved for the fabrication of high-quality perovskite films by the solution processing method. However, the fabrication of large-area pinhole-free reproducible perovskite films for device applications in the industrial-scale is still challenging. There are several chemical processes for the synthesis of perovskite NCs and QDs, which often show the very high efficiency of light emission. The current synthesis strategies are mostly limited to tedious methods that involve the use of toxic volatile organic solvents with high reaction temperature, inert gas atmosphere, and complicated apparatus. There is a need to look for facile alternative processes for the synthesis of perovskite NCs and QDs without the use of toxic solvents. Perovskite NCs/QDs confined in porous inorganic templates show interesting optoelectronic properties with superior ambient stability. Thus, the confinement of perovskite NPs in the alternative porous template is very promising for different optoelectronic applications. Few major issues related to perovskite solar cells and optoelectronic devices are: (a) poor ambient stability in the presence of oxygen and water molecules, (b) ion migration resulting in poor storage stability of the devices, (d) reproducible methods of device fabrication, (c) toxicity of lead.[80, 115]

Perovskite-based devices can degrade when they are exposed to thermal-stress, light, oxygen, or moisture.[116] Further research is required to gain deeper insights into degradation and ion migration in halide perovskites. The toxicity of lead on humans and the environment has been a challenge for the development and future applications of perovskite-based devices. Lead-free perovskite-based devices also have been reported. However, lead-free devices possess poor ambient and storage stability compared to lead-based devices.[117] Further, investigation is required on lead-free perovskite. Substitution of lead with other metal atoms at high concentration in perovskites has been challenging, and it requires a thorough investigation.

1.8. Focus of the Present Thesis

Despite the significant advancement, there are still several challenges in the fabrication of perovskite NPs/NCs and films for their wide range of optoelectronic applications. In the present thesis, we have made an effort for controlled fabrication of perovskite NPs in the porous template, solid-state synthesis of perovskite NCs, and doping in perovskite NCs, a new strategy for deposition of perovskite films for different optoelectronic applications. The main objectives of the present thesis are as follows:

- Controlled growth of perovskite NPs confined in mesoporous Si NWs array and investigation of its high PL QY.
- Detailed investigation on the origin of strong cathodoluminescence and fast photoresponse of perovskite NPs embedded in mesoporous Si NWs array with high ambient stability.
- Solvent-free, room temperature, solid-state synthesis and doping of color tunable all inorganic perovskite NCs and investigation of its superior photophysical properties and high ambient stability.
- Fabrication and investigation of the mechanism of ultrafast 2D/0D heterojunction photodetector made with perovskite NCs and CVD grown large area monolayer MoS_2.
- Fabrication of color-tunable and white light down-converting LEDs using perovskite NCs.
- Fabrication and investigation of the mechanism of self-powered plasmonic perovskite photodetector without use of charge transport layer.
- Fabrication of perovskite film deposited by a novel vaccum-solution method for efficient perovskite solar cells.

1.9. Organization of the Thesis

The complete thesis work is presented in eight chapters. **Chapter 1** presents a brief overview of the important properties, different growth and fabrication techniques, and the promising applications of metal halide perovskites. **Chapter 2** presents the controlled fabrication of $CH_3NH_3PbI_3$ perovskite NPs on a mesoporous Si NW template and the mechanism of its high PL QY. **Chapter 3** discusses a detailed investigation on the correlation between the strong cathodoluminescence (CL) and the PL emission, and the photoresponse characteristics of $CH_3NH_3PbBr_3$ perovskite NPs embedded in a mesoporous Si NWs template with high ambient stability. **Chapter 4** presents a facile room-temperature bulk scale solid-state synthesis of highly luminescent color-tunable $CsPbX_3$ nanocrystals (NCs) with varying composition exhibiting superior optoelectronic performance and exceptional ambient stability. Further, a vertical type-II heterojunction photodetector was fabricated using $CsPbBr_3$ NCs on direct CVD grown large-area monolayer MoS_2 on SiO_2 substrates. In **Chapter 5,** we demonstrate a facile, solvent-free, bulk scale room temperature solid-state synthesis of highly stable and luminescent Mn-doped $CsPbCl_3$ NCs with high Mn substitution (40%), and investigate the origin and tunability of its dual-color emission. **Chapter 6** presents an air processed high-performance self-powered hybrid perovskite photodetector with plasmonic Ag nanoparticles embedded in the hole-transport-layer, without the use of any electron-transporting layer. **Chapter 7** demonstrates on the elevated substrate temperatures vacuum deposition of lead iodide thin film and its conversion into high-quality $CH_3NH_3PbI_3$ perovskite film using two-step vapor-solution deposition process for large-area perovskite solar cells. **Chapter 8** presents a summary of the significant findings and important conclusions of the present thesis and the future scope of work.

References

1. A. Kojima, K. Teshima, Y. Shirai and T. Miyasaka, *J. Am. Chem. Soc.*, 2009, **131**, 6050-6051.
2. N. J. Jeon, J. H. Noh, W. S. Yang, Y. C. Kim, S. Ryu, J. Seo and S. I. Seok, *Nature*, 2015, **517**, 476-480.
3. T. C. Sum and N. Mathews, *Energy Environ. Sci.*, 2014, **7**, 2518-2534.
4. P. Gao, M. Grätzel and M. K. Nazeeruddin, *Energy Environ. Sci.*, 2014, **7**, 2448-2463.
5. T. Xu, L. Chen, Z. Guo and T. Ma, *Phys. Chem. Chem. Phys.*, 2016, **18**, 27026-27050.
6. C. Eames, J. M. Frost, P. R. F. Barnes, B. C. O'Regan, A. Walsh and M. S. Islam, *Nat. Commun.*, 2015, **6**, 7497.
7. Z. Shi and A. H. Jayatissa, *Materials (Basel)*, 2018, **11**, 729.
8. K. Korshunova, L. Winterfeld, W. J. D. Beenken and E. Runge, *Phys. Status Solidi B*, 2016, **253**, 1907-1915.

9. H. C. Woo, J. W. Choi, J. Shin, S.-H. Chin, M. H. Ann and C.-L. Lee, *J. Phys. Chem. Lett.*, 2018, **9**, 4066-4074.
10. K. Tomanová, V. Čuba, M. G. Brik, E. Mihóková, R. Martinez Turtos, P. Lecoq, E. Auffray and M. Nikl, *APL Mater.*, 2019, **7**, 011104.
11. F. Brivio, K. T. Butler, A. Walsh and M. van Schilfgaarde, *Phys. Rev. B*, 2014, **89**, 155204.
12. S. X. Tao, X. Cao and P. A. Bobbert, *Sci. Rep.*, 2017, **7**, 14386.
13. J. Burschka, N. Pellet, S.-J. Moon, R. Humphry-Baker, P. Gao, M. K. Nazeeruddin and M. Grätzel, *Nature*, 2013, **499**, 316-319.
14. M. Liu, M. B. Johnston and H. J. Snaith, *Nature*, 2013, **501**, 395-398.
15. M. Ahmadi, T. Wu and B. Hu, *Adv. Mater.*, 2017, **29**, 1605242.
16. V. D'Innocenzo, A. R. Srimath Kandada, M. De Bastiani, M. Gandini and A. Petrozza, *Journal of the American Chemical Society*, 2014, **136**, 17730-17733.
17. J. A. Sichert, Y. Tong, N. Mutz, M. Vollmer, S. Fischer, K. Z. Milowska, R. García Cortadella, B. Nickel, C. Cardenas-Daw, J. K. Stolarczyk, A. S. Urban and J. Feldmann, *Nano Lett.*, 2015, **15**, 6521-6527.
18. J. Shamsi, A. S. Urban, M. Imran, L. De Trizio and L. Manna, *Chemical Reviews*, 2019, **119**, 3296-3348.
19. Q. A. Akkerman, S. G. Motti, A. R. Srimath Kandada, E. Mosconi, V. D'Innocenzo, G. Bertoni, S. Marras, B. A. Kamino, L. Miranda, F. De Angelis, A. Petrozza, M. Prato and L. Manna, *J. Am. Chem. Soc.*, 2016, **138**, 1010-1016.
20. A. B. Wong, Y. Bekenstein, J. Kang, C. S. Kley, D. Kim, N. A. Gibson, D. Zhang, Y. Yu, S. R. Leone, L.-W. Wang, A. P. Alivisatos and P. Yang, *Nano Lett.*, 2018, **18**, 2060-2066.
21. F. Zheng, L. Z. Tan, S. Liu and A. M. Rappe, *Nano Lett.*, 2015, **15**, 7794-7800.
22. T. Zhao, W. Shi, J. Xi, D. Wang and Z. Shuai, *Sci. Rep.*, 2016, **6**, 19968.
23. Y. Zhao, A. M. Nardes and K. Zhu, *J. Phys. Chem. Lett.*, 2014, **5**, 490-494.
24. Q. Dong, Y. Fang, Y. Shao, P. Mulligan, J. Qiu, L. Cao and J. Huang, *Science*, 2015, **347**, 967-970.
25. H. Wei, Y. Fang, P. Mulligan, W. Chuirazzi, H.-H. Fang, C. Wang, B. R. Ecker, Y. Gao, M. A. Loi, L. Cao and J. Huang, *Nat. Photonics*, 2016, **10**, 333-339.
26. H. Oga, A. Saeki, Y. Ogomi, S. Hayase and S. Seki, *J. Am. Chem. Soc.*, 2014, **136**, 13818-13825.
27. B. Saparov and D. B. Mitzi, *Chem. Rev.*, 2016, **116**, 4558-4596.
28. X. Wu, M. T. Trinh, D. Niesner, H. Zhu, Z. Norman, J. S. Owen, O. Yaffe, B. J. Kudisch and X. Y. Zhu, *J. Am. Chem. Soc.*, 2015, **137**, 2089-2096.
29. S. D. Stranks, V. M. Burlakov, T. Leijtens, J. M. Ball, A. Goriely and H. J. Snaith, *Phys. Rev. Appl.*, 2014, **2**, 034007.
30. A. Baumann, S. Väth, P. Rieder, M. C. Heiber, K. Tvingstedt and V. Dyakonov, *J. Phys. Chem. Lett.*, 2015, **6**, 2350-2354.
31. D. Shi, V. Adinolfi, R. Comin, M. Yuan, E. Alarousu, A. Buin, Y. Chen, S. Hoogland, A. Rothenberger, K. Katsiev, Y. Losovyj, X. Zhang, P. A. Dowben, O. F. Mohammed, E. H. Sargent and O. M. Bakr, *Science*, 2015, **347**, 519-522.
32. S. Aharon, B. E. Cohen and L. Etgar, *J. Phys. Chem. C*, 2014, **118**, 17160-17165.
33. H. Zhou, Q. Chen, G. Li, S. Luo, T.-b. Song, H.-S. Duan, Z. Hong, J. You, Y. Liu and Y. Yang, *Science*, 2014, **345**, 542-546.
34. W. Nie, H. Tsai, R. Asadpour, J.-C. Blancon, A. J. Neukirch, G. Gupta, J. J. Crochet, M. Chhowalla, S. Tretiak, M. A. Alam, H.-L. Wang and A. D. Mohite, *Science*, 2015, **347**, 522-525.
35. Z. Xiao, C. Bi, Y. Shao, Q. Dong, Q. Wang, Y. Yuan, C. Wang, Y. Gao and J. Huang, *Energy Environ. Sci.*, 2014, **7**, 2619-2623.
36. X. Li, D. Bi, C. Yi, J.-D. Décoppet, J. Luo, S. M. Zakeeruddin, A. Hagfeldt and M. Grätzel, *Science*, 2016, **353**, 58-62.

37. M. Xiao, F. Huang, W. Huang, Y. Dkhissi, Y. Zhu, J. Etheridge, A. Gray-Weale, U. Bach, Y.-B. Cheng and L. Spiccia, *Angew. Chem. Int. Ed.* , 2014, **53**, 9898-9903.
38. N.-G. Park, M. Grätzel, T. Miyasaka, K. Zhu and K. Emery, *Nat. Energy.*, 2016, **1**, 16152.
39. P. Fan, D. Gu, G.-X. Liang, J.-T. Luo, J.-L. Chen, Z.-H. Zheng and D.-P. Zhang, *Sci. Rep.*, 2016, **6**, 29910.
40. C.-W. Chen, H.-W. Kang, S.-Y. Hsiao, P.-F. Yang, K.-M. Chiang and H.-W. Lin, *Adv. Mater.*, 2014, **26**, 6647-6652.
41. G. Longo, L. Gil-Escrig, M. J. Degen, M. Sessolo and H. J. Bolink, *ChemComm*, 2015, **51**, 7376-7378.
42. F. Fu, T. Feurer, T. Jäger, E. Avancini, B. Bissig, S. Yoon, S. Buecheler and A. N. Tiwari, *Nat. Commun.*, 2015, **6**, 8932.
43. F. Deschler, M. Price, S. Pathak, L. E. Klintberg, D.-D. Jarausch, R. Higler, S. Hüttner, T. Leijtens, S. D. Stranks, H. J. Snaith, M. Atatüre, R. T. Phillips and R. H. Friend, *The Journal of Physical Chemistry Letters*, 2014, **5**, 1421-1426.
44. W. W. Yu and X. Peng, *Angew. Chem. Int. Ed.* , 2002, **41**, 2368-2371.
45. L. Protesescu, S. Yakunin, M. I. Bodnarchuk, F. Krieg, R. Caputo, C. H. Hendon, R. X. Yang, A. Walsh and M. V. Kovalenko, *Nano Lett.*, 2015, **15**, 3692-3696.
46. O. Vybornyi, S. Yakunin and M. V. Kovalenko, *Nanoscale*, 2016, **8**, 6278-6283.
47. Y. Bekenstein, B. A. Koscher, S. W. Eaton, P. Yang and A. P. Alivisatos, *J. Am. Chem. Soc.*, 2015, **137**, 16008-16011.
48. D. Zhang, S. W. Eaton, Y. Yu, L. Dou and P. Yang, *J. Am. Chem. Soc.*, 2015, **137**, 9230-9233.
49. S. Das Adhikari, S. K. Dutta, A. Dutta, A. K. Guria and N. Pradhan, *Angew. Chem. Int. Ed.* , 2017, **56**, 8746-8750.
50. Y. Zhou, J. Chen, O. M. Bakr and H.-T. Sun, *Chem. Mater.*, 2018, **30**, 6589-6613.
51. Z. Zeng, Y. Xu, Z. Zhang, Z. Gao, M. Luo, Z. Yin, C. Zhang, J. Xu, B. Huang, F. Luo, Y. Du and C. Yan, *Chem. Soc. Rev.*, 2020, **49**, 1109-1143.
52. B. Luo, F. Li, K. Xu, Y. Guo, Y. Liu, Z. Xia and J. Z. Zhang, *J. Mater. Chem. C*, 2019, **7**, 2781-2808.
53. D. Parobek, B. J. Roman, Y. Dong, H. Jin, E. Lee, M. Sheldon and D. H. Son, *Nano Lett.*, 2016, **16**, 7376-7380.
54. F. Zhang, H. Zhong, C. Chen, X.-g. Wu, X. Hu, H. Huang, J. Han, B. Zou and Y. Dong, *ACS Nano*, 2015, **9**, 4533-4542.
55. X. Li, Y. Wu, S. Zhang, B. Cai, Y. Gu, J. Song and H. Zeng, *Adv. Funct. Mater.*, 2016, **26**, 2435-2445.
56. V. Malgras, S. Tominaka, J. W. Ryan, J. Henzie, T. Takei, K. Ohara and Y. Yamauchi, *J. Am. Chem. Soc.*, 2016, **138**, 13874-13881.
57. Z. Zhang, M. Wang, L. Ren and K. Jin, *Sci. Rep.*, 2017, **7**, 1918.
58. S. Demchyshyn, J. M. Roemer, H. Groiß, H. Heilbrunner, C. Ulbricht, D. Apaydin, A. Böhm, U. Rütt, F. Bertram, G. Hesser, M. C. Scharber, N. S. Sariciftci, B. Nickel, S. Bauer, E. D. Głowacki and M. Kaltenbrunner, *Sci. Adv.*, 2017, **3**, e1700738.
59. D. N. Dirin, L. Protesescu, D. Trummer, I. V. Kochetygov, S. Yakunin, F. Krumeich, N. P. Stadie and M. V. Kovalenko, *Nano Lett.*, 2016, **16**, 5866-5874.
60. L. Chouhan, S. Ghimire, C. Subrahmanyam, T. Miyasaka and V. Biju, *Chem. Soc. Rev.*, 2020, **49**, 2869-2885.
61. H.-S. Kim, C.-R. Lee, J.-H. Im, K.-B. Lee, T. Moehl, A. Marchioro, S.-J. Moon, R. Humphry-Baker, J.-H. Yum, J. E. Moser, M. Grätzel and N.-G. Park, *Sci. Rep.*, 2012, **2**, 591.
62. Y. Zhou, X. Yin, Q. Zhang, N. Wang, A. Yamamoto, K. Koumoto, H. Shen and H. Lin, *Mater. Today Energy*, 2019, **12**, 363-370.
63. P. Wang, R. Li, B. Chen, F. Hou, J. Zhang, Y. Zhao and X. Zhang, *Adv. Mater.*, 2020, **32**, 1905766.
64. N. K. Elumalai, M. A. Mahmud, D. Wang and A. Uddin, *Energies*, 2016, **9**, 861.
65. T. Swetha and S. P. Singh, *J. Mater. Chem. A*, 2015, **3**, 18329-18344.

66. M. Saliba, S. Orlandi, T. Matsui, S. Aghazada, M. Cavazzini, J.-P. Correa-Baena, P. Gao, R. Scopelliti, E. Mosconi, K.-H. Dahmen, F. De Angelis, A. Abate, A. Hagfeldt, G. Pozzi, M. Graetzel and M. K. Nazeeruddin, *Nat. Energy.*, 2016, **1**, 15017.
67. C.-C. Chueh, C.-Z. Li and A. K. Y. Jen, *Energy Environ. Sci.*, 2015, **8**, 1160-1189.
68. K.-C. Wang, P.-S. Shen, M.-H. Li, S. Chen, M.-W. Lin, P. Chen and T.-F. Guo, *ACS Appl. Mater. Interfaces*, 2014, **6**, 11851-11858.
69. Y. Rong, Z. Ku, A. Mei, T. Liu, M. Xu, S. Ko, X. Li and H. Han, *J. Phys. Chem. Lett.*, 2014, **5**, 2160-2164.
70. A. Yella, L.-P. Heiniger, P. Gao, M. K. Nazeeruddin and M. Grätzel, *Nano Lett.*, 2014, **14**, 2591-2596.
71. X. Xu, Z. Liu, Z. Zuo, M. Zhang, Z. Zhao, Y. Shen, H. Zhou, Q. Chen, Y. Yang and M. Wang, *Nano Lett.*, 2015, **15**, 2402-2408.
72. S. You, H. Wang, S. Bi, J. Zhou, L. Qin, X. Qiu, Z. Zhao, Y. Xu, Y. Zhang, X. Shi, H. Zhou and Z. Tang, *Adv. Mater.*, 2018, **30**, 1706924.
73. S. Shi, Y. Li, X. Li and H. Wang, *Mater. Horiz.*, 2015, **2**, 378-405.
74. M. Li, Y.-G. Yang, Z.-K. Wang, T. Kang, Q. Wang, S.-H. Turren-Cruz, X.-Y. Gao, C.-S. Hsu, L.-S. Liao and A. Abate, *Adv. Mater.*, 2019, **31**, 1901519.
75. J. Zhang, W. Zhang, H.-M. Cheng and S. R. P. Silva, *Mater. Today*, 2020, DOI: https://doi.org/10.1016/j.mattod.2020.05.002.
76. X. Xu, Q. Chen, Z. Hong, H. Zhou, Z. Liu, W.-H. Chang, P. Sun, H. Chen, N. D. Marco, M. Wang and Y. Yang, *Nano Lett.*, 2015, **15**, 6514-6520.
77. C. Liu, L. Zhang, X. Zhou, J. Gao, W. Chen, X. Wang and B. Xu, *Adv. Funct. Mater.*, 2019, **29**, 1807604.
78. J.-W. Lee, S.-H. Bae, N. De Marco, Y.-T. Hsieh, Z. Dai and Y. Yang, *Mater. Today Energy*, 2018, **7**, 149-160.
79. R. Wang, M. Mujahid, Y. Duan, Z.-K. Wang, J. Xue and Y. Yang, *Adv. Funct. Mater.*, 2019, **29**, 1808843.
80. X. Qin, Z. Zhao, Y. Wang, J. Wu, Q. Jiang and J. You, *J. Semicond.*, 2017, **38**, 011002.
81. F. Arabpour Roghabadi, M. Alidaei, S. M. Mousavi, T. Ashjari, A. S. Tehrani, V. Ahmadi and S. M. Sadrameli, *J. Mater. Chem. A*, 2019, **7**, 5898-5933.
82. C. Xie, C.-K. Liu, H.-L. Loi and F. Yan, *Adv. Funct. Mater.*, 2020, **30**, 1903907.
83. N. Huo and G. Konstantatos, *Adv. Mater.*, 2018, **30**, 1801164.
84. Y. Dong, Y. Zou, J. Song, X. Song and H. Zeng, *J. Mater. Chem. C*, 2017, **5**, 11369-11394.
85. R. Ghosh and P. K. Giri, *Nanotechnology*, 2016, **28**, 012001.
86. C. Li, W. Huang, L. Gao, H. Wang, L. Hu, T. Chen and H. Zhang, *Nanoscale*, 2020, **12**, 2201-2227.
87. Z. Xu, Y. Yu, S. Arya, I. A. Niaz, Y. Chen, Y. Lei, M. A. R. Miah, J. Zhou, A. C. Zhang, L. Yan, S. Xu, K. Nomura and Y.-H. Lo, *Nano Lett.*, 2020, **20**, 2144-2151.
88. X. Geng, F. Wang, H. Tian, Q. Feng, H. Zhang, R. Liang, Y. Shen, Z. Ju, G.-Y. Gou, N. Deng, Y.-t. Li, J. Ren, D. Xie, Y. Yang and T.-L. Ren, *ACS Nano*, 2020, **14**, 2860-2868.
89. H. Wang and D. H. Kim, *Chem. Soc. Rev.*, 2017, **46**, 5204-5236.
90. K.-J. Baeg, M. Binda, D. Natali, M. Caironi and Y.-Y. Noh, *Adv. Mater.*, 2013, **25**, 4267-4295.
91. C. Wang, X. Zhang and W. Hu, *Chem. Soc. Rev.*, 2020, **49**, 653-670.
92. L. Dou, Y. Yang, J. You, Z. Hong, W.-H. Chang, G. Li and Y. Yang, *Nat. Commun.*, 2014, **5**, 5404.
93. C. Bao, W. Zhu, J. Yang, F. Li, S. Gu, Y. Wang, T. Yu, J. Zhu, Y. Zhou and Z. Zou, *ACS Appl. Mater. Interfaces*, 2016, **8**, 23868-23875.
94. B. R. Sutherland, A. K. Johnston, A. H. Ip, J. Xu, V. Adinolfi, P. Kanjanaboos and E. H. Sargent, *ACS Photonics*, 2015, **2**, 1117-1123.
95. D. Zhang, C. Liu, K. Li, W. Guo, F. Gao, J. Zhou, X. Zhang and S. Ruan, *Adv. Opt. Mater.*, 2018, **6**, 1701189.

96. J. Li, S. Yuan, G. Tang, G. Li, D. Liu, J. Li, X. Hu, Y. Liu, J. Li, Z. Yang, S. F. Liu, Z. Liu, F. Gao and F. Yan, *ACS Appl. Mater. Interfaces*, 2017, **9**, 42779-42787.
97. M. Spina, M. Lehmann, B. Náfrádi, L. Bernard, E. Bonvin, R. Gaál, A. Magrez, L. Forró and E. Horváth, *Small*, 2015, **11**, 4823-4823.
98. C. Xie and F. Yan, *ACS Appl. Mater. Interfaces*, 2017, **9**, 1569-1576.
99. D.-H. Kwak, D.-H. Lim, H.-S. Ra, P. Ramasamy and J.-S. Lee, *RSC Adv.*, 2016, **6**, 65252-65256.
100. X. Song, X. Liu, D. Yu, C. Huo, J. Ji, X. Li, S. Zhang, Y. Zou, G. Zhu, Y. Wang, M. Wu, A. Xie and H. Zeng, *ACS Appl. Mater. Interfaces*, 2018, **10**, 2801-2809.
101. Z.-Y. Peng, J.-L. Xu, J.-Y. Zhang, X. Gao and S.-D. Wang, *Adv. Mater. Interfaces*, 2018, **5**, 1870089.
102. D. Kufer, T. Lasanta, M. Bernechea, F. H. L. Koppens and G. Konstantatos, *ACS Photonics*, 2016, **3**, 1324-1330.
103. J. Lu, A. Carvalho, H. Liu, S. X. Lim, A. H. Castro Neto and C. H. Sow, *Angew. Chem. Int. Ed.* , 2016, **55**, 11945-11949.
104. Q. Xu, Z. Yang, D. Peng, J. Xi, P. Lin, Y. Cheng, K. Liu and C. Pan, *Nat. Energy.*, 2019, **65**, 104001.
105. R. Lin, X. Li, W. Zheng and F. Huang, *ACS Appl. Nano Mater.*, 2019, **2**, 2599-2605.
106. Z. Li, J. Li, D. Ding, H. Yao, L. Liu, X. Gong, B. Tian, H. Li, C. Su and Y. Shi, *ACS Appl. Mater. Interfaces*, 2018, **10**, 36493-36504.
107. Q. Van Le, H. W. Jang and S. Y. Kim, *Small Methods*, 2018, **2**, 1700419.
108. L. Zhang, X. Yang, Q. Jiang, P. Wang, Z. Yin, X. Zhang, H. Tan, Y. Yang, M. Wei, B. R. Sutherland, E. H. Sargent and J. You, *Nat. Commun.*, 2017, **8**, 15640.
109. W. Xu, Q. Hu, S. Bai, C. Bao, Y. Miao, Z. Yuan, T. Borzda, A. J. Barker, E. Tyukalova, Z. Hu, M. Kawecki, H. Wang, Z. Yan, X. Liu, X. Shi, K. Uvdal, M. Fahlman, W. Zhang, M. Duchamp, J.-M. Liu, A. Petrozza, J. Wang, L.-M. Liu, W. Huang and F. Gao, *Nat. Photonics*, 2019, **13**, 418-424.
110. K. Lin, J. Xing, L. N. Quan, F. P. G. de Arquer, X. Gong, J. Lu, L. Xie, W. Zhao, D. Zhang, C. Yan, W. Li, X. Liu, Y. Lu, J. Kirman, E. H. Sargent, Q. Xiong and Z. Wei, *Nature*, 2018, **562**, 245-248.
111. Y. Ling, Z. Yuan, Y. Tian, X. Wang, J. C. Wang, Y. Xin, K. Hanson, B. Ma and H. Gao, *Adv. Mater.*, 2016, **28**, 305-311.
112. M. Bidikoudi, E. Fresta and R. D. Costa, *ChemComm*, 2018, **54**, 8150-8169.
113. M. Cao, Y. Xu, P. Li, Q. Zhong, D. Yang and Q. Zhang, *J. Mater. Chem. C*, 2019, **7**, 14412-14440.
114. J. Zhou, F. Huang, H. Lin, Z. Lin, J. Xu and Y. Wang, *J. Mater. Chem. C*, 2016, **4**, 7601-7606.
115. S. Kundu and T. L. Kelly, *EcoMat*, 2020, **2**, e12025.
116. T. Leijtens, G. E. Eperon, N. K. Noel, S. N. Habisreutinger, A. Petrozza and H. J. Snaith, *Adv. Energy Mater.*, 2015, **5**, 1500963.
117. H. Fu, *Sol. Energy Mater Sol.*, 2019, **193**, 107-132.

Chapter 2

Controlled Fabrication of Perovskite Nanoparticles with High Photoluminescence Quantum Yield on a Mesoporous Si Nanowire Template

In this chapter, the controlled fabrication of $CH_3NH_3PbI_3$ perovskite nanoparticles (NPs) on a mesoporous silicon nanowire (Si NW) template and the mechanism of its high photoluminescence (PL) quantum yield are presented. Crystalline perovskite NPs are grown by spin-coating of perovskite precursor on the surface of mesoporous Si NWs fabricated by a metal-assisted chemical etching (MACE) method. The size of the perovskite NPs and its photo-physical properties were tuned by controlling the porosity of the Si NW template and perovskite precursor concentrations. Depending on the size of the perovskite NPs, the center of the PL peak of the NPs shows a large blue shift with high PL quantum yield (QY) as compared to that of the bulk perovskite film. A detailed systematic study reveals that a decrease in particle size and the quantum confinement in perovskite NPs are primarily responsible for the enhanced yield as well as the blue shift of PL peak. With the help of the plasma-treated Si NW template, the contribution of the photon recycling effect to the enhanced PL of NPs was quantitatively assessed and found to be ~10%. This study demonstrates an easy and cost-effective fabrication of perovskite NPs on a novel mesoporous Si NWs template, and it unravels the mechanism behind its superior photophysical properties.

2.1. Introduction

Over the past few years, organic-inorganic halide perovskites have drawn tremendous research attention for their extraordinary performance in solar cells and light-emitting devices with the advantages of high absorption in the UV-visible region, low cost and low-temperature processing, tunable optical band gap, and superior charge transport. [1-5] These solution-processed perovskites, especially $CH_3NH_3PbX_3$ (where, X= Cl, Br, and I), have also shown great promises in light-emitting diodes (LEDs) and lasing applications with tunable emission color by varying the halide anion.[6] Perovskite nanocrystals (NCs) have shown interesting size-dependent optical and electronic properties that differ significantly from their bulk counterparts.[7-10] Colloidal and self-assembled perovskite NCs in a solid organic matrix with lower dimensionality have been reported.[11-13] Though these colloidal NCs show very high light emission efficiency, the

luminescent NPs are necessary in solid or thin-film form for practical device application. The emission intensity tends to substantially reduce, when NCs are processed as thin films due to spontaneous aggregation.[14] On the other hand, the growth of perovskite NCs inside an ordered inorganic mesoporous host matrix is an alternative, ligand-free route to study the effects on the optical properties due to size reduction. Interestingly, the growth of perovskite NPs using porous aluminum oxide (Al_2O_3) and silica (SiO_2) templates have been reported, which show very interesting optical properties due to the quantum size effect.[15]

We have investigated the growth of $CH_3NH_3PbI_3$ NPs on mesoporous Si NWs templates grown by MACE method and explored its photo-physical properties. The size of the perovskite NPs was controlled by controlling: (a) the porosity of NWs during the etching process, and (b) the concentration of perovskite precursor solution. Effect of the size of the perovskite NPs on the PL emission energy and the PL quantum yield (QY) is studied thoroughly. The mechanism behind the large blue shift and high PL QY is studied thoroughly by steady-state and time-resolved PL supported by high-resolution TEM analysis. Our study revealed that the decrease in particle size, quantum confinement of carriers in the perovskite NPs, and re-absorption of the photon emitted from Si NWs by the perovskite NPs followed by the PL emission are primarily responsible for the large enhancement of PL from the perovskite NPs on mesoporous Si NW template.

2.2. Experimental Details

2.2.1. Sample Preparation

2.2.1.1. Growth of Mesoporous Si NWs

The mesoporous Si NWs were grown by a well-known one-step or two-step metal-assisted chemical etching method at room temperature using doped Si wafers.[16] For the two-step process, first, a thin layer of Ag NPs was deposited on the Si wafers by dipping it in a solution containing 5.55 M HF and 0.015 M $AgNO_3$ for 5 seconds. Next, the Ag coated substrates with resistivity 0.01 Ω-cm were immersed in a solution containing 5 ml HF (48 %), 2 ml H_2O_2 (50 %) and 23 ml DI water for 20 min, 10 min and 5 min. In the case of one-step process, Si wafers with resistivity 0.01 Ω-cm were immersed into a solution containing 0.015 M $AgNO_3$ and 5.55 M HF for one hour. We have also performed a two-step MACE for 20 min on Si wafer with resistivity 1 Ω-cm and 0.001 Ω-cm. In order to remove the residual Ag NPs after etching, all the samples were dipped in a 10 % HNO_3 solution after growth. A detailed account of the different Si NWs samples is summarized in **Table 2.1.**

Table 2.1: *Details of the growth conditions of MACE grown Si NWs, which are used as a template for the growth of perovskite NPs.*

Sample code	*MACE process*	*Etching time*	*Wafer resistivity (ρ, Ω-cm)*
NW1	Two-step	20 min	0.01
NW1A		10 min	
NW1B		5 min	
NW1X		20 min	1.0
NW1Y			0.001
NW2	One-step	60 min	0.01

2.2.1.2. Synthesis of $CH_3NH_3PbI_3$

At first, CH_3NH_3I was synthesized by the reaction of 24 mL of methylamine solution (33 wt % in ethanol), 10 mL of hydroiodic acid (HI, 57 wt %), and 100 mL of ethanol in 250 mL round-bottom flask at 0 °C for 2 h with stirring at 400 rpm. Then, the precipitate was collected by evaporating the solvent. The precipitate was washed 3 times with diethyl ether and dried overnight at 60 °C in a vacuum oven. $CH_3NH_3PbI_3$ was deposited using a conventional single-step deposition method on different Si NW samples (NW1 and NW2) and bare Si wafer. 0.100 g of CH_3NH_3I and 0.250 g of PbI_2 were dissolved in 1 mL of anhydrous N, N-dimethylformamide (DMF) to produce a clear 22.5 wt % perovskite precursor (Pe1). We have also prepared 11.2 wt % (Pe2), 5.6 wt % (Pe3), and 2.8 wt % (Pe3) perovskite precursor in DMF. The prepared solutions were spin-coated at 2500 rpm for 45 s on different NW templates. Next, the samples were transferred on a hot plate and annealed at 80 °C for 20 min for the formation of the crystalline perovskite layer. The samples were termed with generic code NWxPey, where 'x' refers to different Si NWs, and 'y' refers to different concentrations of perovskite precursor. The perovskite film deposited on bulk Si wafer is referred to as Pe on bulk Si. **Fig. 2.1** illustrates the processes involved in the fabrication of the perovskite NPs on the mesoporous Si NWs that are grown by a two-step etching process.

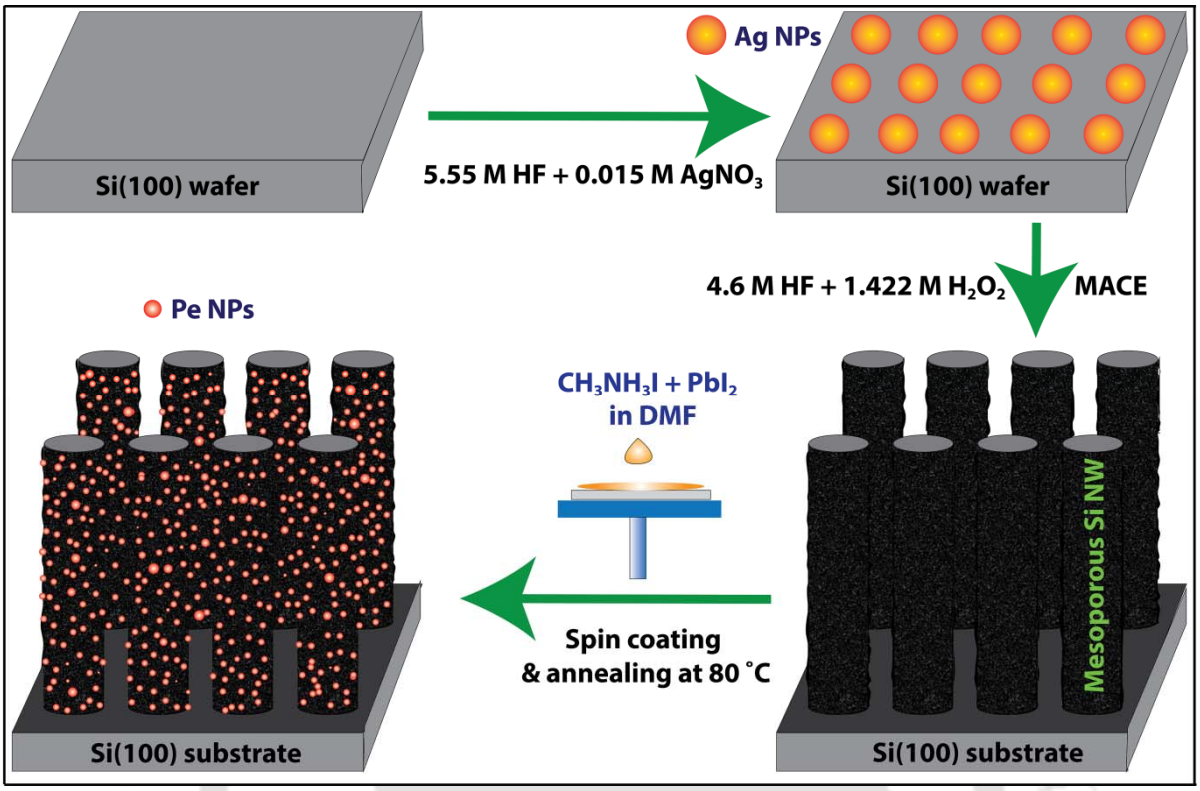

Fig. 2.1: An illustration of the growth of mesoporous Si NWs by a two-step MACE process followed by the spin-coating of the perovskite precursor to fabricate the perovskite NPs on the Si NW template.

2.2.2. Characterization Techniques

The morphology and elemental compositions of different samples were characterized using a field emission scanning electron microscope (FESEM, Sigma, Zeiss) equipped with an energy dispersive X-ray (EDX) spectrometer. The high magnification surface morphology and elemental mapping were studied using a field emission transmission electron microscope (FETEM) (JEOL-2100F). For structural characterizations, an X-ray diffractometer (XRD) (Rigaku RINT 2500 TRAX−III, Cu Kα radiation) was used for different samples. UV–vis diffuse reflectance spectra (DRS) of the samples were measured using a commercial spectrophotometer equipped with an integrating sphere (PerkinElmer, Lamda 950). The steady-state PL spectra were recorded using a 405 nm diode laser (CNI Laser) excitation with the help of a commercial fluorimeter (Horiba Jobin Yvon, Fluoromax-4). The PL QY of the samples was measured with an integrating sphere (FM-SPHERE, Horiba) attached to the fluorimeter. Fluorescence image of perovskite NPs coated Si NW was taken with Zeiss LSM 880 confocal microscope with 405 laser excitation. Time-resolved PL (TRPL) measurements were performed using a 405 nm pulsed laser excitation, with an instrument time response of <50 ps (LifeSpecII, Edinburgh Instruments). All the measurements

including XRD, PL, DRS, TRPL were carried out in open-air atmosphere with relatively high humidity without any humidity control /glove box.

2.3. Results and Discussion

2.3.1. Morphology and Structural Analyses

2.3.1.1 FESEM and TEM Analyses

Fig. 2.2 shows the FESEM images of NW1 and NW2 before (1st column) and after (2nd column) the deposition of the perovskite layer. **Fig. 2.2(a)** and **Fig. 2.2(c)** are the top view and cross-sectional view images of NW1, while **Fig. 2.2(b)** and **2.2(d)** correspond to sample NW1Pe1. Likewise, **Fig. 2.2(e)** and **2.2(g)** are the top view and cross-sectional view FESEM images of NW2, while **Fig. 2.2(f)** and **2.2(h)** correspond to sample NW2Pe1. From the FESEM images, it is evident that the top and side surfaces of the Si NWs are covered by the perovskite NPs (Pe NPs) containing film. FESEM images also reveal that the Si NWs in NW1 have higher roughness than that in NW2. Note that the porosity of Si NWs and the presence of Pe NPs on the Si NWs surface are not clearly discernible from the FESEM images due to its resolution limit. From the FESEM image of NW2Pe1, some bigger size Pe NPs are observed, while no such particles were observed on NW1.

In order to figure out the elemental composition, we have carried out the EDX analysis. **Fig. 2.3(a)** shows the EDX mapping and elemental composition of NW1Pe1. The elemental color mappings of the selective portion are shown in **Fig. 2.3(b-g)**. The images reveal that the Pe NPs are uniformly coated on the entire surface of Si NW arrays down to the bottom of the NWs. **Fig. 2.3(h)** shows the elemental composition of NW1Pe1 in the selective portion in **Fig. 2.3(a)**.TEM analysis provides a detailed view of surface morphology of individual Si NW and the formation of Pe NPs nucleated at the pores of the NWs. **Fig. 2.3(i)** and **2.3(l)** show the TEM images of single Si NW in sample NW1 and NW2, respectively. It is clear that the NW surface in each case is mesoporous in nature due to the lateral etching of the NWs during the MACE process. **Fig. 2(j)** and **2(m)** show the TEM images of a single NW/perovskite heterostructure in sample NW1Pe1 and NW2Pe1, respectively. It is clear that Pe NPs are formed on the surface of Si NWs in each case. The porous sites of the Si NWs acted as the nucleation center for the formation of Pe NPs.

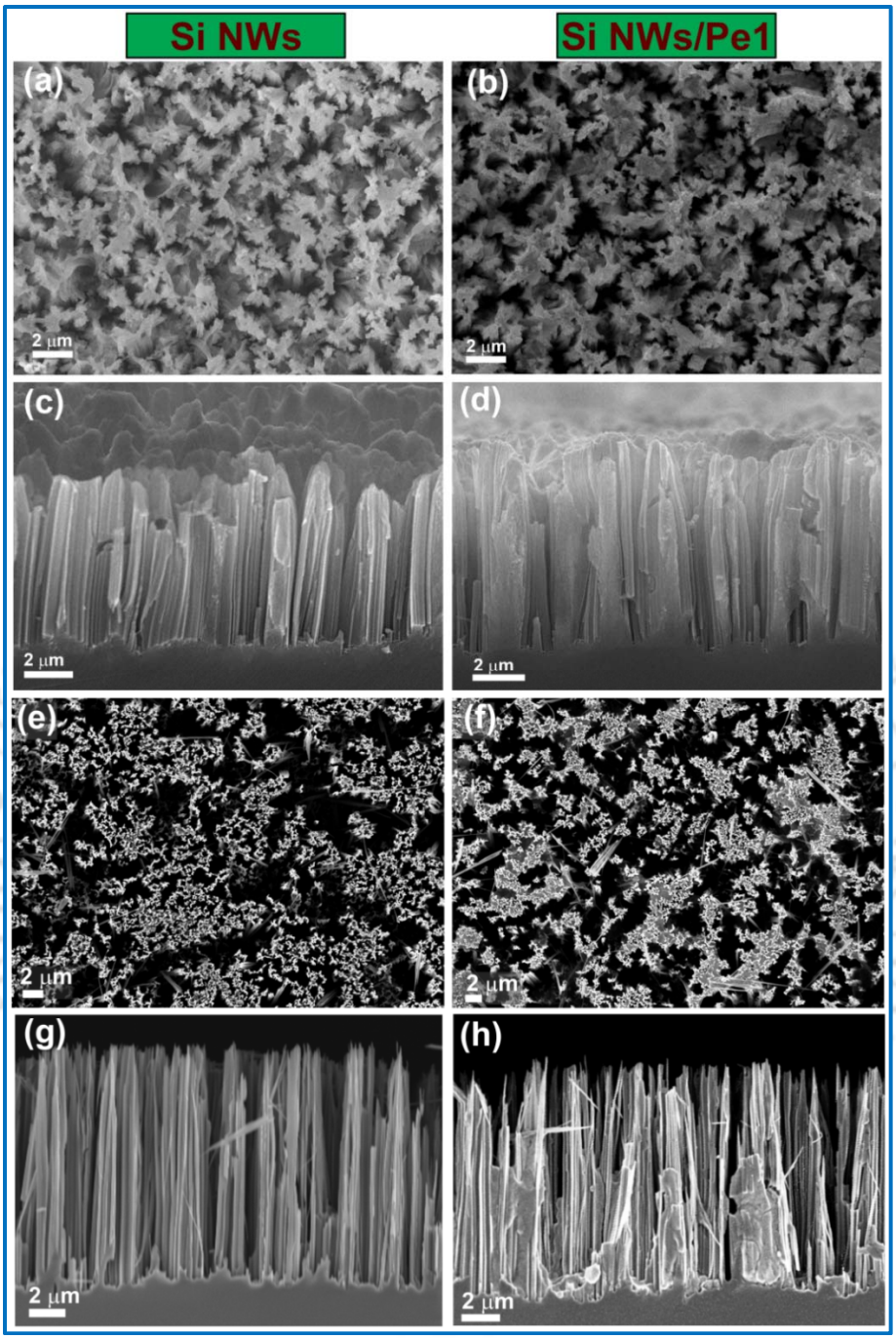

Fig. 2.2: (a, c) top and cross-sectional view FESEM images of NW1. (b, d) top and cross-sectional FESEM images of NW1Pe1. (e, g) top and cross-sectional view FESEM images of NW2. (f, h) top and cross-sectional view FESEM images of NW2Pe1.

For NW1Pe1, the size of the Pe NPs varies in the range 5-40 nm, while for NW2Pe1 the size varies in the range 10-70 nm. As confirmed from the TEM images, both the NWs are mesoporous, though the porosity and the roughness of NW1 are much higher than that of NW2. This is due to the stronger sidewall etching in the case of two-step MACE in NW1.

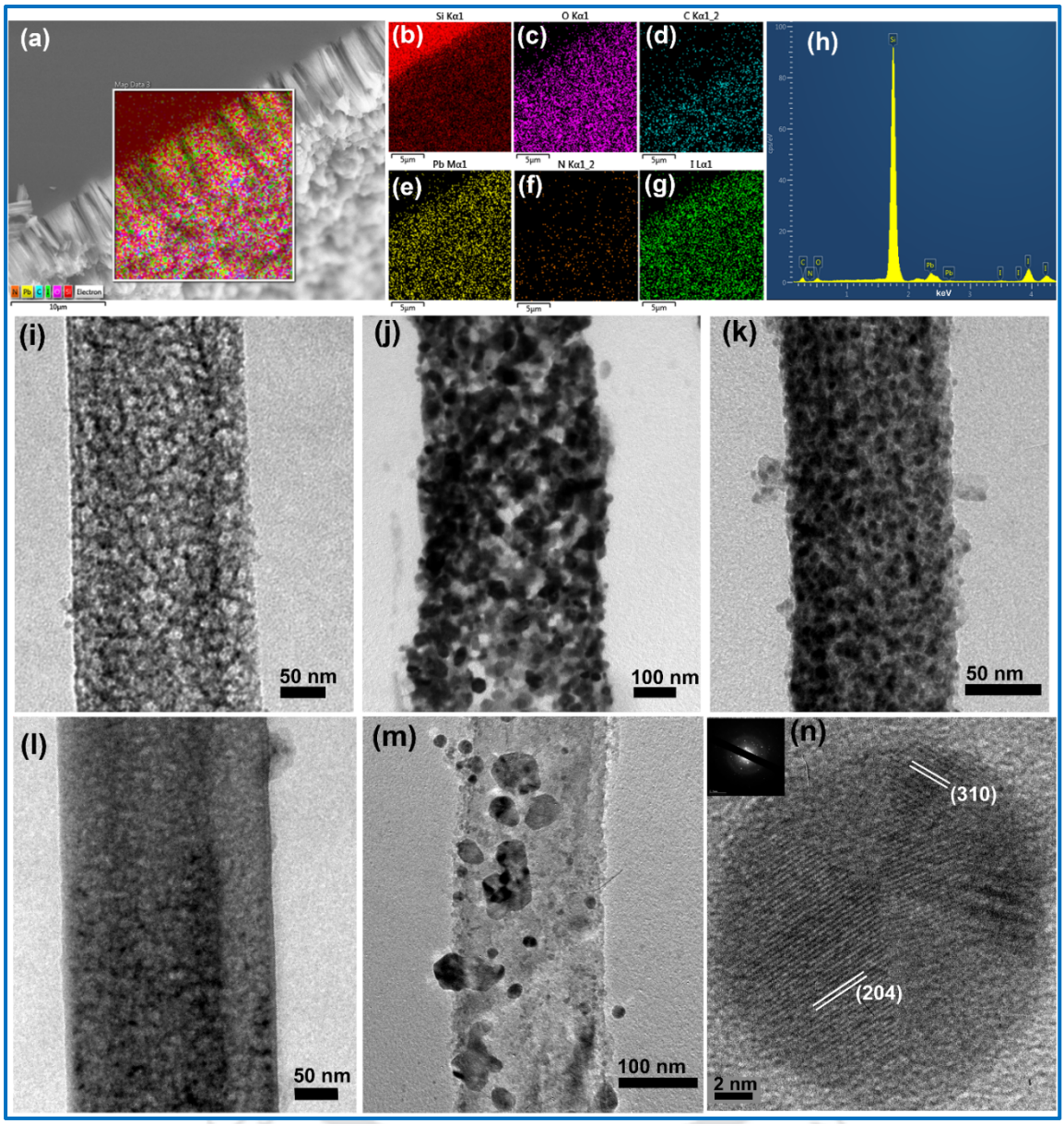

Fig. 2.3: (a) FESEM image and EDX compositional mapping of NW1Pe1. The corresponding elemental color mapping of (b) silicon, (c) oxygen, (d) carbon, (e) lead, (f) nitrogen, and (g) iodine. (h) The EDX spectrum of the selective portion of NW1Pe1. The TEM images of single NW in samples: (i) NW1, (j) NW1Pe1, (k) NW1Pe2, (l) NW2, (m) NW2Pe1. (n) HRTEM lattice image of perovskite NPs on NW surface from sample NW1Pe1, the inset shows the SAED pattern, which confirms the crystallinity of $CH_3NH_3PbI_3$ NPs.

The highly porous and rough surface of NW1 causes the formation of the high-density Pe NPs on NW1 surface. The size of the NPs on NW2 is bigger than that on NW1, which played a significant role in the enhanced PL intensity and blue-shifted PL from the sample NW1Pe1, as discussed later. **Fig. 2.3(k)** shows the TEM image of a single Si NW in sample NW1Pe2, and it is clear that the average size of the Pe NPs is smaller in this case as compared to that of the sample NW1Pe1.

When the concentration of perovskite precursor is lower, the perovskite starts nucleation at the porous sites of the Si NWs and as a result, the size of the Pe NPs is of the order of pore size of the Si NWs. Thus, the size of the Pe NPs in sample NW1Pe2 varies in the range of 1-12 nm. Interestingly, in the NW/perovskite heterostructure, when the concentration of perovskite precursor is high, the size of the Pe NPs becomes larger than the size of the pores on the NW. Thus, we obtained larger size Pe NPs for sample NW1Pe1 as compared to sample NW1Pe2. Note that the surface of the Si NWs in sample NW2 is much smoother than that of sample NW1, and hence we obtained larger Pe NPs for sample NW2Pe1 as compared to the sample NW1Pe1. **Fig. 2.3(n)** shows the HRTEM lattice image of a single Pe NP on the surface of a Si NW for sample NW1Pe1, while the inset represents the corresponding selected area electron diffraction (SAED) pattern. The lattice fringes and SAED pattern confirm the crystalline nature of the Pe NP grown on the Si NW template. The lattice spacing of 0.26 nm and 0.28 nm correspond to (204) and (310) planes of $CH_3NH_3PbI_3$ crystal.

2.3.1.2 XRD Analysis

The crystal structure and phase of the $CH_3NH_3PbI_3$ were confirmed by XRD analysis. **Fig. 2.4(a)** shows a comparison of the XRD patterns of Pe on silicon wafer along with those of the NW1Pe1 and NW2Pe1. The different XRD peaks of crystalline $CH_3NH_3PbI_3$ were distinguished and well-matched with the literature. The strong diffraction peaks at 2θ equals to 14.09º, 19.97º, 23.48º, 24.47º, 28.43º, 31.85º, 34.94º, 40.49º, 43.04º, and 50.18º can be assigned to (110), (112), (211), (202), (220), (310), (312), (224), (314) and (404) crystal planes of crystalline $CH_3NH_3PbI_3$, respectively.[17] These peaks indicate the tetragonal structure of $CH_3NH_3PbI_3$.[17] A broad background peak (2θ = 20º - 30º) present in case of Si NW/perovskite heterostructure is due to the amorphous oxide layer on Si NW.[18] XRD also confirms that the Pe NPs are of the same phase that of the bulk film. In the case of Pe on bulk Si, the intensity of the XRD peak is much higher due to the thicker layer of perovskite. A careful analysis of the XRD peak profile indicates that the line width of the XRD peaks is higher in the case of Pe NPs due to the decrease in crystallite size, which indicates the nanocrystalline nature of the Pe NPs. A comparison of normalized intensity of (110) XRD peak is shown in the inset of **Fig. 2.4(a)**. Interestingly, the broadening of XRD peaks in NW1Pe1 is much higher than that in NW2Pe1, which indicates the formation of smaller size Pe NPs on NW1 than that on NW2.

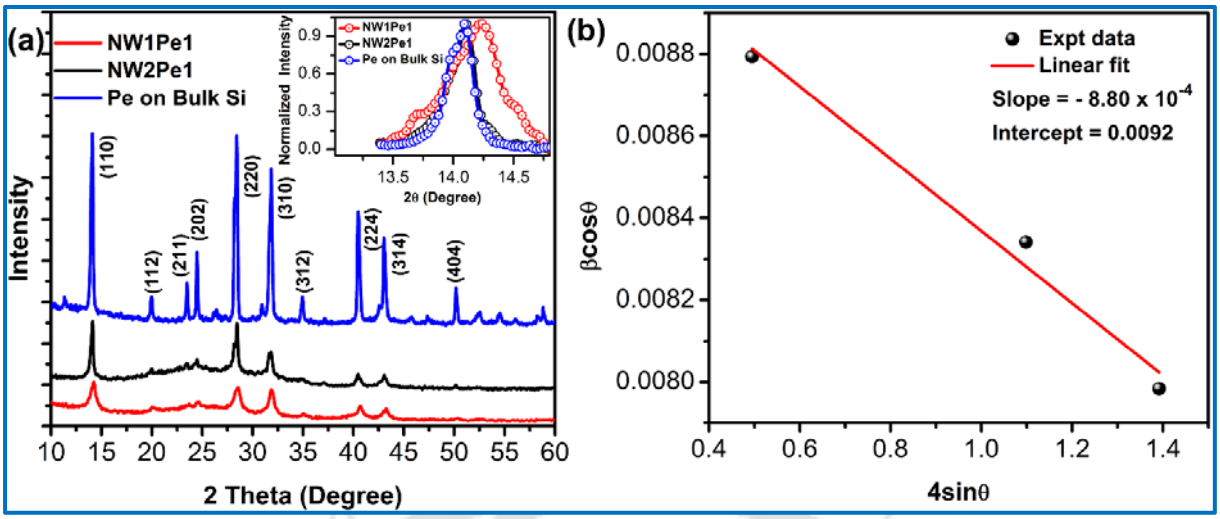

Fig. 2.4: (a) Comparison of XRD patterns of the samples NW1Pe1, NW2Pe1, and perovskite film on Si wafer. The inset shows the normalized XRD pattern of (110) peak for different samples, which indicates the broadening and peak shift in the case of NPs. (b) Williamson-Hall (W-H) plot of sample NW1Pe1, where the negative slope implies a compressive strain.

The crystallite sizes of different samples were calculated from (110) peak using Scherrer's formula[19]:

$$D = \frac{k\lambda}{\beta cos\theta} \qquad (2.1)$$

where k is Scherrer's constant, λ is the wavelength of X-ray of Cu K_α-line (1.54 Å), β is the calculated full width at half maximum (FWHM), θ is the Bragg angle. The calculated crystallite sizes for the samples NW1Pe1, NW2Pe2, and Pe on bulk Si are about 16 nm, 34 nm, and 44 nm, respectively. These values are quite consistent with the TEM results discussed earlier. The XRD peaks are marginally shifted towards the higher angle in the sample NW1Pe1 and NW2Pe1, which may due to the compressive strain produced in the Pe NPs on Si NW.[20] To account for the lattice strain, we have also calculated the crystallite size and strain in Pe NPs using Williamson-Hall (W-H) plot based on the equation: [20]

$$\beta \cos\theta = \frac{k\lambda}{D} + 4e\ sin\theta \qquad (2.2)$$

where *e* represents the strain. **Fig. 2.4(b)** shows the W-H plot of sample NW1Pe1. We obtained the crystallite size of 15.9 nm and a compressive strain of 0.088 % in sample NW1Pe1, which are consistent with the TEM analysis.

2.3.2. Diffuse Reflectance Spectroscopy

For a better understanding of the change in the band structure of perovskite due to the NP formation, we have carried out the DRS measurement of various samples, which are opaque in nature. The absorption coefficient/ absorbance of a sample is related to the diffused reflectance (R) by the Kubelka−Munk (K-M) function, F(R), given by

$$F(R) = \frac{(1-R)^2}{2R} = \frac{K}{S} \qquad (2.3)$$

where R is the diffuse reflectance, *K*, and *S* are the absorption coefficient and scattering coefficient, respectively. **Fig. 2.5** shows a plot of the F(R)) of the samples NW1Pe1, NW2Pe1, and Pe on bulk Si in the range 450-850 nm.

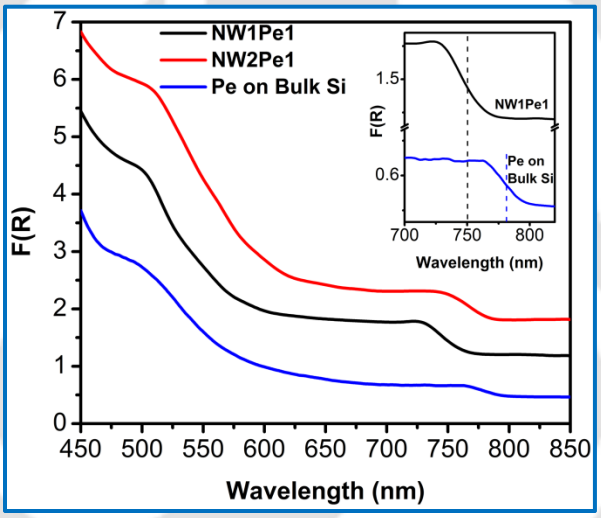

Fig. 2.5: Comparison of the F(R) for samples NW1Pe1, NW2Pe1, and perovskite film on Si wafer. The inset shows a magnified view of the absorption edges, indicating a blue shift of the absorption edge for the Pe NPs with respect to that of the bulk Pe film on Si wafer.

It is clear from the figure that all the samples have a high absorption coefficient over the entire visible region, and the F(R) increases with decreasing wavelength, as expected for the perovskite layer/NPs.[21] From the K-M plot, it is clear that the absorption coefficient of the samples NW1Pe1 and NW2Pe1 is higher than that of the Pe film on Si wafer. Note that though the absorption coefficient of NW2Pe1 is higher than that of NW1Pe1, the PL intensity (discussed later) of NW1Pe1 is much higher than that of NW2Pe1. The inset of **Fig. 2.5** shows a magnified view of the comparison of F(R) for NW1Pe1 and Pe on bulk Si clearly revealing the blue shift in the absorption edge (indicated by the vertical dashed lines) for the Pe NPs with respect to that of Pe

on bulk Si. Interestingly, such a blue shift indicates the higher bandgap of the Pe NPs, which may be due to quantum confinement effect.[8, 12, 15, 22] Note that the blue shift is higher for NW1Pe1 as compared to that of NW2Pe1, which reveals a stronger quantum confinement effect in the NPs for NW1Pe1. Dawei et al. showed that the small effective mass of electrons in $CH_3NH_3PbBr_3$ is responsible for the quantum confinement effect even in relatively large grain sizes (d > 10 nm), in comparison to the II−VI nanocrystals, such as CdS and CdSe.[12] In the present case, the average size of the Pe NPs is ≥10 nm in both NW1Pe1 and NW2Pe1. We believe that lattice strain/distortion is also partly responsible for the blue shift of the absorption edge.[23, 24]

2.3.3. Steady-State Photoluminescence Study

To study the impact of the nanoscale dimension of perovskite on the PL emission, we measured the PL spectra of different samples using a 405 nm laser at room temperature. The comparison of the PL spectra of the mesoporous Si NW samples before and after Pe NPs decoration is shown in **Fig. 2.6(a)** and **Fig. 2.6(b)** for NW1 and NW2, respectively. For comparison, the PL spectrum of Pe on bulk Si is presented in each case. **Fig. 2.6(c)** depicts the comparison of the normalized PL spectra of sample NW1Pe1, NW2Pe1, and Pe on bulk Si. A single PL peak centered at ~ 779 nm was detected in the Pe on bulk Si, which corresponds to the photoemission peak for bulk $CH_3NH_3PbI_3$ perovskite due to the band to band transition. The sample NW1 shows a broad (520-850 nm) and high-intensity PL peak. The broad PL emission from MACE grown Si NWs has been well studied and explained based on the following contributions: (a) nonbridging oxygen hole center (NBOHC) defects in the Si/SiO_x interface, (b) the quantum confinement effect in the Si NCs, which are formed due to the lateral etching of the Si NWs, and (c) oxygen vacancy (V_O) defects in the SiO_x structure. However, after the decoration of Pe NPs on mesoporous Si NWs, the NW1Pe1 shows enhancement in PL intensity and a significant amount of blue shift (~38 nm) as compared to bulk perovskite film. This type of blue shift in Pe NPs is attributed primarily to the quantum confinement effect in the Pe NPs, which are formed on the mesoporous surface of the Si NWs. [8, 12, 15, 22] Note that the intensity of the PL peak in sample NW1Pe1 is enhanced by ~ 11.9 times than that of for the Pe on bulk Si. Several factors may be responsible behind the enhancement of PL intensity for the sample NW1Pe1. These are: (a) decrease in particle size and the NP formation, (b) quantum size effect in the recombination dynamics of the Pe NPs, (c) reabsorption of photons from mesoporous NWs followed by re-emission by the Pe NPs; and (d) large surface area of the Pe NPs on Si NWs due to the high aspect ratio of the mesoporous Si NWs.

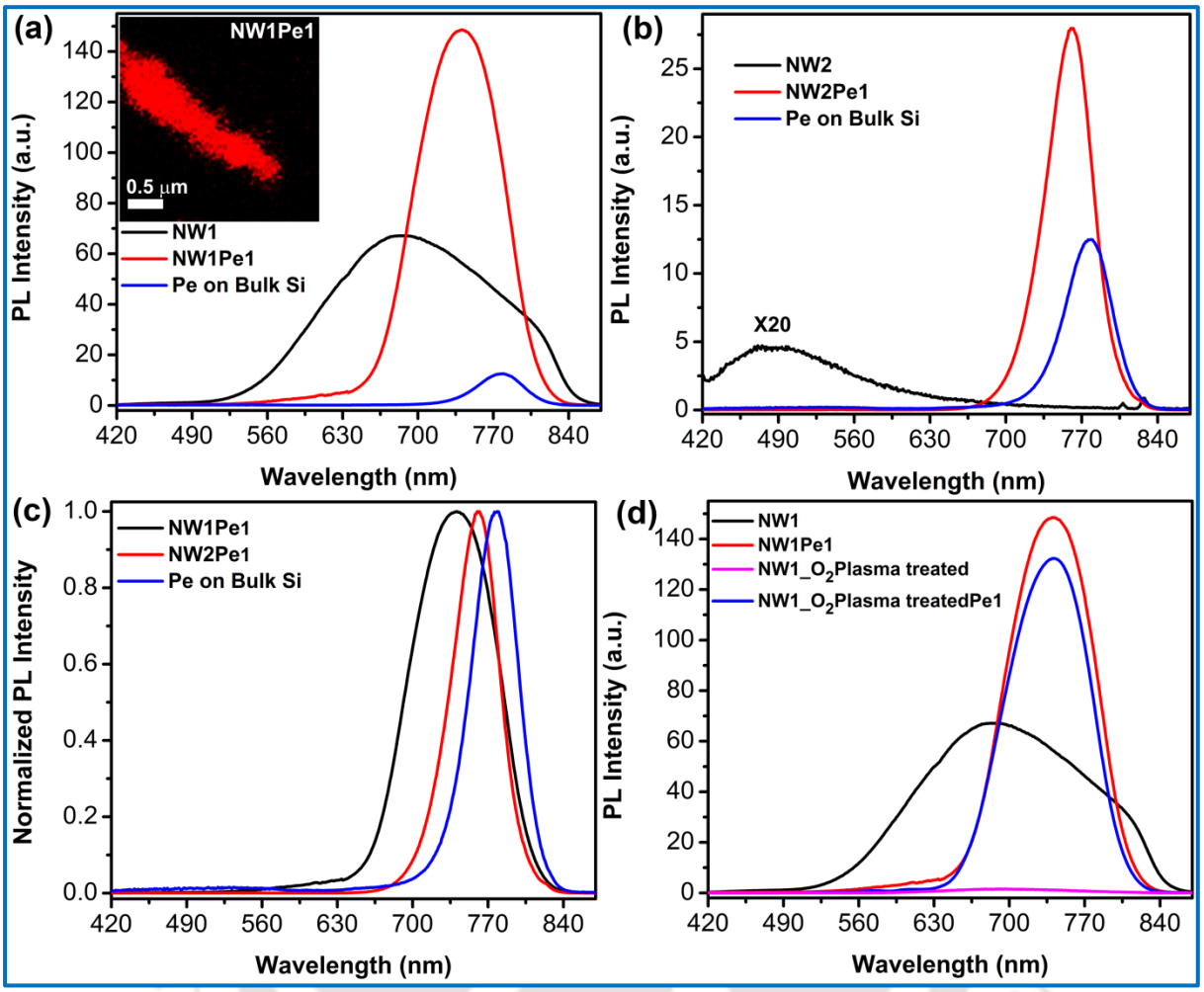

Fig. 2.6: (a) Comparison of PL spectra of the samples NW1, NW1Pe1, and perovskite film on Si wafer, inset shows the fluorescence confocal microscopy image of Pe NPs coated single Si NW in the sample NW1Pe1. (b) Comparison of PL spectra of the samples NW2, NW2Pe1, and perovskite film on Si wafer. The PL spectrum of NW2 is magnified by 20 times to enable comparison with the other samples. (c) Normalized PL spectra of NW1Pe1, NW2Pe1, and bulk perovskite film showing blue shift of peaks for perovskite NPs. (d) Comparison of PL spectra of bare NW1, Oxygen plasma treated NW1, and perovskite NPs on NW1 before and after the plasma treatment.

It has been reported that Pe NPs and quantum dots show very high-intensity PL emission compared to that of bulk counterpart, due to high radiative recombination in quantum structure. In the present case, high density and quantum size Pe NPs are decorated on the surface of the Si NWs. Hence, the quantum confinement effect in Pe NPs is most likely responsible for the huge enhancement in the PL intensity of sample NW1Pe1. Note that sample NW2Pe1 possesses the bigger size and lower density Pe NPs as compared to that of sample NW1Pe1 (as confirmed from the TEM analysis shown in **Fig. 2.3(j)** and **Fig. 2.3(m)**). Thus, the quantum confinement effect would be less prominent in sample NW2Pe1 as compared to the sample NW1Pe1. As a result, we

obtained only 2.2 times enhancement in PL intensity for NW2Pe1 as compared to that of Pe on bulk Si, as shown in **Fig. 2.6(b)**. Due to the larger size Pe NPs, the PL spectrum of NW2Pe1 shows only 18 nm blue shift, while it is 38 nm for sample NW1Pe1 from that of the bulk perovskite film (**Fig. 2.6(c)**). This is fully consistent with our DRS analysis.

It is also likely that the PL emission intensity of Pe NPs increased partly due to the restricted charge diffusion in smaller size Pe NPs than the bulk Pe crystal case. The density of nonradiative centers is directly proportional to the particle size when the concentration of the luminescent material is unaltered. On the other hand, charge carriers become locally confined within the ultrasmall Pe NPs, and these smaller NP are less affected by the deep trapping sites present in the bigger NPs/ bulk crystal with grain boundary. Thus, for a fixed concentration of perovskite, a group of smaller NPs will have higher PL QY as compared to that of the group of larger NPs and bulk perovskite crystals, and this result in higher PL QY from the confined Pe NPs.

Note that the bare Si NW in NW1 has high-intensity PL emission centered at ~ 670 nm with a large broadening (in the range of 520-850 nm), as depicted in **Fig. 2.6(a)**. The perovskite film/NPs have a very high absorbance over the entire visible range, as discussed earlier.[4] Thus, Pe NPs can reabsorb the emitted photons by mesoporous Si NWs in NW1Pe1 besides the direct absorption, which may result in higher intensity PL from the Pe NPs. Thus photon recycling phenomenon may be partly responsible for the enhanced PL emission by the Pe NPs in sample NW1Pe1.[25-27] Note that the bare Si NWs in NW2 show very weak PL intensity **(Fig. 2.6(b))** as compared to that in NW1 (I_{NW1}/I_{NW2} = 293). Therefore, the PL intensity enhancement is lesser in NW2Pe1 than that of the NW1Pe1. The inset of **Fig. 2.6(a)** is the fluorescence confocal microscopy image of Pe NPs decorated single NW of the sample NW1Pe1.

To understand quantitatively the amount of PL enhancement due to reabsorption and re-emission, we have further quenched the PL of NW1 by oxygen plasma treatment. In the case of oxygen plasma-treated NW, PL is disappeared due to passivation/removal of NBOHC defects, which is mainly responsible for the PL emission from Si NWs. **Fig. 2.6(d)** shows a comparison of the PL spectra of NW1, oxygen plasma-treated NW1, and Pe NPs on NW1 before and after oxygen plasma treatment. After the deposition of perovskite on oxygen plasma treated NW1, we obtained ~10.6 fold enhancement in PL intensity, while the enhancement factor was ~11.9 before the plasma treatment (sample NW1Pe1). Therefore, the contribution of photon recycle due to the Si NWs on the PL enhancement of Pe NPs is ~1.1, i.e., ~10%. Note that there is no change in the spectral

shape and position of the PL spectra of NW1_O_2plasma treatedPe1 as compared to that of for NW1Pe1. Thus, the 10.6 fold enhancement in PL intensity of Pe NPs is only due to the quantum confinement effect of high-density Pe NPs on the NW surface. We have also measured the PL quantum yield of the Pe NPs in different samples. We obtained PL quantum yields of 9.82 %, 2.86%, and 0.69% for NW1Pe1, NW2Pe1, and Pe on bulk Si, respectively, which are considerably high and comparable to the QY reported for $CH_3NH_3PbI_3$ film grown by sophisticated low-pressure vapor assisted solution process method [28, 29]. The FWHM OF PL peak for NW1Pe1 and NW2Pe1 are ~94.6 nm and ~51.0 nm, respectively, whereas it is ~50.1 for the Pe on bulk Si. The broad PL peak in NW1Pe1 is due to the wide range of size distribution of the NPs, as confirmed from TEM. A summary of the PL features of different samples is presented in **Table 2.2.**

Table 2.2: *Summary of the PL spectral features of different samples.*

Sample code	***PL peak center (nm)***	***PL intensity enhancement factor***	***PL QY***
NW1Pe1	741	11.9	9.82 %
NW2Pe1	761	2.2	2.86 %
Pe on bulk Si	779	1	0.69 %

Due to the high aspect ratio of the Si NWs and the multiple reflections in the vertical NW array, a large number of Pe NPs are exposed to the laser excitation. Therefore, the absorption and PL intensity are high in the case of the Si NW/perovskite heterostructure. Note that the effects of quantum confinement of carriers and reabsorption of light are less in the case of sample NW2Pe1, though we observed enhanced PL intensity. This may be due to the high surface area of the Si NWs of sample NW2.

For further confirmation of the size effect and quantum confinement effect in Pe NPs, we have studied the PL spectra of different perovskite heterostructure samples, which are grown with spin-coating of different concentration perovskite precursor on NW1. **Fig. 2.7(a)** shows the comparison of PL spectra of samples NW1, NW1Pe1, NW1Pe2, NW1Pe3, and NW1Pe4, while **Fig. 2.7(b)** shows the corresponding normalized spectra, which clearly shows a large blue shift for the smaller Pe NPs obtained with a lower concentration of perovskite. For example, with the increasing concentrations of perovskite precursor, the PL contribution of the Si NWs is decreased,

and it is minimum for the sample NW1Pe1, where the entire surfaces of the Si NWs are covered by the Pe NPs.

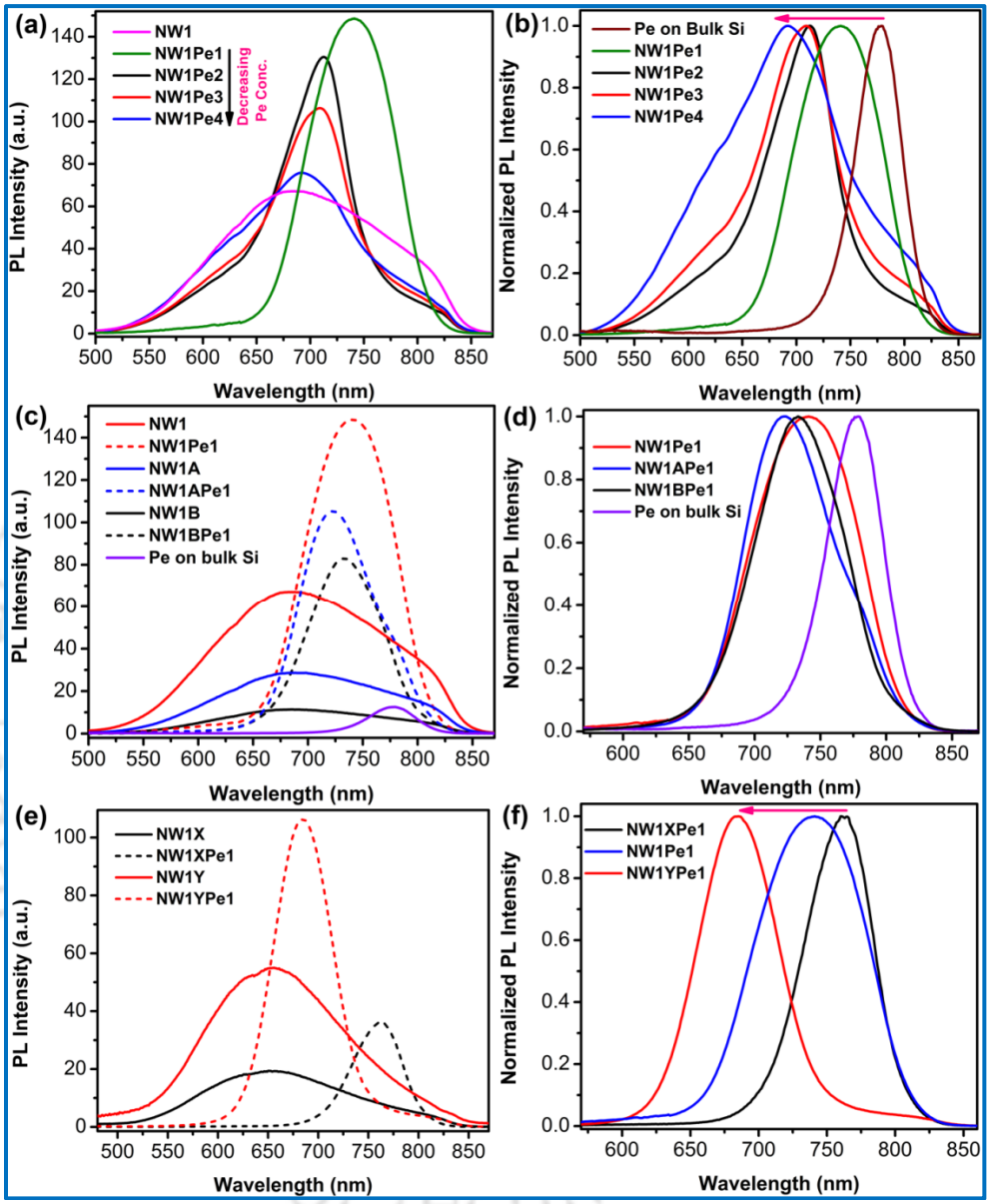

Fig. 2.7: (a) Comparison of PL spectra of NW1/perovskite heterostructure samples for different concentrations of perovskite precursor. (b) Corresponding normalized PL spectra. The normalized PL spectrum of perovskite film on Si wafer is also shown for comparison. (c) Comparison of PL spectra of different bare Si NWs, which are etched for different etching duration with their heterostructure with Pe1. (d) Normalized PL spectra of NW1Pe1, NW1APe1, NW1BPe1, and perovskite film on Si wafer. (e) Comparison of PL spectra of Si NWs, which are grown with different wafer resistivity before and after its heterostructure formation with Pe1. (f) Normalized PL peak of NW1XPe1, NW1Pe1, and NW1YPe1.

The density and size of the Pe NPs were increased with the increase of perovskite concentration. Note that the average size of the Pe NPs is smallest when the concentration of perovskite is lowest.

With the increase in the concentration of perovskite, the smaller NPs are merged together and form comparatively larger size NPs. Hence, corresponding to the smallest size NPs in NW1Pe4 we obtained the largest blue shift in the sample, and then it gradually decreases with the increase in the concentration of perovskite **(Fig. 2.7(b))**.

For a quantitative assessment of the quantum confinement effect on the Pe NPs, we used the well-known Brus formula to calculate the blue shift in band gap from the measured size of the Pe NPs using the relation:

$$E_0 = E_g + \frac{h^2}{8\mu R^2} - \frac{1.786e^2}{4\pi\varepsilon_0\varepsilon_r R} \qquad (2.4)$$

which assumes a hydrogen-like model to depict the interaction between electron-hole pairs confined in spherical semiconductor nanocrystals. In Eqn. (2.4), E_0 is the energy of the lowest excited state of the exciton inside the nanocrystal, E_g is the energy bandgap of bulk $CH_3NH_3PbI_3$ (in our case 1.592 eV), h is Planck's constant, μ is the exciton reduced mass, R is the radius of the nanoparticle, e is the electron charge, and ε_0 and ε_r are the dielectric constants of vacuum and $CH_3NH_3PbI_3$, respectively. The second term in Eqn. (2.4) corresponds to the first energy level of a quasiparticle of reduced mass μ confined in a spherical well of radius R limited by a wall of infinite potential. Note that in the case of NW1Pe2, the average size of the Pe NPs is ~5 nm, and using the known values of constants for $CH_3NH_3PbI_3$ ($\mu=0.08m_0$, ε_r = 18) in Eqn. (2.4), we estimate a peak shift of 0.158 eV. Interestingly, this is very close to the experimentally observed value of 0.150 eV corresponding to the peak at 712 nm (see **Fig. 2.7(b)**). This strongly supports the QC model for the observed blue shift of the PL peak in Pe NPs. In the case of NW1Pe1, the average size of the NPs is ~20 nm, with some of them in size <10nm. Since only the smaller size NPs are expected to contribute toward the blue-shift of the PL peak, taking R=10 nm in Eqn. (2.4) yields a calculated blue shift of ~0.05 eV, while the experimentally observed blue-shift in 0.08 eV. Such a deviation may hint toward the weak confinement of the NPs due to the larger size NPs in NW1Pe1 as compared to its excitonic Bohr diameter. Note that Eqn. (2.4) assumes a simple model mostly valid for a strong confinement case. Nevertheless, our calculation provides convincing evidence for the quantum confinement of carriers in Pe NPs grown on a Si NW template.

In order to understand the effect of surface area on the PL enhancement of NW1/perovskite heterostructure, we have analyzed the PL spectrum of NW1/perovskite heterostructure for two different Si NWs samples etched for the different duration (NW1A -etching time 10 min, and NW1B - etching time 5 min). **Fig. 2.7(c)** shows the comparison of the PL spectra of NW1Pe1,

NW1APe1, NW1BPe1 and Pe on bulk Si, while **Fig 2.7(d)** shows the corresponding normalized spectra. The PL spectra of bare Si NWs in sample NW1A, NW1B and NW1 are also presented in **Fig 2.7(c)** for comparison. Note that NW1 is etched for 20 min for the mesoporous NW formation. As compared to the bulk perovskite film, the PL intensity enhancements in samples NW1Pe1, NW1APe1 and NW1BPe1 are found to be 11.9, 8.4, and 6.7 times, respectively. It is clear that the PL enhancement factor increases with increasing the etching time of Si wafers. Longer etching time leads to a higher length, higher surface area, and higher density of pores on the NW surface. Thus, the PL intensity is higher for sample NW1Pe1 due to the high surface area and a higher density of Pe NPs. The normalized PL spectra of the NW1/perovskite heterostructure shown in **Fig 2.7(d)** reveals a higher blue-shift for the lower etching time for the Si NW formation. For the shorter length of Si NWs, the pore density and pore sizes are less as compared to that in longer Si NWs. Thus, during the formation of Pe NPs, the possibility of forming smaller size and isolated Pe NPs is higher in the case of shorter Si NWs with the lower density of pores, and it results in the higher blue-shift. The surface states and surface phenomena can also cause the blue shift of PL peaks.

In order to control the size of the Pe NPs on Si NWs, we have controlled the porosity of NW1 by choosing different resistivity (ρ) Si wafers as starting material. **Fig 2.7(e)** shows the comparison of the PL spectra of bare Si NW sample NW1X (ρ = 1 Ω-cm) and NW1Y (ρ = 0.001 Ω-cm) along with its heterostructure made with Pe1. **Fig. 2.7(f)** shows the comparison of the normalized PL spectra of the sample NW1XPe1, NW1Pe1, and NW1YPe1. Note that the resistivity of the starting Si wafer of sample NW1 is 0.01 Ω-cm. With lower resistivity Si wafer, the porosity of the Si NW increases, which causes an increase in the density of smaller size Pe NPs on NW surface. Therefore, we observed a higher blue-shift of PL peak for the lower resistivity Si wafer (see **Fig. 2.7(f)**).

2.3.4. Time-Resolved Photoluminescence Study

To gain an insight into the exciton recombination dynamics, TRPL decay of each sample was measured using a pulsed diode laser of 405 nm (average power ~1.0 mW). **Fig. 2.8(a)** shows a comparison of the TRPL decay profiles of NW1Pe1, NW2Pe1, and Pe on bulk Si monitored at the PL peak center of each sample. TRPL data in each case were fitted by a bi-exponential decay function as:

$$A(t) = A_1 \exp(\frac{-t}{\tau_1}) + A_2 \exp(\frac{-t}{\tau_2}) \qquad (2.5)$$

Where A_1 and A_2 are the amplitudes of the TRPL decay with lifetimes τ_1 and τ_2, respectively. We estimated the average lifetimes (τ_{ave}) using the relation.[18]

$$\tau_{ave} = \frac{\sum A_i \tau_i}{\sum A_i} \qquad (2.6)$$

The average lifetimes are found to be 2.44 ns, 3.88 ns and 5.21 ns for Pe on bulk Si wafer, NW1Pe1 and NW2Pe1, respectively. The two time constants are correlated with the radiative electron-trapping and the radiative electron-hole recombination of halide perovskite. Thus, as compared to the bulk $CH_3NH_3PbI_3$ film, average recombination lifetimes of Pe NP on Si NWs are higher. This type of prolonged PL lifetime has been observed for $CH_3NH_3PbBr_3$ nanoplatelet, which indicates an extraordinary low nonradiative recombination rate in the perovskite nanoplatelet than the bulk counterpart.[30] In the present case, the recombination lifetime is higher for Pe NPs, which may be due to reduced nonradiative recombination and higher radiative recombination than the bulk $CH_3NH_3PbI_3$ film. Thus, the higher radiative recombination is believed to be responsible for the large PL enhancement in the Si NW/perovskite NPs heterostructure. In the present case, NW1Pe1 has faster decay than the sample NW2Pe1, which is due to the quantum size effect. Literature reports suggest that in case of quantum confinement effect, smaller NPs have faster TRPL decay than that of larger NPs. [16, 31] This is consistent with our interpretation of quantum size effect in Pe NPs.

To study the emission wavelength dependence of the PL decay profile, we have measured the decay profiles of NW1Pe1 in the emission wavelength range of 640 nm to 780 nm at an interval of 20 nm, and the results are shown in **Fig. 2.8(b)**. In each case, the data points are fitted with a bi-exponential decay, and the fitted curves are shown by the solid lines. From TRPL analysis (**Fig. 2.8(b)**), it is clear that the broad PL peak of NW1Pe1 originates mostly due to different sizes of Pe NPs. The decay time constant decreases with increasing the energy of emission. On the basis of the quantum confinement effect, the higher energy PL arises mainly from a group of smaller size NPs, and smaller size NPs have a shorter lifetime, as reported in the literature.[16, 31] **Fig. 2.8(c)** shows the TRPL decay profile of bare NW1 fitted by a tri-exponential decay function and an average recombination lifetime of ~ 14.87 μs is obtained. The inset in **Fig. 2.8(c)** is the TRPL decay profile of NW2 fitted with a bi-exponential function with a decay lifetime of ~ 0.71 ns. Note that bare NW1 has a very large decay lifetime (~15 μs), which will have a negligible contribution

to the TRPL decay (in ns) of NW1Pe1. From the TEM analysis, we observed that the size of the Pe NPs is smaller for a lower concentration of perovskite precursor. The TRPL decay profiles of NW1 after the deposition of different concentrations of perovskites are shown in **Fig. 2.8(d)**.

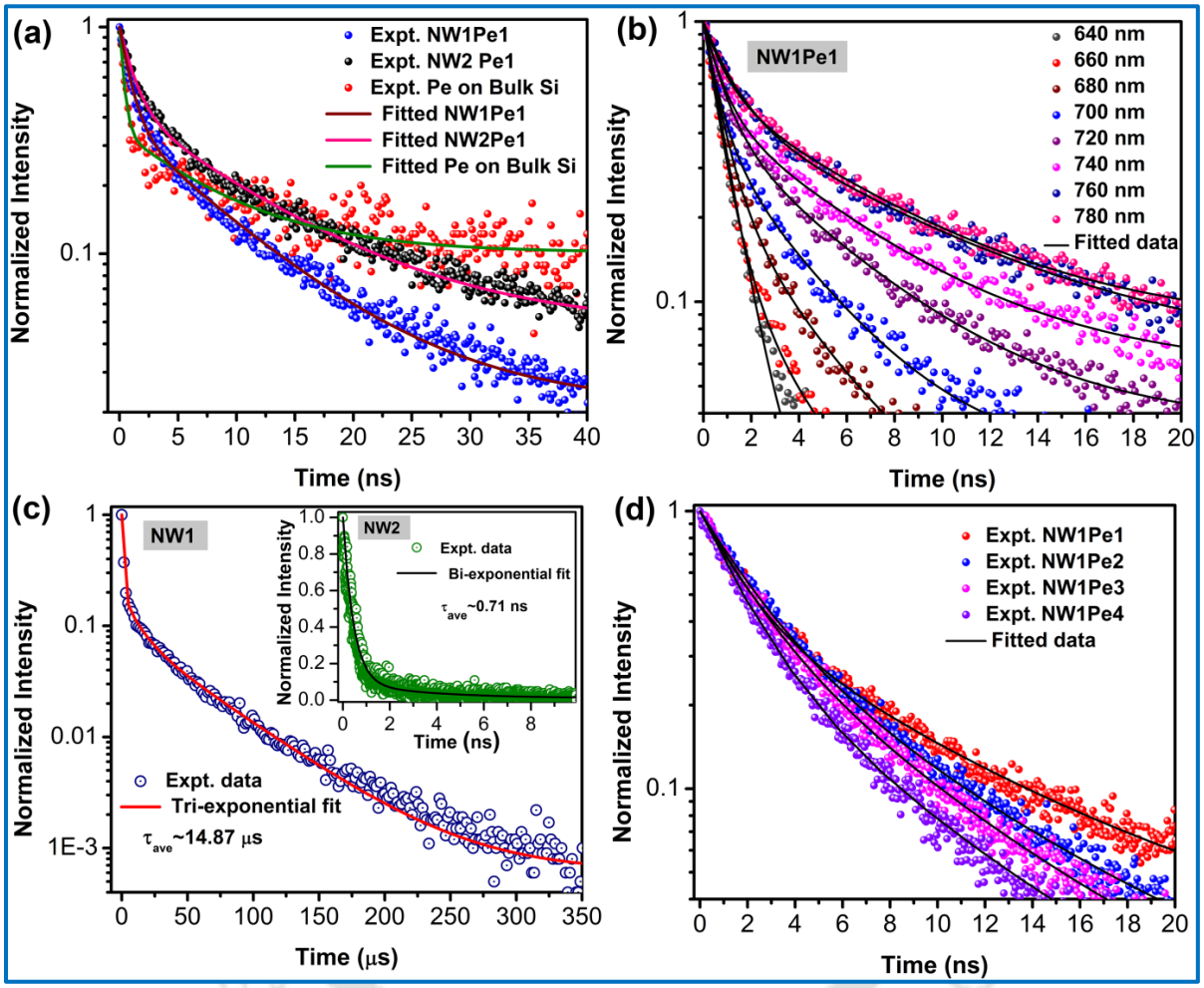

Fig. 2.8: (a) TRPL decay of sample NW1Pe1, NW2Pe2, and perovskite film on Si wafer. (b) PL decay of sample NW1Pe1 at emission wavelengths 640-780 nm, with interval of 20 nm. (c) TRPL decay profile of bare Si NWs in NW1. Inset is the TRPL decay of bare NW2. (d) TRPL decay profiles of the samples NW1Pe1, NW1Pe2, NW1Pe3, and NW1Pe4. In each case, symbols represent the experimental data, and solid lines represent the fitted data.

As expected, at lower concentrations of the precursor, the decay becomes faster, and the average recombination lifetime is reduced, which again supports the quantum size effect of the Pe NPs.

2.4. Conclusions

We investigated the controlled fabrication of $CH_3NH_3PbI_3$ NPs on the mesoporous Si NW template and reported its high PL quantum yield, which is significant for light-emitting application. Highly crystalline Pe NPs with controlled sizes were synthesized by spin-coating of perovskite precursor

on the surface of MACE grown mesoporous Si NWs followed by annealing at 80 ºC in ambient condition. Our results demonstrate that the porous sites of the Si NWs act as the nucleation sites for the growth of the Pe NPs. We have tuned the size and PL properties of the Pe NPs by controlling the porosity of the mesoporous Si NWs and perovskite precursor concentrations. The systematic studies by FESEM, TEM, XRD, and EDX confirm that the crystalline Pe NPs confined within the pores of the NWs and are uniformly decorated over the surface of the NWs. Under ambient conditions, the Pe NPs on Si NWs are ~12 times more PL efficient than the perovskite thin film on Si substrate. It is demonstrated that the ultra-small size and the quantum confinement effect in the Pe NPs are primarily responsible for the enhanced PL intensity and the blue-shift of the PL peak. The reabsorption of photons by Pe NPs from the highly luminescent mesoporous Si NWs followed by the re-emission by the Pe NPs (photon recycling) partly contributes to the PL intensity enhancement of Pe NPs. We achieved a PL QY of 9.82 % for the Pe NPs grown on the Si NW template under the normal ambient condition. The systematic studies on Pe NPs by time-resolved PL analysis strongly support our explanation on the origin of PL enhancement. This study demonstrates the fabrication of Si NWs/perovskite NPs heterostructure, and it unravels the mechanism behind the superior photophysical properties of the confined Pe NPs decorated on mesoporous Si NWs, which are fabricated by an easy, cost-effective and novel template-based technique. Our results open up the possibility of using perovskite NPs/mesoporous Si NW heterostructure for various kinds of cutting edge applications including LEDs, laser, photovoltaic cells, etc.

References

1. J.-P. Correa-Baena, A. Abate, M. Saliba, W. Tress, T. Jesper Jacobsson, M. Gratzel and A. Hagfeldt, *Energy Environ Sci*, 2017, **10**, 710-727.
2. Z. Zhu, Y. Bai, X. Liu, C.-C. Chueh, S. Yang and A. K. Y. Jen, *Adv. Mater.*, 2016, **28**, 6478-6484.
3. N.-G. Park, M. Grätzel, T. Miyasaka, K. Zhu and K. Emery, *Nat. Energy*, 2016, **1**, 16152.
4. Y. Liyan, T. B. Alexander, G. L. David and W. Tao, *Rep. Prog. Phys.*, 2016, **79**, 026501.
5. Y. H. Lee, J. Luo, M.-K. Son, P. Gao, K. T. Cho, J. Seo, S. M. Zakeeruddin, M. Grätzel and M. K. Nazeeruddin, *Adv. Mater.*, 2016, **28**, 3966-3972.
6. M. F. Aygüler, M. D. Weber, B. M. D. Puscher, D. D. Medina, P. Docampo and R. D. Costa, *J. Phys. Chem. C*, 2015, **119**, 12047-12054.
7. V. D'Innocenzo, A. R. Srimath Kandada, M. De Bastiani, M. Gandini and A. Petrozza, *J. Am. Chem. Soc.*, 2014, **136**, 17730-17733.
8. J. A. Sichert, Y. Tong, N. Mutz, M. Vollmer, S. Fischer, K. Z. Milowska, R. García Cortadella, B. Nickel, C. Cardenas-Daw, J. K. Stolarczyk, A. S. Urban and J. Feldmann, *Nano Lett.*, 2015, **15**, 6521-6527.

9. L. C. Schmidt, A. Pertegás, S. González-Carrero, O. Malinkiewicz, S. Agouram, G. Mínguez Espallargas, H. J. Bolink, R. E. Galian and J. Pérez-Prieto, *J. Am. Chem. Soc.*, 2014, **136**, 850-853.
10. J. Chen, K. Žídek, P. Chábera, D. Liu, P. Cheng, L. Nuuttila, M. J. Al-Marri, H. Lehtivuori, M. E. Messing, K. Han, K. Zheng and T. Pullerits, *J. Phys. Chem. Lett.*, 2017, **8**, 2316-2321.
11. V. A. Hintermayr, A. F. Richter, F. Ehrat, M. Döblinger, W. Vanderlinden, J. A. Sichert, Y. Tong, L. Polavarapu, J. Feldmann and A. S. Urban, *Adv. Mater.*, 2016, **28**, 9478-9485.
12. D. Di, K. P. Musselman, G. Li, A. Sadhanala, Y. Ievskaya, Q. Song, Z.-K. Tan, M. L. Lai, J. L. MacManus-Driscoll, N. C. Greenham and R. H. Friend, *J. Phys. Chem. Lett.*, 2015, **6**, 446-450.
13. K. Zheng, K. Žídek, M. Abdellah, M. E. Messing, M. J. Al-Marri and T. Pullerits, *J. Phys. Chem. C*, 2016, **120**, 3077-3084.
14. G. Longo, A. Pertegas, L. Martinez-Sarti, M. Sessolo and H. J. Bolink, *J. Mater. Chem. C*, 2015, **3**, 11286-11289.
15. Z. Zhang, M. Wang, L. Ren and K. Jin, *Sci. Rep.*, 2017, **7**, 1918.
16. R. Ghosh, P. K. Giri, I. Kenji and F. Minoru, *Nanotechnology*, 2014, **25**, 045703.
17. J. Qiu, Y. Qiu, K. Yan, M. Zhong, C. Mu, H. Yan and S. Yang, *Nanoscale*, 2013, **5**, 3245-3248.
18. R. Ghosh, P. K. Giri, K. Imakita and M. Fujii, *J. Alloy. Comp.*, 2015, **638**, 419-428.
19. J. Chen, D. Liu, M. J. Al-Marri, L. Nuuttila, H. Lehtivuori and K. Zheng, *Sci. China Mater.*, 2016, **59**, 719-727.
20. P. K. Giri, S. Bhattacharyya, D. K. Singh, R. Kesavamoorthy, B. K. Panigrahi and K. G. M. Nair, *J. Appl. Phys.*, 2007, **102**, 093515.
21. Y. Tian and I. G. Scheblykin, *J. Phys. Chem. Lett.* , 2015, **6**, 3466-3470.
22. S. Demchyshyn, J. M. Roemer, H. Groiß, H. Heilbrunner, C. Ulbricht, D. Apaydin, A. Böhm, U. Rütt, F. Bertram, G. Hesser, M. C. Scharber, N. S. Sariciftci, B. Nickel, S. Bauer, E. D. Głowacki and M. Kaltenbrunner, *Sci. Adv.*, 2017, **3**, e1700738.
23. V. Malgras, S. Tominaka, J. W. Ryan, J. Henzie, T. Takei, K. Ohara and Y. Yamauchi, *J. Am. Chem. Soc.*, 2016, **138**, 13874-13881.
24. R. Prasanna, A. Gold-Parker, T. Leijtens, B. Conings, A. Babayigit, H.-G. Boyen, M. F. Toney and M. D. McGehee, *J. Am. Chem. Soc.*, 2017, **139**, 11117-11124.
25. J. Y. Woo, K. Kim, S. Jeong and C.-S. Han, *J. Phys. Chem. C*, 2011, **115**, 20945-20952.
26. N. J. L. K. Davis, F. J. de la Peña, M. Tabachnyk, J. M. Richter, R. D. Lamboll, E. P. Booker, F. Wisnivesky Rocca Rivarola, J. T. Griffiths, C. Ducati, S. M. Menke, F. Deschler and N. C. Greenham, *J. Phys. Chem. C*, 2017, **121**, 3790-3796.
27. M. Saliba, W. Zhang, V. M. Burlakov, S. D. Stranks, Y. Sun, J. M. Ball, M. B. Johnston, A. Goriely, U. Wiesner and H. J. Snaith, *Adv. Funct. Mater.*, 2015, **25**, 5038-5046.
28. C. M. Sutter-Fella, Y. Li, M. Amani, J. W. Ager, F. M. Toma, E. Yablonovitch, I. D. Sharp and A. Javey, *Nano Lett.*, 2016, **16**, 800-806.
29. J. M. Richter, M. Abdi-Jalebi, A. Sadhanala, M. Tabachnyk, J. P. H. Rivett, L. M. Pazos-Outón, K. C. Gödel, M. Price, F. Deschler and R. H. Friend, *Nat. Commun.*, 2016, **7**, 13941.
30. Y. Ling, Z. Yuan, Y. Tian, X. Wang, J. C. Wang, Y. Xin, K. Hanson, B. Ma and H. Gao, *Adv. Mater.*, 2016, **28**, 305-311.
31. H. Rinnert, O. Jambois and M. Vergnat, *J. Appl. Phys.*, 2009, **106**, 023501.

भारतीय प्रौद्योगिकी संस्थान गुवाहाटी
Indian Institute of Technology Guwahati

Chapter 3

Origin of Strong Cathodoluminescence and Fast Photoresponse from Embedded Perovskite Nanoparticles Exhibiting High Ambient-Stability

This chapter presents a comprehensive analysis of the strong cathodoluminescence (CL), photoluminescence (PL), and photoresponse characteristics of $CH_3NH_3PbBr_3$ perovskite nanoparticles (Per NPs) embedded in a mesoporous Si NWs template. Our study revealed a direct correlation between the CL and PL emissions from the Per NPs, for the first time. Per NPs were fabricated by simple spin-coating of a perovskite precursor on the surface of metal-assisted chemically etched mesoporous Si NW arrays. The Per NPs confined in the mesopores show blue-shifted and enhanced CL emission as compared to the bare perovskite film, while the PL QY of Per NPs is dramatically high (~40.5%) compared to that of their bulk counterpart. A systematic analysis of the CL/PL spectra reveals that the quantum confinement effect and ultralow defects in Per NPs are mainly responsible for the enhanced CL and PL emissions. The Per NPs show improved ambient air stability than the bare film due to the protection provided by the dense NW array. Interestingly, the Si NW/Per NP heterojunction shows superior visible light photodetection and the prototype photodetector (PD) shows a high responsivity (0.223 A/W) with response speeds of 0.32 and 0.28 s of growth and decay in photocurrent, respectively, at 2 V applied bias.

3.1. Introduction

The unique optical and electronic properties of hybrid perovskite have shown great promises in different optoelectronic devices, such as photodetectors, light-emitting diodes, and laser.[1-4] Perovskite NPs and quantum dots (QDs) show much superior optoelectronic properties than its bulk counterpart due to the size reduction and quantum confinement effect.[5-7] However, the application of perovskites in different optoelectronic devices suffers from poor air-stability. Generally, the organometal halide perovskite material starts degrading upon exposure to water and oxygen molecule. To overcome this issue, an alternative approach is the growth of Per NPs/ NCs confined in porous inorganic templates. Several groups reported the synthesis of Per NCs on porous aluminum oxide (Al_2O_3) and silica (SiO_2) templates, which show improved optical properties due to the size reduction and quantum confinement effects with superior ambient

stability due to the encapsulation from the surrounding atmosphere by the stable inorganic host matrix.[8-11] Thus, it is interesting to study the photophysical, and optoelectronic properties of Per NPs confined within high aspect ratio mesoporous templates.

In the previous chapter, we discussed on the controlled growth of $CH_3NH_3PbI_3$ NPs with size variation using a mesoporous Si NW template with different porosity. In this chapter, we have studied the growth of $CH_3NH_3PbBr_3$ NPs on a highly porous Si NW template and investigated it's CL, PL, and photoresponse characteristics at room temperature as well as low temperature. Perovskite precursor solutions with different concentrations were deposited by the spin coating method, and post-deposition annealing produces $CH_3NH_3PbBr_3$ NPs nucleated at the porous sites of Si NW surface. The nature and origin of CL emission from the Per NPs on NW array was systematically studied for different size NPs and different energies of the incident electron beam. The origin of enhanced optical absorption and high PL QY from Per NPs was investigated. We investigated the air stability of the Per NPs embedded in between the NW array, and it showed superior performance as compared to the bulk film. Finally, we explored the Si NW/Per NPs heterojunction as an efficient PD. We demonstrate the superior luminescence properties (CL and PL) of $CH_3NH_3PbBr_3$ NPs on the mesoporous Si NW template and its application in photodetection using this novel heterostructure.

3.2. Experimental Details

3.2.1. Sample Preparation

3.2.1.1. Growth of Mesoporous Si NWs

The mesoporous Si NWs templates were fabricated by the two-step metal-assisted chemical etching (MACE) method using n-type Si wafer at room temperature for 10, 15, and 20 min of chemical etching. More details of the growth of mesoporous Si NWs were described in section **2.2.1.1** of **Chapter 2.**

3.2.1.2. Synthesis of CH_3NH_3Br

A 250 mL round-bottom flask was filled with 28 mL of a 33% solution of methylamine (CH_3NH_2) in absolute ethanol, 10 mL of a 48% solution of hydrogen bromide (HBr) in water, and 100 mL of ethanol under the nitrogen atmosphere and left under stirring for 2 h keeping in an ice bath.[12] Then, the precipitate was collected by evaporating the solvent at 55 °C. The product was collected,

thoroughly dried, and finally recrystallized from ethanol. Next, CH_3NH_3Br crystals were dried overnight at 60 °C in a vacuum oven and stored.

3.2.1.3. Synthesis of $CH_3NH_3PbBr_3$ NPs

The $CH_3NH_3PbBr_3$ precursor solution were prepared in N,N-dimethylformamide (DMF) at concentrations 0.6, 0.3, 0.15, and 0.075 M using CH_3NH_3Br and $PbBr_2$. The prepared solutions were deposited on the Si NW template by the spin-coating method at 2500 rpm for 45 s. After spin-coating, the samples were annealed on a hot plate at 85 °C for 15 min, which results in the formation of Per NPs on the NW surface. For comparison of the properties of Per NPs with their bulk counterpart, the 0.6 M precursor solution was deposited on bare Si wafer to form perovskite film, and this is referred to as a bulk Per film. The sample details are summarized in **Table 3.1.**

Table 3.1: *Details of the different Perovskite NPs grown on Si NWs with sample codes.*

Sample code	***Sample feature***	***Substrate***	***Sample growth condition***
Bulk	Bulk Per film	Si Wafer	$CH_3NH_3PbBr_3$ bulk film
N1	Si NWs		20 min MACE
N2			15 min MACE
N3			10 min MACE
N1P1	Per NPs on Si NWs	Si NWs	0.6 M Per precursor
N1P2			0.3 M Per precursor
N1P3			0.15 M Per precursor
N1P4			0.075 M Per precursor
N2P1			0.6 M Per precursor
N2P2			0.3 M Per precursor
N3P1			0.6 M Per precursor
N3P2			0.3 M Per precursor

3.2.2. Characterization Techniques

The details of the characterization techniques (FETEM, EDX, XRD, UV-vis absorbance, PL, PL QY, TRPL, etc.) used to study the systems were described in **Chapter 2, Section 2.2.2.** High-angle annular dark-field scanning TEM (HAADF-STEM) of Per NP-decorated NWs was performed using an aberration-corrected STEM (JEM 2100F, 200 kV). Room temperature cathodoluminescence spectra were recorded using Gatan Mono CL4 attached to the FESEM with varying beam accelerating voltages. Low-temperature PL measurements were performed using a liquid He cryostat along with a charge-coupled device detector. The photocurrent characteristics

of the $CH_3NH_3PbBr_3$ NP/Si NW PD were measured using a homemade setup equipped with a 405 nm laser, Xenon lamp with a monochromator, chopper, and a Keithley 2400 source meter.

3.3. Results and Discussion

3.3.1. Morphology and Structural Analyses

3.3.1.1. FESEM and FETEM Analyses

The surface morphology of the as-grown Si NW template without/with the perovskite layer was studied using FESEM and FETEM imaging. MACE-grown Si NWs are vertically aligned and the sidewalls of the NWs are mesoporous in nature.[21] Top-view FESEM images of the MACE grown Si NWs without and with the perovskite layer are shown in **Fig. 3.1(a,b)**, while the side-view cross-sectional FESEM images of the NWs are shown in the *insets* of **Fig. 3.1(a,b)**. The length of the NW is ~9.9 μm for sample N1.

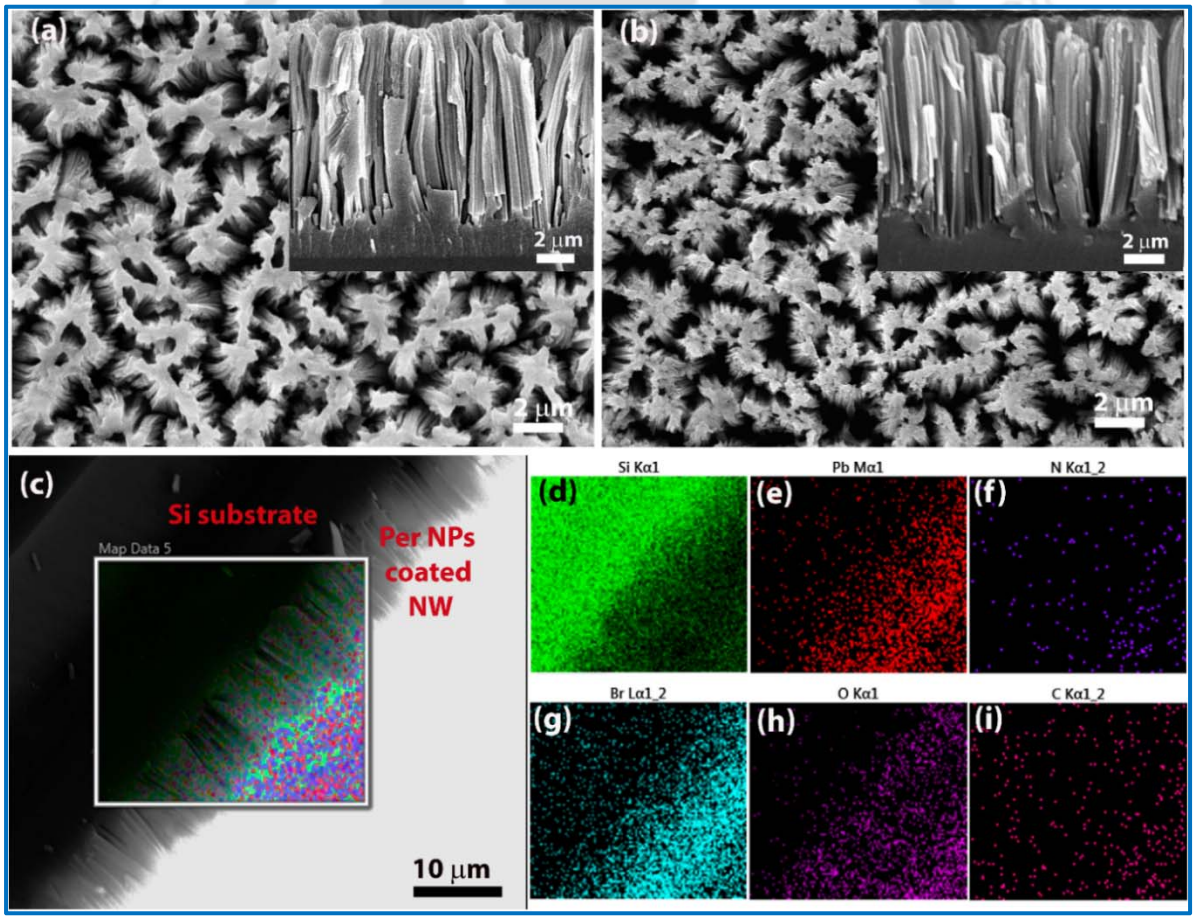

Fig. 3.1: (a) Top view FESEM image of bare Si NWs. Inset shows the cross-sectional FESEM image of bare Si NWs. (b) Top view FESEM image of Per NPs decorated Si NWs in N1P2. Inset shows a cross-sectional image of Per NPs decorated Si NWs. (c) FESEM image and EDX cross-sectional mapping of N1P2. The EDX elemental color mapping showing the distribution of (d) Si, (e) Pb, (f) N, (g) Br, (h) O, and (i) C in the sample.

Fig. 3.1(c-i) shows the EDX elemental mapping of the cross-sectional area of the Per NPs-coated NW (N1P2), which shows the distribution of different elements. From the figure, it is clear that the Per NPs are uniformly coated on the entire surface of NW down to the bottom of the NW. It confirms the uniform coating and the presence of Si, Pb, N, Br, O, and C, as expected.

The high-resolution surface morphology of the individual mesoporous Si NW and the formation of the Per NPs on its surface are characterized in detail by HADF-STEM analysis.

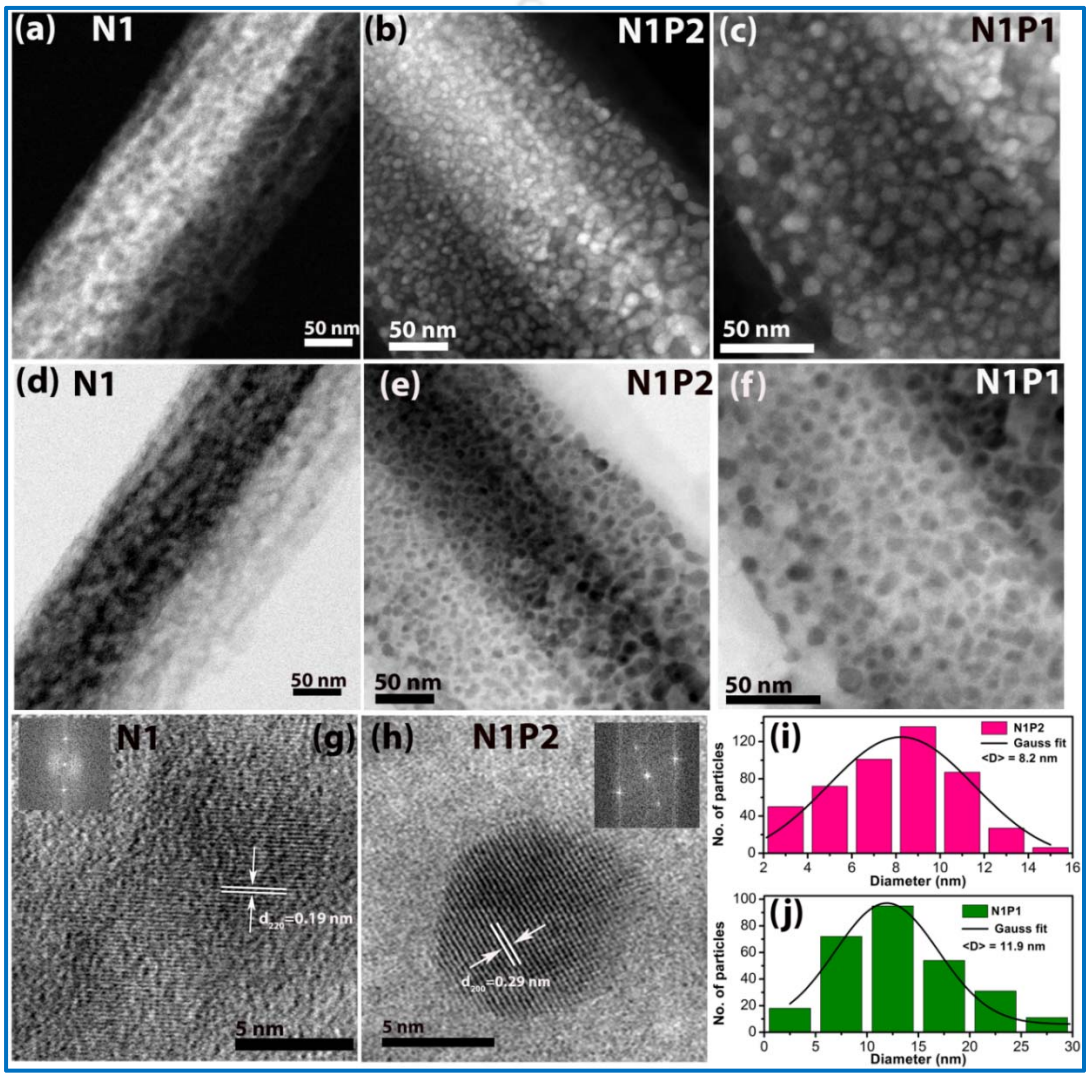

Fig. 3.2: HAADF STEM images of (a) a single mesoporous Si NW (N1), (b, c) $CH_3NH_3PbBr_3$ NPs decorated on Si NW in sample N1P2 and N1P1, respectively. Bright-field STEM images of (d) a single mesoporous Si NW (N1), (e, f) $CH_3NH_3PbBr_3$ NPs decorated on Si NW in sample N1P2 and N1P1, respectively. (g) HRTEM lattice fringe image of bare NW surface showing Si NCs lattice, while the inset shows the corresponding IFFT pattern. (h) HRTEM lattice fringe image of Per NPs in N1P2; the inset shows the corresponding FFT pattern, which confirms the crystallinity of $CH_3NH_3PbBr_3$ NPs. (i, j) the size distribution of Per NPs in sample N1P2 and N1P1, respectively. The solid lines in each case show the corresponding Gaussian fitting, and <D> indicates the average diameter of the NPs.

Fig. 3.2(a) shows the HAADF-STEM image of a single NW, which clearly reveals that the NW surface is highly porous and rough in nature. This is due to the sidewall etching during the MACE process.[13, 14] These pores act as nucleation sites for the growth of the Per NPs, which show strong room temperature CL and PL emissions. **Fig. 3.2(b)** and **Fig. 3.2(c)** depicts the HAADF-STEM images of uniformly decorated Per NPs grown on the NW surface in samples N1P2 and N1P1, respectively. It is evident from the figures that high-density Per NPs are grown and decorated on the entire NW surface. **Fig. 3.2(d)** shows the bright-field STEM image of bare NW, while **Fig. 3.2(e)** and **Fig. 3.2(f)** depict the bright-field STEM image of sample N1P2 and N1P1, respectively. These images also clearly depict the uniform decoration of the Per NPs on the NW surface. **Fig. 3.2(g)** shows the HRTEM image of the mesoporous NW surface, depicting the crystalline Si NCs decorated on the Si NW as a result of preferential etching. Due to sidewall etching, ultrasmall Si NCs are formed on the surface of the Si NWs, and these Si NCs strongly influence the optical properties of the Si NWs.[14] The size distribution of the Per NPs is calculated from **Fig. 3.2(b)** and **Fig. 3.2(c),** and it is depicted in **Fig. 3.2(i)** and **Fig. 3.2(j)**, respectively. For N1P2, the size of the Per NPs is in the range 2-14 nm with a mean size ~8.2 nm (**Fig. 3.2(i)**), while for N1P1 the size varies in the range 2-27 nm with a mean size ~11.9 nm (**Fig. 3.2(j)**). From **Fig. 3.2(b)** and **Fig. 3.2(c)**, it is evident that most of the porous sites of the Si NW surface are filled with the Per NPs, and the Per NPs are partially embedded in the Si pores, since the average size of the NPs is larger than the average pore size. Thus, the pore sites act as the nucleation center for Per NPs and they crystallize during the post-deposition annealing. Interestingly, with increasing the concentration of the perovskite precursor, the size of the NPs becomes larger (N1P1). We find that the density of the NPs is higher in N1P2 than that of N1P1 with lesser size variation. During the post-deposition annealing, higher concentration of precursor results in the growth of bigger size NPs. The smaller size and higher density of Per NPs in N1P2 have strong effects on the high-intensity CL emission and high PL QY (discussed later). **Fig. 3.2(g)** shows the HRTEM lattice fringe pattern of bare Si NW (N1), while the inset represents the corresponding fast Fourier transform (FFT) pattern, confirming the crystalline nature of the Si NCs.[13] The lattice spacing 0.19 nm corresponds to the Si (220) planes. **Fig. 3.2(h)** shows the HRTEM lattice fringe of a single Per NP of N1P2 on the surface of Si NW, while the inset represents the corresponding IFFT pattern, which confirms the crystalline quality of the Per NP. The lattice spacing (0.29 nm) is related to the (200) plane of

cubic $CH_3NH_3PbBr_3$ structure.[5] Similar crystallinity has been observed from HRTEM for Per NPs in N1P1.

The elemental distribution of the Per NPs decorated NW in sample N1P2 was further characterized by STEM- EDS elemental mappings. **Fig. 3.3(a)** shows the TEM image of a single Si NW decorated with Per NPs in sample N1P2, while **Fig. 3.3(b-f)** shows the corresponding spatial mapping for elements Si, Pb, Br, O, and N. The high contrast of Pb and Br over Si is due to the uniform decoration of NPs over the entire NW surface. The contribution of oxygen in the mapping comes due to the native oxide layer on the Si NW surface. However, the contribution of carbon is not considered in the mapping, as the TEM grid consists of carbon coating.

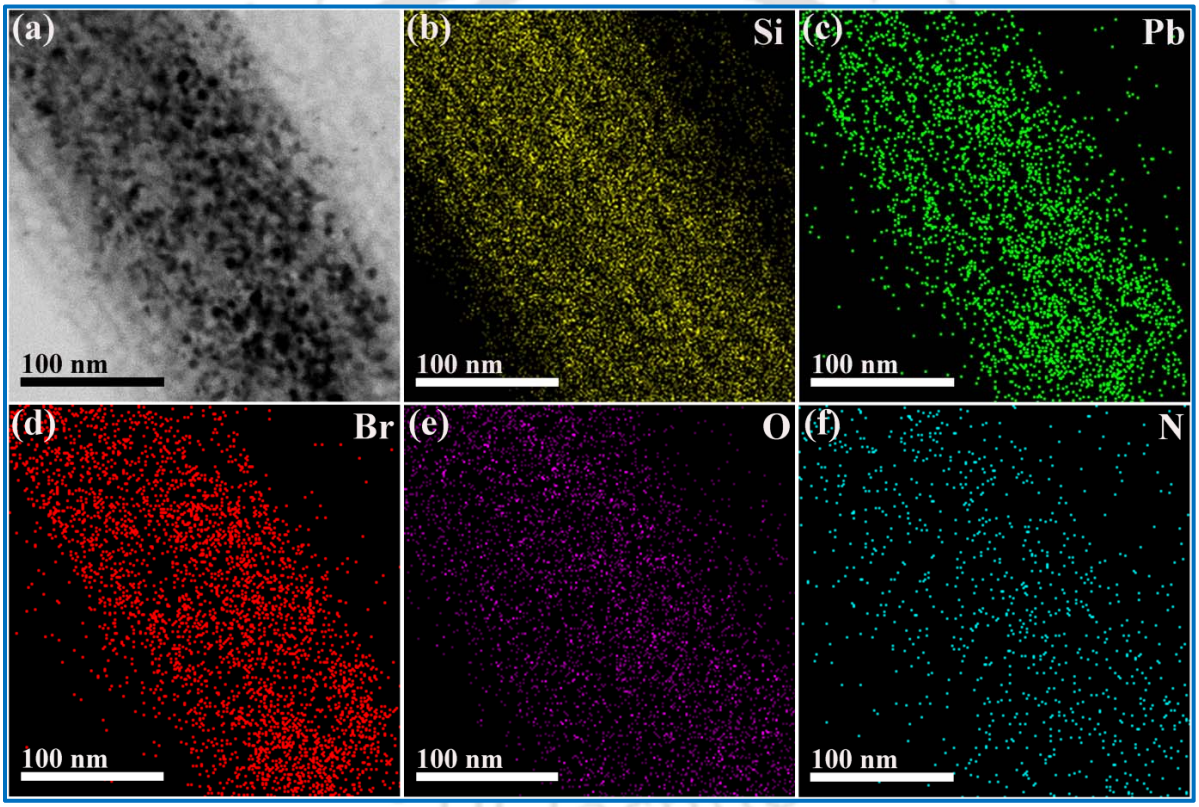

Fig. 3.3: (a) TEM image of Per NPs decorated single Si NW in sample N1P2, (b-f) STEM-EDS elemental color mapping of Si, P, Br, O, and N, respectively.

3.3.1.2. XRD Analysis

XRD analysis was performed to confirm the phase and crystalline quality of Per NPs on the NW template and the Per film on Si wafer. A comparison of the XRD patterns of the $CH_3NH_3PbBr_3$ NPs with different precursor concentrations deposited on NW and the bulk film is shown in **Fig. 3.4(a)**. The sharp diffraction peaks imply the highly crystalline nature of Per NPs and the Per film.

The diffraction peaks correspond to the cubic-phase $CH_3NH_3PbBr_3$ perovskite. [15] Note that the intensity of the XRD pattern of the bulk film is much higher than that of the NPs (N1P1− N1P4). This is due to the decreasing amount of perovskite material from sample bulk to N1P4. Note that the line widths of the XRD peaks are relatively higher in the Per NP case as compared to that of the bulk film, which is due to the decrease in the crystallite sizes in the NPs. From the analysis of the FWHM of the (100) peak, it is found that the FWHM is much higher for the NPs than that for the bulk film, as shown in **Fig. 3.4(b)**. The higher FWHM indicates the presence of perovskite nanocrystallites in the Per NPs.

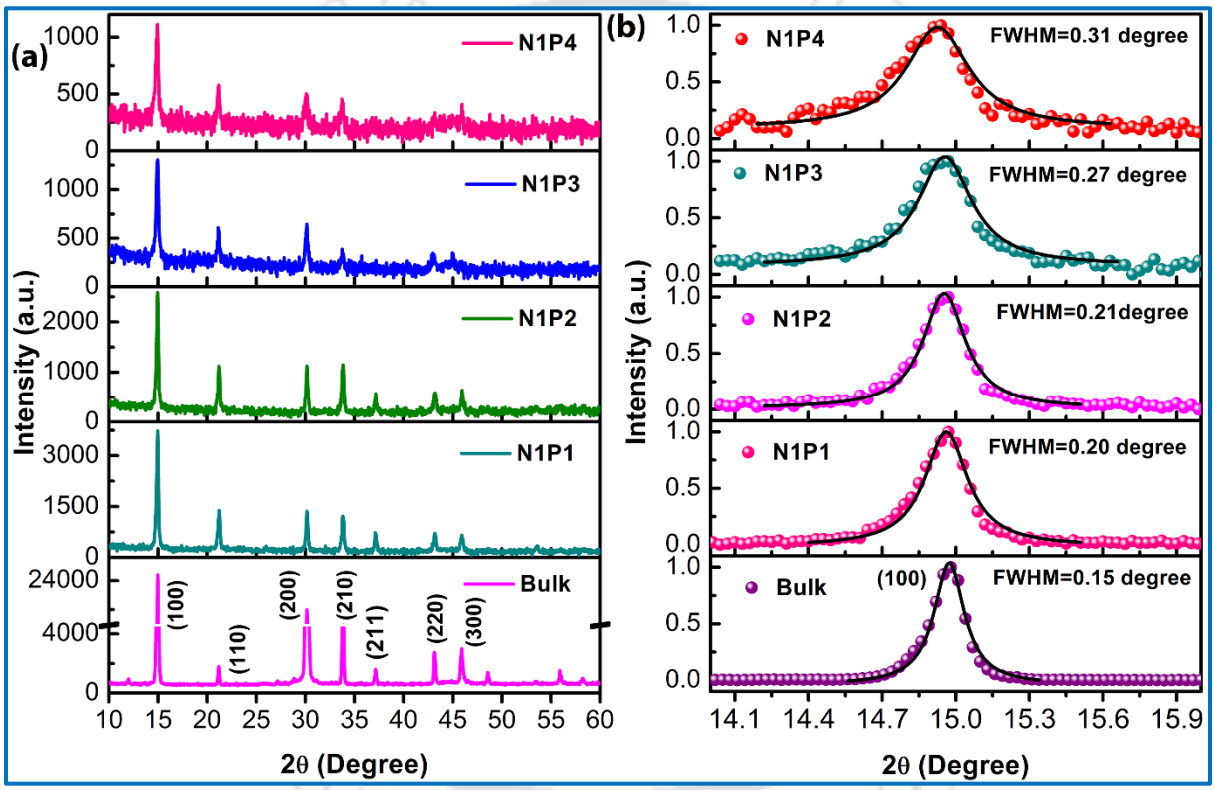

Fig. 3.4: (a) Comparison of XRD patterns of the samples N1P1, N1P2, N1P3, N1P4, and bulk $CH_3NH_3PbBr_3$ film on Si wafer. (b) Comparison of XRD (100) peak of different samples with Gaussian fitting. The FWHM of the (100) peak is indicated in each case.

3.3.2. Diffuse Reflectance Spectroscopy

To investigate the absorbance and bandgap of the Per NPs and the Per film, the diffuse reflectance measurement was performed. From the DRS data, the Kubelka-Munk (K-M) function, F(R), which is related to the absorption coefficient/ absorbance, was calculated**. Fig. 3.5(a)** shows the comparison of the K-M function of the Per bulk film, bare NW, and different concentration perovskite precursors coated on NWs, while **Fig. 3.5(b)** depicts the K-M function of Per NPs

decorated on Si NWs of different lengths (different etching duration). From **Fig. 3.5(a)**, it is clear that the bare NW template shows the highest broadband absorbance, which is due to the well-known light trapping effect by the NW array. This may partly influence the light emission characteristics of the Per NPs grown on the NWs. Note that it is very difficult to isolate and quantify the absorbance of NWs template and Per NPs separately from the absorbance data of Per NPs coated NWs.

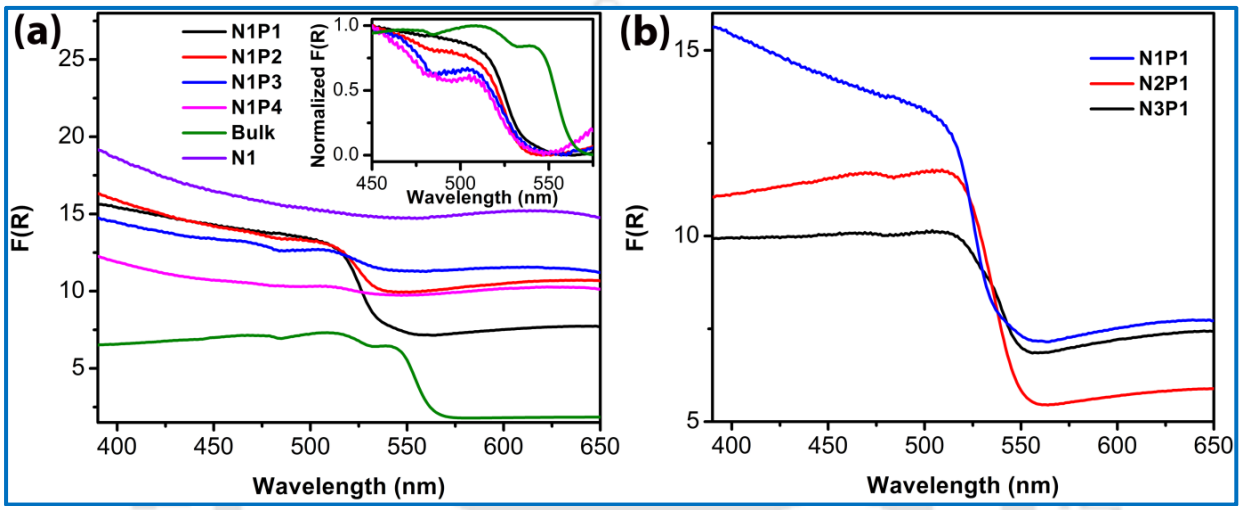

Fig. 3.5: (a) Comparison of the K-M function of samples N1P1, N1P2, N1P3, N1P4, and perovskite film on Si wafer. The inset displays the magnified view of the absorption edges indicating a systematic blue shift of the absorption edge for the Per NPs with respect to that of the perovskite film. (b) Comparison of the K-M function of Per NPs on different time etched Si NW template.

The inset of **Fig. 3.5(a)** shows the normalized F(R) in the wavelength region 450-550 nm, which clearly reveals the absorption edge of different Per NPs and bulk film. Interestingly, the absorption edge is systematically blue-shifted for the Per NPs as compared to the Per film, which may be due to the quantum confinement effect.[11, 16] Note that the blue shift of the absorption edge increases with a decrease in the precursor concentration, though the relative shift is very small for N1P3 and N1P4. Particle size distribution in the TEM image confirms that the higher precursor concentration leads to bigger Per particles in the case of N1P1 as compared to that in N1P2. In sample N1P2, due to the small size of the NPs and high absorbance of Per NPs, high CL and PL QY are observed in this sample (discussed later). **Fig. 3.5(b)** depicts that the absorbance is increased systematically with the increase in the length of the NW, which results in high CL and PL intensities.

3.3.3. Cathodoluminescence Study

To study the luminescence behavior of the Per NPs and Per film under the high-energy incident electron beam, CL of the samples was measured. All of the CL spectra were acquired with a spot size of 300 μm^2 of the incident beam with acquisition time 2 min for each spectrum. **Fig. 3.6(a)** shows the comparison of CL spectra of different Per NPs on NW template and the Per film at 15 kV incident beam accelerating voltage. The symbols correspond to the experimental data, while the solid lines correspond to the Gaussian fitting. The relative intensity count in **Fig. 3.6(a)** reveals a significant enhancement in CL intensity of the NP samples as compared to that of the bulk film. The CL peak intensity is enhanced by 2.7, 3.7, 2.9, and 1.5 times for the samples N1P1, N1P2, N1P3, and N1P4, respectively, as compared to the Per film. The enhanced CL peak intensity in Per NPs is attributed to the high surface area, quantum confinement of carriers in Per NPs embedded in the mesoporous NW surface, and the enhanced absorption by the Per NPs. Note that though the perovskite precursor concentration is higher in N1P1 than that in N1P2, the CL peak intensity is greater in N1P2. The enhanced CL peak intensity in N1P2 is due to the high density of smaller-size Per NPs, as evident from the TEM analysis shown in **Fig. 3.6(a)**. The smaller-size NPs in N1P2 have lower defects and higher absorbance than those in N1P1. CL peak broadening of the samples is believed to be due to the high-energy electron excitation, leading to population of higher vibrational modes, as well as electron beam-induced defect creation in the Per NPs and Per film.[17] There may be creation of defects and dynamic healings during the electron beam irradiation, which may be partly responsible for the higher-energy CL peak and hence the broadening of the CL emission peak. To investigate the origin of CL emission, we deconvoluted the CL spectrum of NPs samples with two Gaussian peaks, while that of the bulk film was deconvoluted with three Gaussian peaks, as shown in **Fig. 3.6(a)**. Note that the penetration depth of electrons is much lower than that of the photons; as a result, the CL emission primarily comes from the near-surface region of the NPs.[18] The higher-energy peak 1 of the Per NPs contains the emission from the higher-energy states of the NPs or the near-surface region of the NPs, while peak 2 corresponds to the emission from the interior of the NPs. Interestingly, peak 2 of the CL spectrum closely matches with the PL peak position (single peak) and the absorption edge of the NPs. Thus, peak 2 of the CL spectrum of the NPs corresponds to the near-band-edge emission. For the bulk film, peak 3 corresponds to the band edge emission (discussed later), while peaks 1 and 2 may be related to the surface and defect emissions. Thus, a direct correlation between the CL and

PL emission peaks could be made from our data. From **Fig. 3.6(a)**, it is also evident that the FWHM of the CL peak of Per film is higher than that of the NPs, which may be due to the higher defects in the bulk crystals than in the NPs. Due to the presence of defects, the CL and PL emissions may be partially quenched within the bulk $CH_3NH_3PbBr_3$ crystals. The CL emission peaks are blue-shifted systematically in the Per NPs than in Per film, which is attributed to the increased bandgap due to the formation of NPs. Note that with a decrease in perovskite precursor concentration, the peaks are blue-shifted due to the reduced size of the Per NPs.

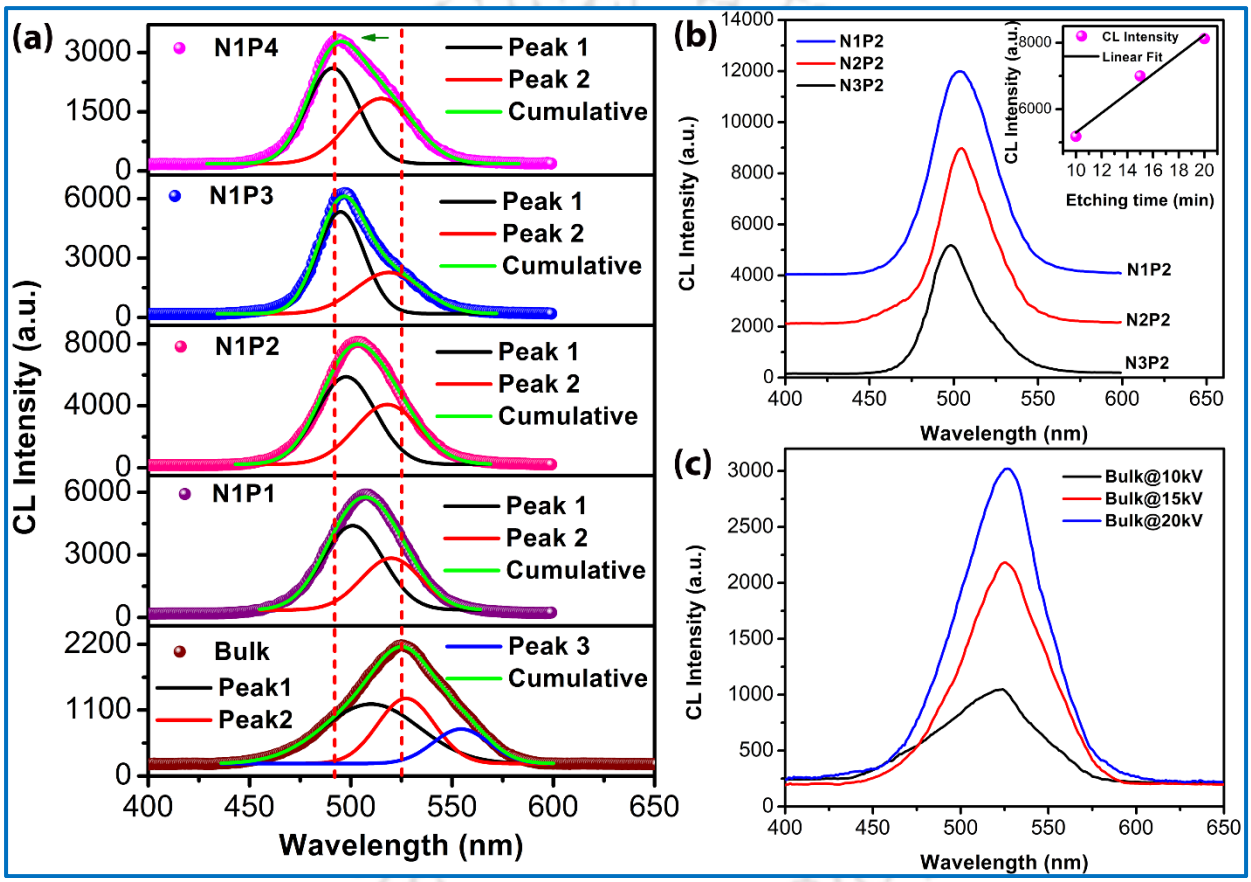

Fig. 3.6: (a) Comparison of CL spectra for the samples N1P1, N1P2, N1P3, N1P4, and perovskite film characterized at 15 kV incident electron beam accelerating voltage, the solid lines correspond to the Gaussian fitting. (b) Comparison of CL spectra for Per NPs on different time etched Si NW template. The inset shows the variation of CL intensity with NW etching time. (c) CL spectra of perovskite film at 10 kV, 15 kV and 20 kV incident beam accelerating voltage.

The high surface area of the Si NW/NCs also plays a crucial role in the enhancement of CL intensity, which is further probed by the measurement on the Si NWs of different lengths. **Fig. 3.6(b)** shows the variation of CL intensity of the Per NPs (P2) with different lengths of NWs. The sample N3 represents the Si NW with 10 min etching time, while N2 corresponds to 15 min etching. Note that the regular NW (N1) is 20 min etched. **Fig. 3.6(b)** shows a systematic

enhancement in CL intensity upon increasing the surface area of the NW template. The CL intensity of Per NPs as a function of etching time shows a linear increase, as shown in the inset of **Fig. 3.6(b)**. The CL emission spectra of the Per film for the electron beam with different accelerating voltages are shown in **Fig. 3.6(c)**, which shows that the CL intensity increases with the increase in accelerating voltage. As the acceleration voltage increases, the number of electron-optical interactions is increased, and as a result, the CL emission intensity is increased. A careful observation of **Fig. 3.6(c)** reveals that at higher accelerating voltage, the broadening of CL peak decreases, and redshift is observed. The FWHM of the CL peak of the bulk film is ~75 nm for 10 kV, while it is ~63 and ~61 nm for accelerating voltages 15 and 20 kV, respectively. It is considered that for the low accelerating voltage, the electrons are scattered with phonons resulting in higher FWHM, while at a higher accelerating voltage, the scattering is less, and the FWHM is lower. As the accelerating voltage increases, the electron beam affects the deeper interior region of the $CH_3NH_3PbBr_3$ crystals, and hence CL photons generate in the interior region of the crystals. These CL photons are partially reabsorbed by the crystal, which results in the red shift of the CL peak. Note that for the lower accelerating voltage, the interaction between the electron and the sample is probably near the surface of the crystals, which corresponds to lower reabsorption. Our results are consistent with Diab *et al.*, who reported the red shift with the increasing accelerating voltage in the CL spectrum of the $CH_3NH_3PbBr_3$ single-crystal.[18]

3.3.4. Photoluminescence Study

To evaluate the light emission properties of the Per NPs, we have measured the PL spectra of the Per NPs on the Si NWs by varying the perovskite precursor concentrations, and the results are shown in **Fig. 3.7(a)**. The Per film shows a sharp PL peak at 555 nm corresponding to the band edge transition of the $CH_3NH_3PbBr_3$ crystal. From **Fig. 3.7(a)**, it is evident that the PL intensity of Per NPs is dramatically higher than that of the Per film. The inset of **Fig. 3.7(a)** shows the variation of PL peak intensity and position of Per NPs with the precursor concentration. Note that N1P1 corresponds to the highest precursor concentration (0.6 M), and it decreases gradually for samples N1P2 (0.3 M), N1P3 (0.15 M), and N1P4 (0.075 M). Interestingly, N1P2 shows the highest peak intensity, which may be due to the optimum density and size of the NPs decorated on the NWs. N1P1 possesses bigger-size Per NPs as compared to that of N1P2 (as shown in the TEM analysis), which results in the lower intensity of the PL peak than in N1P2. For samples N1P3 and N1P4, the PL peak intensity is lesser than that of N1P2, which is due to the decrease in the density of the Per

NPs on the NW surface. A significant amount of blue shift of the PL peak is observed for Per NPs embedded on the NW template as compared to that of the bulk Per film. The blue shifts are 30, 39, 41, and 41 nm for samples N1P1, N1P2, N1P3, and N1P4, respectively. This systematic blue shift in PL peak is attributed to the change in the bandgap of the Per NPs with decreasing size.[16, 18]

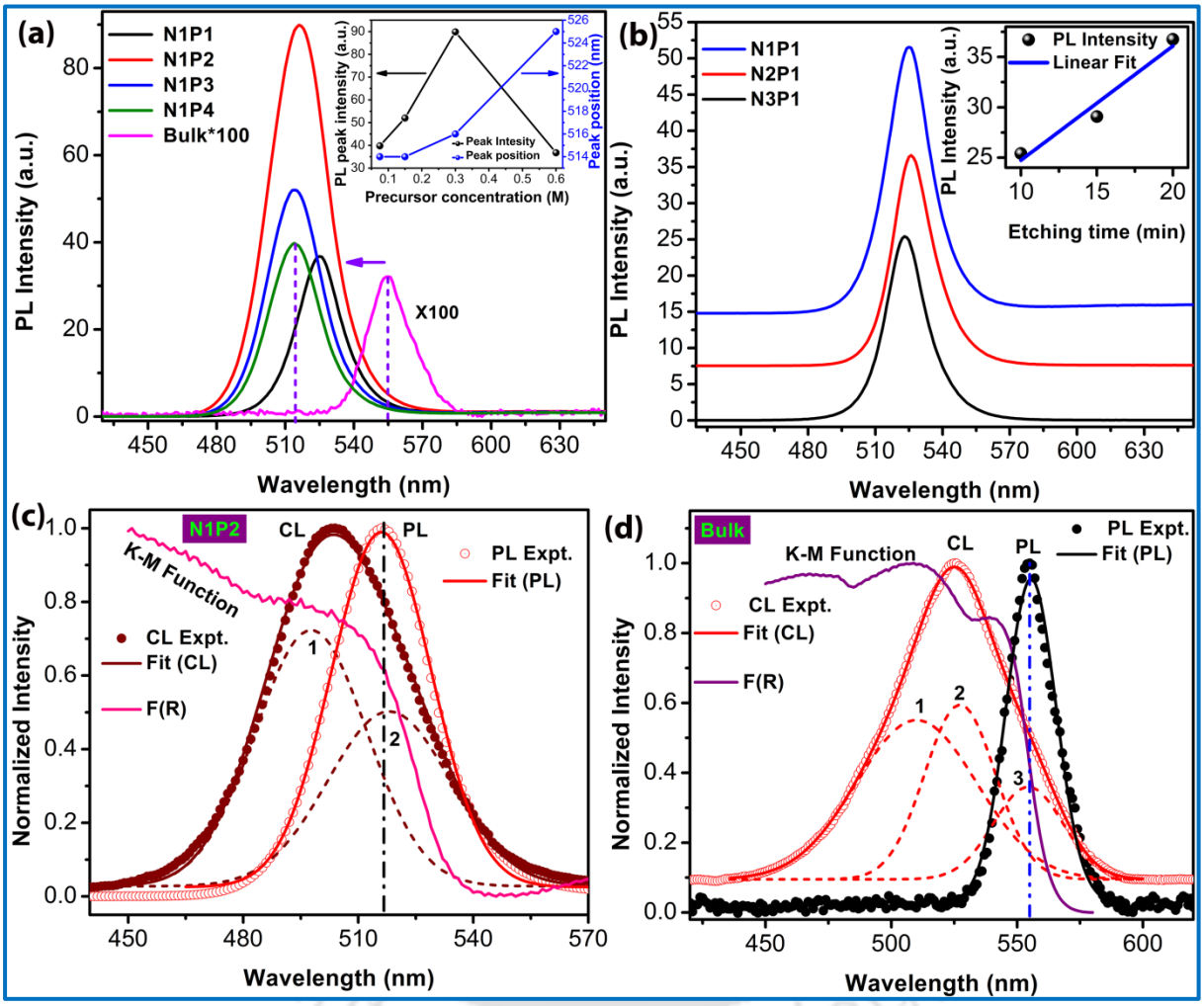

Fig. 3.7: (a) Comparison of PL spectra of samples N1P1, N1P2, N1P3, N1P4, and perovskite film. The PL spectrum of Bulk is scaled up by 100 times to enable comparison with the others. The inset displays the variation of PL peak intensity and position with precursor concentration. (b) Comparison of PL spectra of Per NPs on different time etched Si NW template. The inset shows the variation of PL peak intensity with NW etching time. (c) Comparison of normalized CL, PL spectra, and K-M function of N1P2. (d) Comparison of normalized CL, PL spectra, and K-M function of the sample Bulk.

The dramatically high PL intensity from Per NPs is attributed to the (a) quantum confinement effect and high radiative recombination in the Per NPs, and (b) high surface area and enhanced optical absorption by the NPs on the NW template. It is well known that the quantum structured particles show enhanced emission due to the high radiative recombination than their bulk

counterpart. The restricted charge diffusion and less nonradiative defect centers are partly responsible for the enhanced PL of the NPs. Thus, in our case, the enhanced PL intensity of Per NPs embedded on the NW surface is most likely due to the quantum confinement of carriers and high radiative recombination. Note that the light-induced defect curing study also confirms that the bulk crystals are more defect-enriched (discussed later) than the Per NPs. From the PL peak position of the bulk film (~555 nm), the calculated bandgap, E_g = 2.23 eV, is very close to the bandgap derived from the DRS analysis (2.22 eV). The size of the NPs observed here falls in the weak confinement region. However, a rough estimate of the bandgap for the 8.2 nm particles (in N1P2) from the well-known Brus equation reveals a bandgap of 2.41 eV for the Per NPs, assuming the effective mass to be same as that of the bulk effective mass of the electron (μ= 0.12 m_0) in $CH_3NH_3PbBr_3$.[11, 19] Interestingly, the estimated band gap value matches fairly well with the value measured from the PL spectrum (2.40 eV) of Per NPs. Thus, the quantum confinement effect is believed to play the dominant role in the observed blue shift and strong enhancement of CL/PL intensity for the Per NPs. The surface states and surface phenomena can also cause the blue shift of PL peaks. The high surface area of mesoporous Si NWs and enhanced optical absorption play important roles in the enhanced PL of the Per NPs. It is well known that the MACE grown NW shows enhanced optical absorption due to the multiple reflections and light trapping by the NW array. [20] This leads to the high absorption by the Per NPs, as shown in the DRS analysis, and it plays an important role in the enhancement of PL intensity. The PL spectra of Per NPs on different time etched NWs further support this assertion. **Fig. 3.7(b)** shows the comparative PL spectra of Per NPs on NWs etched for 10 min (N3P1), 15 min (N2P1), and 20 min (N1P1), and it shows a systematic increase in PL intensity with the increasing etching time/NW length. The PL intensity of Per NPs as a function of etching time shows a linear increase, as shown in the inset of **Fig. 3.7(b)**. To quantify the PL emission efficiency, the PL QY of different samples was measured. The PL QYs of the bulk, N1P1, N1P2, N1P3, and N1P4 samples are 2.78, 32.21, 39.38, 40.3, and 40.5%, respectively. Note that the enhancement factor in PL QY of the NPs with respect to the bulk film is much lesser than the enhancement factor of PL peak intensity because the PL QY measurement takes into account the contribution of PL enhancement due to increased optical absorption in the Per NPs. The PL QY of the Per NPs on mesoporous NW is considerably high as compared to the reported value for $CH_3NH_3PbBr_3$ in a solid film form.[16] Note that the measured PL QY of the Per NPs may be partly affected by the contribution from Si NCs/NWs where they

are embedded. We expect partial quenching of the PL intensity of the Per NPs by Si NCs/NWs due to reabsorption and possible energy transfer effects. The details of PL spectra and calculated bandgap from the PL peak center are summarized in **Table 3.2**.

Table 3.2: *Summary of the average size of the Per NPs and their PL spectral features.*

Sample code	Per NPs size (mean) (nm)	PL peak center (nm)	PL peak energy (eV)	PL quantum yield
Bulk	--	555	2.23	2.8 %
N1P1	11.9	525	2.36	32.2 %
N1P2	8.2	516	2.40	39.4 %
N1P3	7.2	514	2.41	40.3%
N1P4	7.0	514	2.41	40.5%

Fig. 3.7(c) shows the normalized CL, PL emission, and K-M plots for sample N1P2 with deconvoluted peaks, which shows a direct correlation between the CL spectrum and the PL spectrum as well as the absorption spectrum. The CL peak of Per NPs is deconvoluted with two peaks, while the PL peak contains a single peak. Interestingly, the Peak 2 of CL emission closely matches with the PL emission peak and absorption edge representing the near-band-edge emission.[21] The origin of peak 1 of CL spectrum corresponds to the photons coming from the near-surface region/higher-lying states of the NPs.[17] Note that due to higher-energy electron excitation, the CL peak contains additional contribution from higher-energy transitions in the NP energy states. A similar correlation can be made between the PL, CL, and absorbance data for the bulk film, as shown in **Fig. 3.7(d)**. In **Fig. 3.7(d)**, peak 3 of CL emission of the bulk film represents the band edge emission, while peaks 1 and 2 represent the defect and surface emission peaks, respectively. The details of the different CL and PL peak parameters are summarized in **Table 3.3**. Thus, our results demonstrate a direct correlation between the CL and PL emission spectra for Per NPs.

Table 3.3: Details of the fitting parameters of CL and PL emission peaks and their correlation.

Sample code	CL Peak1		CL Peak 2 (PL peak)		CL Peak 3 (PL peak)	
	Position (nm)	FWHM (nm)	Position (nm)	FWHM (nm)	Position (nm)	FWHM (nm)
N1P1	501.0	35.4	520.1 (525.0)	34.6 (24.3)	-	-
N1P2	497.7	34.2	518.2 (516.2)	37.5 (30.5)	-	-
N1P3	494.9	27.2	518.5 (514.2)	38.8 (28.6)	-	-
N1P4	491.1	33.2	514.9 (514.8)	38.7 (27.4)	-	-
Bulk	510.0	56.3	527.3	33.0	554.4 (555.1)	33.1 (23.3)

3.3.5. Stability of Per NPs under High Humidity Ambient

Generally, an organometal halide perovskite material starts degrading upon exposure to water and oxygen molecules, which is a well-known phenomenon. In this work, the stability of Per NPs embedded in NWs and Per films on Si wafers has been compared through PL measurement. The light-induced in-situ defect curing and the light-induced degradation of the Per NPs and the Per film were studied using a 405 nm laser. **Fig. 3.8(a)** shows the variation of PL peak intensity with the irradiation time of both N1P2 and bulk samples. Interestingly, the PL peak intensity increased up to 20 min of irradiation, and it is maximum for 20 min irradiation time for both samples. This type of enhancement of PL intensity due to light irradiation is attributed to the self-healing/removal of defects with light irradiation. [22] Light irradiation may help reducing the nonradioactive deep-level defect centers in the crystal, which eventually leads to an increase in the PL intensity.

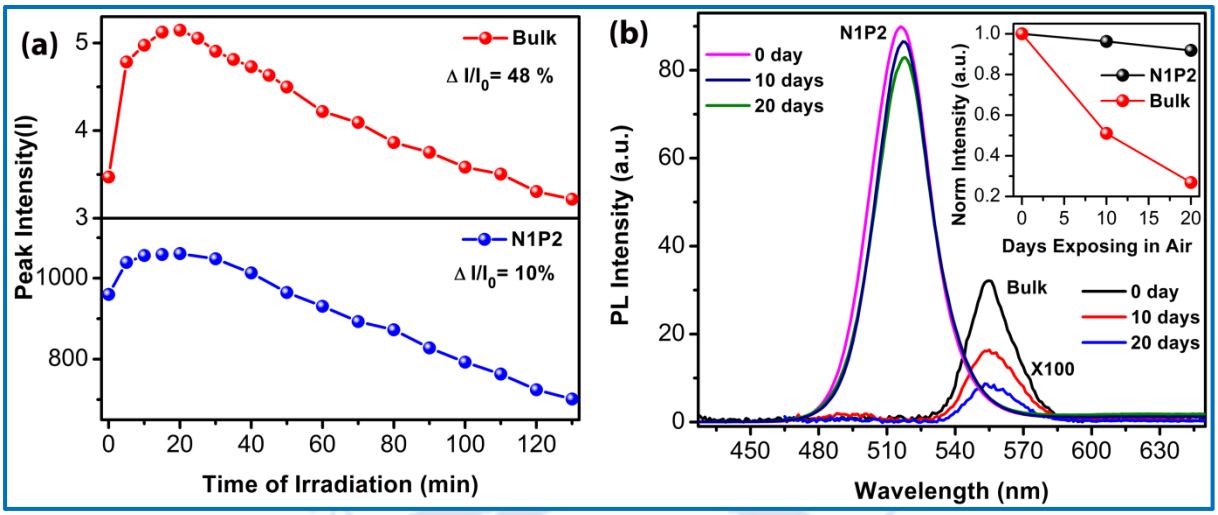

Fig. 3.8: (a) Variation of PL peak intensity of N1P2 and Bulk with laser irradiation time. (b) Comparison of the PL spectra of sample N1P2 and perovskite films: as-deposited, 10 days, and 20 days old (kept in ambient air with 70 % humidity). The inset shows the variation of normalized PL peak intensity with days exposed in the air for samples N1P2 and Bulk.

Note that with light irradiation for 20 min, the PL intensity of the bulk film is enhanced by 1.5 times that of the initial PL intensity, whereas PL intensity of N1P2 is enhanced by 1.1 times. The higher enhancement in the case of the bulk sample suggests that the bulk crystals are more defect-enriched than the NPs, which is responsible for its low PL QY. With prolonged irradiation (beyond 20 min), the PL peak intensity decreases monotonically with time for both the samples (Per film and Per NPs). This decrease in PL may be due to the enhancing phonons of the crystals by laser heating and degradation of $CH_3NH_3PbBr_3$ for continuous high-intensity light irradiation in ambient air. Interestingly, $CH_3NH_3PbBr_3$ NPs on NW show significantly higher ambient stability that the bulk films. The decomposition of the layer was monitored by measuring the intensity of PL peak after storage. The samples N1P2 and bulk were stored in ambient air with 70% humidity after fabrication, PL spectra were measured after 10 and 20 days of storage, and results are shown in **Fig. 3.8(b)**. The inset of **Fig. 3.8(b)** shows the variation of PL peak intensity of the samples with days of exposure in air. Interestingly, after 20 days of exposure to the humid atmosphere, the PL peak intensity of the perovskite thin film is decreased by ~73%, while that for N1P2 is decreased by only 9%. Thus, the ambient air degradation process of the Per NPs embedded in NW is extremely slow as compared to that of the bulk film. The high density of porous NW arrays acts as a kind of encapsulation for the Per NPs from the air, which results in the enhanced air stability of the Per NPs confined in porous NW. In perovskite thin films, there are pinholes and grain boundaries through which water molecules from the atmosphere can easily diffuse to trigger

decomposition. The significantly improved air stability of Per NPs embedded in the NW pores can be rationalized by considering the effective protection provided by the dense stable vertical Si NW array. The dense NW array can slow down the lateral diffusion of oxygen and water molecules in Per NPs, which results in better stability and slower decomposition rate.[23] Thus, the stability of the NPs is much improved due to the encapsulation from the surrounding atmosphere by the stable Si NW.

3.3.6. Low-Temperature Photoluminescence Study

To investigate the origin of high PL QY of Per NPs, we further performed the temperature-dependent PL measurements. **Fig. 3.9(a,b)** shows the PL spectra of N1P2 and bulk samples, respectively, in the temperature range 15-300 K. From the low-temperature PL analysis, we can estimate two important parameters: exciton-phonon scattering, and exciton binding energy, which play important roles in the high PL QY of the NPs.[24] It is clear from the figure that the PL peak intensity is decreased and a gradual blue shift of the peak is observed as the temperature is increased from 15 to 300 K. In general, for semiconductors, with an increase in the temperature, the bandgap decreases, and a red shift is expected due to enhanced electron-phonon interaction caused by increased phonon population and weak contribution of thermal expansion.[24] Note that perovskite materials show the unusual blue shift of PL emission, i.e., the bandgap increases with increasing the temperature.[24, 25] Yu et al. argued that in perovskite semiconductor, the contribution of electron-phonon interaction is negligible and the dominant contribution of lattice thermal expansion with positive temperature coefficient results in the increase in the bandgap with the decreasing temperature.[26] **Fig. 3.9(c)** shows the variation of the integrated PL intensity with temperature for Per NPs and the Per film. The integrated intensity of each PL spectrum has been normalized by PL intensity at room temperature (300 K) for easy comparison. At higher temperatures, the nonradiative recombination channels are more active, which results in the decrease in PL intensity. In the low-temperature region (<50 K), a more rapid change in PL intensity for the Per film is associated with the low exciton binding energy/defects related to PL quenching in the bulk film. For the Per film, the integrated PL intensity at 15 K is enhanced by 57 times as compared to that at 300 K, while for Per NPs, it is enhanced only by 33 times. Thus, the PL spectra of the Per film show high quenching of PL at room temperature due to the high density of nonradiative trap sites, which are inactivated at low temperatures, causing a higher intensity PL.

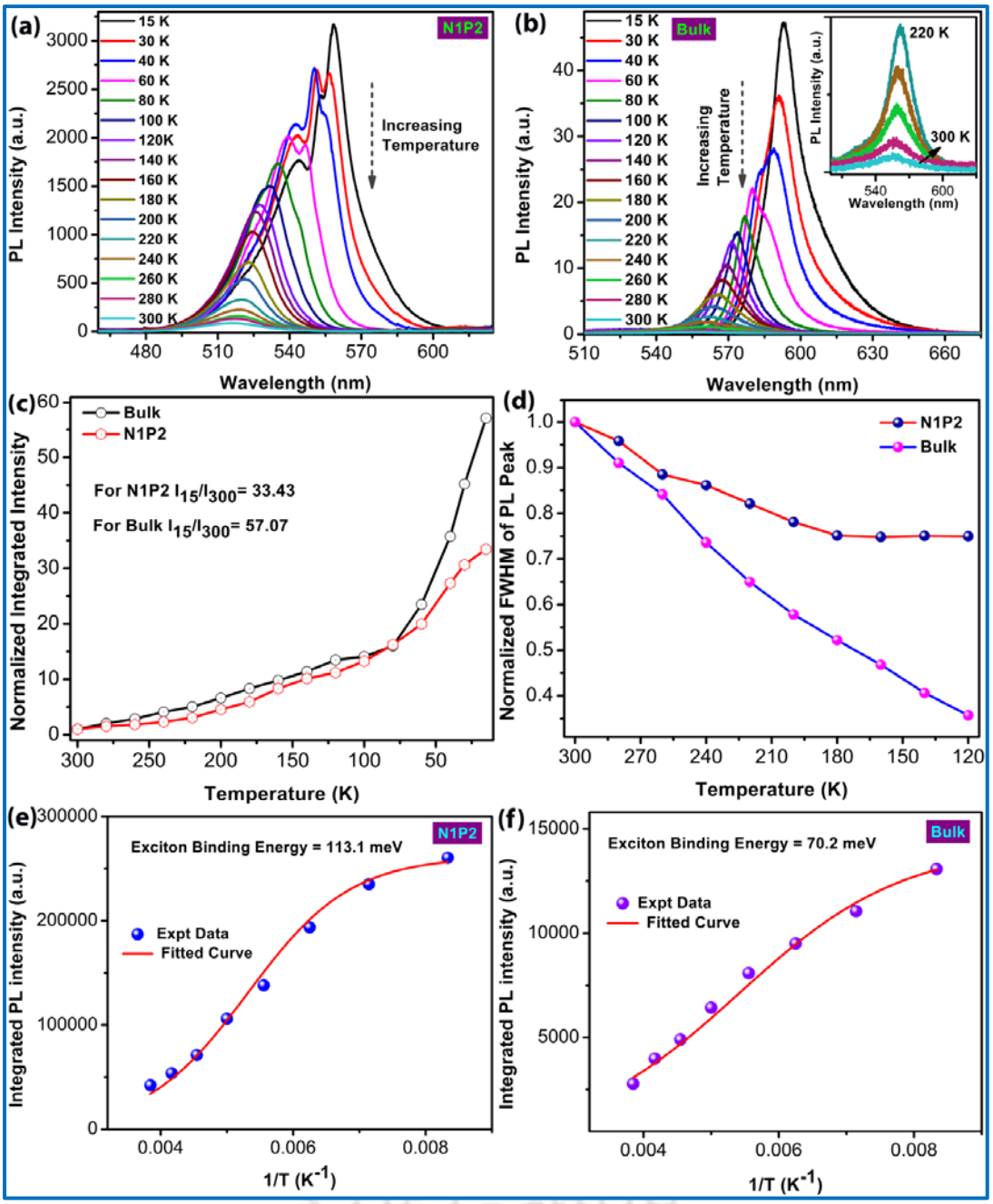

Fig. 3.9: (a) Temperature-dependent PL spectra of Per NPs confined on NW (N1P2) (b) Comparison of temperature-dependent PL spectra of $CH_3NH_3PbBr_3$ film. The inset shows the variation of PL intensity in temperature range 220-300K (c) Variation of normalized integrated PL intensity with the temperature of sample N1P2 and Bulk. (d) Variation of FWHM of PL peak with temperature for sample N1P2 and Bulk film. (e, f) Arrhenius plot of samples N1P2 and Bulk film, respectively.

In contrast, Per NPs show much lower quenching of PL at room temperature due to the lower contribution of nonradiative recombination centers. Temperature-dependent PL line width was measured for explaining the exciton-phonon scattering. **Fig. 3.9(d)** shows the comparison of

temperature-dependent FWHM of PL peaks for Per NPs and Per film in the temperature region 120-300 K. Note that the low-temperature PL spectra show a single peak in the temperature range 300-120 K, while below 120 K, each spectrum splits into multiple peaks. For a better comparison of the evolution of FWHM with temperature for the two samples, the FWHM at each temperature is normalized to the FWHM at 300 K. For the Per film, the increase in FWHM with temperature is faster than that of Per NPs. The higher broadening in the Per film is due to the enhanced carrier-phonon scattering and nonradiative decay of excitons. We further investigated the exciton binding energy of Per NPs and Per film from the temperature-dependent integrated PL intensity using the Arrhenius equation

$$I(t) = \frac{I_0}{1 + A\exp(-\frac{E_b}{k_B T})} \qquad (3.1)$$

where I_0 is the integrated PL intensity at very low temperature, A is a constant, E_b is the exciton binding energy, and k_B is the Boltzmann constant. **Fig. 3.9(e,f)** shows the variation of integrated PL intensity with the inverse of temperature (1/T) for N1P2 and Per film samples, respectively. The data points are well-fitted with the Arrhenius equation (3.1), and the obtained exciton binding energy for Per NPs is ~113.1 meV, while that of Per film is ~70.2 meV. The higher E_b value of Per NPs originates from the quantum confinement of carriers in the NPs. The lower E_b in Per films implies thermal escape of carriers and dissociation of excitons more easily than that in Per NPs. Thus, at room temperature, the nonradiative decay process due to the thermal dissociation of excitons is less probable for Per NPs, which results in the high PL QY. In the low-temperature region (<80 K), the PL spectra of Per NPs and Per film contain multiple peaks. PL emission with multiple peaks that appear for organic-inorganic lead halide perovskite in the low-temperature PL measurements has remained a controversial issue. The origin of multiple-peak PL emission in low-temperature region is mostly explained by the coexistence of different phases of $CH_3NH_3PbBr_3$, emissions from defect states, and emission from bound and free excitons. Depending on the temperature, $CH_3NH_3PbBr_3$ crystals show three different phases, orthorhombic (<145 K), tetragonal (145-237 K), and cubic (>237 K), which result in PL peaks with different energies. Chen et al. reported that the different sub-peaks of $CH_3NH_3PbBr_3$ originate from bound and free excitons.[25] In our case, three peaks are observed for the bulk film at low temperature, which may be related to the intrinsic emission and defect-related emission peaks. In the case of Per NPs,

additional peaks are observed, which may be related to the coexistence of multiple phases of the Per nanocrystals. The defect contribution is expected to be lower in Per NPs. However, at low temperature, radiative and nonradiative peaks both contribute to the PL spectrum, and thus, the additional peaks appear in the spectrum.

3.3.7. Time-Resolved Photoluminescence Study

To investigate the recombination kinetics of photogenerated charge carriers, TRPL measurements were performed on the $CH_3NH_3PbBr_3$ NPs, and the Per film with 405 nm laser excitation and the emission intensity was monitored at the steady-state PL peak center of each sample.

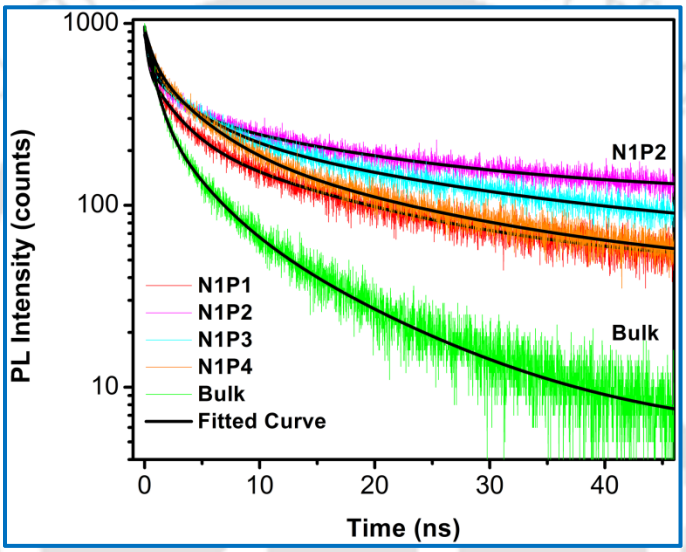

Fig. 3.10: TRPL decay dynamics of sample N1P1, N1P2, N1P3, N1P4, and perovskite Bulk film.

Fig. 3.10 shows a comparison of the TRPL decay profiles of different Per NP samples and the Per film. TRPL data profiles were fitted using a tri exponential decay function as[27]

$$A(t) = A_1 \exp(-\frac{t}{\tau_1}) + A_2 \exp(-\frac{t}{\tau_2}) + A_3 \exp(-\frac{t}{\tau_3}) \qquad (3.2)$$

where A_1, A_2, and A_3 are the amplitudes of the TRPL decay with lifetimes τ_1, τ_2, and τ_3, respectively. The average lifetimes (τ_{ave}) were estimated using the following relation.

$$\tau_{ave} = \frac{\sum_{i=1}^{i=3} A_i \tau_i^2}{\sum_{i=1}^{i=3} A_i \tau_i} \qquad (3.3)$$

The average lifetimes were found to be 10.2, 14.9, 18.2, 22.1, and 18.0 ns for bulk film, N1P1, N1P2, N1P3, and N1P4, respectively. The three time constants are correlated with the radiative electron-trapping and the radiative electron-hole recombination of halide perovskite. It is clear

from the TRPL decay profiles that the average recombination lifetime in Per NPs is significantly higher than that of the bulk film. The higher PL decay time or carrier lifetime may imply high radiative recombination of carriers in the Per NPs than in the bulk counterpart. Usually, the nonradiative lifetime is shorter than the radiation lifetime, and as a result, the effective lifetime comes out to be shorter than the actual radiative lifetime in semiconductors containing nonradiative channels. Ling et al. showed the prolonged lifetime for $CH_3NH_3PbBr_3$ nanoplatelet due to the extraordinarily high radiative recombination rate than that for the bulk perovskite.[27] Note that light-irradiation-dependent PL evolution and low-temperature PL studies support the high radiative recombination in the Per NPs confined on the mesoporous NW surface. The CL study also confirms the high defect density in the bulk $CH_3NH_3PbBr_3$ crystals. Thus, the high radiative recombination of the Per NPs is the main cause of dramatically enhanced PL from the Per NPs on the NW template. Interestingly, the lifetimes are higher for N1P2 and N1P3 than those of N1P1, which is consistent with the fact that NP sizes are lower for N1P2 and N1P3.

3.3.8. Performance of a Per NP/Si NW Heterojunction Photodetector

The ultrahigh surface area and enhanced optical absorption by the Per NP-decorated NW array make this heterostructure also promising in other optoelectronic applications along with different light-emitting applications. Here, we have fabricated photodetectors using the $CH_3NH_3PbBr_3$ NPs grown on mesoporous Si NWs, and the device architecture is schematically shown in **Fig. 3.11(a)**. In the device structure, gold is used as the bottom electrode at the back side of the Si wafer where NWs were grown, and a thin layer of Au serves as the semitransparent top electrode deposited on top of the Per NP-decorated NW (N1P2). Note that the starting Si wafer is heavily doped, and it makes a reasonably good Ohmic contact with the Au layer on the back side. **Fig. 3.11(b)** shows time-dependent photocurrent response curves with the light on/off intervals of 5 s under 405 nm incident light at an intensity of 8 mW/cm^2 and an applied bias of 2 V. The dynamic photoresponse of the $CH_3NH_3PbBr_3$/Si NW heterojunction PD indicates that the devices possess a good photoswitching behavior. To quantitatively understand the response speed, the rise and decay edges of the time-dependent photocurrent were fitted using a single exponential function given by[28]

$$I_{growth}(t) = I_{0r} + A_1\,(1 - \exp(-\frac{t}{\tau_g})) \qquad (3.4)$$

and

$$I_{decay}(t) = I_{0d} + A_2 \exp(-\frac{t}{\tau_d})\,, \qquad (3.5)$$

where I_{0r}, I_{0d}, A_1, and A_2 are constants, while τ_g and τ_d are time constants for the photocurrent growth and decay, respectively.

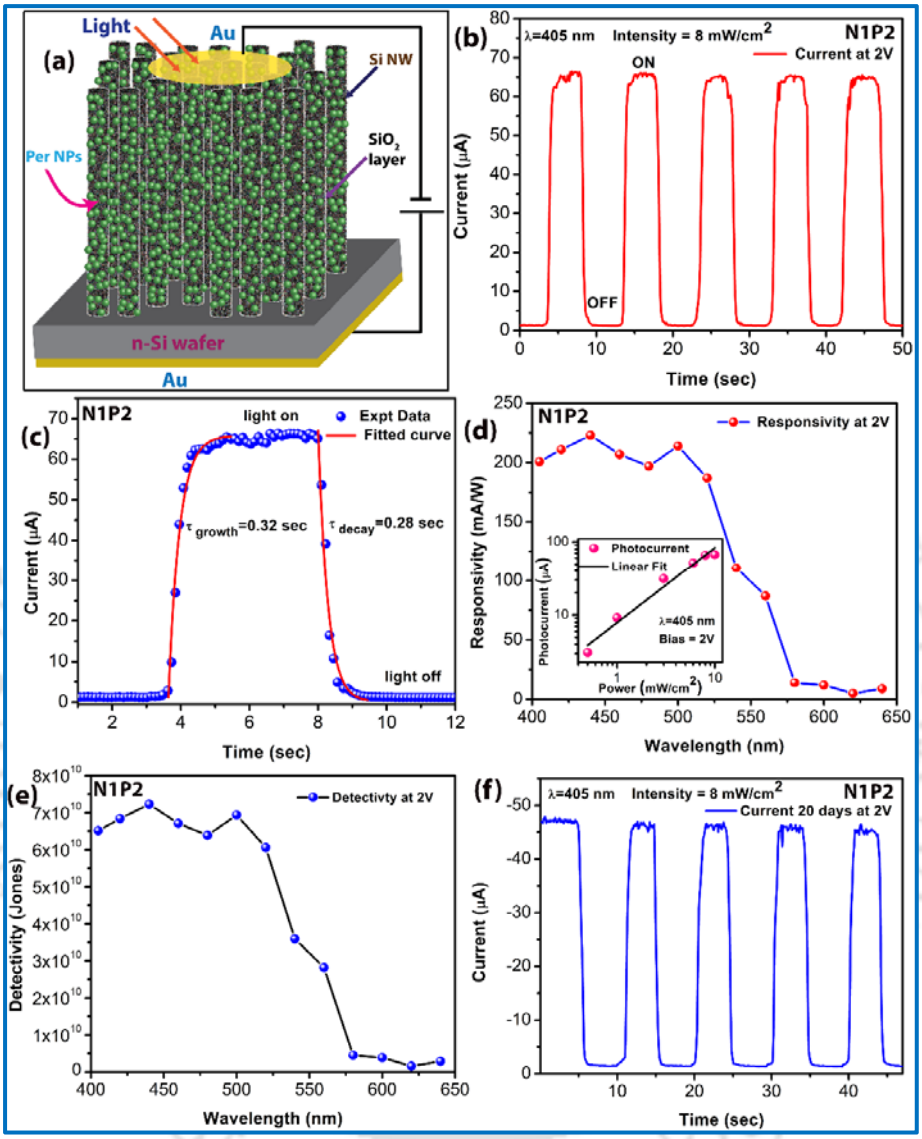

Fig. 3.11: (a) An schematic illustration of Per NPs/Si NW heterojunction photodetector. (b) Time-dependent photoresponse of $CH_3NH_3PbBr_3$ NPs/Si NW photodetector under 405 nm laser with intensity 8 mW/cm^2 at 2V bias. (c) An enlarged view of growth and decay of time-dependent photocurrent fitted with single exponential function in each case. (d) The wavelength-dependent responsivity of the photodetector; the inset shows light intensity-dependent photocurrents under 405 nm laser irradiation with linear fitting. (e) Wavelength dependent detectivity of the photodetector. (f) Time-dependent photoresponse of the photodetector after 20 days of storage in ambient air with 70% humidity.

The photocurrent growth time constant (τ_g) was obtained to be ~0.32 s, whereas photocurrent decay time constant (τ_d) was obtained to be ~0.28 s from the fitting, as shown in **Fig. 3.11(c)**. The spectral responsivity (R_λ) is an important parameter for the estimation of the performance of the

PD, which shows how efficiently the detector responds to an optical signal. The responsivity (R_λ) of the PD was calculated using the equation,

$$R_\lambda = \frac{I_{Ph}}{P*S} \qquad (3.6)$$

where I_{Ph} refers to the photocurrent, P is the incident light power density, and S is the effective illuminated area. **Fig. 3.11(d)** depicts the wavelength-dependent responsivity of the heterojunction PD at 2 V reverse bias, which shows a maximum responsivity of 223 mA/W at 440 nm incident light. The inset of **Fig. 3.11(d)** shows the dependence of photocurrent on the incident light intensity, which reveals that with the increase in incident light intensity, the photocurrent increases linearly. On increasing the incident light intensity, more photogenerated carriers are produced, and hence the photocurrent of the device is increased linearly at a low-intensity level. The detectivity (D*) of the PD signifies the capability of detecting low-level light signals, taking into account the contributions of the photocurrent and dark current. D* is expressed as

$$D^* = \frac{R_\lambda}{(2qJ_d)^{\frac{1}{2}}} \qquad (3.7)$$

where J_d is the dark current density and q is the charge of the electron. The maximum detectivity of the PD was found as 7.22×10^{10} Jones at 440 nm, as shown in **Fig. 3.11(e)**. To check the stability of the PD, we measured the time-dependent photocurrent under the same measurement conditions keeping the device for 20 days in ambient air with 70% humidity. **Fig. 3.11(f)** shows time-dependent photocurrent response curves with on/off intervals of 5 s under 405 nm incident light with an illumination intensity of 8 mW/cm^2 under a 2 V reverse bias. After 20 days of storage of the device in ambient air, the photocurrent decreased from 66 to 46 μA i.e., by ~30%, which shows the reasonable stability of the device under humid air.

Fig. 3.12 shows the schematic representation of the band diagram of the Si NW/$CH_3NH_3PbBr_3$ NP heterostructure without and with reverse bias condition.[29] It is well known that the MACE-grown Si NW array is covered with a thin SiO_2 layer due to the wet etching process. This insulating SiO_2 layer plays a crucial role in enhancing the PL emission from the Per NPs confined in the mesopores of the NW surface. The oxide layer acts as an energy barrier between Si NW and $CH_3NH_3PbBr_3$ NPs. As shown in **Fig. 3.12(a)**, due to the photoexcitation, electron-hole pairs are generated inside Per NPs. These electrons cannot overcome the energy barrier at the oxide layer between Si NW and Per NPs and hence they recombine radiatively

causing high-yield PL emission. Therefore, any possible quenching effect due to charge transfer to the underlying Si layer is less probable owing to the presence of the oxide layer.

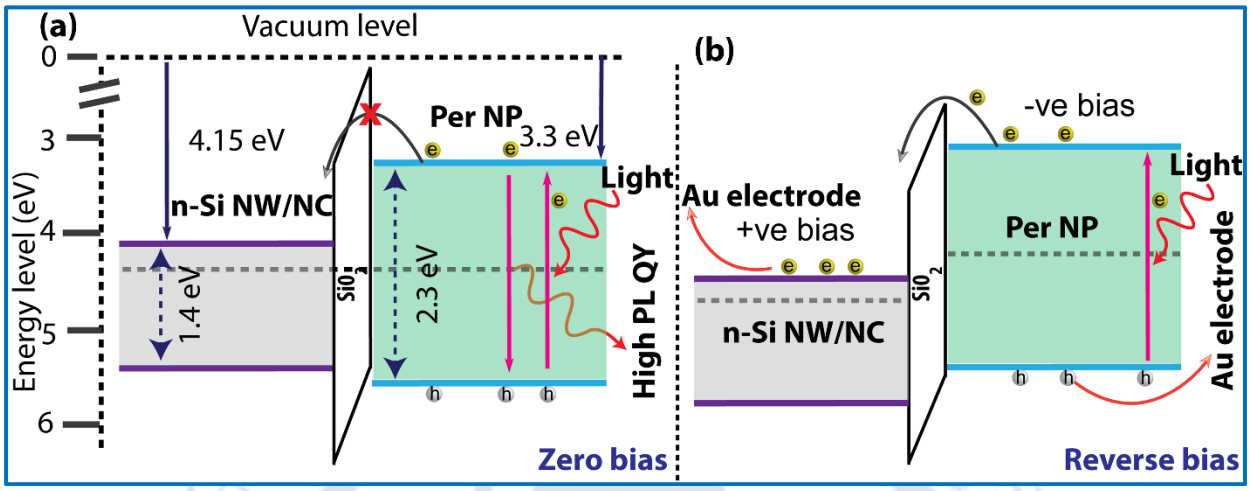

Fig. 3.12: (a, b) Energy band diagram of Per NPs and Si NW without bias and with reverse bias conditions, respectively.

In the case of the perovskite/Si NW PD, when a reverse bias is applied, the photogenerated electrons-holes acquire the energy to partly overcome the oxide barrier level or tunnel through the thin layer to contribute to the photocurrent, as shown in **Fig. 3.12(b)**. As a result, the photocurrent is enhanced in the external circuit.

3.4. Conclusions

In this chapter, we have demonstrated the superior optoelectronic properties of $CH_3NH_3PbBr_3$ NPs grown on a mesoporous Si NW template by means of their strong cathodoluminescence, stable photoluminescence, and fast photoresponse characteristics. Per NPs are fabricated by simple spin-coating of a perovskite precursor on the surface of a mesoporous Si NW array, which was grown by metal-assisted chemically etching. The FESEM, FETEM, XRD, and EDX analyses confirm the uniform decoration of embedded crystalline Per NPs over the entire surface of the mesoporous Si NWs. For the first time, we have shown that the Per NPs confined in Si NWs show enhanced CL emission with a marked blue shift as compared to the bare perovskite film, which is fully consistent with the PL spectra of Per NPs. A systematic study reveals that the quantum confinement effect and ultralow defects in Per NPs are primarily responsible for their enhanced CL and PL emissions. Low-temperature PL and time-resolved PL analyses confirm the high radiative recombination in Per NPs. High exciton binding energy for Per NPs (113 meV) as compared to the bulk film (70 meV) is fully consistent with the quantum confinement of carrier in Per NPs. We obtained a high

PL quantum yield of 40.5% for the Per NP film embedded in Si NW, while it is only 2.8% for the Per film on Si wafer. The embedded Per NPs show higher ambient air stability than the bare film due to the protection provided by the dense Si NW array as the dense Si NW array can slow down the lateral diffusion of oxygen and water molecules in Per NPs. The as-grown Per NPs exhibited superior visible light photodetection, and the prototype photodetector shows a responsivity of 0.223 A/W and a response speed of ~0.28 s at a low bias voltage (2 V). In this study, we demonstrate a low-cost and easy fabrication of $CH_3NH_3PbBr_3$ NPs on a novel mesoporous Si NW template, which shows excellent photophysical and optoelectronic properties with superior ambient stability.

References

1. M. Cao, J. Tian, Z. Cai, L. Peng, L. Yang and D. Wei, *Appl. Phys. Lett.*, 2016, **109**, 233303.
2. F. Chen, C. Xu, Q. Xu, Y. Zhu, F. Qin, W. Zhang, Z. Zhu, W. Liu and Z. Shi, *ACS Appl. Mater. Interfaces*, 2018, **10**, 25763-25769.
3. M. R. Leyden, L. Meng, Y. Jiang, L. K. Ono, L. Qiu, E. J. Juarez-Perez, C. Qin, C. Adachi and Y. Qi, *J. Phys. Chem. Lett.*, 2017, **8**, 3193-3198.
4. H. Cho, S.-H. Jeong, M.-H. Park, Y.-H. Kim, C. Wolf, C.-L. Lee, J. H. Heo, A. Sadhanala, N. Myoung, S. Yoo, S. H. Im, R. H. Friend and T.-W. Lee, *Science*, 2015, **350**, 1222-1225.
5. L. C. Schmidt, A. Pertegás, S. González-Carrero, O. Malinkiewicz, S. Agouram, G. Mínguez Espallargas, H. J. Bolink, R. E. Galian and J. Pérez-Prieto, *J. Am. Chem. Soc.*, 2014, **136**, 850-853.
6. J. A. Sichert, Y. Tong, N. Mutz, M. Vollmer, S. Fischer, K. Z. Milowska, R. García Cortadella, B. Nickel, C. Cardenas-Daw, J. K. Stolarczyk, A. S. Urban and J. Feldmann, *Nano Lett.*, 2015, **15**, 6521-6527.
7. S. Parveen, K. K. Paul, R. Das and P. K. Giri, *J. Colloid Interface Sci.*, 2019, **539**, 619-633.
8. G. Longo, A. Pertegas, L. Martinez-Sarti, M. Sessolo and H. J. Bolink, *J. Mater. Chem. C*, 2015, **3**, 11286-11289.
9. V. Malgras, J. Henzie, T. Takei and Y. Yamauchi, *Angew. Chem.*, 2018, **57**, 8881-8885.
10. S. Demchyshyn, J. M. Roemer, H. Groiß, H. Heilbrunner, C. Ulbricht, D. Apaydin, A. Böhm, U. Rütt, F. Bertram, G. Hesser, M. C. Scharber, N. S. Sariciftci, B. Nickel, S. Bauer, E. D. Głowacki and M. Kaltenbrunner, *Sci. Adv.*, 2017, **3**, e1700738.
11. M. Anaya, A. Rubino, T. C. Rojas, J. F. Galisteo-López, M. E. Calvo and H. Míguez, *Adv. Opt. Mater.*, 2017, **5**, 1601087.
12. C. M. Sutter-Fella, Y. Li, M. Amani, J. W. Ager, F. M. Toma, E. Yablonovitch, I. D. Sharp and A. Javey, *Nano Lett.*, 2016, **16**, 800-806.
13. R. Ghosh and P. K. Giri, *Nanotechnology*, 2017, **28**, 012001.
14. R. Ghosh, P. K. Giri, I. Kenji and F. Minoru, *Nanotechnology*, 2014, **25**, 045703.
15. Q. Liao, K. Hu, H. Zhang, X. Wang, J. Yao and H. Fu, *Adv. Mater.*, 2015, **27**, 3405-3410.
16. D. Di, K. P. Musselman, G. Li, A. Sadhanala, Y. Ievskaya, Q. Song, Z.-K. Tan, M. L. Lai, J. L. MacManus-Driscoll, N. C. Greenham and R. H. Friend, *J. Phys. Chem. Lett.*, 2015, **6**, 446-450.
17. D. Cortecchia, K. C. Lew, J.-K. So, A. Bruno and C. Soci, *Chem. Mater.*, 2017, **29**, 10088-10094.
18. H. Diab, C. Arnold, F. Lédée, G. Trippé-Allard, G. Delport, C. Vilar, F. Bretenaker, J. Barjon, J.-S. Lauret, E. Deleporte and D. Garrot, *J. Phys. Chem. Lett.*, 2017, **8**, 2977-2983.

19. K. Tanaka, T. Takahashi, T. Ban, T. Kondo, K. Uchida and N. Miura, *Solid State Commun.*, 2003, **127**, 619-623.
20. E. Garnett and P. Yang, *Nano Lett.*, 2010, **10**, 1082-1087.
21. M. I. Dar, G. Jacopin, M. Hezam, N. Arora, S. M. Zakeeruddin, B. Deveaud, M. K. Nazeeruddin and M. Grätzel, *ACS Photonics*, 2016, **3**, 947-952.
22. Y. Tian, M. Peter, E. Unger, M. Abdellah, K. Zheng, T. Pullerits, A. Yartsev, V. Sundström and I. G. Scheblykin, *Phys. Chem. Chem. Phys.*, 2015, **17**, 24978-24987.
23. A. Waleed, M. M. Tavakoli, L. Gu, Z. Wang, D. Zhang, A. Manikandan, Q. Zhang, R. Zhang, Y.-L. Chueh and Z. Fan, *Nano Lett.*, 2017, **17**, 523-530.
24. H. C. Woo, J. W. Choi, J. Shin, S.-H. Chin, M. H. Ann and C.-L. Lee, *J. Phys. Chem. Lett.*, 2018, **9**, 4066-4074.
25. C. Cheng, H. Xiangmin, L. Wengao, C. Shuai, S. Lijie, L. Liang, Z. Haizheng and H. Jun-Bo, *J. Phys. D*, 2018, **51**, 045105.
26. C. Yu, Z. Chen, J. J. Wang, W. Pfenninger, N. Vockic, J. T. Kenney and K. Shum, *J. Appl. Phys.*, 2011, **110**, 063526.
27. Y. Ling, Z. Yuan, Y. Tian, X. Wang, J. C. Wang, Y. Xin, K. Hanson, B. Ma and H. Gao, *Adv. Mater.*, 2016, **28**, 305-311.
28. A. Sharma, B. Bhattacharyya, A. K. Srivastava, T. D. Senguttuvan and S. Husale, *Sci. Rep.*, 2016, **6**, 19138.
29. A. Guvenc, A. Funda Aksoy, M. Emre, U. Husnu Emrah and T. Rasit, *J. Phys. D*, 2014, **47**, 065106.

भारतीय प्रौद्योगिकी संस्थान गुवाहाटी
Indian Institute of Technology Guwahati

Chapter 4

Solid-State Synthesis of Stable and Color Tunable Perovskite Nanocrystals and Mechanism of High-Performance Photodetection in a Monolayer $MoS_2/CsPbBr_3$ Vertical Heterojunction

In this chapter, we present on a facile room-temperature bulk scale solid-state synthesis of highly luminescent color-tunable $CsPbX_3$ nanocrystals (NCs) with superior optoelectronic performance and exceptional ambient stability. The composition tuned all-inorganic perovskite NCs exhibit high photoluminescence quantum yield with adjustable emission color over the entire visible region. The highly luminescent perovskite NCs were utilized for the demonstration of color-tunable down-converted light-emitting diodes with high luminous efficiency. We further integrate the $CsPbBr_3$ NCs on direct CVD grown large-area monolayer MoS_2 on Si/SiO_2 substrates and fabricate a vertical type-II heterojunction photodetector (PD) which exhibit high responsivity (24.3 A/W at 405 nm) and fast photo-response with photocurrent growth and decay times of 5.5 μs and 24.0 μs, respectively. The superior performance of the heterojunction PD is attributed to the fast transfer of photogenerated electrons from $CsPbBr_3$ NCs to monolayer MoS_2 and the n-doping of the MoS_2. Our interpretation is fully supported by the density functional theory based electronic structure calculations and Kelvin probe force microscopy measurement on the heterojunction.

4.1. Introduction

All-inorganic metal halide perovskites with the structural formula of $CsPbX_3$ NCs and quantum dots (QDs) (where X is a single or mixed halide (Cl, Br and I)) have attracted intensive attention with the superior optical performance of high PL QY, narrow line width of emission, high photostability, wide color gamut and the extraordinary performance in LEDs, solar cells, photodetectors, etc.[1-4] The widely explored synthesis strategy for $CsPbX_3$ NCs is the hot injection method.[1] However, the synthesis of perovskite NCs and QDs by hot injection involves complex, time-consuming experimental procedures. Several other synthesis methods, such as anion exchange, solvothermal synthesis, microwave-assisted synthesis, etc. have also been reported for the growth of perovskite NCs.[5-7] The current synthesis strategies of $CsPbX_3$ NCs are mostly limited to tedious methods that involve the use of toxic volatile organic solvents with high reaction

temperature, inert gas atmosphere, and complicated apparatus. However, a facile, low cost, and room temperature synthesis process for $CsPbX_3$ NCs in a solvent-free environment is not well explored.

Interestingly, 2D materials especially transition metal dichalcogenides (TMDs), such as molybdenum disulfide (MoS_2), molybdenum diselenide ($MoSe_2$), tungsten disulfide (WS_2), and tungsten diselenide (WSe_2) exhibit interesting optical and electronic properties for different technological interests.[8-10] Due to the high carrier mobility, unique optical properties, and superior mechanical flexibility, monolayer and few-layer TMDs have been widely applied in photodetectors, which show very fast response speed along with high photoresponsivity. However, the performances of these 2D TMD based photodetectors (PDs) are limited by the low light absorbance of the monolayer and few-layer TMDs. Thus, the integration of 2D TMD materials with other low-dimensional high light-harvesting materials, such as perovskite NCs/QDs, can lead to substantial enhancement in the light absorption resulting in higher photoresponsivity along with fast response due to high carrier mobility in 2D TMDs. [4, 11-14]

Herein, we report on a facile, room-temperature, nearly solvent-free, and bulk scale solid-state synthesis of highly luminescent $CsPbX_3$ NCs with emission over the entire visible region. The structural and the optical properties of the composition and color-tunable all-inorganic perovskite NCs were systematically studied. These NCs show superior ambient stability due to the unique nearly solvent-free, solid-state synthesis process. These highly luminescent perovskite NCs were utilized for the color-tunable light-emitting devices by employing NC composite films with Poly(methyl methacrylate) (PMMA) on commercial UV LED chips, which show superior operational stability (>100 h). We further integrate our $CsPbBr_3$ NCs with direct CVD grown monolayer MoS_2 (1L-MoS_2) grown on Si/SiO_2 substrates and fabricate a vertical heterojunction PD. The type-II heterojunction PD fabricated here shows asymmetric photo I-V characteristics similar to that of a p-n junction and high photoresponsivity with a very fast photoresponse. We investigate the mechanism of high photoresponsivity and fast photoresponse in the heterojunction PD through Kelvin probe force microscopy (KPFM) analysis and first-principles DFT based electronic structure calculations. The DFT calculations showed clear evidence of charge transfer across the heterojunction through the change in the density of states. These results are further corroborated by steady-state and time-resolved PL and Raman analyses.

4.2. Experimental Details

4.2.1. Sample Preparation and Device Fabrication

4.2.1.1. Solid-state Synthesis of $CsPbX_3$ NCs

The desired amounts of cesium halide (CsX) and lead halide (PbX_2) were added with 40 g zirconia balls of 5 mm diameter in a zirconia vial of volume 50 ml (Retsch, Germany) under ambient condition and subsequently ball milled in a planetary mill (Retsch, Germany) at a rotation speed of 500 rpm for 2 h, which results in a fine powder of $CsPbX_3$ of 0.8 mM. Next, 0.2 mL oleylamine (OAM) was added to the milling vial, and the milling process was continued for another 1 h for the surfactant-assisted formation of $CsPbX_3$ NCs. Further, the synthesized product was dispersed in 20 mL of toluene. Next, the mixture was centrifuged for 10 min at 8000 rpm, and the precipitation was separated, discarded, and re-dispersed in toluene to obtain the final product. The final volume of NCs dispersion was 20 ml.

4.2.1.2. Construction of Color-tunable LEDs

2 mL of different $CsPbX_3$ NCs dispersed in toluene was added with 0.5 g of PMMA power and subsequently mixed by vigorous stirring until the PMMA particles completely dissolved. Each of the solutions was drop cast on a low-cost commercial UV LED chip of emission wavelength 396 nm. The LEDs were operated at 3 V to obtain bright emission.

4.2.1.3. Growth of Large-area Monolayer MoS_2 by CVD Method

Large area 1L-MoS_2 was grown on SiO_2 layer (300 nm of SiO_2 on Si wafer) by a one-step thermal chemical vapor deposition (CVD) process.[8] In a typical process, a ceramic boat containing sulfur powder is positioned at 15 cm upstream inside a quartz tube away from the position of the boat containing MoO_3 powder in a two-zone muffle furnace. A quartz mask with circular openings was placed on the boat containing MoO_3 powder, and Si/SiO_2 substrates were kept over the mask. High-purity Ar gas (99.999%) served as the carrier gas throughout the experiment. S source and MoO_3 temperatures were raised to 150 °C and 700 °C at a rate of 3.5 and 15 °C/min, respectively, and maintained for 5 min for the growth of MoS_2 at an Ar flow rate of 10 sccm. Then, the system was allowed to cool down to room temperature at a cooling rate of 6.5 °C/min. Note that the 1L-MoS_2 film was grown on each substrate only on the portions of the substrate covered by the quartz mask, whereas the open regions directly exposed to the source vapor are observed to be deposited

with few-layer and multilayer MoS_2. Note that the PD was fabricated on the monolayer region of MoS_2.

4.2.2. Characterization Techniques

The details of the characterization techniques (FETEM, EDX, XRD, UV-vis absorbance, PL, PL QY, TRPL, etc.) used to study the systems were described in **Chapter 2, Section 2.2.2.** The details of HAADF-STEM and EDS measurements were described in **Chapter 3, Section 3.2.2.** X-ray photoelectron spectroscopy (XPS) measurements were performed with a PHI X-Tool automated photoelectron spectrometer (PHI X-tool, ULVAC-PHI Inc.). Atomic force microscope (AFM, Bruker, Innova) was used in the tapping mode for the examination of the topography of the CVD grown MoS_2 layer. Further, electrostatic force microscopy (EFM, Bruker) toolkit with probe carrier and sample holder enabled with biasing leads was utilized for Kelvin probe force microscopy (KPFM) measurement. Temperature-dependent (80-300 K) PL measurements were performed using a liquid nitrogen-cooled optical cryostat (Optistat DNV, Oxford Instruments). The temporal response of the photocurrent and I-V measurement of the PDs were carried out using a microprobe station (ECOPIA, EPS-500), a 405 nm laser with TTL modulation and a source meter (Keithley 2400). The spectral photoresponsivity of the PD was measured using a Xenon lamp (Newport) with a manual monochromator (Newport), and a source meter (Keithley 2400).

4.2.3. Computational Methodology

In order to envisage the hidden electronic structure and the charge transfer mechanism of the $MoS_2/CsPbBr_3$ composite system, we have performed systematic electronic structure calculations within the framework of density functional theory (DFT). The individual systems and their composite have been optimized through ionic relaxation to attain the minimum energy configurations. After finding the relaxed optimized structures of all the considered systems, the projected density of states and charge density have been determined using Vienna Ab-initio Simulation Package (VASP) code, where projector augmented wave (PAW) formalism is implemented. Throughout our calculations, we have used General Gradient Approximation (GGA) approach as implemented in Perdew-Burke-Ernzerhof (PBE) functional to treat the exchange and correlation energies. The converged energy cut-off used throughout the calculation has been set at 500 eV. The Brillouin zone has been sampled using 3×3×1 Monkhorst-Pack k-mesh for the ionic relaxation in case of MoS_2 and $MoS_2/CsPbBr_3$ systems, whereas it has been sampled using 1×1×1 Gamma point in case of $CsPbBr_3$ NCs. We have kept adequate vacuum along Z-axis in order to

nullify the interaction between the periodic images of the surface system. One of the prime focus of this investigation is the charge transfer mechanism between MoS_2 and $CsPbBr_3$ NCs. In order to explore the possible charge transfer between the surface and NCs system, we have obtained charge density distribution of the composite system, while doing self-consistent electronic structure calculation.

4.3. Results and Discussion

4.3.1. Synthesis Strategy of $CsPbX_3$ NCs

We adopted a solid-state synthesis method to grow stable perovskite NCs. **Fig. 4.1** illustrates the synthesis steps of highly luminescent $CsPbX_3$ NCs by using the solid-state method.

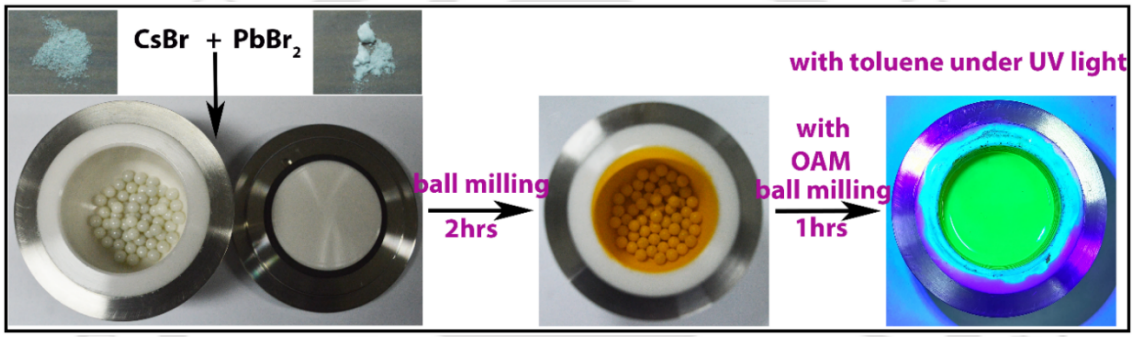

Fig. 4.1: Photographs of the solid-state synthesis steps of all inorganic perovskite NCs by ball milling method.

The most explored synthesis process for all inorganic $CsPbX_3$ perovskite NCs and QDs is the hot injection method. In the hot injection method, which is multistep tedious, time-consuming process, different polar solvents such as DMSO and DMF, or organic surfactants/ligands like 1-octadecene, oleic acid are used to dissolve different raw reagents, like Cs_2CO_3, CsOAc (cesium acetate), PbX_2 (X = Cl, Br, I) metal salts by heating at high temperature. However, the residue of polar solvents and organic surfactants/ligands may accelerate the degradation process of the NCs. In stark contrast, in our solid-state method, no solvent was used. In the 2nd step of the growth, a minimal amount of surfactant (oleylamine, OAM) was used to control the size of the NCs. High-speed mechanical mixing provides the required reaction energy in a similar way to heating or ultrasonication needed for the cocrystal formation. Kaupp et al. suggested a three-step reaction mechanism to explain the molecular solid reactivity.[15] First, the raw reactants diffused through a mobile phase similar to the amorphous solid and chemical reaction followed; second, nucleation and growth of the product phase occurred, and finally, the product separated and unreacted reactant surface was exposed for further reaction cycles. In our case, we have explored a two-step

mechanical reaction process for the growth of composition and color-tunable $CsPbX_3$ perovskite NCs. The 1st phase of mixing for 2 h ensures the completion of the reaction, while the 2nd phase of OMA assisted mixing results in the formation of nearly monodispersed cubic shaped NCs. Note that the addition of OMA ligand in minute quantity plays an important role in functionalizing the surface of the NCs that exhibits strong fluorescence and better stability. We also varied OMA content from 0 mL to 0.4 mL and observed that 0.2 mL OMA shows the optimized growth of nearly monodispersed perovskite NCs with superior optical properties.

4.3.2. Morphology and Structural Analyses

4.3.2.1. FETEM Analysis

The morphology of the as-grown all-inorganic perovskite NCs was studied using FETEM imaging.

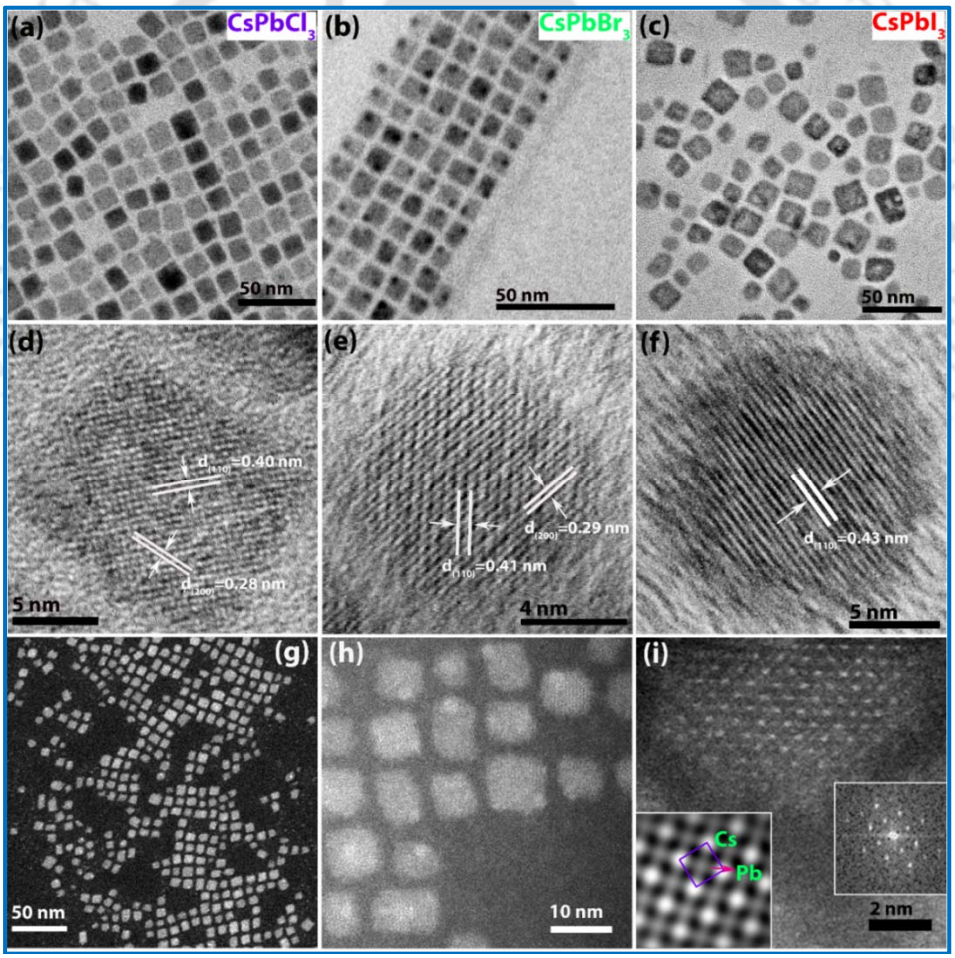

Fig. 4.2: TEM images of: (a) $CsPbCl_3$ NCs, (b) $CsPbBr_3$ NCs and (c) $CsPbI_3$ NCs. HRTEM lattice fringe images of: (d) $CsPbCl_3$ NCs, (e) $CsPbBr_3$ NCs and (f) $CsPbI_3$ NCs. (g, h) HAADF-STEM images of $CsPbBr_3$ NCs. (i) High magnification HAADF-STEM image showing atomic columns in a $CsPbBr_3$ NC. The FFT pattern shown in the right inset confirms the good crystallinity of the NCs. The lower left inset is the IFFT pattern showing the atomic positions in the crystal.

The FETEM images of $CsPbCl_3$, $CsPbBr_3$, and $CsPbI_3$ NCs are shown in **Fig. 4.2(a-c)**, respectively. All the images show the cubic shaped morphology of the perovskite NCs.[1] During the FETEM imaging, degradation of the $CsPbI_3$ NCs was observed due to phase instability caused by the high energy electron beam irradiation, as shown in **Fig. 4.2(c)**. The average particle size was observed to be 10.6 nm, 7.1 nm, 9.4 nm for $CsPbCl_3$, $CsPbBr_3$, and $CsPbI_3$ NCs, respectively. **Fig. 4.2(d-f)** shows the HRTEM lattice fringes of individual $CsPbCl_3$, $CsPbBr_3$, and $CsPbI_3$ NCs. The lattice spacing of 0.28 and 0.40 nm for $CsPbCl_3$ NCs correspond to the (200) and (110) planes, respectively, as shown in **Fig. 4.2(d)**. The lattice spacing of 0.29 and 0.41 nm for $CsPbBr_3$ NCs correspond to the (200) and (110) planes, respectively, as shown in **Fig. 4.2(e)** whereas for $CsPbI_3$ 0.43 nm lattice spacing corresponds to the (110) plane. The systematic increase in d spacing due to the halide ion substitution from Cl to I is consistent with the crystal structure.[6]

The high-resolution surface morphology of perovskite NCs is further characterized by HAADF-STEM analysis. **Fig. 4.2(g-h)** show the HAADF-STEM images of $CsPbBr_3$ NCs at different magnifications, which clearly depicts the cubic shape of the NCs. A high magnification HAADF-STEM image of $CsPbBr_3$ NC is shown in **Fig. 4.2(i)**. The right inset of **Fig. 4.2(i)** represents the corresponding fast Fourier transform of the $CsPbBr_3$ NC image, which confirms the good crystalline quality of the NC. The left inset of **Fig. 4.2(i)** depicts the inverse fast Fourier transform pattern of $CsPbBr_3$ NC, representing the atomic resolution image of the crystal lattice.

4.3.2.2. XRD and XPS Analyses

The crystalline quality and phase of $CsPbX_3$ NCs were studied using the XRD pattern.[6] Depending upon the different temperatures, $CsPbX_3$ crystallizes in orthorhombic, tetragonal, and cubic polymorphs of the perovskite lattice, while the cubic phase is the high-temperature (~160-200°C) synthesis state for all compounds. The comparison of the XRD pattern of $CsPbX_3$ NCs film is shown in **Fig. 4.3**. Note that no impurity peak of raw reactants was observed in the XRD profiles (see **Fig. 4.3(a)**) confirming the proper reaction and full conversion of reactants in the solid-state reaction. Thus, the solid-state synthesis strategy produced perovskite NCs of high crystalline quality comparable to those prepared by the conventional hot-injection procedure, but with the great advantage of the facile and green nearly solvent-free protocol. Interestingly, the XRD pattern confirms the cubic phase of all $CsPbX_3$ NCs despite the room temperature synthesis process.[16] This can be attributed to the high reaction energy in the pressure mediated synthesis process and local heating produced in the ball milling method. Note that the cubic phase of $CsPbI_3$ NCs is the

metastable state, and at room temperature, it converts to the orthorhombic phase, while the cubic polymorphs of other NCs ($CsPbCl_3$-$CsPbBr_3$) exhibit good stability over a few months. The XRD peaks marked as '*' in **Fig. 4.3(a)** correspond to the orthorhombic phase of $CsPbI_3$. **Fig. 4.3(b)** shows the enlarged view of the XRD peak corresponding to (110) planes showing the systematic shift of the peak with changing composition.

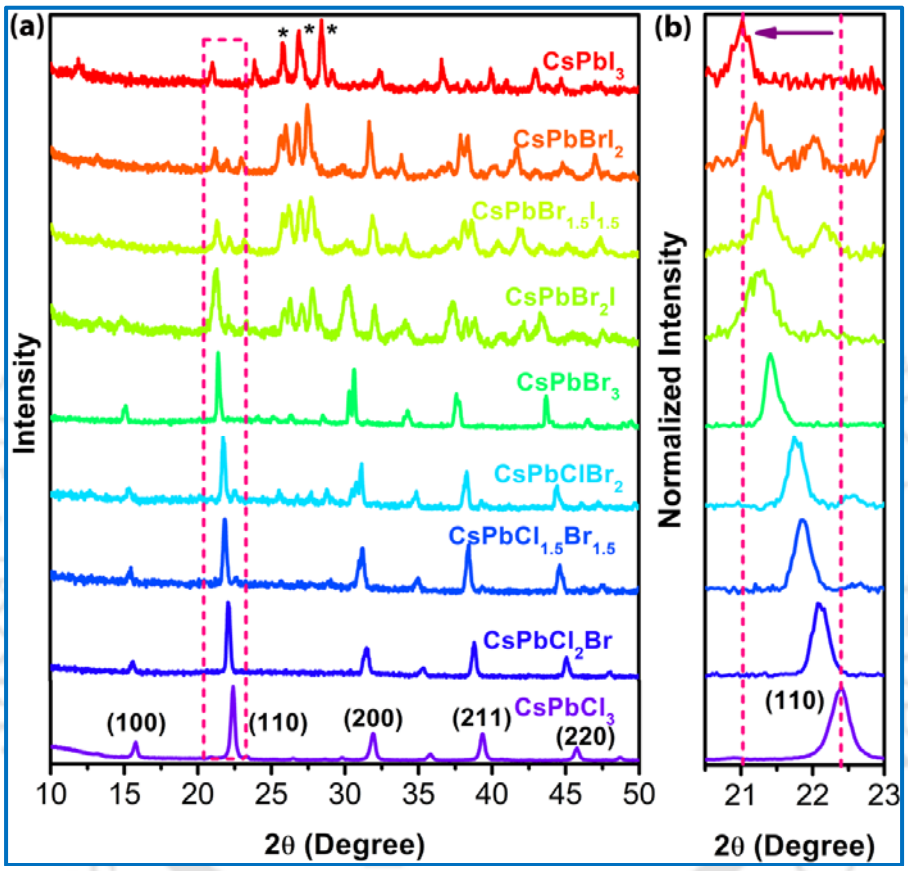

Fig. 4.3: (a) XRD pattern of all-inorganic halide perovskite NCs ($CsPbX_3$, X = Cl, Br, and I) with different halide substitution. The peaks marked as '*' correspond to the orthorhombic phase of $CsPbI_3$. (b) Magnified view of the (110) normalized XRD peaks of different samples, which shows the shift in peak positions with changing compositions.

The systematic shift in the XRD peak was observed towards higher diffraction angles with the halide ion substitution from I to Br to Cl, which is attributed to the decreased radii of halide ions from I to Br and Cl.

Furthermore, XPS measurements were performed to investigate the chemical composition and environment of $CsPbBr_3$ NCs. **Fig. 4.4(a)** depicts the survey scan XPS spectra of the $CsPbBr_3$ NC film in the energy range 0-800 eV, revealing the presence of Cs, Pb, Br, O, and C.[17] Carbon and oxygen were observed mainly due to the adsorption by the sample or chemisorbed OMA. **Fig.**

4.4(b) shows the Pb 4f core-level XPS spectrum with the corresponding fitting. The peaks with centers ~136.9 eV and 141.7 eV represent Pb $4f_{7/2}$ and $4f_{5/2}$, while the separation of 4.8 eV between the two peaks indicate the Pb (II) state.[17] The Cs 3d XPS spectrum shows two symmetric peaks with center ~722.9 eV and 736.8 eV with a peak separation of 13.9 eV, indicating the Cs (I) state, as shown in **Fig. 4.4(c)**. The broad Br 3d peak is fitted into two peaks ($3d_{5/2}$, $3d_{3/2}$) with binding energies of 67.0 eV and 68.1 eV, as shown in **Fig. 4.4(d)**.

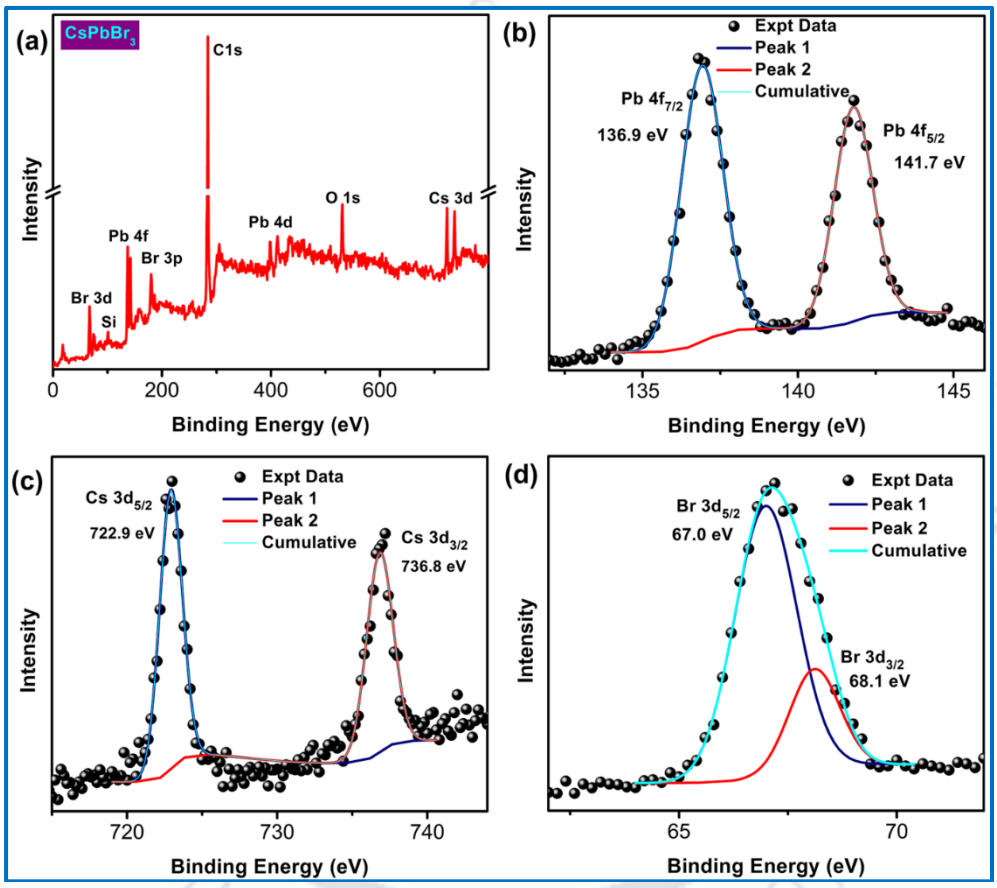

Fig. 4.4: (a) XPS survey scan spectrum of $CsPbBr_3$ NCs. (b) Pb 4f core-level XPS spectrum of $CsPbBr_3$ NCs with the Gaussian fitting. (c) Cs 3d core-level XPS spectrum of $CsPbBr_3$ NCs with the Gaussian fitting. (d) Br 3d core-level XPS spectrum of $CsPbBr_3$ NCs with the Gaussian fitting.

4.3.3. Absorbance and Photoluminescence Studies

The solid-state synthesis strategy was expanded to synthesize $CsPbX_3$ perovskite NCs with varied halide compositions/ratios. **Fig. 4.5(a)** shows the vertically staked absorption spectra of different samples. From the absorption edges of the different NCs, it is clear that the optical band gap can be tuned from 415 to 670 nm, across almost the entire visible range, by adjusting the halide composition during the synthesis.

The most attractive property of perovskite NCs and QDs is their strong color-tunable light emission. **Fig. 4.5(b)** shows the room-temperature normalized PL emission spectra of different $CsPbX_3$ NCs colloidal dispersion in toluene. It is evident that the PL emission can be tuned to cover the entire visible spectral range (from 416 to 691 nm) by adjusting the halide anions.

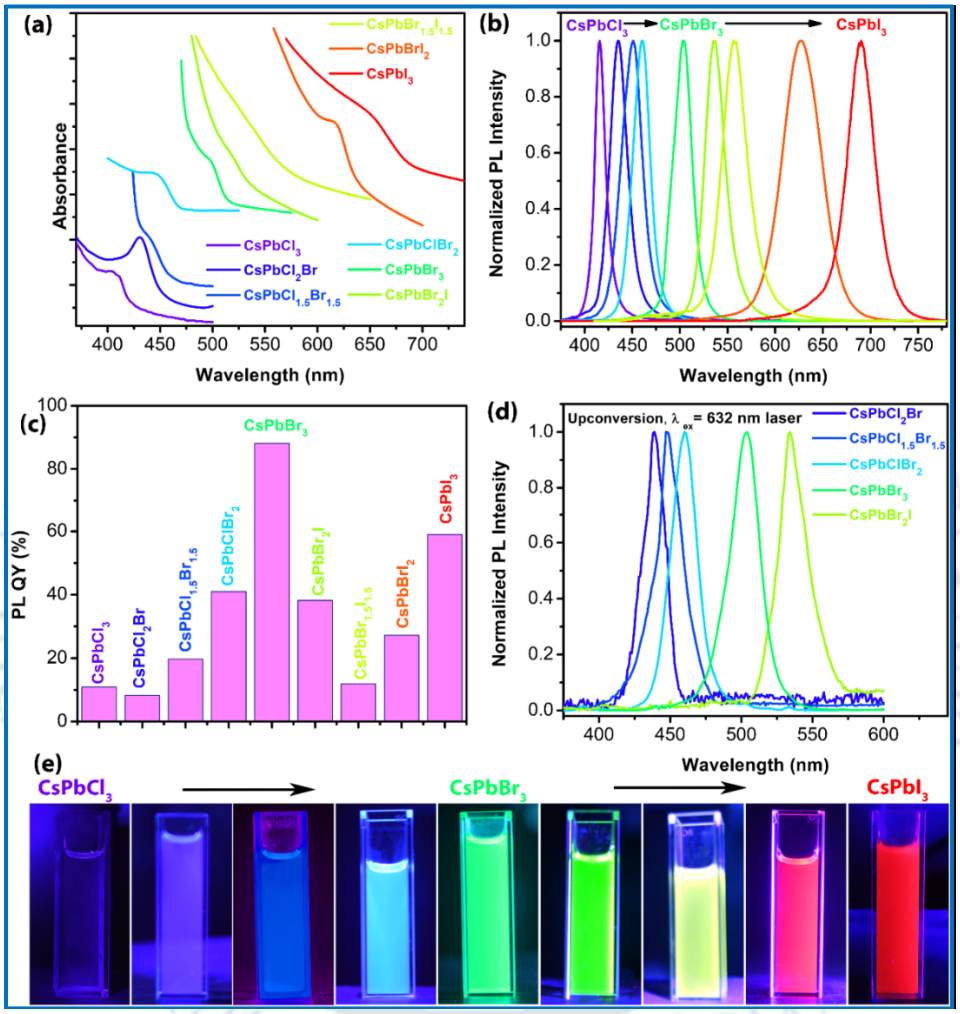

Fig. 4.5: (a) UV-vis absorption spectra (stacked) of $CsPbX_3$ NCs with different halide (X = Cl, Br, and I) compositions. (b) Comparison of the normalized PL spectra of different $CsPbX_3$ NCs samples. (c) Comparison of PL quantum yields of different $CsPbX_3$ NCs samples before annealing. (d) Normalized upconversion PL spectra of different $CsPbX_3$ NCs samples using laser excitation of 632 nm. (e) Photographs of the colloidal dispersions of $CsPbX_3$ NCs in toluene under UV light illumination (395 nm).

The sharp PL peaks of each NCs sample originate from the near band edge excitonic recombination. The as-grown $CsPbX_3$ NCs dispersed in toluene exhibit very sharp PL peaks with FWHM of 14-47 nm for the excitonic emission. The FWHM of PL peak increases by changing the halide anion from Cl to I, which is possibly due to the size-induced inhomogeneous broadening. The NCs size distribution from TEM imaging also suggests the same.

Strong PL emissions of $CsPbX_3$ NCs were further characterized by PL QY measurements. The $CsPbX_3$ NCs show very high PL QY of 8-88%, as shown in **Fig. 4.5(c)**. The PL QY of the perovskite NCs synthesis by our facile solid-state method is comparable to the well-known hot injection method.[18] Note that after post-growth annealing, the PL QY is increased to 9-95% due to the reduction of nonradiative recombination centers/ defects. Among all NCs, $CsPbBr_3$ exhibits the highest PL QY of 95%, which is higher than the previous report, whereas the mixed halides exhibit considerably lower PL QYs.[18] The surface-functionalized states of perovskite NCs greatly affect the PL quantum yield. The ligand (oleylamine) attached to the surface of the NCs also results in high PL quantum yield and better stability. The PL QY, peak position, FWHM and calculated band gaps of different NCs are tabulated in **Table 4.1**. We have further studied the photon upconversion by the as-synthesized perovskite NCs. **Fig. 4.5(d)** shows the normalized upconversion emission spectra for $CsPbX_3$ NCs under 632 nm CW diode laser excitation.[19] Interestingly, in the upconversion spectra, we observed the characteristic band-edge exciton emissions from the perovskite NCs. These results depict the excellent fluorescence properties $CsPbX_3$ NCs synthesized by the simple solid-state process. **Fig. 4.5(e)** shows the photographs of the colloidal dispersions of $CsPbX_3$ NCs with different halide compositions in toluene under UV light irradiation of wavelength 395 nm, which shows color-tunable bright emission from each sample.

***Table 4.1**: Summary of the PL spectral features and quantum yields of different perovskite NCs made by the solid-state process.*

Perovskite NCs	PL peak position (nm)	FWHM (nm)	PL quantum yield (%)	Calculated ban gap from absorption (eV)
$CsPbCl_3$	416	14	11	2.98
$CsPbCl_2Br$	435	22	9	2.80
$CsPbCl_{1.5}Br_{1.5}$	451	25	21	2.76
$CsPbClBr_2$	461	22	44	2.70
$CsPbBr_3$	503	23	95	2.45
$CsPbBr_2I$	537	25	41	2.34
$CsPbBr_{1.5}I_{1.5}$	557	32	13	2.25
$CsPbBrI_2$	626	47	29	1.97
$CsPbI_3$	690	35	63	1.85

4.3.4. Stability Study

We have further studied the long-term stability of our $CsPbBr_3$ NCs. Due to the metastable phase of $CsPbI_3$, it degrades within a few days, while other NCs show storage stability for several months. Among all the nine different perovskite NCs studied, $CsPbBr_3$ colloidal NCs in toluene shows the highest storage stability of over 7 months of storage. **Fig. 4.6(a)** shows the comparison of PL spectra after 3 months, 5 months, and 7 months of storage in ambient condition The PL peak intensity was decreased by only 24% from its initial PL intensity after 7 months of storage in the ambient condition (with high humidity), which is significantly better than the reported stabilities.[20, 21] The left inset depicts the digital photograph showing the bright emission under UV light of $CsPbBr_3$ NCs after 7 months of storage. **Fig. 4.6(b)** shows the comparison of the XRD pattern of as-grown $CsPbBr_3$ NCs and the same after 5 months of storage. The XRD peaks retained in the sample after 5 months of storage confirm the high stability of our $CsPbBr_3$ NCs. We also studied the photostability and thermal stability of the $CsPbBr_3$ NCs film. Interestingly, with laser exposure the PL intensity first increased for 1½ hr and then reduced by ~35% after 5 hr of irradiation and then remained stable for 30 hr of irradiation with 405 nm CW laser (see **Fig. 4.6(c)**). The initial increase in PL is due to the light-induced defect curing. **Fig. 4.6(d)** depicts the change in relative PL intensity of $CsPbBr_3$ NCs film as a function of heating time when continuously heated at 85 °C. Here again, initially, the PL intensity increased due to the removal of the nonradiative centers, and then it decreases by ~53% after 10 hr of heating.

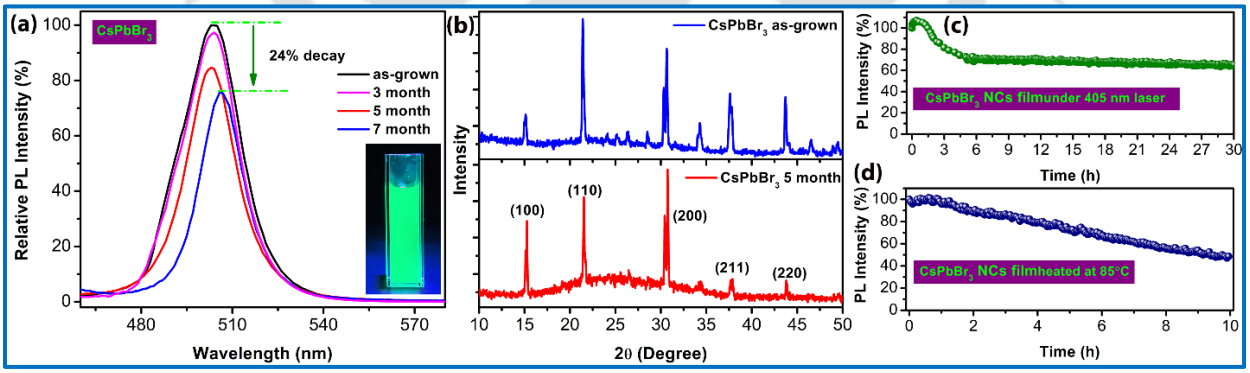

Fig. 4.6: (a) Evolution of the PL spectra of a colloidal dispersion of $CsPbBr_3$ NCs in toluene after different storage times in ambient conditions. The inset shows the photograph of $CsPbBr_3$ NCs in toluene under UV light after 7 months of storage. (b) Comparison of the XRD pattern of as-grown and after 5 months of storage of $CsPbBr_3$ NCs in ambient conditions. (c) PL intensity of $CsPbBr_3$ NCs film as a function of laser exposure time under continuous irradiation of 405 nm CW laser. (d) Change in PL intensity with a heating time of $CsPbBr_3$ NCs film heated at 85° C.

Thus, the as-grown $CsPbBr_3$ NCs show excellent photo and thermal stability. Our results are significantly better than the reported stability of the solution-processed perovskite NCs. Zhang et al. reported that the coordination of different solvents used in the synthesis process played an important role in the stability of the perovskite.[22] In the hot injection method, different solvents, organic surfactants/ligands are used to dissolve the raw reactants. The residue of these solvents may lead to the poor stability of the perovskite NCs, while in our case, no organic solvent surfactants/ligands were used in the synthesis process.

4.3.5. Low-Temperature Photoluminescence Study

To investigate the origin of high PL QY of the perovskite NCs, temperature-dependent PL measurements were carried out. PL spectra of $CsPbBr_3$ NCs film in the temperature range 80-300 K are shown in **Fig. 4.7(a)**. The intensity of the PL peak increased systematically with the decrease in temperature.

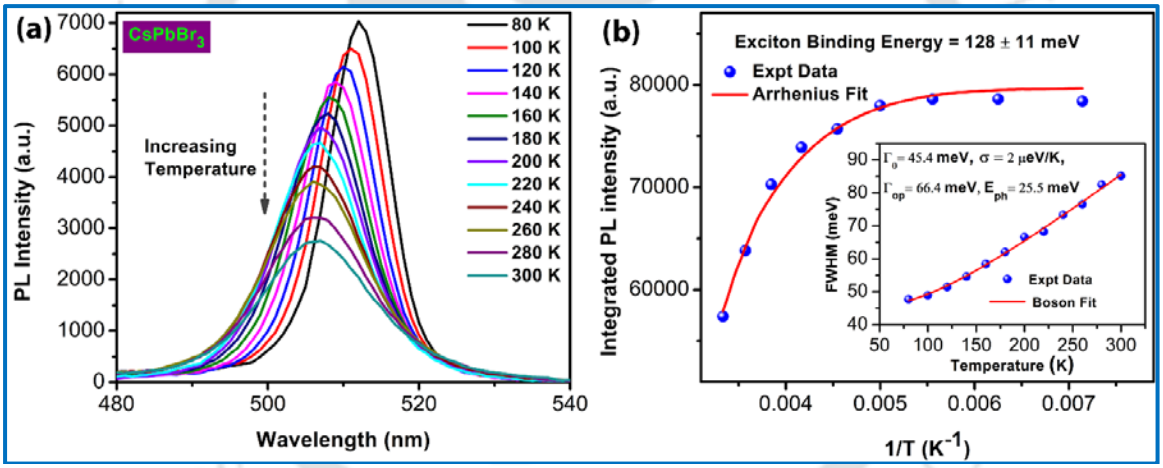

Fig. 4.7: (a) Temperature-dependent PL spectra of $CsPbBr_3$ NCs film. (b) Integrated PL intensity of $CsPbBr_3$ NCs as a function of the inverse of temperature and its fitting with the Arrhenius equation. The inset shows the variation of FWHM of the excitonic peak with temperatures and its Boson fit.

The decrease in PL peak intensity of perovskite NCs with increasing temperature is mainly attributed to the thermal quenching of PL by carrier trapping at higher temperatures.[23] At higher temperatures, the nonradiative deep level trap states are more active, and photogenerated excitons dissociate, which results in a decrease in PL intensity. Note that with the decrease in measurement temperature, a systematic redshift of the PL peak is observed, as shown in **Fig. 4.7(a)**. Typically, a semiconductor shows a blue shift in excitonic PL peak with decrease in temperature due to the electron-phonon interaction. However, $CsPbBr_3$ shows the unusual redshift of PL emission, i.e.,

the bandgap increases with the increasing temperature. This is attributed to the dominant contribution of lattice thermal expansion with a positive temperature coefficient as compared to the contribution of electron-phonon interaction in perovskite NCs. From the low-temperature PL analysis, we can estimate two important parameters, the exciton binding energy (E_b) and exciton-phonon scattering, which play important roles for the high PL QY of the NCs.[23] **Fig. 4.7(b)** shows the variation of integrated PL intensity with the inverse of temperature (1/T) fitted with the Arrhenius equation (described in chapter 3). The exciton binding energy of $CsPbBr_3$ NCs is obtained to be 128.6 meV, which is much less than the lattice thermal energy at room temperature (~26 meV). The high exciton binding energy of $CsPbBr_3$ NCs implies that at room temperature thermal dissociation of the exciton is less probable resulting in the high PL QY (~ 95%).[24]

The line width (FWHM) of the excitonic PL emission increases systematically with increasing temperature, as shown in the inset of **Fig. 4.7(b)**. The higher broadening at higher temperature is attributed to the enhanced exciton-phonon scattering and non-radiative decay of photogenerated excitons near room temperature. The temperature-dependence of the emission linewidth is fitted using the Boson model with the following equation:

$$\Gamma(T) = \Gamma_0 + \sigma T + \frac{\Gamma_{op}}{\exp(E_{ph}/k_B T) - 1} \qquad (4.1)$$

where Γ_0 is the inhomogeneous broadening constant, σ is the exciton-acoustic phonon coupling coefficient, Γ_{op} is the exciton-longitudinal optical phonon coupling coefficient or the Fröhlich coupling coefficient, and E_{ph} is the optical phonon energy.[25] From the fitting of temperature-dependent FWHM shown in the inset of **Fig. 4.7(b)**, the obtained parameters for $CsPbBr_3$ are: Γ_0= 45.4 meV, σ = 2 μeV/K, Γ_{op}= 66.4 meV, and E_{ph} = 25.5 meV. These parameters are comparable to the other reported $CsPbBr_3$ NCs/QDs synthesized by the hot injection method.[24] Thus, our results imply the versatility of perovskite NCs synthesized by the low-cost facile solid-state method with the impressive optical properties.

4.3.6. Time-Resolved Photoluminescence Study

Time-resolved photoluminescence (TRPL) measurements were performed to investigate the recombination kinetics of photogenerated charge carriers in the $CsPbX_3$ colloidal NCs. **Fig. 4.8** shows the TRPL decay profiles of different perovskite NCs monitored at the corresponding PL peak energy of each sample, and the data are fitted using a tri-exponential decay function. The three time constants are correlated with the radiative electron-trapping and the radiative electron-

hole recombination of halide perovskite. The average lifetimes (τ_{ave}) of the TRPL decay profiles were found to be 13.7 ns, 15.0 ns, 18.6 ns, 31.8 ns and 100.9 ns for $CsPbCl_3$, $CsPbCl_{1.5}Br_{1.5}$, $CsPbBr_3$, $CsPbBr_{1.5}I_{1.5}$ and $CsPbI_3$ NCs, respectively. The average lifetimes decreased systematically with the widening of the bandgap of the perovskite NCs, and it is consistent with the literature.[1] Note that the lower PLQYs of $CsPbCl_3$ (~11%) and $CsPbI_3$ (~63%) NCs than that of $CsPbBr_3$ (~95%) NCs and the difference of decay rates are attributed to the intrinsic optical properties of the halide perovskites.[1, 16]

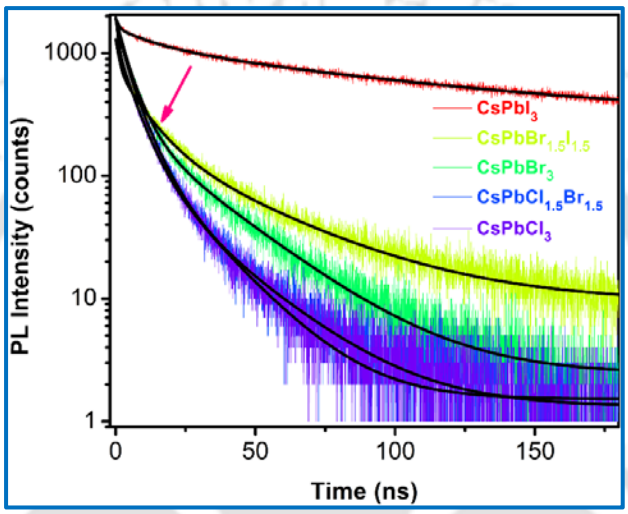

Fig. 4.8: TRPL decay profiles of $CsPbX_3$ NCs with different halide (X = Cl, Br, and I) compositions.

4.3.7. Applications in Light Emitting Diodes

The color-tunable perovskite NCs with excellent PL QY and high stability are further utilized for their application in down-converted light-emitting diodes (LEDs).[7, 26] As-synthesized $CsPbX_3$ NCs dispersed in toluene were mixed with PMMA and coated on a low-cost commercial UV LED chip with emission wavelength 395 nm. **Fig. 4.9(a)** shows the photographs of different fabricated $CsPbX_3$ NCs LED devices. LED devices emit different bright colors from the violet to the red region under 3 V bias. The corresponding normalized electroluminescence (EL) emission spectra of different devices are shown in **Fig. 4.9(b)** depicting the fully tunable luminescence from the violet to the red region. The CIE coordinates of the LED devices are found to be (0.15, 0.11), (0.16, 0.03), (0.16, 0.02), (0.16, 0.12), (0.08, 0.58), (0.25, 0.62), (0.28, 0.53), (0.66, 0.33) and (0.68, 0.30) for $CsPbCl_3$, $CsPbCl_2Br$, $CsPbCl_{1.5}Br_{1.5}$, $CsPbClBr_2$, $CsPbBr_3$, $CsPbBr_2I$, $CsPbBr1.5I_{1.5}$, $CsPbBr_2I$ and $CsPbI_3$ NC perovskite LEDs, respectively confirming full spectral tunability. Thus, our results indicate that the as-prepared low-cost $CsPbX_3$ NCs are promising for

future LED and display applications over the entire visible region. The luminous efficiency of the $CsPbBr_3$ LED was measured to be ~42 lm/W using a lux meter, which is significant for their practical application. We have further studied the operational stability of the $CsPbBr_3$ LED in ambient air without any encapsulation. The variation of EL emission intensity as a function of time is shown in **Fig. 4.9(c)**, and it exhibits the significant operational stability of the $CsPbBr_3$ LED up to ~200 hours without any encapsulation. The insets in **Fig. 4.9(c)** show the images of the LEDs after continuous operation of 50 h and 200 h.

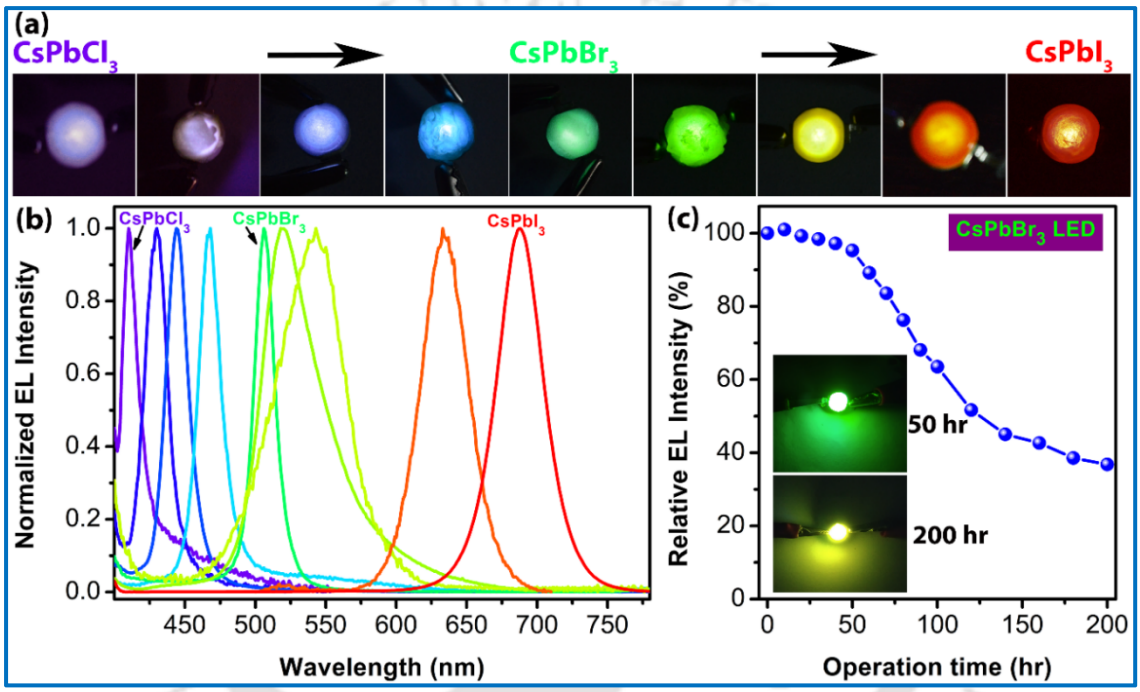

Fig. 4.9: (a) Digital photographs of the fabricated LEDs using $CsPbX_3$ (X = Cl, Br, and I) perovskite NCs on a commercial UV chip. (b) The normalized emission spectrum of the fabricated $CsPbX_3$ LED devices. (c) Relative EL emission intensity of $CsPbBr_3$ LED as a function of operation (continuous) time. The inset shows the photographs of the LEDs after 50 hours and 200 hours of operation in ambient condition.

The performance of the LED devices can be further improved using an encapsulation, better quality LED chips, and controlling the deposition of NCs/PMMA films coated on the chip.

4.3.8. 1L-MoS_2/ $CsPbBr_3$ NCs Heterojunction Photodetector

Among all the as-grown inorganic halide perovskite NCs, $CsPbBr_3$ NCs show excellent stability with good crystallinity and high optical absorbance suitable for various optoelectronic applications. Taking advantage of the large absorption coefficient in the UV-visible region of perovskite and fast carrier mobility of 1L-MoS_2, we have integrated $CsPbBr_3$ NCs with direct CVD grown large-area 1L-MoS_2 on Si/SiO_2 substrates, to achieve high-performance TMD-based

photodetectors.[27] The optical microscope image of CVD grown large-area 1L-MoS_2 is shown in **Fig. 4.10(a)**, while **Fig. 4.10(b)** depicts the AFM image at the edge of the 1L-MoS_2 film. **Fig. 4.10(c)** shows the corresponding height profile along the black line in **Fig. 4.10(b)**. The flake height of 0.7 nm from the height profile confirms the formation of 1L-MoS_2. [8, 28]

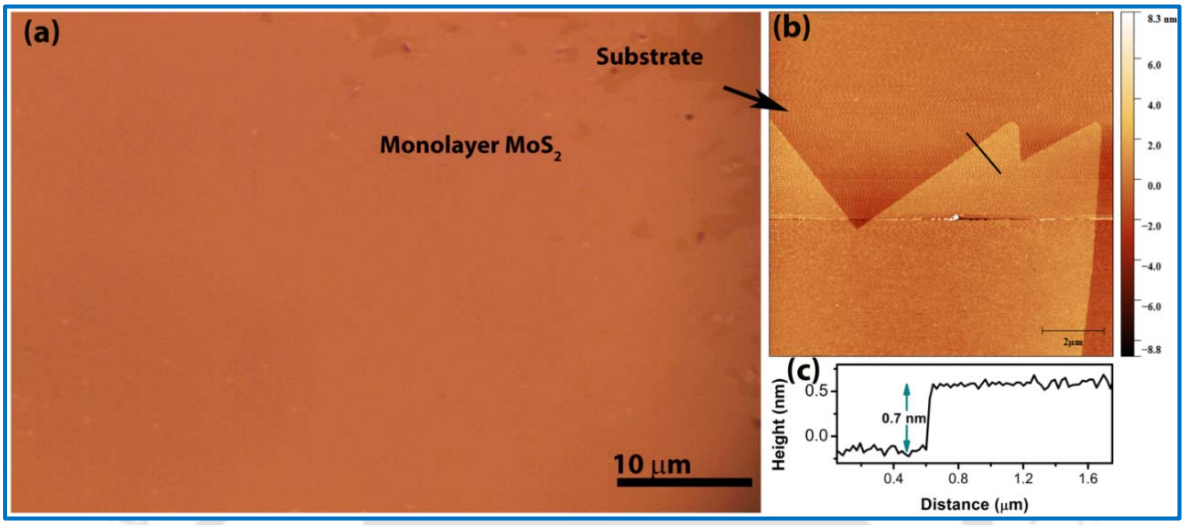

Fig. 4.10: (a) Optical microscope image of large area 1L- MoS_2 layer grown on Si/SiO_2 by direct CVD technique. (b) AFM image of 1L-MoS_2 on Si/SiO_2 substrate. (c) AFM height profile of 1L-MoS_2.

Fig. 4.11(a) shows a schematic illustration of the hybrid 1L-MoS_2/$CsPbBr_3$ NCs vertical type heterojunction PD.[27] The inset shows a cross-sectional FESEM image of the heterojunction PD showing the perovskite layer of thickness 80 nm. **Fig. 4.11(b)** presents a plot of the Kubelka-Munk (K-M) function, F(R), which is related to the absorption coefficient/absorbance of different films. Three peaks are observed in the K-M function plot of pristine 1L-MoS_2. Two peaks with centers ~ 671 nm (A) and ~621 nm (B) are attributed to the excitonic transitions between the spin-orbit split valence band and the conduction band at K and K' points of the Brillouin zone, while the third peak (C) centered at ~455 nm is associated with direct transitions from the deep valence band to the conduction band in 1L-MoS_2.[4, 28] $CsPbBr_3$ NCs film shows sharp absorption edge at ~515 nm due to the band to band transition, as shown in **Fig. 4.11(b)**. In the 1L-MoS_2/$CsPbBr_3$ NCs hybrid, enhanced absorption was observed in the UV-vis region as compared to the individual films due to the co-absorption of 1L-MoS_2 and $CsPbBr_3$ NCs films. The enhanced optical absorption of the 1L-MoS_2/$CsPbBr_3$ NCs hybrid film is utilized for the efficient photodetection by the heterojunction PD.

The charge transfers and photogenerated carrier recombination dynamics in 1L-MoS_2/$CsPbBr_3$ heterojunction are further studied using steady-state and time-resolved PL measurements. **Fig. 4.11(c)** shows a comparison of the PL spectra of $CsPbBr_3$ NCs film and 1L-MoS_2/$CsPbBr_3$ NCs film.

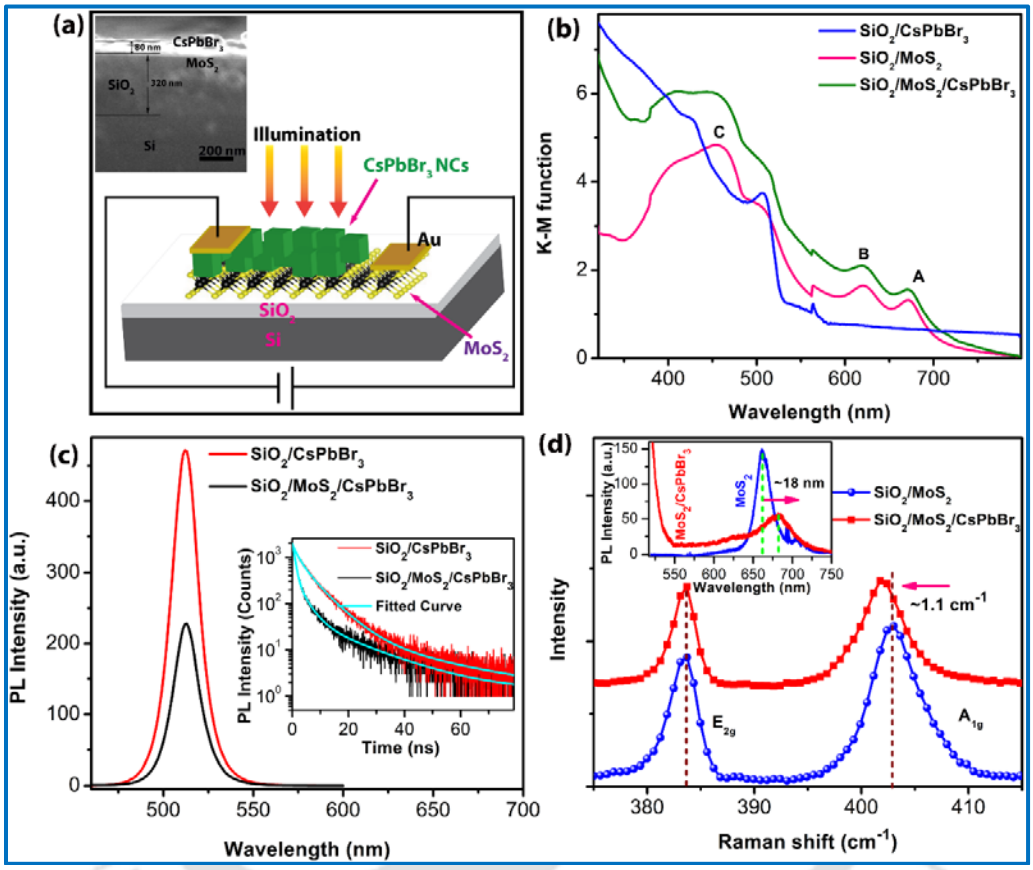

Fig. 4.11: (a) Schematic illustration of 1-LMoS_2/$CsPbBr_3$ NCs vertical heterojunction PD. The inset shows a cross-sectional FESEM image of the heterojunction PD showing the perovskite layer of thickness 80 nm. (b) Comparison of the K-M functions of $CsPbBr_3$ NCs film, 1L-MoS_2, and 1L-MoS_2/$CsPbBr_3$ NCs films on SiO_2 substrate as derived from the respective diffused reflectance spectrum. (c) Comparison of the PL spectra of $CsPbBr_3$ NCs film and 1L-MoS_2 on SiO_2 substrate. The inset shows a comparison of the TRPL decay profiles of the two samples. (d) Comparison of the Raman spectra of 1L-MoS_2 and 1L-MoS_2/$CsPbBr_3$ NCs on SiO_2 substrate. The vertical dotted lines show the shift of Raman peaks associated with MoS_2. The inset shows the comparison of the PL spectra of pristine1L-MoS_2 and 1L-MoS_2/$CsPbBr_3$ NCs.

Both the films show a PL peak of ~512 nm corresponding to the near band edge exciton recombination in $CsPbBr_3$. Interestingly, the PL peak intensity is quenched dramatically by ~52 % in 1L-MoS_2/$CsPbBr_3$ NCs film as compared to the bare $CsPbBr_3$ NCs film, and it is attributed to the transfer of photogenerated carriers from $CsPbBr_3$ to 1L-MoS_2 at the heterojunction resulting in the decrease in radiative recombination in $CsPbBr_3$ NCs.[4, 10] The TRPL decay profiles of $CsPbBr_3$ NCs film and 1L-MoS_2/$CsPbBr_3$ NCs film are shown in the inset of **Fig. 4.11(c)**. The

average decay constants were obtained to be 16.6 ns and 13.1 ns for $CsPbBr_3$ and 1L-MoS_2/$CsPbBr_3$ NCs films, respectively. The shortening in the decay time constant in the 1L-MoS_2/$CsPbBr_3$ hybrid compared to the pristine film is attributed again to the efficient transfer of photogenerated charges from $CsPbBr_3$ to 1L-MoS_2 at the 1L-MoS_2/$CsPbBr_3$ interface. The efficient transfer of photogenerated electrons from $CsPbBr_3$ to 1L-MoS_2 results in the enhanced photocurrent (PC) with superior response time in the hybrid device.

The charge transfers and the doping effect of 1L-MoS_2 /$CsPbBr_3$ heterojunction are further probed by Raman measurement. **Fig. 4.11(d)** shows a comparison of the Raman spectra of pristine 1L-MoS_2 and 1L-MoS_2/$CsPbBr_3$. Two major first-order Raman modes, E_{2g} and A_{1g}, are detected at ~383.6 and ~403.0 cm^{-1}, respectively, which correspond to 1L-MoS_2.[8] The frequency difference (Δk) between the E_{2g} and A_{1g} modes of pristine 1L-MoS_2 is observed to be 19.4 cm^{-1}, which confirms the formation of monolayer MoS_2.[28] The E_{2g} and A_{1g} modes are attributed to the in-plane vibration of two S atoms with respect to the Mo atoms and out-of-plane vibration of only S atoms in opposite directions with respect to the Mo atoms, respectively.[8] As shown in **Fig. 4.11(d)**, we observed a relative redshift of the A_{1g} peak of 1L-MoS_2/$CsPbBr_3$ by ~1.1 cm^{-1} with respect to that of the pristine 1L-MoS_2, whereas no shift was detected in the E_{2g} peak. Note that the doping state of 1L-MoS_2 can be determined from the A_{1g} mode because of the strong electron-phonon coupling along the c-axis.[9] The redshift of the A_{1g} peak is attributed to the higher n-type doping of 1L-MoS_2 due to the electron transfer from $CsPbBr_3$ to 1L-MoS_2.[9, 29] Note that the as-grown 1L-MoS_2 is lightly n-type due to the presence of charged impurities in the CVD growth process.[8] In the hybrid device, due to the charge transfer, MoS_2 becomes more n-type, while $CsPbBr_3$ becomes lightly p-type. A comparison of the PL spectra of the pristine 1L-MoS_2 and 1L-MoS_2/$CsPbBr_3$ NCs heterostructure is shown in the inset of **Fig. 4.11(d)**. The sharp increase in PL below 550 nm corresponds to the high emission of perovskite NCs in the hybrid sample. The redshift by ~18 nm and broadening of MoS_2 PL peak in the heterojunction is attributed to the increase of trion spectral weight owing to the n-type doping effect of 1L-MoS_2 in the hybrid system.[29]

To gain a better insight into the electronic structure and band alignment of 1L-MoS_2/$CsPbBr_3$ NCs heterojunction, we further performed KPFM analysis, as it is sensitive to the surface work function (ϕ) of materials. The KPFM measurement allows one to find the conduction band offset of 1L-MoS_2 and 1L-MoS_2/$CsPbBr_3$ NCs heterojunction. The work function of the Pt/Ir-coated tip

for KPFM measurement was calibrated using ordered pyrolytic graphite (HOPG) standard sample. The work function of the tip (ϕ_{tip}) was calibrated to be ~4.5 eV. The contact potential difference (CPD) between the tip and the sample is given by[30, 31]

$$CPD = \frac{\phi_{tip} - \phi_{sample}}{e} \qquad (4.2)$$

Where ϕ_{sample} is the work functions of the sample, and e is the elementary charge. The topography profiles of the pristine 1L-MoS_2 and hybrid 1L-MoS_2/ $CsPbBr_3$ are shown in **Fig. 4.12(a, e)**, while the corresponding CPD distribution images are shown in **Fig. 4.12(b, f)**, respectively. **Fig. 4.12(c, g)** shows the height profiles of 1L-MoS_2 and 1L-MoS_2/$CsPbBr_3$ along the line marked in (a, e), respectively. Note that the height profile in **Fig. 4.12(c)** confirms the formation of 1L-MoS_2. **Fig. 4.12(d, h)** shows the CPD line profiles along the black line marked in **Fig. 4.12(b, f)**, respectively. Considering ϕ_{tip} as constant, the local surface work function of the samples could be measured by the change in CPD values.[30]

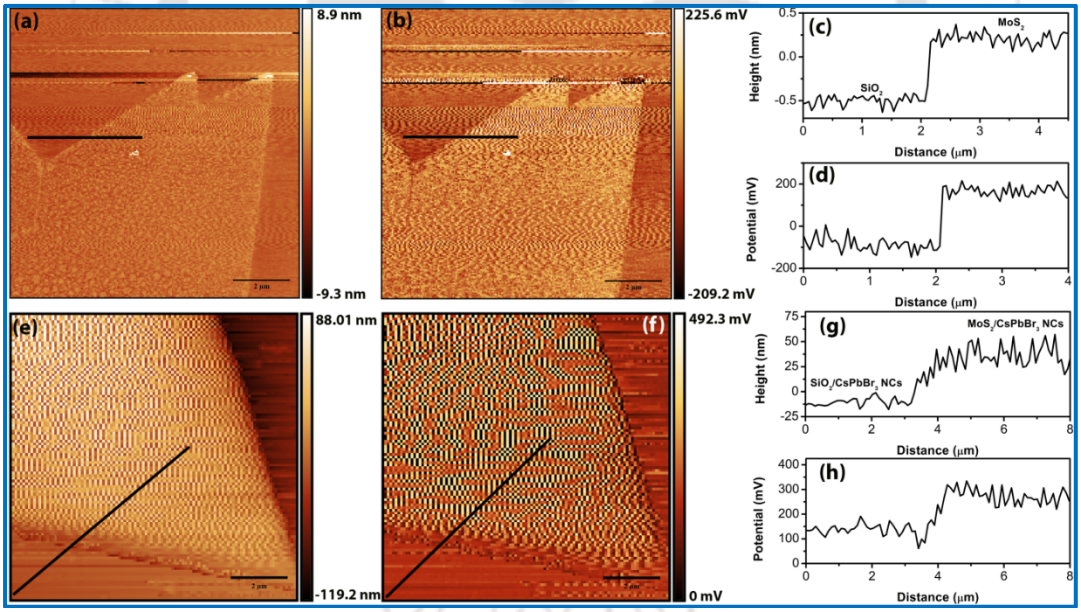

Fig. 4.12: (a, e) AFM surface topography images of 1L-MoS_2 and 1L-MoS_2/$CsPbBr_3$ NCs, respectively. (b, f) The corresponding spatial maps of the contact potential difference (CPD). (c, g) Height profiles of the pristine 1L-MoS_2 and 1L-MoS_2/ $CsPbBr_3$, respectively. (d, h) CPD profiles of pristine 1L-MoS_2 and 1L-MoS_2/$CsPbBr_3$, respectively.

For 1L-MoS_2, the CPD was measured as ~ 180 mV. Thus, the work function of the 1L-MoS_2 layer was obtained as ~4.32 eV calculated from equation (4.5).[30] In the case of 1L-MoS_2/$CsPbBr_3$, a higher CPD was observed in the heterojunction as compared to the NCs on SiO_2, as shown in **Fig. 4.12(h)**. The work function of 1L-MoS_2/$CsPbBr_3$ is calculated to be ~4.20 eV.[31 30] This implies

that 1L-MoS_2 has a higher work function than the $CsPbBr_3$, which leads to the formation of a type-II heterojunction. Note that it is difficult to calculate the exact work function of $CsPbBr_3$ NCs, as it does not form a uniform film on Si/SiO_2. However, it is clear from the KPFM measurement that the work function of bare $CsPbBr_3$ NCs is lower than the pristine 1L-MoS_2. Thus, the decrease in work function in the heterostructure confirms rise in the Fermi level implying the increase in the electron density due to the suitable band bending that leads to the efficient transfer of electrons from perovskite NCs to MoS_2.

The PC response and sustainability of 1L-MoS_2/$CsPbBr_3$ heterojunction PD were measured at different applied biases in the range 0.1V to 7 V under the illumination of 405 nm pulsed laser, as shown in **Fig. 4.13(a)**. Note that the heterojunction PD can detect light even at very low applied bias, which is attributed to the suitable band alignment and built-in potential across the type-II heterojunction. At 5V, the PC on/off ratio is estimated to be ~223. Note that the PC on/off ratio for bare 1L-MoS_2 PD was observed to be 28. Thus, the PC was significantly higher in the hybrid PD as compared to that of pristine 1L-MoS_2 PD. To analyze the quantitative dependence of the PC on the incident light intensity, we measured the PC as a function of the light intensity. **Fig. 4.13(b)** shows the intensity-dependent PC for the heterojunction PD under 405 nm (pulsed) laser irradiation. It is clear that with increasing light intensity, the PC increased systematically. The photocurrent on/off ratio is estimated to about 342, which indicates good photoswitching behavior of the heterojunction device. The variation of photocurrent (I) with incident light intensity (P) is fitted by the power-law given by

$$I = AP^{\theta} \qquad (4.3)$$

where A is a constant for a given wavelength, and the exponent θ determines the response of the photocurrent-to-light intensity. From the fitting, θ is obtained as 0.23.[32] The sub-linear power dependence of PC is likely to be due to the presence of trap states at the interface of $CsPbBr_3$ and 1L-MoS_2, which can lead to recombination of photoexcited carriers, thus reducing the overall photocurrent.[4, 32] Note that residue of some ligands on the surface of the $CsPbBr_3$ NCs can trap electrons and holes, which lead to the saturation of the generated PC. Since the entire experiment is carried out in the ambient air, defects are created in the perovskite layer due to its high moisture sensitivity.

The current-voltage (I-V) characteristics of 1L-MoS_2/$CsPbBr_3$ heterojunction PD under dark and light (405 nm) conditions are shown in **Fig. 4.13(c)**. The typical linear and symmetrical plots

of dark current versus voltage of the PD indicate that the Au/1L-MoS_2/$CsPbBr_3$/Au form low resistance contacts with the gold electrodes.

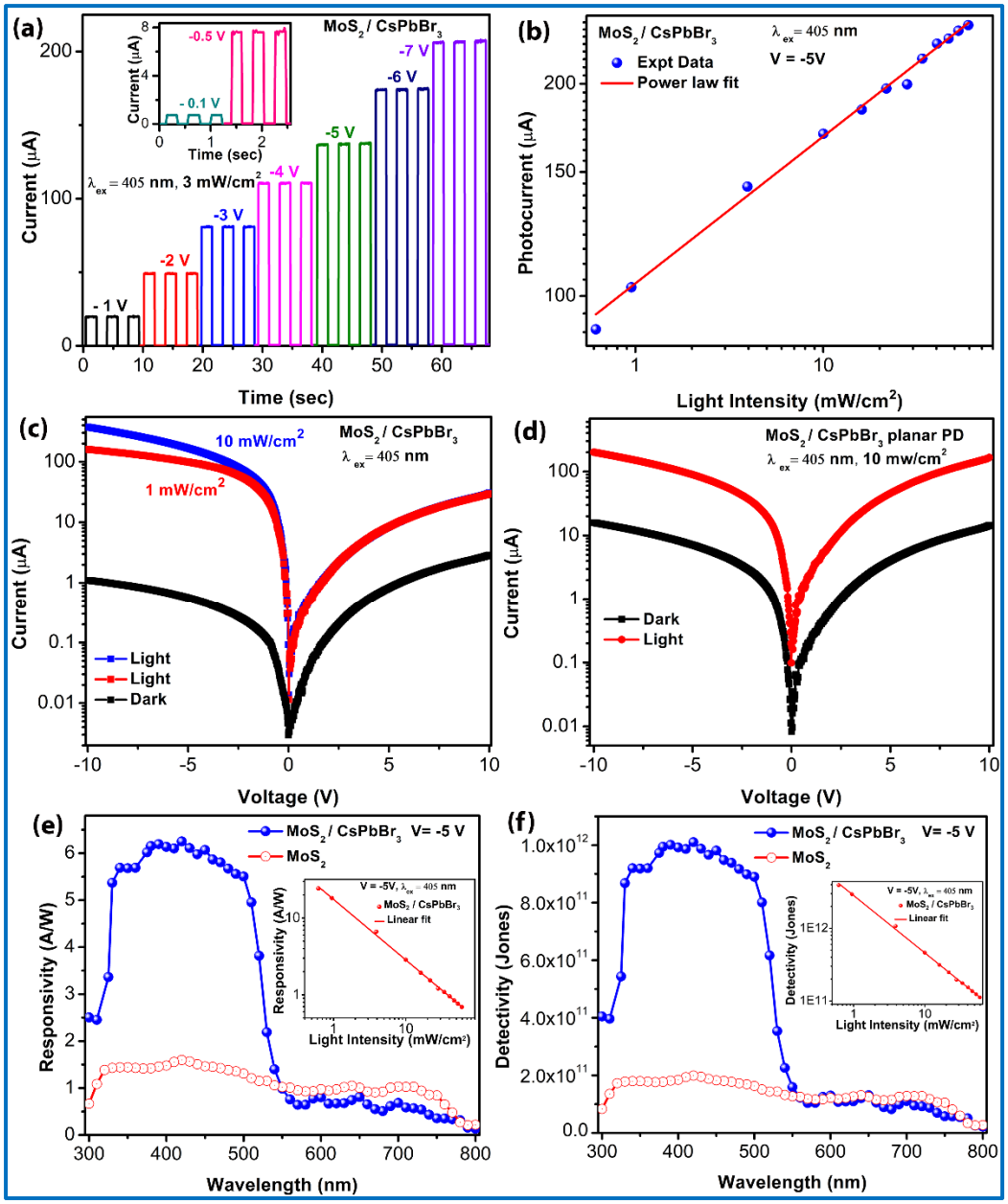

Fig. 4.13: (a) Transient response of the photocurrent in the vertical heterojunction photodetector at different applied biases under the illumination of 405 nm laser of intensity 3 mW/cm^2. (b) Photocurrent as a function of illumination intensity for the heterojunction PD and its fitting with the power law. (c) Dark and photo I-V characteristics of the vertical heterojunction PD of 405 nm light of different intensity. (d) Dark and photo I-V characteristics of the planar PD. (e) Comparison of the spectral responsivity of the heterojunction PD and pristine MoS_2 PD in the wavelength 300-800 nm at 5V. The inset shows the responsivity of the PD as a function of the incident light intensity. (f) Spectral detectivity of the heterojunction PD and pristine MoS_2 PD in the wavelength 300-800 nm at 5V. The inset shows the detectivity of the hybrid PD as a function of incident light intensity.

Interestingly, the I-V curve with light exhibits asymmetric diode like rectifying behavior, as shown in **Fig. 4.13(c)**, which is attributed to the type-II heterojunction at the 1L-MoS_2/$CsPbBr_3$ interface. Under the reverse bias, the suitable band bending at the heterojunction enables superior charge separation, which leads to a dramatic increase in the PC. This is further probed by I-V measurement at different intensities: 1 mW/cm^2 and 10 mW/cm^2. At 10 mW/cm^2, the PC in reverse bias is much higher than the PC at forward bias. Note that our heterojunction PD is of the vertical type junction, where the bottom 1L-MoS_2 and top $CsPbBr_3$ layers are connected with separate Au electrodes.
We observed the superior performance of the vertical heterojunction device as compared to the planar structured device, where both the electrodes were connected to the 1L-MoS_2 layer.[27] For comparison, a planar device structure was also tested. However, the planar device showed nearly symmetrical I-V characteristics under dark and light conditions, as shown in **Fig. 4.13(d)**, and the dark current of the planar PD device is much higher than the vertical type PD for the same composition.

The figures of merit, such as photoresponsivity (R_λ), detectivity (D*), and response speed were further measured to evaluate the performance of the heterojunction PD. **Fig. 4.13(e)** shows the comparison of spectral responsivity of the heterojunction PD and pristine 1L-MoS_2 PD at 5V bias in the wavelength range of 300-800 nm. The hybrid PD shows a very high responsivity in the wavelength region of 350-550 nm and a relatively lower responsivity in the longer wavelength region, as shown in **Fig. 4.13(e)**. This is consistent with the higher absorption of 1L-MoS_2/$CsPbBr_3$, as shown in **Fig. 4.11(b)**. The highest responsivity of 6.7 A/W was observed at a wavelength of 400 nm, as shown in **Fig. 4.13(e)**, whereas the responsivity for bare 1L-MoS_2 was found to be 1.47 A/W at 400 nm. This value of the responsivity is comparable/higher than the other 2D-based $CsPbBr_3$ PDs.[4]

Next, we measured the specific detectivity of the hybrid PD. The peak detectivity of the heterojunction PD is obtained to be 1.08×10^{12} Jones at 400 nm, while that of 1L-MoS_2 PD is 1.86×10^{11} Jones at 400 nm, as shown in **Fig. 4.13(f)**. Thus, the responsivity and detectivity of the heterojunction PD are significantly better than the bare 1L-MoS_2 based PD. Inset of **Fig. 4.13(e)** and **Fig. 4.13(f)** shows the responsivity and detectivity of heterojunction PD under different intensities of 405 nm excitation. The heterojunction PD shows a very high responsivity of 24.34 A/W at an incident intensity of 0.6 mW/cm^2. The R_λ and D* are observed to be decreased with the

increase in light intensity. The higher probability of scattering and recombination of photoexcited carriers under stronger illumination results in the decrease in R_λ and D* values.[30]

Furthermore, the response time of PD is an important parameter for the practical applications of the high-performance PD. The photoresponse speed of the heterojunction PD and bare 1L-MoS_2 are quantified, as shown in **Fig. 4.14(a-b)**. The experimental data of the rise and decay processes are fitted by a single exponential function given by

$$I(t) = I_0 + A\exp(-t/\tau) \qquad (4.4)$$

where I_0 and A are the constants, τ is the time constant. The PC growth and decay time constants of the 1L-MoS_2/$CsPbBr_3$ heterojunction PD were found to be 5.48 and 24.01 μs, respectively, as shown in **Fig. 4.14(a)**. However, for bare 1L-MoS_2 PC growth and decay time constants were found to be 68.15 and 403.19 μs, respectively (**Fig. 4.14(b)**).

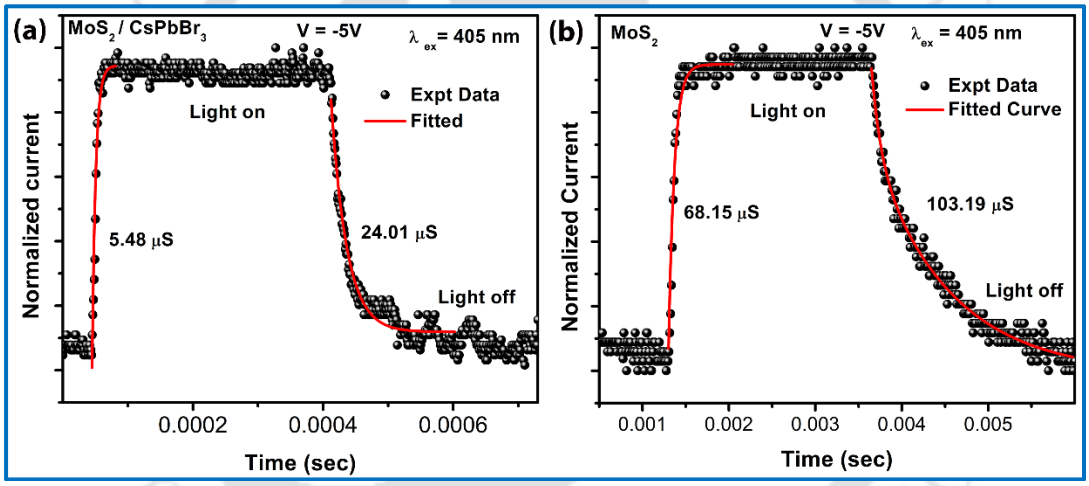

Fig. 4.14: (a) Temporal response of the growth and decay of PC (symbols) in the heterojunction PD with exponential fits (solid line). (b) Transient response of the PC in bare MoS_2 PD with the exponential fit for the growth and decay of PC.

Thus, the significant improvement in the response time, i.e., rise and fall time of the PC is attributed to the efficient charge separation at the 1L-MoS_2/$CsPbBr_3$ heterojunction. Note that in the case of most of the reported MoS_2 based PD, 1L-MoS_2 is usually wet transferred on to Si/SiO_2, which may result in the poor interface of the devices. However, in our case, the direct CVD grown 1L-MoS_2 on Si/SiO_2 gives a very fast photoresponse. Moreover, the PC response can be further improved by a suitable approach for trap passivation.

4.3.9. Electronic Structure Calculation and Charge Transfer Mechanism in 1L-MoS_2/$CsPbBr_3$ Heterojunction Photodetector

To have a profound understanding of the hidden electronic structure of the 1L-MoS_2/$CsPbBr_3$ hybrid system, we have determined the projected density of states (PDOS), which would reveal the orbital contribution of the consisting elements.

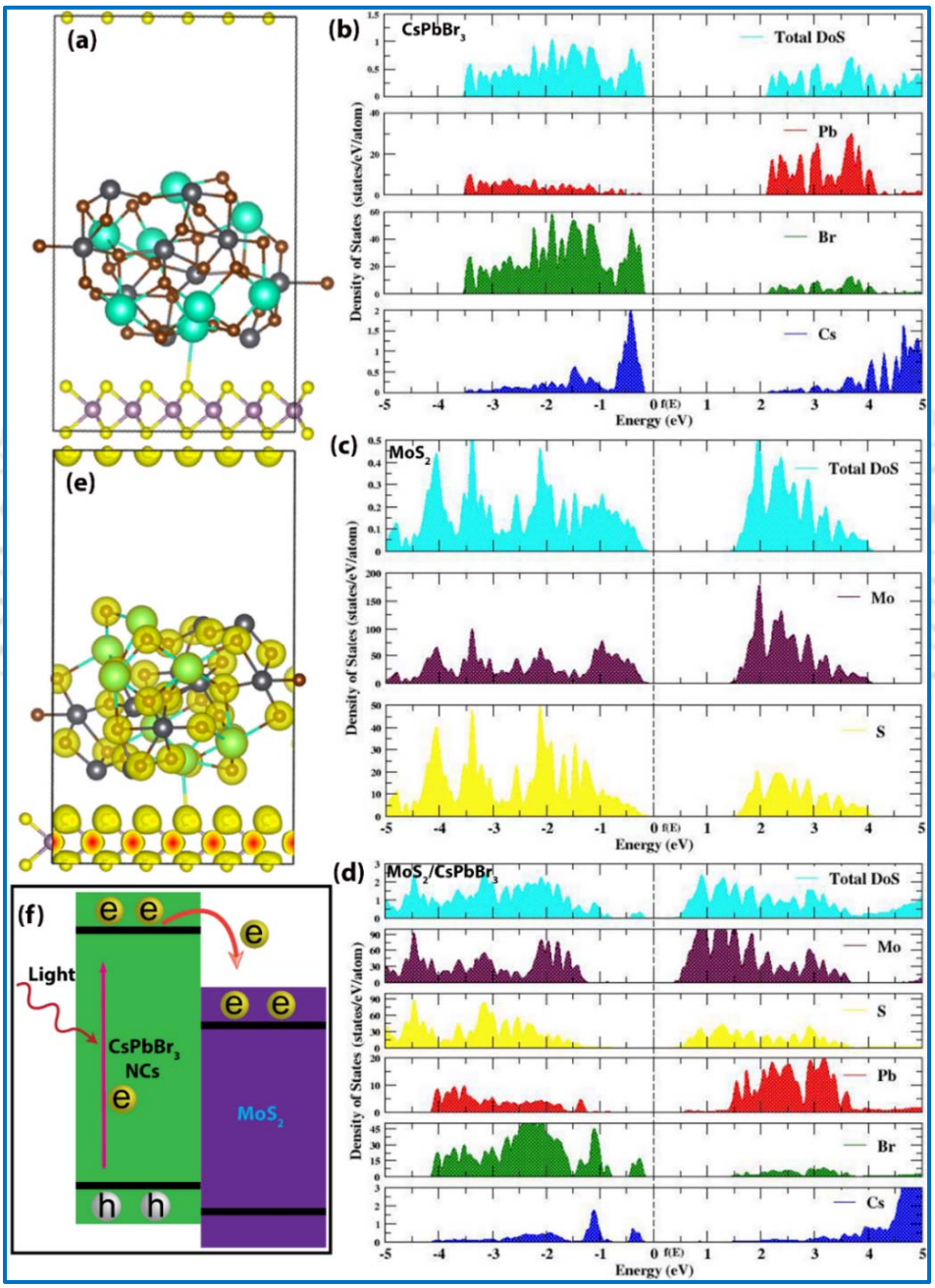

Fig. 4.15: (a) Minimum energy configuration of 1L-MoS_2/$CsPbBr_3$ hybrid. Projected density of states of (b) $CsPbBr_3$ NCs, (c) 1L-MoS_2 surface, (d) 1L-MoS_2/$CsPbBr_3$ hybrid; (e) Charge density distribution, and (f) schematic of energy band diagram and charge transfer in 1L-MoS_2/$CsPbBr_3$ heterojunction.

Fig. 4.15(a) shows the minimum energy configuration of the composite system, whereas **Fig. 4.15(b-d)** show the projected density of states of $CsPbBr_3$ NCs, MoS_2 surface, and $MoS_2/CsPbBr_3$ hybrid system. From the PDOS of $CsPbBr_3$ NCs, as depicted in **Fig. 4.15(b)**, we have observed two regimes of Pb-6p contribution in the valence band regime, one is around -3.5 eV, and another is around -8.0 eV. The contribution prevails in the range between 2 eV and 4 eV in the conduction band regime. The substantial contributions of Br-4p and Cs-6s are observed in the Fermi vicinity of the valence band, whereas Cs-6p prevails in the deeper valance states. **Fig. 4.15(c)** represents the PDOS of 1L-MoS_2, where one can observe the overlap between Mo-5s and S-3p orbital both in the valence band and conduction band regime, whereas in the valance band regime the overlap is substantial in the Fermi vicinity. The PDOS of the $MoS_2/CsPbBr_3$ hybrid system is depicted in **Fig. 4.15(d)**, where we can observe that the contribution of Mo-5s and S-3p is more in the conduction band regime as compared to the other elemental contribution in the Fermi vicinity. Their orbital contributions in the valence band regime mostly prevailed until -7.0 eV, whereas Pb-6p and Cs-6s contributions are seen in the deeper states of the valence band regime. From the total density of states of the hybrid system, it is observed that Br-4p and Cs-6s contribute more to the valence band regime as compared to the other elements near the Fermi level. There is another substantial overlap between Pb-6p and Cs-6s orbital in the deeper states of the valence band, which has been reflected in the total density of states as well. By comparing the PDOS of all the three systems in **Fig. 4.15(b-d)**, we can infer that substantial charge transfer occurs from $CsPbBr_3$ NCs to MoS_2 layer, which manifests in the additional density of states in the conduction band and some states in deeper energy levels of the valence bands, as evident from **Fig. 4.15(d)**. The PDOS also suggests a type-II heterojunction formation between MoS_2 and $CsPbBr_3$ NCs, which results in the superior performance of the heterojunction PD. This inference regarding charge transfer has been envisaged from the charge density calculations of the composite, as depicted in **Fig. 4.15(e)**. The charge density distribution of the composite reveals a substantial charge sharing and, therefore, delocalization between the surface S atoms with the Pb atoms. This synergistic effect of charge delocalization in the MoS_2 surface and $CsPbBr_3$ NCs has also been reflected in the total density of states of the composite system. This theoretical inference is in excellent agreement with the experimental signature of the charge transfer between MoS_2 and $CsPbBr_3$ system, which leads to the enhanced performance of the heterojunction PD. A schematic of the band diagram of $MoS_2/CsPbBr_3$ heterojunction and the photogenerated electron transfer from $CsPbBr_3$ to MoS_2 is

shown in **Fig. 4.15(f)**. Thus, the superior charge transfer results in the enhanced PC in the heterojunction PD.

4.4. Conclusions

In summary, a facile, room-temperature, nearly solvent-free, bulk scale solid-state synthesis process is reported here for highly stable and color-tunable $CsPbX_3$ NCs. A minute amount of surfactant-assisted milling process results in perovskite NCs, which exhibit incredibly high PL quantum yield and color-tunable PL emission over the entire visible region with excellent ambient stability up to several months. Post-growth annealing results in reduced nonradiative recombination centers and improved PL quantum yield (up to 95%) in the perovskite NCs. These highly luminescent perovskite NCs were utilized in color-tunable light-emitting devices by employing NCs composite films with PMMA on commercial UV LED chips with superior operational stability >100 hr. We further integrate the as-synthesized $CsPbBr_3$ NCs with direct CVD grown 1L-MoS_2 on Si/SiO_2 substrates and fabricate a vertical heterojunction PD by taking advantage of the high absorbance of perovskite NCs and fast carrier transport in 1L-MoS_2. Our 1L-MoS_2/$CsPbBr_3$ NCs heterojunction PD can operate at a very low applied bias (0.1V), while the photo responsivity of the device is obtained to be 24.34 A/W at 400 nm, which is about one order of magnitude higher than that of bare 1L-MoS_2. The transient response of the PC growth and decay is found to be 5.48 μs and 24.01 μs, respectively. The performance of the heterojunction PD is much superior to that of the pristine 1L-MoS_2 based PD. The enhanced performance of the heterojunction PD is attributed to the efficient transfer of photogenerated electrons from $CsPbBr_3$ NCs to 1L-MoS_2, which is probed by steady-state and time-resolved PL and Raman analyses. Direct evidence for charge transfer in the heterojunction is obtained from the Kelvin probe force microscopy that shows a type-II heterojunction formation and a suitable band bending at the 1L-MoS_2/$CsPbBr_3$ interface. These conclusions are supported by DFT calculations showing the distinct change in the density of states in the heterostructure, thus providing clear evidence for charge transfer from perovskite NCs to the MoS_2 layer. Thus, our work demonstrates a low-cost synthesis strategy for highly luminescent and color-tunable $CsPbX_3$ NCs and their application in bright LEDs and high-performance photodetection with 1L-MoS_2.

References

1. L. Protesescu, S. Yakunin, M. I. Bodnarchuk, F. Krieg, R. Caputo, C. H. Hendon, R. X. Yang, A. Walsh and M. V. Kovalenko, *Nano Lett.*, 2015, **15**, 3692-3696.

2. Y.-H. Suh, T. Kim, J. W. Choi, C.-L. Lee and J. Park, *ACS Appl. Nano Mater.*, 2018, **1**, 488-496.
3. C. Li, Z. Zang, W. Chen, Z. Hu, X. Tang, W. Hu, K. Sun, X. Liu and W. Chen, *Opt. Express*, 2016, **24**, 15071-15078.
4. X. Song, X. Liu, D. Yu, C. Huo, J. Ji, X. Li, S. Zhang, Y. Zou, G. Zhu, Y. Wang, M. Wu, A. Xie and H. Zeng, *ACS Appl. Mater. Interfaces*, 2018, **10**, 2801-2809.
5. D. Chen, G. Fang, X. Chen, L. Lei, J. Zhong, Q. Mao, S. Zhou and J. Li, *J. Mater. Chem. C*, 2018, **6**, 8990-8998.
6. G. Nedelcu, L. Protesescu, S. Yakunin, M. I. Bodnarchuk, M. J. Grotevent and M. V. Kovalenko, *Nano Lett.*, 2015, **15**, 5635-5640.
7. H. Liu, Z. Wu, H. Gao, J. Shao, H. Zou, D. Yao, Y. Liu, H. Zhang and B. Yang, *ACS Appl. Mater. Interfaces*, 2017, **9**, 42919-42927.
8. L. P. L. Mawlong, K. K. Paul and P. K. Giri, *J. Phys. Chem. C*, 2018, **122**, 15017-15025.
9. B. Chakraborty, A. Bera, D. V. S. Muthu, S. Bhowmick, U. V. Waghmare and A. K. Sood, *Phys. Rev. B*, 2012, **85**, 161403.
10. Q. Xu, Z. Yang, D. Peng, J. Xi, P. Lin, Y. Cheng, K. Liu and C. Pan, *Nano Energy*, 2019, **65**, 104001.
11. Z.-Y. Peng, J.-L. Xu, J.-Y. Zhang, X. Gao and S.-D. Wang, *Adv. Mater. Interfaces*, 2018, **5**, 1800505.
12. L. Zhang, S. Shen, M. Li, L. Li, J. Zhang, L. Fan, F. Cheng, C. Li, M. Zhu, Z. Kang, J. Su, T. Zhai and Y. Gao, *Adv. Opt. Mater.*, 2019, **7**, 1801744.
13. E. Shi, Y. Gao, B. P. Finkenauer, Akriti, A. H. Coffey and L. Dou, *Chem. Soc. Rev.*, 2018, **47**, 6046-6072.
14. R. Lin, X. Li, W. Zheng and F. Huang, *ACS Appl. Nano Mater.*, 2019, **2**, 2599-2605.
15. G. Kaupp, *CrystEngComm*, 2003, **5**, 117-133.
16. D. Chen and X. Chen, *J. Mater. Chem. C*, 2019, **7**, 1413-1446.
17. Y. Cai, L. Wang, T. Zhou, P. Zheng, Y. Li and R.-J. Xie, *Nanoscale*, 2018, **10**, 21441-21450.
18. S.-T. Ha, R. Su, J. Xing, Q. Zhang and Q. Xiong, *Chem. Sci.*, 2017, **8**, 2522-2536.
19. Y. V. Morozov, S. Zhang, M. C. Brennan, B. Janko and M. Kuno, *ACS Energy Lett.*, 2017, **2**, 2514-2515.
20. J. Hai, H. Li, Y. Zhao, F. Chen, Y. Peng and B. Wang, *ChemComm* 2017, **53**, 5400-5403.
21. Y. Zu, J. Dai, L. Li, F. Yuan, X. Chen, Z. Feng, K. Li, X. Song, F. Yun, Y. Yu, B. Jiao, H. Dong, X. Hou, M. Ju and Z. Wu, *J. Mater. Chem. A*, 2019, **7**, 26116-26122.
22. F. Zhang, S. Huang, P. Wang, X. Chen, S. Zhao, Y. Dong and H. Zhong, *Chem. Mater*, 2017, **29**, 3793-3799.
23. J. Ghosh, R. Ghosh and P. K. Giri, *ACS Appl. Mater. Interfaces*, 2019, **11**, 14917-14931.
24. S. Yuan, Z.-K. Wang, M.-P. Zhuo, Q.-S. Tian, Y. Jin and L.-S. Liao, *ACS Nano*, 2018, **12**, 9541-9548.
25. A. Shinde, R. Gahlaut and S. Mahamuni, *J. Phys. Chem. C*, 2017, **121**, 14872-14878.
26. X. Lao, X. Li, H. Ågren and G. Chen, *Nanomaterials (Basel)*, 2019, **9**, 172.
27. F. Bai, J. Qi, F. Li, Y. Fang, W. Han, H. Wu and Y. Zhang, *Adv. Mater. Interfaces*, 2018, **5**, 1701275.
28. K. K. Paul, L. P. L. Mawlong and P. K. Giri, *ACS Appl. Mater. Interfaces*, 2018, **10**, 42812-42825.
29. T. Noh, H. S. Shin, C. Seo, J. Y. Kim, J. Youn, J. Kim, K.-S. Lee and J. Joo, *Nano Res.*, 2019, **12**, 405-412.
30. H. Wu, H. Si, Z. Zhang, Z. Kang, P. Wu, L. Zhou, S. Zhang, Z. Zhang, Q. Liao and Y. Zhang, *Adv. Sci.*, 2018, **5**, 1801219.
31. M. Moun, M. Kumar, M. Garg, R. Pathak and R. Singh, *Sci Rep*, 2018, **8**, 11799-11799.
32. C.-Y. Huang, C. Chang, G.-Z. Lu, W.-C. Huang, C.-S. Huang, M.-L. Chen, T.-N. Lin, J.-L. Shen and T.-Y. Lin, *Appl. Phys. Lett.*, 2018, **112**, 233106.

Chapter 5

Origin and Tunability of Dual Color Emission in Highly Stable Solid-State Synthesized Mn Doped $CsPbCl_3$ Nanocrystals and its Application in White LED

In this chapter, we demonstrate a facile, nearly solvent-free, bulk scale room temperature solid-state synthesis of highly stable and luminescent Mn-doped $CsPbCl_3$ NCs with high Mn substitution. We investigate the origin and tunability of its dual-color emission from Mn-doped $CsPbCl_3$ NCs. The Mn-doped $CsPbCl_3$ NCs exhibit distinct excitonic PL in the UV region and Mn related PL in the orange-red region with high PL QY (up to 35%). These excitonic PL and Mn related PL emissions can be tunable by doping concentration, excitation intensity, and measurement temperature. Remarkably, the Mn-doped $CsPbCl_3$ NCs synthesized by our method exhibit high storage stability due to the high Mn doping efficiencies achieved by strain-induced enhanced doping. Finally, white light-emitting diodes (WLEDs) were fabricated by employing blue-emitting $CsPbCl_{1.5}Br_{1.5}$ NCs, green-emitting $CsPbBr_3$ NCs, and orange-red emitting 10% Mn-doped $CsPbCl_3$ NCs all grown by the same method. Our work demonstrates a low-cost synthesis strategy of high Mn doping in $CsPbCl_3$ NCs with superior ambient stability and highly tunable emission.

5.1. Introduction

The major challenges of perovskite materials are poor stability and device performance in the presence of oxygen and water molecules, and the toxicity of lead. Lead-free perovskite QDs and NCs are also reported, though the lead-free materials exhibit low PL QY and poor stability as compared to the lead-based NCs and QDs.[1] On the other hand, the partial substitution of Pb^{2+} in lead-based perovskite by other impurity ions, such as Mn, and other main group metal cations, transition metal cations, and rare earth metal cations are also explored to improve the optoelectronic properties of the perovskite NCs. In particular, Mn doping of all inorganic $CsPbCl_3$ NCs/QDs has received much attention in order to reduce toxic Pb content and improve the PL QY. Parobek et al. first reported the doping of Mn^{2+} ions in $CsPbCl_3$ NCs by a high-temperature hot injection method.[2] Since the bond dissociation energy of Pb-Cl and Mn-Cl bonds are nearly similar, this permits the partial substitution of Pb in $CsPbCl_3$ NCs with Mn without much distortion

in the crystal lattice structure.[3] These Mn-doped $CsPbCl_3$ NCs show dual-color emission. The sharp PL peak in the UV region is due to the band edge excitonic recombination of the host $CsPbCl_3$ NCs, while the orange-red PL is attributed to the energy transfer from excited states of $CsPbCl_3$ to Mn^{2+} followed by radiative recombination from $^4T_1$ state to $^6A_1$ state of Mn.[3-6] Interestingly, the Mn doping in $CsPbCl_3$ effectively improve the structural stability and optical properties of perovskite, besides the partial substitution of toxic Pb.[4]

In **chapter 4,** we have described the solid-state synthesis of color and composition tunable all-inorganic perovskite NCs. In this chapter, we have investigated the origin and tunability of dual-color emission of solid-state synthesized highly luminescent Mn-doped $CsPbCl_3$ NCs with high Mn substitution. Low-temperature PL and excitation intensity-dependent PL study reveals important insights into the origin of Mn related orange-red PL in the dual color emitting Mn-doped $CsPbCl_3$ NCs. Further, it is demonstrated that Mn-doped $CsPbCl_3$ NCs synthesized by the physical milling method exhibit superior stability due to the high Mn doping efficiencies achieved through the nonequilibrium synthesis conditions. Furthermore, white LED devices were constructed by employing blue-emitting $CsPbCl_{1.5}Br_{1.5}$ NCs, green-emitting $CsPbBr_3$ NCs, and orange-red emitting 10% Mn-doped $CsPbCl_3$ NCs composite films with PMMA. Implications of these results for a low-cost synthesis strategy for Mn-doped $CsPbCl_3$ NCs with superior ambient stability for WLED are discussed.

5.2. Experimental Details

5.2.1. Sample Preparation and Device Fabrication

5.2.1.1. Solid-State Synthesis of Undoped and Mn-doped $CsPbCl_3$ NCs

Undoped $CsPbCl_3$ NCs were synthesized by the two-step surfactant-assisted ball milling method, as discussed in **chapter 4 (**section **4.2.1.1)**. For the growth of Mn-doped $CsPbCl_3$ NCs, different amount of $PbCl_2$ was replaced by $MnCl_2$ depending upon the desired Mn doping concentration. Typically, 0.5 mM CsCl, x mM $MnCl_2$ and (0.5-x) mM $PbCl_2$ were mixed and milled at 500 rpm for 2 h. For example, for 10% Mn-doped $CsPbCl_3$ NCs, 0.5 mM CsCl, 0.45 mM $PbCl_2$ and 0.05 mM $MnCl_2$ were used. For the synthesis of Mn-doped $CsPbCl_3$ NCs, we followed the same milling conditions as used for the synthesis of $CsPbCl_3$ NCs. For optimizing the milling time dependence of doping, we varied the duration of ball milling from 0.5 hr to 4 hrs. Interestingly, the Mn related PL intensity increases with the duration of milling up to 2 hrs. No further increase of Mn related PL has observed for samples milled up to 4 hrs. Thus, 2hrs of milling was chosen as the optimum

for substitution of Pb by Mn ions. The undoped (0%) and different Mn-doped (X %) NCs are named as Mn0 and MnX, respectively. We further synthesized $CsPbBr_3$ and $CsPbCl_{1.5}Br_{1.5}$ NCs, which were used as green and blue-emitting materials, respectively, for a WLED.

5.2.1.2. Preparation of the NCs-PMMA film and fabrication of WLED

PMMA powders (0.5 g) were mixed with 2 ml of different NCs ($CsPbCl_{1.5}Br_{1.5}$, $CsPbBr_3$ and 10 % Mn-doped $CsPbCl_3$ NCs) dispersed in toluene. After complete dissolution of PMMA particles by ultrasonication, each of the solutions was drop cast on cleaned transparent quartz substrates and dried by vacuum heating (50 °C) to obtain the NCs-PMMA solid films. The light emissions from the films were measured by placing the film on a commercial UV LED chip of emission wavelength 396 nm. For the construction of WLED, first $CsPbCl_{1.5}Br_{1.5}$ NCs/PMMA solution was drop cast on a cleaned quartz substrate and then dried. Next $CsPbCl_{1.5}Br_{1.5}$ NCs/PMMA and 10% Mn-doped $CsPbCl_3$ NCs/PMMA solutions were drop casted sequentially on top of the film. Finally, the perovskite film on quartz is placed carefully on a UV LED chip, which gives bright white light emission.

5.2.2. Characterization Techniques

The details of the characterization techniques (FETEM, EDX, XRD, UV-vis absorbance, PL, PL QY, TRPL, etc.) used to study the systems were described in **Chapter 2, Section 2.2.2**. The details of XPS and temperature-dependent (80-350 K) PL measurements were described in **Chapter 4, Section 4.2.2**.

5.3. Results and Discussion

5.3.1. Synthesis Strategy and Doping of NCs by Physical Milling

We have optimized a two-step low-surfactant assisted facile physical milling method for the synthesis of Mn-doped $CsPbCl_3$ NCs. **Fig. 5.1** illustrates a schematic of the synthesis steps of dual-color emitting highly luminescent Mn-doped $CsPbCl_3$ NCs by the facile physical milling method. The most explored synthesis process for undoped and Mn-doped $CsPbCl_3$ perovskite NCs/QDs is the hot injection method, where the escape of Mn ions form $CsPbCl_3$ NCs results in poor storage stability.[3, 7] In our case, we have explored a two-step solid-state method for the growth of undoped and Mn-doped $CsPbCl_3$ perovskite NCs. For the Mn-doped perovskite NCs, high Mn doping efficiencies were achieved through the pressure-mediated synthesis conditions in physical milling, resulting in enhanced PL emission related to Mn doping. It is well known that the ball milling

process produces strain in the synthesized NCs. This strain may result in lowering the dopant energy and effective substitution of Pb by Mn with high Mn doping efficiency.[8]

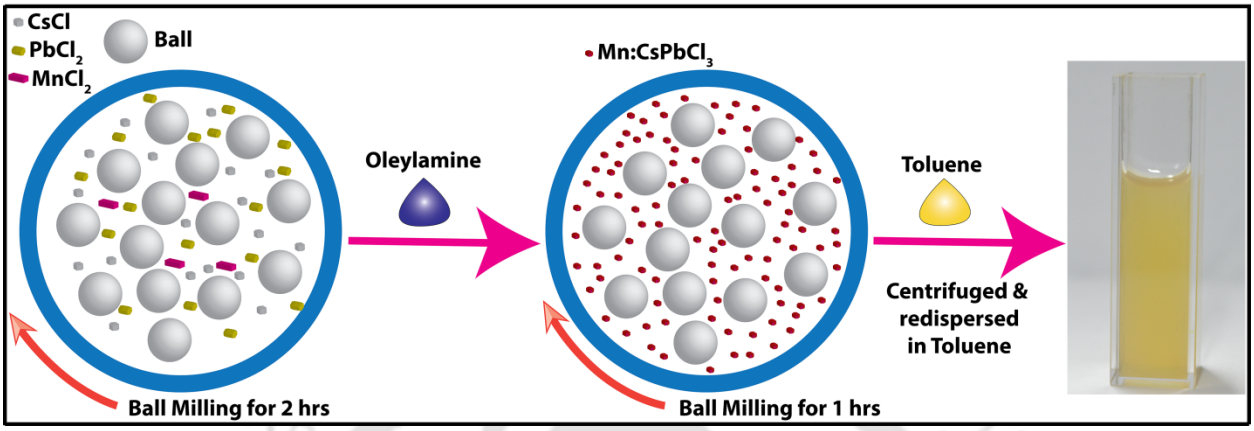

Fig. 5.1: Schematic illustration of the synthesis steps of Mn-doped $CsPbCl_3$ NCs by the physical milling process.

5.3.2. Morphology and Structural Analyses

5.3.2.1. FETEM Analysis

Fig. 5.2(a-d) shows the FETEM images of as-grown Mn0, Mn3, Mn5, and Mn10 samples, respectively. All the images show the cubic shaped structure of $CsPbCl_3$ NCs. Note that the bare $CsPbCl_3$ NCs are perfectly cubic shaped as shown in **Fig. 5.2(a)**, while with increasing Mn doping concentration the NCs shape is partly distorted.[3] This may be due to some structural deformation with high Mn substitution. The inset in each figure shows the digital photographs depicting the emission colors of the corresponding samples under the illumination of 395 nm UV light. **Fig. 5.2(e-h)** depicts the size distributions of NCs for different samples with corresponding Gaussian fitting. From the size distributions analysis, the average sizes of the NCs were found to be 13.7, 12.4, 9.1, and 8.7 nm for Mn0, Mn3, Mn5, and Mn10, respectively. Interestingly, with the increase in Mn doping concentration, the average size of the NCs is decreased systematically.[4, 9] This may be due to the partial substitution of Pb^{2+} ions (r = 0.133 nm) by Mn^{2+} ions with smaller ionic radius (r = 0.097 nm). This decrease in NCs size with the increase in Mn doping concentration causes the blue shift of band edge excitonic PL peak positions and absorption edges (discussed later). **Fig. 5.2(i-l)** shows the HRTEM lattice fringes of single NC of Mn0, Mn3, Mn5, and Mn10, respectively. The lattice spacing were found to be 0.41 nm, 0.40 nm, 0.40 nm and 0.39 nm for 0%, 3%, 5% and 10 % Mn-doped $CsPbCl_3$ NCs, respectively, which correspond to the (110) lattice plane of $CsPbCl_3$. It is clear that with the increase in Mn doping concentration, the lattice spacing

decreased. Thus, the gradual decrease in lattice spacing due to Mn doping corresponds to the substitution of bigger Pb atom by the smaller size Mn atom. These results are consistent with the XRD analysis (discussed later). The inset of **Fig. 5.2(i)** represents the corresponding FFT pattern of undoped $CsPbCl_3$ NC, which confirms the good crystalline quality of the NC.

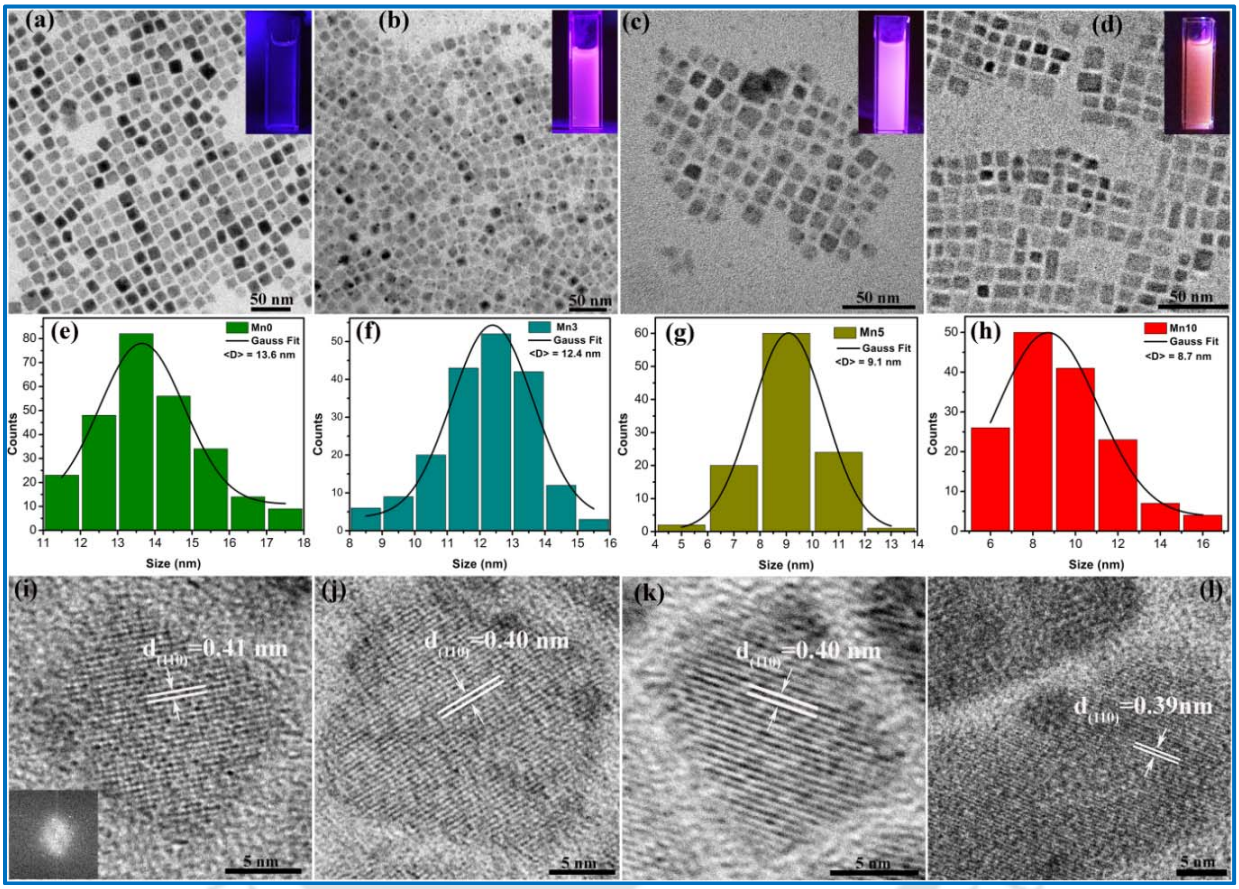

Fig. 5.2: FETEM images of $CsPbCl_3$ NCs (a) undoped (b) 3% Mn-doped, (c) 5% Mn-doped, (d) 10 % Mn-doped. Inset in each case shows the digital photograph depicting the emission colors of the corresponding samples under UV light irradiation. (e, f, g, h) Particle size distributions of undoped, 3%, 5% and 10% Mn-doped $CsPbCl_3$ NCs, respectively. The solid curve in each case shows the corresponding Gaussian fitting, and <D> indicates the average size of the NCs. (i, j, k, l) The corresponding HRTEM lattice images of undoped, 3%, 5% and 10% Mn-doped $CsPbCl_3$ NCs, respectively. Inset of (i) shows the FFT pattern of $CsPbCl_3$ confirming its high crystalline quality.

5.3.2.2. XRD Analysis

The crystalline quality and phase of undoped and Mn-doped $CsPbCl_3$ NCs were studied by XRD analysis. **Fig. 5.3** shows the comparison of XRD patterns of samples Mn0, Mn1, Mn3, Mn5, Mn10, and Mn20, respectively. The XRD pattern of undoped $CsPbCl_3$ NCs confirms the desired cubic phase.[4, 9] The XRD patterns of Mn-doped $CsPbCl_3$ NCs indicate that they retain the structures of the parent cubic $CsPbCl_3$ NCs. Note that no impurity peak of raw reactants was observed in the

XRD data profiles as shown in **Fig. 5.3(a)** confirming the proper reaction and full conversion of reactants in physical milling. **Fig. 5.3(b)** shows the magnified view of the XRD peak corresponding to the (110) plane. Interestingly, with the increase in Mn doping concentration, the (110) peak is systematically shifted to higher angles (2θ) with respect to that of undoped cubic $CsPbCl_3$ NCs. For 20% Mn-doped NCs, the shift in 2θ is found to be ~0.17°. The systematic shift of the (110) peak toward higher angle is attributed to Mn incorporation in crystal and progressive lattice contraction due to the substitution of larger Pb^{2+} ions by the isovalent, yet smaller size, Mn^{2+} ions.

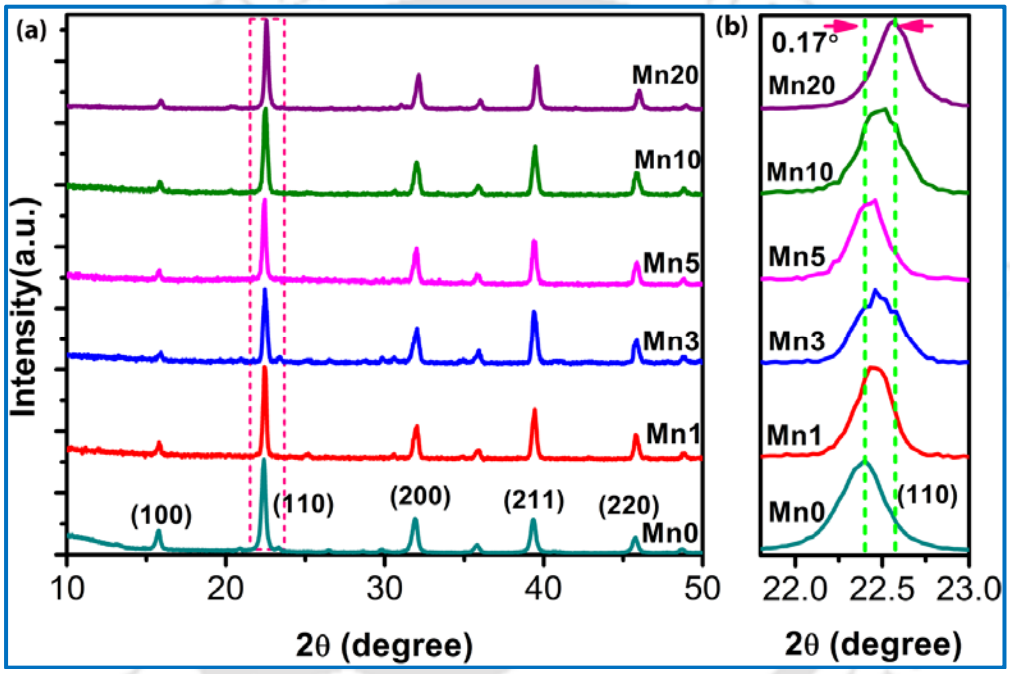

Fig. 5.3: (a) Comparison of the XRD patterns of samples Mn0, Mn1, Mn3, Mn5, Mn10, and Mn20. (b) A magnified view of the (110) peak of different samples, which shows a systematic shift in peak position with doping concentration.

Note that a systematic decrease in lattice spacing with increasing doping concentration was also observed from HRTEM analysis. Thus, the result of XRD is fully consistent with the HRTEM analysis. We further calculated the compressive strain produced in the crystal structure of the doped NCs due to the Mn substitution from the shift of the XRD (110) peak, and the results are shown in **Table 5.1**. For 20% Mn doping, the compressive strain is found to be 0.75%. Note that due to the high-pressure mechanical milling, it naturally produces lattice strain in the crystal structure, and it enhances the doping efficiency.[8] Zhu et al. showed that with 1% compressive strain (i) doping energy of Be in GaP is reduced by 0.2 eV, and (ii) solubility of Be in GaP could

be increased by 3 orders of magnitude at room temperature. [8]. In the present work, we achieved ~40% Mn doping in $CsPbCl_3$ NCs, which is significantly higher than those reported in the literature. Thus, the lattice strain is believed to enable higher doping density in our solid-state synthesis process.

Table 5.1: *Details of the lattice spacing and strain calculated from the XRD pattern due to Mn doping in $CsPbCl_3$ nanocrystals.*

Sample code	XRD (110) peak position (2θ in degrees)	Lattice spacing (d_{110}) in Å	Compressive strain ($\varepsilon=\frac{\Delta d}{d}\times 100\%$)
Mn0	22.40	3.966	0
Mn1	22.43	3.960	0.132
Mn3	22.46	3.955	0.264
Mn5	22.43	3.960	0.132
Mn10	22.52	3.945	0.529
Mn20	22.57	3.936	0.750

5.3.2.3. XPS Analysis

To investigate the chemical state, elemental composition, and doping, XPS analysis was performed on the undoped and 5% Mn-doped $CsPbCl_3$ NCs. **Fig. 5.4(a)** represents the survey scan XPS spectrum in the binding energy range 0-800 eV for Mn5. As shown in **Fig. 5.4(a)**, the signals of Cs, Pb, Cl, Mn, C, and O are clearly observed.[10, 11] Carbon and oxygen peaks with very low intensity were observed mainly due to the contamination/adsorption from the ambient air. **Fig. 5.4(b)** depicts the Mn 2p core-level XPS spectrum of Mn5 with the corresponding fitting. The peak with center at~ 644.6 eV confirms the Mn^{2+} state in the doped NCs.[11] Thus, the XPS spectrum endorses the proper substitution of Pb ions by Mn ions in the Mn-doped $CsPbCl_3$ NCs. **Fig. 5.4(c)** shows the comparison of XPS peaks related to Cs in Mn0 and Mn5 with corresponding peak fittings. The peaks at 723.8 eV and 737.8 eV in undoped NCs correspond to Cs $3d_{5/2}$ and $3d_{3/2}$, respectively, whereas for 5% Mn-doped NCs, Cs $3d_{5/2}$ and $3d_{3/2}$ peaks were observed with binding energies of 724.0 eV and 738.0 eV, respectively.[11] **Fig. 5.4(d)** shows the comparison of XPS peaks related to Pb in Mn0 and Mn5 with corresponding peak fittings. For Mn0, the peaks at ~138.0 eV and 143.0 eV represent Pb $4f_{7/2}$ and $4f_{5/2}$, respectively, while for Mn5 the peaks were observed at ~138.2 eV and 143.1 eV.[11] The broad Cl 2p peak is fitted with two peaks ($2p_{3/2}$, $2p_{1/2}$) with binding energies of 197.4 eV, 199.0 eV for Mn0, and 197.6 eV, 199.2 eV for Mn5, as shown in **Fig. 5.4(e)**. These two closely spaced peaks of Cl may be attributed to the inner and surface Cl ions in the NCs.

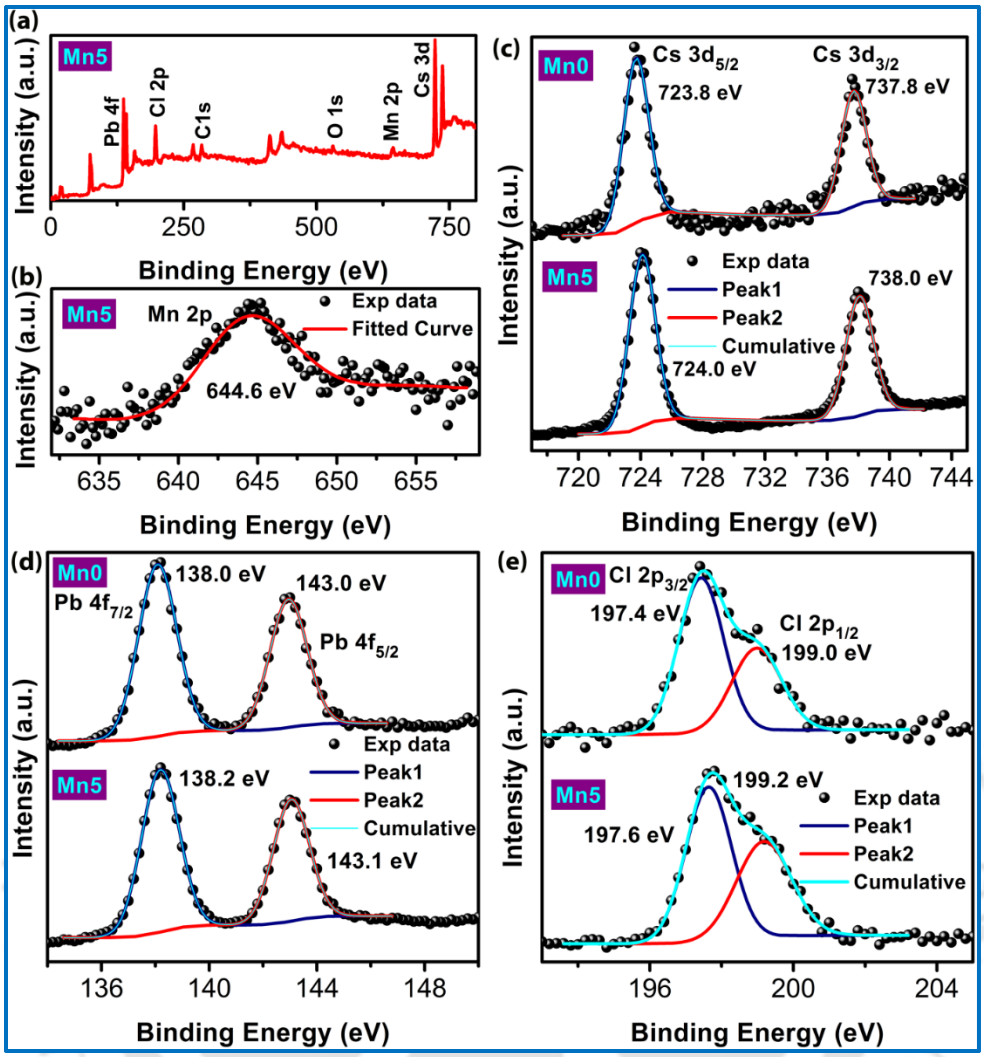

Fig. 5.4: (a) XPS survey scan spectrum in the binding energy range 0-800 eV of sample Mn5. (b) Mn 2p core-level spectrum of Mn5 with corresponding Gaussian fitting. (c) Comparison of Cs 3d core-level XPS spectra of Mn0 and Mn5 with Gaussian fittings. (d) Comparison of Pb 4f core-level XPS spectra of Mn0 and Mn5 with Gaussian fittings. (e) Comparison of Cl 2p core-level XPS spectra of Mn0 and Mn5 with fittings.

5.3.3. Absorbance Study

To investigate the effect of Mn doping on the optical bandgap of $CsPbCl_3$ NCs, the absorption measurement was performed. Interestingly, with the increase in Mn doping concentration, the absorption edges of the doped samples are gradually blue shifted, as shown in **Fig. 5.5**. The blue shift may be attributed to the quantum confinement of carriers due to the decrease in NCs size with high Mn substitution. However, since the NC sizes are much higher than the quantum confinement region (<5 nm), quantum confinement effect is unlikely to play any role in the observed blue shift. The excitonic PL emission is also blue-shifted due to Mn doping (discussed later). The lattice contraction of the $PbCl_6$ octahedral unit and consequent enhancement of the interaction between

Pb and Cl may affect the blue shift of the absorption edge.[4] It has been reported that lattice distortion in perovskite NCs causes change in the bandgap, which is quite likely in the present case due to the presence of lattice strain.[12]

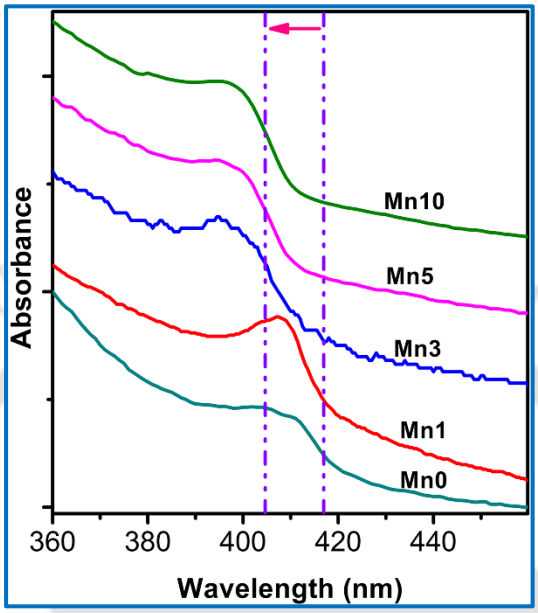

Fig. 5.5: Comparison of absorbance spectra of Mn0, Mn1, Mn3, Mn5, and Mn10 showing a systematic blue shift in the absorption edge with increasing doping concentration.

5.3.4. Photoluminescence Study

The light-emitting property of undoped and Mn-doped $CsPbCl_3$ NCs was investigated by the PL measurements. **Fig. 5.6(a)** shows the PL spectra of undoped and Mn-doped $CsPbCl_3$ NCs with different Mn concentrations under 360 nm excitation. The PL peak at ~416 nm with narrow FWHM for undoped $CsPbCl_3$ NCs corresponds to the band-to-band/ excitonic recombination of photogenerated carriers. The Mn-doped $CsPbCl_3$ samples show dual-color emission with a broad emission in the orange-red region with a PL peak at ~ 590 nm, besides the excitonic emission in the UV region. The emission in the region ~460-720 nm is attributed to Mn related emission. This orange-red emission originates from the energy transfer of photoexcited excitons from the excited states of the $CsPbCl_3$ host to the doped Mn^{2+} states facilitating recombination of excitons via a radiative pathway in the states of Mn.[2, 3] Thus, the PL spectra of Mn-doped $CsPbCl_3$ NCs further confirm the successful incorporation of Mn^{2+} ions into $CsPbCl_3$ NCs. The XRD and XPS analysis also confirm the substitution of Pb^{2+} ions by Mn^{2+} ions. In this work, we demonstrate the $CsPb_xMn_{1-x}Cl_3$ perovskite NCs with a Mn substitution ratio up to 40 % by physical milling, which is comparable/higher than the reported doping concentration of Mn in $CsPbCl_3$.[4, 13] As shown in

Fig. 5.6(a), with the increase in Mn doping content from 0% to 30%, the relative intensity of the Mn related emission is increased systematically with respect to the intensity of the excitonic PL emission. This is due to the higher transfer of photogenerated excitons to the Mn^{2+} state in the samples with a higher content of Mn substitution. The change in the ratio of Mn PL to excitonic PL peak intensity with Mn doping content is shown in **Fig. 5.6(b)**, which shows nearly a linear increase in PL intensity with doping concentration. Note that the actual Mn content in the NCs may be lower than the actual amount used for the synthesis. EDX spectra reveal the Mn concentration as 2.7%, 8.6% and 13.4% for corresponding Mn doping of 3%, 10% and 20%, respectively. On the other hand, XPS analysis revealed higher content of Mn in each sample due to its high concentration expected near the surface of the NCs, as XPS probes only ~10 nm depth from the surface. Note that beyond 20% doping, the overall PL QY is reduced, which may due to the nonradiative defects and deformation of the crystal structure in the NCs.

The PL emission spectrum of each sample shows dual emission peaks centered at ~406 and ~590 nm, respectively. The band-edge emission peak is narrow with the full width at half-maximum (FWHM) of ~11-16 nm, and it is assigned to the excitonic emission of the $CsPbCl_3$ host, whereas the 590 nm peak is broad with the FWHM of ~75-120 nm, which is due to the doped Mn^{2+} ions in $CsPbCl_3$ NCs. The orange-red PL band with a larger FWHM and homogenous broadening originates due to the existence of a continuous set of vibrational sublevels in each electronic sates related to Mn^{2+}.[3] The systematic increase in FWHM of Mn related PL peak with the increase in Mn doping concentration is shown in the inset of **Fig. 5.6(b),** which further supports our assertion on the origin of broad Mn-related PL emission. Interestingly, with the increase in Mn doping concentration from 0% to 20%, the band edge excitonic peaks are blue-shifted from 416 nm to 402 nm (see **Fig. 5.6(a))**. This is consistent with the blue shift of the absorption spectra. Since the NCs sizes are much higher than the excitonic Bohr radius, the quantum confinement effect is unlikely to play any role in the blue shift of the PL peak. The blue shift of the excitonic PL and band edge may be due to the contraction of the $PbCl_6$ octahedral unit, and consequent enhancement of the interaction between Pb and Cl.[4] However, excess Mn substitution (> 20 %) may distort the lattice heavily and eventually destroy the crystallinity with increasing structural defects in the host $CsPbCl_3$.

The absolute PL QY was measured to be 11%, 19%, 24%, 32%, 36%, 26% for samples Mn0, Mn1, Mn3, Mn5, Mn10 and Mn20, respectively. Note that with doping of a small amount of Mn

(1%), the overall PL QY was increased from 11% to 19%. The low PL QY (11%) of the undoped sample is attributed to the mid-bandgap trap states, which facilitate nonradiative recombination in wide bandgap $CsPbCl_3$ NCs.[4]

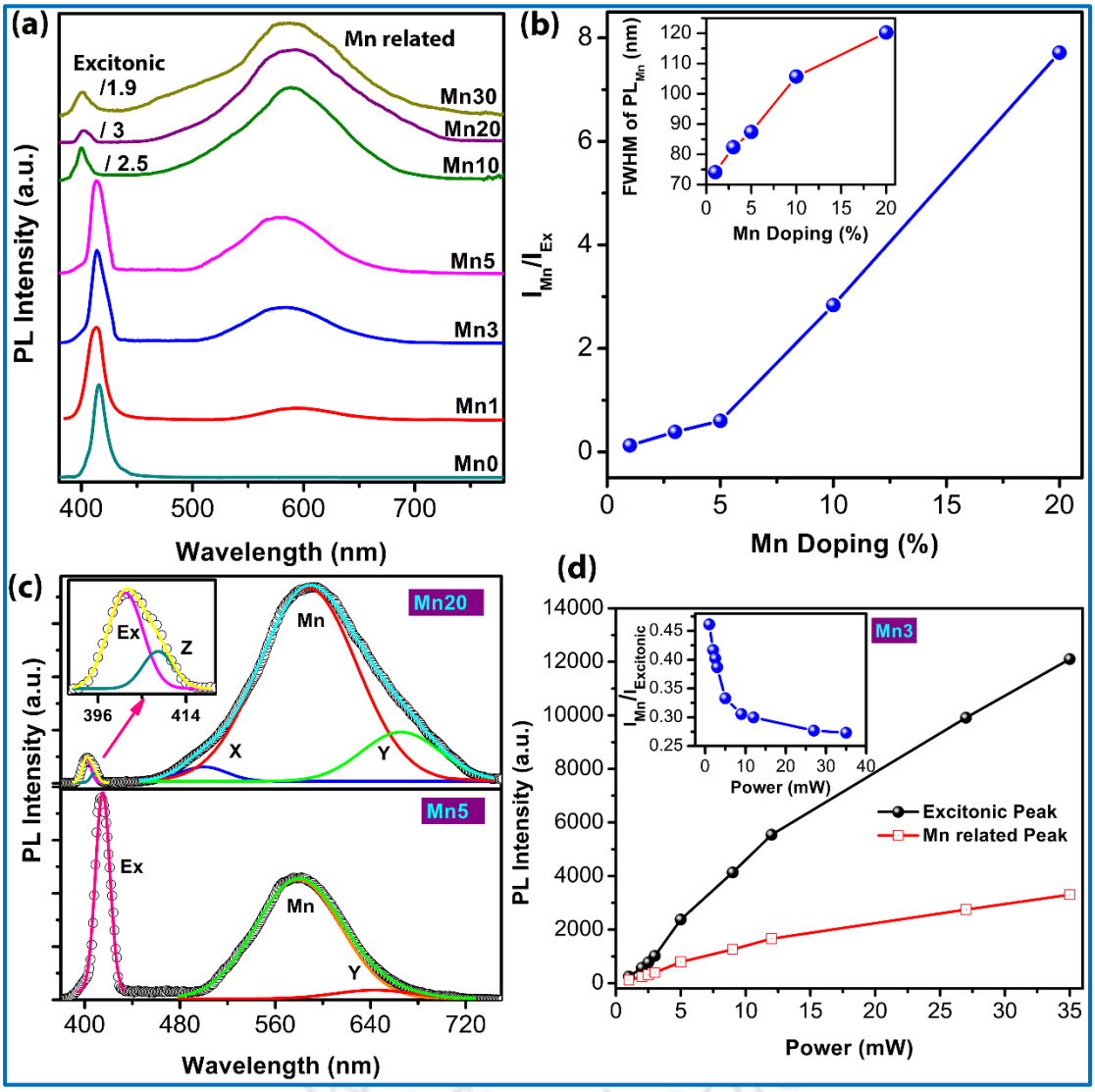

Fig. 5.6: (a) Comparison of PL spectra of undoped and Mn-doped (1-30%) $CsPbCl_3$ perovskite NCs. The plots for Mn10, Mn20, and Mn30 are scaled-down by appropriate factors to enable comparison. (b) Change in the ratio of PL intensity of Mn related peak (I_{Mn}) to that of the excitonic peak ($I_{Excitonic}$) as a function of Mn concentration. Inset shows the variation of FWHM of Mn related PL with Mn doping concentration (c) Deconvoluted PL spectra of Mn5 and Mn20 with corresponding Gaussian fittings. The inset shows a magnified view of the excitonic peak with fitting. (d) Change in PL intensity of Mn related peak and excitonic peak as a function of the excitation laser power. Inset shows the change in the intensity ratio $I_{Mn}/I_{Excitonic}$ with excitation power.

The large increase in excitonic PL intensity with 1% Mn doping is possibly due to the removal of pre-existing structural defects in the host $CsPbCl_3$ NCs due to Mn doping.[4] With the increase in Mn doping content, PL QY is systematically increased by up to 35% for 10% Mn doping, while it

is decreased to 26% for 20% Mn doping. This may be due to a decrease in the crystallinity and structural defects of the NCs with a high content of Mn substitution. The details of excitonic PL and Mn related PL and PL QY of different samples are summarized in **Table 5.2**.

Since physical milling is a non-equilibrium process, structural defects are likely to be introduced during the physical milling process. To analyze the defect-related emission due to high Mn substitution, we have deconvoluted the excitonic and Mn related PL peaks of Mn5 and Mn20, as shown in **Fig. 5.6(c)**. For Mn5, the excitonic PL peak was fitted with one Gaussian peak (excitonic), while the Mn related peak was deconvoluted with two Gaussian peaks (Mn related and X). However, for Mn20, the excitonic PL peak was fitted with two Gaussian peaks (excitonic and Z), while the Mn related peak was deconvoluted with three Gaussian peaks (Mn related and X, Y). The peak X observed in Mn20 with higher amplitude/ weightage than that of Mn5 is due to the radiative recombination from the sub-bandgap defect states in Mn20. We propose that the additional peaks X, Y, Z correspond to the radiative recombination due to the defect-related sub-bandgap states originating from the ball milling process. It is clear that with the increase in Mn doping content, the sub-bandgap defect states (X, Y, Z) increased since high doping density leads to a higher amount of disorder in the crystal lattice and creates more defect states. Further, with higher Mn doping (30% and 40%), the contribution of defect-related peaks increased significantly. The details of the defect-related bands are summarized in **Table 5.2**.

***Table 5.2**: Summary of PL peak positions, relative intensity, PL quantum yields and band gaps of different Mn-doped $CsPbCl_3$ NCs.*

Sample code	Excitonic PL peak (nm)	Mn related peak (nm)	Defect induced peaks (nm)	Intensity ratio I_{Mn}/I_{Ex}	PL quantum yield (%)	Calculated bandgap
Mn0	416	-	-	-	11	2.97
Mn1	414	585	-	0.13	19	3.00
Mn3	414	581	634	0.39	24	3.04
Mn5	414	579	643	0.60	32	3.05
Mn10	400	591	407, 526, 647	2.80	35	3.06
Mn20	402	588	408, 500, 666	7.70	26	3.09
Mn30	401	589	409, 505, 643	3.99	14	3.09
Mn40	398	592	408, 504, 647	0.97	5	3.11

The excitation intensity dependence of transfer of photogenerated excitons to Mn^{2+} state was further studied to achieve a control over the color tunability of emission. Laser light of 360 nm

with incident power 1 mW to 35 mW was used for the excitation. **Fig. 5.6(d)** depicts the comparison of the PL intensity of excitonic peaks and Mn related peaks of 3% Mn-doped $CsPbCl_3$ NCs as a function of incident laser power. The intensity of both the peaks was increased with the increase in incident laser power, as expected. However, the enhancement of the excitonic peak intensity in the UV region is much higher than that of the orange-red Mn related peak. The inset of **Fig. 5.6(d)** shows the variation of the ratio of Mn related PL to excitonic PL intensities ($I_{Mn}/I_{Excitonic}$) with laser power. When Mn-doped $CsPbCl_3$ NCs were excited with 360 nm laser, electron-hole pairs (excitons) are generated and confined inside the NCs. These photogenerated excitons can be deactivated mainly via three pathways: (a) radiative recombination through the band edge, (b) nonradiative recombination, (c) energy transfer to Mn^{2+} ions and subsequent radiative relaxation from $^4T_1$ state to $^6A_1$ state. When the excitation fluence is in the weak excitation regime (less than one photon per NC), $I_{Excitonic}/I_{Mn}$ should be independent of excitation intensity. Note that the PL lifetime of Mn related state is of the order of milliseconds (ms), while the lifetime of excitonic emission is of the order of nanoseconds (ns) (discussed later). Thus, the Mn-doped $CsPbCl_3$ NCs can be additionally excited when the Mn^{2+} ions are already in excited states with sufficient high excitation fluence, which results in the high excitonic PL intensity. Thus, $I_{Excitonic}/I_{Mn}$ can be dependent on excitation intensity in the strong excitation regime. When nearly all Mn^{2+} are in the $^4T_1$ state, the intensity of Mn^{2+} PL nearly saturates with the increase of excitation intensity. This excitation intensity-dependent control of the relative intensity of dual emission is an important phenomenon useful for light intensity driven color-tunable luminescence properties. Thus, Mn-doped $CsPbCl_3$ NCs can also be useful for excitation intensity-dependent color-tunable dual emissions. At low level of excitation, both the colors have comparable intensity, while at high excitation power, the UV emission dominates over the orange emission.

Note that there may be the presence of nonradiative decay pathways in the doped NCs due to room temperature synthesis process, which results in the lower PL QY. To eliminate the structural defects, we have annealed the Mn5 sample at different temperatures for 20 min in Ar environment and studied the improvement in the structural and optical properties. **Fig. 5.7(a)** shows the XRD pattern of Mn5 film annealed at different temperatures. XRD peak intensities were increased systematically due to annealing, which may be attributed to improved crystallinity and removal of structural defects. Interestingly, the FWHM of (110) XRD peak decreases with the increase in annealing temperature, as shown in the inset of **Fig. 5.7(a).** This may be due to the formation of

bigger crystallite size caused by the annealing. Note that the absorbance of annealed films also increased with annealing temperature, as shown in **Fig. 5.7(b)**. Thus, the annealing results in the improved optical properties of the perovskite NCs film. The bandgap also decreased by annealing due to the formation of bigger size NCs and reduction of lattice distortion, as shown in the inset of **Fig. 5.7(b)**. With the increase in annealing temperature up to 100 °C, the PL intensity was increased systematically, as shown in **5.7(c)**, and it confirms the increase in crystallinity and reduction of nonradiative decay centers in the NCs.

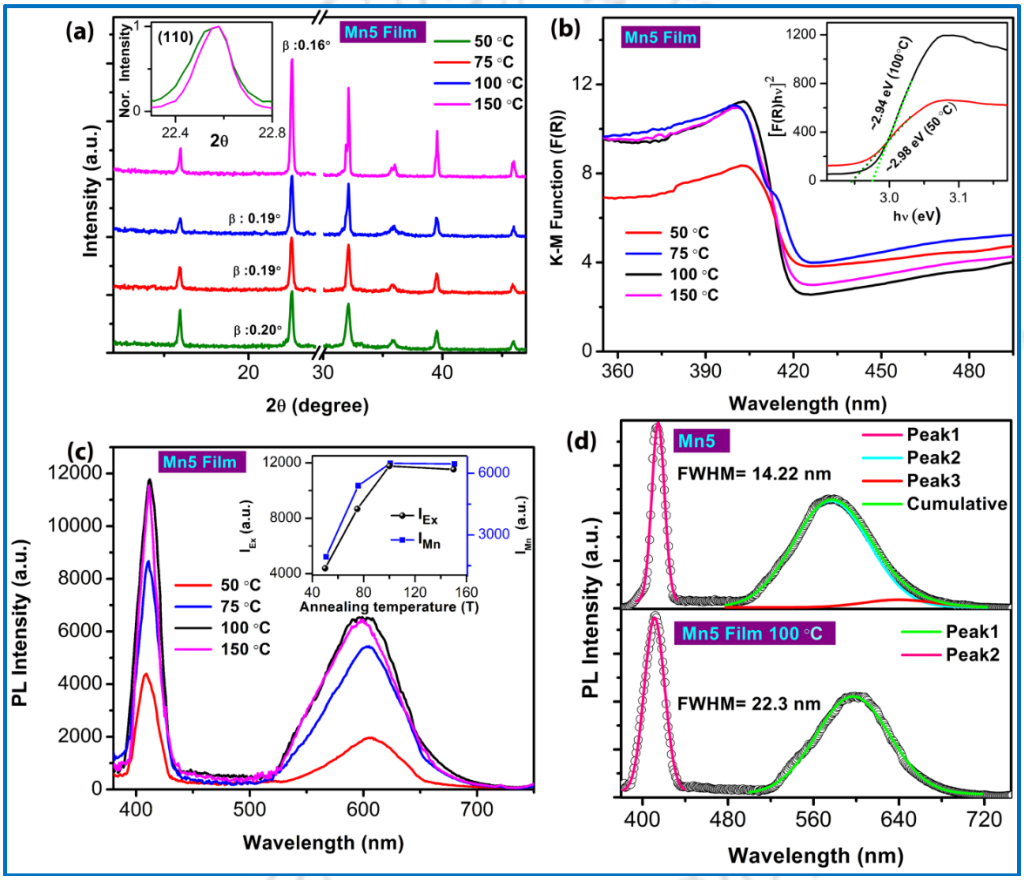

Fig. 5.7: (a) XRD spectra of Mn5 film annealed at different temperatures. Inset shows the normalized line width of (110) XRD peak of Mn5 film annealed at 50 ºC and 100 ºC, respectively. (b) K-M function of Mn5 film annealed at different temperatures. Inset shows the Tauc plot of Mn5 film annealed at 50 ºC and 100 ºC. (c) PL spectra of Mn5 film annealed at different temperatures. The inset of the figure shows the variation of excitonic and Mn related peak intensities with annealing temperatures. (d) Deconvoluted PL spectrum of Mn5 (dispersed in toluene) and Mn5 film annealed at 100 ºC.

We have deconvoluted the PL peaks of as-grown Mn5 (NCs dispersed in toluene) and annealed Mn5 (100°C), as shown in **5.7(d)**. Along with the excitonic peak (peak1) and Mn related broad peak (peak2), a third peak (peak3) is observed for Mn5, which is attributed to sub-bandgap defect-

related emission, which almost vanishes after annealing. Thus, the annealing of the samples improves the structural properties of the samples and yields higher PL QY.

Based on the aforementioned results and literature report, the emission model of $CsPb_xMn_{1-x}Cl_3$ NCs is illustrated through the energy band diagram shown in **Fig. 5.8**.[3, 14] Excited by 360 nm light, the $CsPbCl_3$ host absorbs the photons and emits light at ~410 nm via the radiative recombination of excitons between the ground state and the excited state of $CsPbCl_3$. Besides the radiative recombination, a nonradiative relaxation process also exists, which leads to energy loss through hole traps or electron traps resulting in low PL QY for the undoped sample. The Mn doping in $CsPbCl_3$ NCs generates a new recombination pathway of excitons via the energy transfer from the excited state of host $CsPbCl_3$ to Mn^{2+} and subsequent radiative recombination, which generates orange-red emission, as shown in **Fig. 5.8**.[3, 4, 15] Only the excitons retaining enough thermal activation energy facilitate an intersystem crossing process and finally emit around 590 nm emission, showing a new excitons recombination pathway. This well-known recombination pathway of the d-d transition of Mn^{2+} ions is termed $^4T_1$-$^6A_1$ transition.[3, 16] In case of high doping concentration, defect-related emissions are observed, as denoted by the dashed lines in the band diagram.

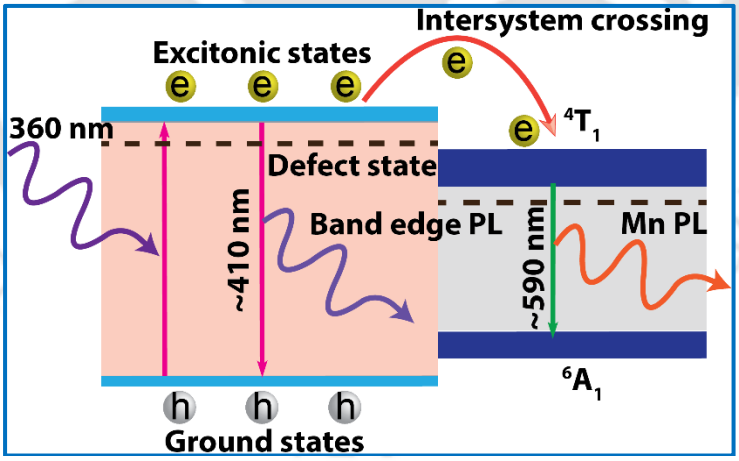

Fig. 5.8: Schematic of the energy band diagram and PL emission mechanisms of $CsPb_xMn_{1-x}Cl_3$ NCs. The horizontal dashed lines represent the defect-related energy levels.

5.3.5. Temperature-Dependent Photoluminescence Study

To investigate the origin of dual-color emissions in Mn-doped $CsPbCl_3$ NCs, we further performed the low-temperature PL measurements at different temperatures. **Fig. 5.9(a)** shows the PL spectra of 3 % Mn-doped $CsPbCl_3$ NCs, in the temperature range 80 K-350 K. The PL spectra at different

temperatures are scaled appropriately to enable a better comparison. Note that the temperature-dependent PL measurement was performed on a film of the NCs deposited on a Si substrate. **Fig. 5.9(a)** clearly shows that with the decrease in temperature, the intensity of the near band edge excitonic PL peak increases systematically. The increase in PL intensity with decreasing temperature is very common in semiconductors, which is mainly due to reduced carrier trapping and lower thermal quenching of PL at lower temperatures. At higher temperatures, the nonradiative recombination channels are more active, and excitons may be dissociated, which results in a decrease in PL intensity. **Fig. 5.9(b)** depicts the comparison of excitonic and Mn related PL peak intensity at different temperatures.

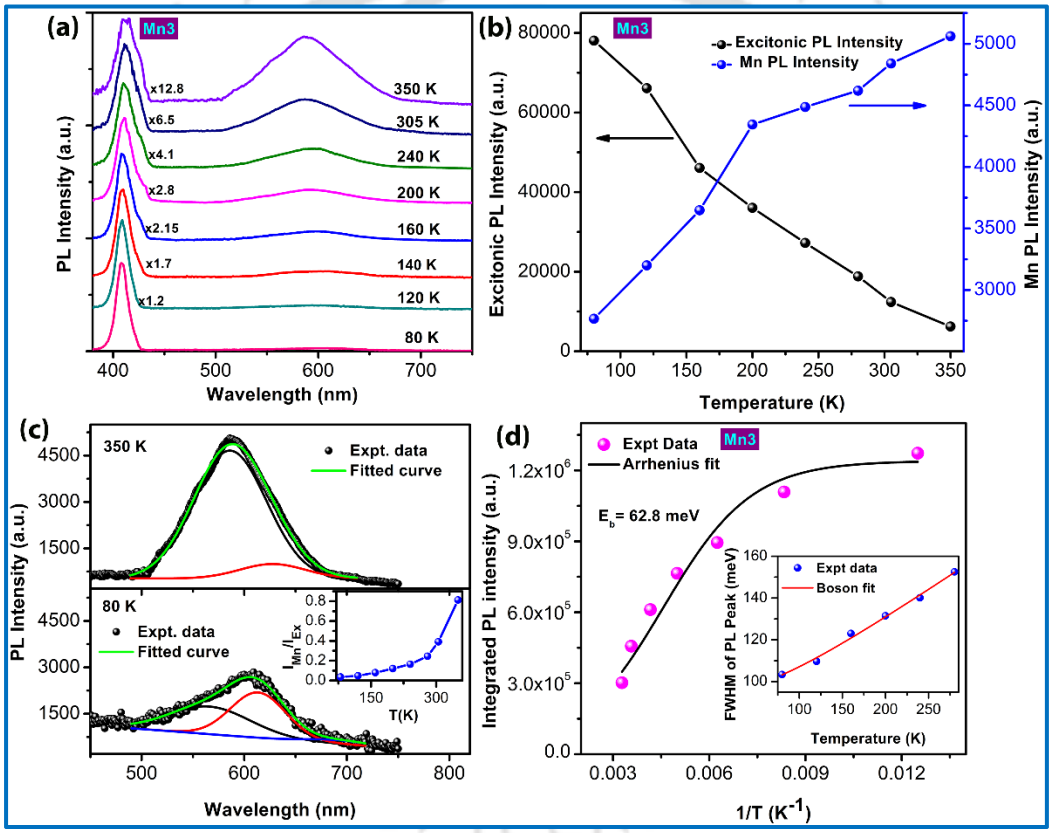

Fig. 5.9: (a) Temperature-dependent PL spectra of 3% Mn-doped $CsPbCl_3$ NCs film. PL spectra at different temperatures are scaled up appropriately to enable better comparison. (b) The evolution of excitonic PL intensity (left Y-axis) and Mn related PL intensity (right Y-axis) with temperature for Mn3. (c) Deconvoluted PL spectra of Mn related peak at temperatures 80K and 350K. (d) Variation of integrated PL intensity of excitonic peak with the inverse of temperature and its fitting with the Arrhenius equation. The inset shows the variation of FWHM of the excitonic peak with temperatures and its Boson fit.

Interestingly, the intensity of Mn related emission peak decreases gradually with the decrease in temperature from 350K to 80K. The unusual temperature dependence of Mn^{2+} PL peak can be

explained by the competitive recombination pathways between the near band edge recombination and $^4T_1$ state to $^6A_1$ state transition in Mn^{2+} after energy transfer from the host $CsPbCl_3$.[4] When we increase the temperature from 80 K to 350 K, the photoexcited carriers located at the excitonic state of $CsPbCl_3$ get extra thermal energy (k_BT) to transit directly to $^4T_1$ state in Mn^{2+} ions. Thus the enhanced radiative recombination from $^4T_1$ state to $^6A_1$ state results in the higher intensity of Mn PL.[4] Thus, the Mn related state shows negative thermal quenching behavior, which is beneficial for it practical applications. At low temperature, the more rapid excitonic recombination than the energy transfer to Mn^{2+} state is responsible for the low-intensity Mn-related PL as compared to the high band edge emission, as shown in **Fig. 5.9(a)**. With the increase in temperature, the excitons dissociate and the excitonic recombination slows down and the energy transfer to the Mn^{2+} becomes more dominant, which results in the higher intensity of Mn PL at 350 K. From **Fig. 5.9(a)**, it is clear that with the decrease in temperature, the Mn PL peak is partly quenched and red-shifted. The redshift of Mn-related PL peak with decreasing temperature is attributed to the decrease in crystal-field strength produced by thermal expansion of the host lattice and the thermal activation of vibronic hot bands.[4] This type of redshift is also observed in Mn-doped ZnS and ZnSe NCs.[17] **Fig. 5.9(c)** shows the deconvoluted PL spectra related to Mn doping at temperature 80K and 350 K. At high temperature, the decrease in weightage of the PL peak at higher wavelength (lower energy) reveals its nonradiative nature.

From the low-temperature PL spectra, we can also estimate two important parameters: (a) exciton binding energy (E_b) and (b) exciton-phonon scattering coefficient. We calculated the exciton binding energy of 3% Mn-doped $CsPbCl_3$ NCs from the temperature-dependent integrated PL intensity of the excitonic peak, using the modified Arrhenius equation. **Fig. 5.9(d)** shows the variation of integrated PL intensity of excitonic peak with the inverse of temperature (1/T) fitted with the Arrhenius equation. The obtained E_b is 62.8 meV.[18] Note that the low-temperature PL measurement was performed on a film of the NCs deposited on silicon substrates, where the spontaneous aggregation of the NCs may partly quench the PL intensity. Thus, the actual exciton binding energy in individual NCs may be higher than the above-calculated value. This relatively low exciton binding energy is consistent with the decrease in excitonic emission and an increase in Mn related emission at higher temperatures.

The inset of **Fig. 5.9(d)** depicts the variation of FWHM of excitonic PL peak with temperature. It is clear from **Fig. 5.9(d)** that the FWHM of PL peaks is increased with increasing temperature.

The higher broadening with the increase in temperature is due to the enhanced exciton-phonon scattering and nonradiative decay of photogenerated excitons in perovskite NCs.[19] The PL peak broadening Γ is fitted using the Boson model with the following equation. [20, 21]

$$\Gamma(T) = \Gamma_0 + \sigma T + \frac{\Gamma_{op}}{\exp(E_{ph}/k_b T) - 1} \qquad (5.1)$$

where Γ_0 is the inhomogeneous broadening constant due to exciton-exciton scattering and σ is the exciton-acoustic phonon coupling coefficient. Γ_{op} corresponds to the exciton-longitudinal optical phonon coupling coefficient or the Fröhlich coupling coefficient, while E_{ph} is the optical phonon energy. From the fitted data, the obtained parameters are as follows: Γ_0 = 91.9 meV, σ = 127.6 μeV/K, Γ_{op}= 47.9 meV, and E_{ph}= 26.1 meV. These parameters indicate a strong exciton-phonon interaction in the doped $CsPbCl_3$ NCs, and it leads to broadening of excitonic PL peak when the temperature is increased from 80 to 350 K.[21] The obtained parameter is consistent with the reported value of optical phonon energy using Raman scattering experiment for $CsPbCl_3$, which showed a E_{ph} of 27.6 meV.[22]

5.3.6. Time-Resolved Photoluminescence Study

To investigate the recombination kinetics of photogenerated charge carriers, TRPL measurements were carried out on the undoped and Mn-doped $CsPbCl_3$ NCs with 375 nm laser excitation. **Fig. 5.10(a)** shows the comparison of TRPL decay profiles of Mn0, Mn3, Mn5, and Mn10 monitored at their corresponding excitonic peaks.

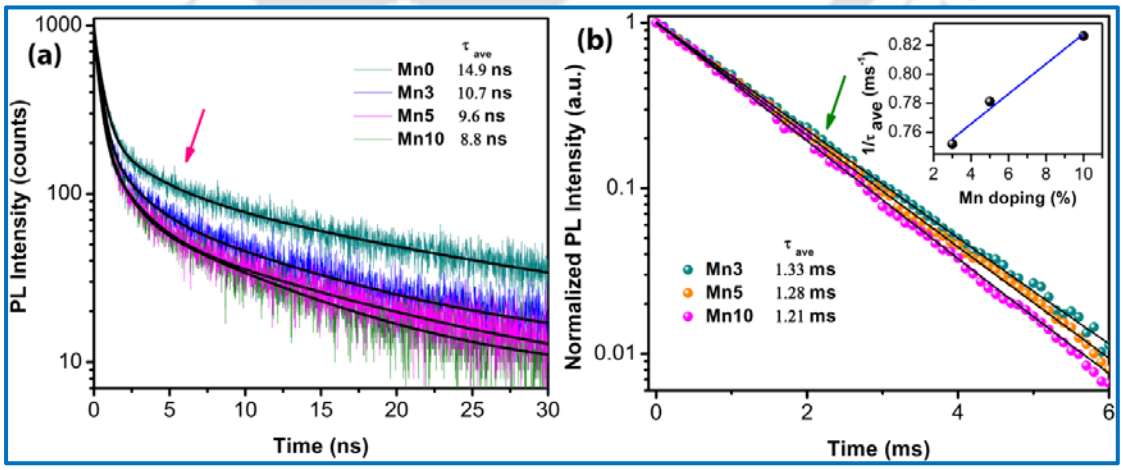

Fig. 5.10: (a) TRPL decay profiles of Mn0, Mn3, Mn5, Mn10 with tri-exponential fitting corresponding to the excitonic PL peak. (b) TRPL decay profiles of Mn3, Mn5, Mn10 with single exponential fit corresponding to the Mn related PL peak. The inset shows the $1/\tau_{ave}$ vs. Mn doping concentration with a linear fit.

Each of the TRPL decay profile was fitted using a tri-exponential decay function (**equation 3.3**). The three time constants are correlated with the radiative electron-trapping and the radiative electron-hole recombination of halide perovskite. The average lifetimes of the excitonic PL peak were obtained to be 14.9, 10.7, 9.6, 8.8 ns for Mn0, Mn3, Mn5, and Mn10, respectively. Thus, the average carrier lifetimes decreased systematically with the increase in Mn doping concentration. This may be due to the decrease in NCs size with the increase in Mn substitution content.[19] Note that due to the Mn doping, parts of the photogenerated carriers are transferred to the Mn ions, and this may effectively shorten the excitonic carrier lifetime. At room temperature, this effect is prominent. However, at low temperature, this effect is less prominent and thus results in high excitonic PL intensity. **Fig. 5.10(b)** shows the TRPL decay profiles of Mn related emission in Mn3, Mn5, and Mn10. For Mn-related emission, TRPL decay profiles were fitted using a single exponential decay function, and the corresponding lifetimes were found to be 1.33 ms,1.28 ms, and 1.21 ms for Mn3, Mn5, and Mn10, respectively. The relatively long lifetime (~ms) of Mn-related PL is attributed to the spin-forbidden nature of the transition from $^4T_1$ state to $^6A_1$ state.[4] The decrease in the lifetime with increasing Mn content may be due to the enhanced Mn-Mn interaction.[4] Further, the carrier lifetime is expected to be inversely proportional to the impurity density, N_t, according to Shockley-Read-Hall (S-R-H) recombination theory.[23] Thus, the carrier lifetime decreases at higher Mn doping density. Inset of **Fig. 5.10(b)** shows the variation of the inverse of decay constants with Mn doping concentration with linear fitting. Thus, these results are consistent with the S-R-H theory.

5.3.7. Stability Study

We have further studied the long-term stability of 3% Mn-doped $CsPbCl_3$ NCs by comparing the PL intensity measurements at certain time intervals. **Fig. 5.11(a)** shows the evolution of the PL spectra (normalized to the excitonic emission) after storing in ambient air (with high humidity) for time duration up to 75 days after synthesis. The variation of Mn PL peak intensity with storage times is shown in the inset of **Fig. 5.11(a)**, which depicts the gradual decrease of PL intensity related to Mn-doping with the increase in storage time. Note that the most explored synthesis method for $CsPbCl_3$ and Mn-doped $CsPbCl_3$ NCs is the hot injection method. In this method, the stability of $CsPb_xMn_{1-x}Cl_3$ NCs is of main concern, as Mn^{2+} ions gradually escape from the host $CsPbCl_3$ with storage time.[13, 24] In the hot injection method, Mn ions are adsorbed and doped near the surface of the NCs. Thus, the Mn related emission usually quenches very fast as Mn diffuses

out of the NCs. Chen et al. reported >50% quenching of Mn related PL emission with respect to excitonic PL intensity after 30 days of storage.[24] In contrast, we observed only 4% quenching in PL intensity after 30 days of storage, and only 18% quenching (relative to the excitonic peak intensity) after 75 days of storage, as shown in **Fig. 5.11(a)**. Thus, the stability of our doped samples is much superior to those reported in the literature. Note that both the excitonic and orange-red PL peak intensities were decreased with the storage time. Due to the high pressure-mediated synthesis conditions and lattice strain induced in the physical milling process, high Mn doping efficiencies are achieved in the $CsPbCl_3$ host NCs.

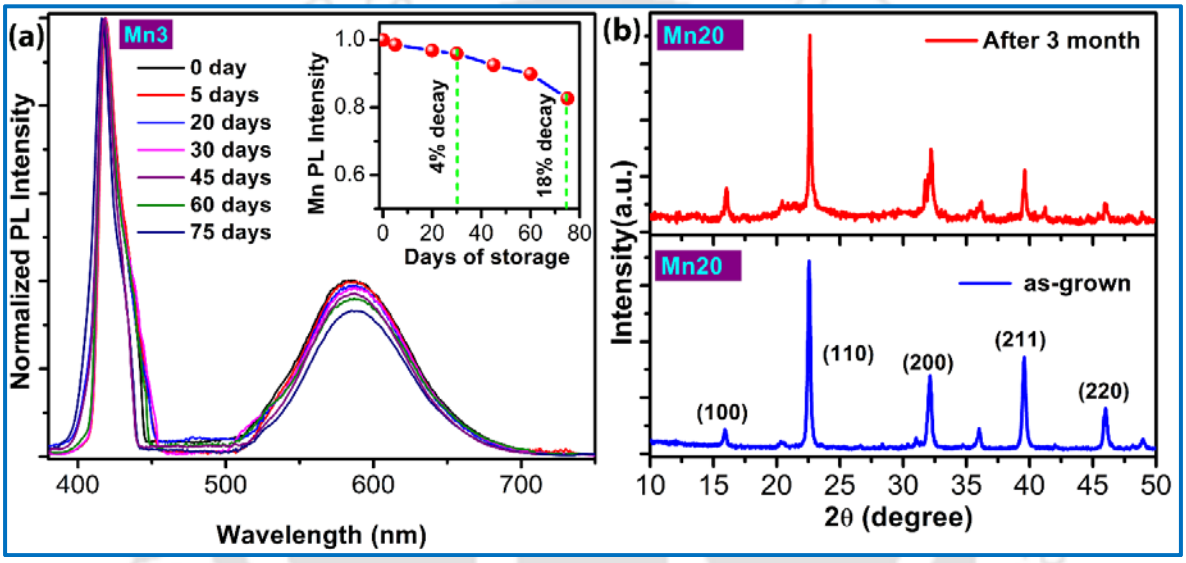

Fig. 5.11: (a) Comparison of normalized PL spectra of Mn3 at different time intervals up to 75 days stored in ambient condition after synthesis. The inset shows the variation of PL intensity (Mn related) as a function of storage time in ambient condition. It shows only 4% decay in Mn PL intensity after 30 days of storage. (b) Comparison of XRD pattern of as-grown and after 5 months of storage of Mn20.

Thus, the solid-state synthesis by the physical milling process possibly provides a more efficient transfer of energy than other synthesis methods to achieve higher Mn substitution and stronger bonding in the $CsPbCl_3$ host lattice. **Fig. 5.11(b)** shows the comparison of the XRD pattern of as-grown and after 3 months of storage of Mn20. The structural stability of the doped NCs after 3 months of storage is evident from the XRD pattern. Thus, our results demonstrate the room temperature solid-state synthesis of Mn-doped $CsPbCl_3$ NCs with much superior ambient stability.

5.3.8. Application of Mn Doped NCs in the WLEDs

We further demonstrate the great potential of orange-red emitting Mn-doped $CsPbCl_3$ NCs for lighting and display applications. As Mn-doped $CsPbCl_3$ NCs exhibit bright orange-red emission,

blue and green light-emitting materials are also required for the white light emission. For the construction of the WLED, we further synthesized two more highly luminescent all-inorganic perovskite NCs by the same physical milling method. $CsPbBr_3$ NCs produce very bright green emission, while $CsPbCl_{1.5}Br_{1.5}$ NCs give bright blue emission. **Fig. 5.12(a)** shows the FETEM image of as-synthesized $CsPbBr_3$ NCs, while **Fig. 5.12(b)** shows the HRTEM lattice fringe of single $CsPbBr_3$ NC. The lattice spacing of 0.29 nm corresponds to the (200) lattice plane of $CsPbBr_3$.

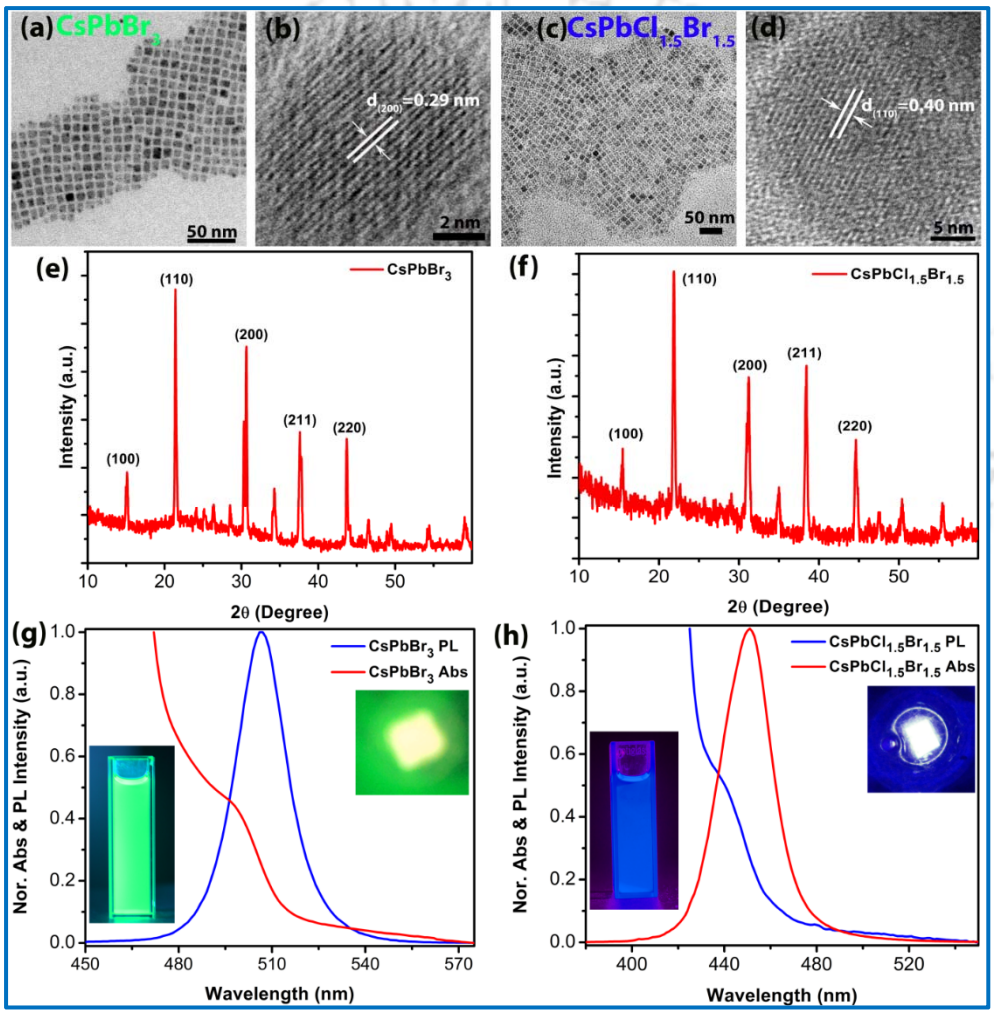

Fig. 5.12: (a) FETEM image of $CsPbBr_3$ NCs and (b) the corresponding HRTEM lattice fringe image. (c) FETEM image of $CsPbCl_{1.5}Br_{1.5}$ NCs and (d) the corresponding HRTEM lattice fringe image. (e, f) XRD pattern of $CsPbBr_3$ and $CsPbCl_{1.5}Br_{1.5}$ NCs. (g) Normalized PL and absorption spectra of $CsPbBr_3$ NCs. The left inset shows the digital photograph of $CsPbBr_3$ NCs under UV light illumination. Right inset depicts the photograph of UV LED chip coated with $CsPbBr_3$ NCs/PMMA composite. (h) Normalized PL and absorption spectra of $CsPbCl_{1.5}Br_{1.5}$ NCs. Left inset shows the digital photograph of $CsPbCl_{1.5}Br_{1.5}$ NCs under UV light illumination. Right inset depicts the photograph of UV LED chip coated with $CsPbCl_{1.5}Br_{1.5}$ NCs/PMMA composite.

Fig. 5.12(c) shows the FETEM image of as-grown $CsPbCl_{1.5}Br_{1.5}$ NCs, while **Fig. 5.12(d)** exhibits the HRTEM lattice fringe of single $CsPbCl_{1.5}Br_{1.5}$ NC. The lattice spacing of 0.40 nm corresponds to the (110) lattice plane of $CsPbCl_{1.5}Br_{1.5}$. The XRD pattern of $CsPbBr_3$ is shown in **Fig. 5.12(e)**, while **Fig. 5.12(f)** shows the XRD pattern of $CsPbCl_{1.5}Br_{1.5}$. The XRD patterns confirm the proper crystalline phase of the NCs. **Fig. 5.12(g)** depicts the normalized absorbance and PL spectra $CsPbBr_3$ NCs dispersed in toluene. The left inset shows a digital photograph of the bright green emission of the NCs under UV light, while the right inset shows that of a UV LED chip coated with $CsPbBr_3$ NCs/PMMA composite exhibiting the green emission. The normalized absorbance and emission spectra $CsPbCl_{1.5}Br_{1.5}$ NCs are shown in **Fig. 5.12(h)**. The left inset shows the bright blue emission of the NCs under UV light irradiation, and the right inset shows a UV LED chip coated with $CsPbCl_{1.5}Br_{1.5}$ NCs /PMMA composite showing the blue emission. The PL QYs of $CsPbBr_3$ NCs and $CsPbCl_{1.5}Br_{1.5}$ NCs were obtained to be 88.1% and 19.7 %, respectively, which are very significant.

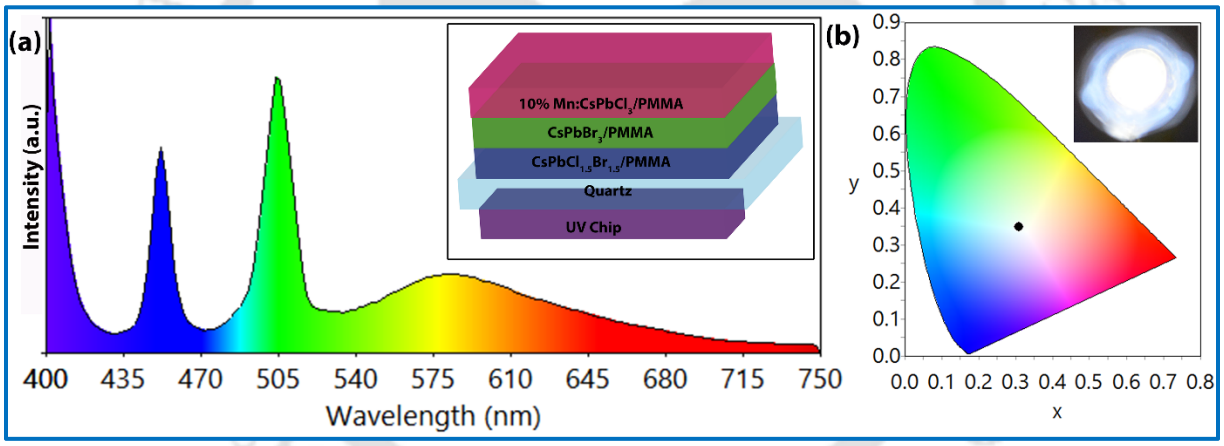

Fig. 5.13: (a) EL emission spectrum of 10% Mn-doped $CsPbCl_3/CsPbBr_3/CsPbCl_{1.5}Br_{1.5}$ NCs film with PMMA on a UV LED chip. The inset shows a schematic of the device structure of WLED. (b) Chromaticity diagram showing the CIE coordinates of the WLED. Inset shows the digital photograph of the constructed WLED.

Note that the undoped $CsPbBr_3$, $CsPbCl_{1.5}Br_{1.5}$, and Mn-doped $CsPbCl_3$ all the three NCs have the high absorbance in the UV region. Thus, blue, green, and orange-red emissions can be observed simultaneously by UV light excitation. A prototype down-converted white light-emitting device was developed by coupling a low cost and commercially available 396 nm UV LED chip with blue-emitting $CsPbCl_{1.5}Br_{1.5}$/PMMA film, green-emitting $CsPbBr_3$/PMMA film and orange-red emitting 10% Mn-doped $CsPbCl_3$/PMMA film vertically stacked together. The electroluminescence (EL) spectrum of the device is shown in **Fig. 5.13(a)**, while schematic of the

WLED device is depicted in the inset of **Fig. 5.13(a)**.[15] [11]The coupled $CsPbCl_{1.5}Br_{1.5}$/$CsPbBr_3$/ 10% Mn-doped $CsPbCl_3$ film with UV chip yields blue-green-orange tri-color emissions leading to bright pure white light emission with corresponding CIE color coordinates of (0.31, 0.34), as shown in **Fig. 5.13(b)**. Thus, the CIE color coordinates lie very close to that of the pure white light (0.33,0.33).[15, 25] Therefore, our results indicate that the orange-red emitting Mn-doped $CsPbCl_3$ is significantly beneficial for obtaining white light. The optoelectronic performance of the constructed WLEDs using perovskite NCs synthesized by a physical milling process may be further improved by optimizing the thickness of different layers and device structure/ geometry.

5.4. Conclusions

We described a facile, low-cost nearly solvent-free, bulk scale, room-temperature mechanochemical synthesis of highly luminescent Mn-doped $CsPbCl_3$ NCs with high Mn substitution through a physical ball milling method. A two-steps physical milling process with a very low amount of surfactant results in perovskite NCs of sizes 9-14 nm, which exhibit superior optical properties. The structural and chemical analyses by XRD and XPS confirm the successful doping of Mn in $CsPbCl_3$ NCs by substitution of Pb with Mn ions. We demonstrated the tunability of the Mn-related orange-red PL emission intensity by controlling the doping concentration, excitation intensity, and measurement temperature. The low-temperature PL and excitation intensity-dependent PL study reveals important insights into the origin and color tunability of Mn related orange-red PL in the dual color emitting Mn-doped $CsPbCl_3$ NCs. Importantly, it is demonstrated that Mn-doped $CsPbCl_3$ NCs synthesized by the physical milling method exhibit better emission stability over a long time due to the high Mn doping efficiencies achieved through the non-equilibrious synthesis conditions in the physical milling process. Deconvolution of the PL spectra revealed the contribution of the defect-related emissions, besides the excitonic emission and Mn-related emission in the overall PL spectra. Further, WLED device was demonstrated by employing blue-emitting $CsPbCl_{1.5}Br_{1.5}$ NCs, green-emitting $CsPbBr_3$ NCs and orange-red emitting 10% Mn-doped $CsPbCl_3$ NCs composite films with PMMA. All the NCs were synthesized by the same physical method. Thus, our work demonstrates a low-cost room temperature synthesis strategy for Mn-doped $CsPbCl_3$ NCs with high color tunability and superior ambient stability for white light-emitting applications. Our report may stimulate further investigation of novel low-cost physical synthesis of perovskite NCs and quantum dots for different optoelectronic applications.

References

1. T. C. Jellicoe, J. M. Richter, H. F. J. Glass, M. Tabachnyk, R. Brady, S. E. Dutton, A. Rao, R. H. Friend, D. Credgington, N. C. Greenham and M. L. Böhm, *J. Am. Chem. Soc.*, 2016, **138**, 2941-2944.
2. D. Parobek, B. J. Roman, Y. Dong, H. Jin, E. Lee, M. Sheldon and D. H. Son, *Nano Lett.*, 2016, **16**, 7376-7380.
3. H. Liu, Z. Wu, J. Shao, D. Yao, H. Gao, Y. Liu, W. Yu, H. Zhang and B. Yang, *ACS Nano*, 2017, **11**, 2239-2247.
4. X. Yuan, S. Ji, M. C. De Siena, L. Fei, Z. Zhao, Y. Wang, H. Li, J. Zhao and D. R. Gamelin, *Chem. Mater.*, 2017, **29**, 8003-8011.
5. S. Das Adhikari, S. K. Dutta, A. Dutta, A. K. Guria and N. Pradhan, *Angew. Chem. Int. Ed.*, 2017, **56**, 8746-8750.
6. J. Zhu, X. Yang, Y. Zhu, Y. Wang, J. Cai, J. Shen, L. Sun and C. Li, *J. Phys. Chem. Lett.*, 2017, **8**, 4167-4171.
7. W. Wu, W. Liu, Q. Wang, Q. Han and Q. Yang, *J. Alloys Compd.*, 2019, **787**, 165-172.
8. J. Zhu, F. Liu, G. B. Stringfellow and S.-H. Wei, *Phys. Rev. Lett.*, 2010, **105**, 195503.
9. W. Liu, J. Zheng, S. Cao, L. Wang, F. Gao, K.-C. Chou, X. Hou and W. Yang, *Inorg. Chem. Front.*, 2018, **5**, 2641-2647.
10. Y. Liu, G. Pan, R. Wang, H. Shao, H. Wang, W. Xu, H. Cui and H. Song, *Nanoscale*, 2018, **10**, 14067-14072.
11. W. Chen, T. Shi, J. Du, Z. Zang, Z. Yao, M. Li, K. Sun, W. Hu, Y. Leng and X. Tang, *ACS Appl. Mater. Interfaces*, 2018, **10**, 43978-43986.
12. R. Prasanna, A. Gold-Parker, T. Leijtens, B. Conings, A. Babayigit, H.-G. Boyen, M. F. Toney and M. D. McGehee, *J. Am. Chem. Soc.*, 2017, **139**, 11117-11124.
13. C. C. Lin, K. Y. Xu, D. Wang and A. Meijerink, *Sci. Rep.*, 2017, **7**, 45906.
14. D. Rossi, D. Parobek, Y. Dong and D. H. Son, *J. Phys. Chem. C*, 2017, **121**, 17143-17149.
15. S. Ye, J.-Y. Sun, Y.-H. Han, Y.-Y. Zhou and Q.-Y. Zhang, *ACS Appl. Mater. Interfaces*, 2018, **10**, 24656-24664.
16. S. Zou, Y. Liu, J. Li, C. Liu, R. Feng, F. Jiang, Y. Li, J. Song, H. Zeng, M. Hong and X. Chen, *J. Am. Chem. Soc.*, 2017, **139**, 11443-11450.
17. X. Yuan, J. Zheng, R. Zeng, P. Jing, W. Ji, J. Zhao, W. Yang and H. Li, *Nanoscale*, 2014, **6**, 300-307.
18. L. Protesescu, S. Yakunin, M. I. Bodnarchuk, F. Krieg, R. Caputo, C. H. Hendon, R. X. Yang, A. Walsh and M. V. Kovalenko, *Nano Lett.*, 2015, **15**, 3692-3696.
19. J. Ghosh, R. Ghosh and P. K. Giri, *ACS Appl. Mater. Interfaces*, 2019, **11**, 14917-14931.
20. S. Parveen, K. K. Paul, R. Das and P. K. Giri, *J. Colloid Interface Sci.*, 2019, **539**, 619-633.
21. A. A. Lohar, A. Shinde, R. Gahlaut, A. Sagdeo and S. Mahamuni, *J. Phys. Chem. C*, 2018, **122**, 25014-25020.
22. C. Carabatos-Nédelec, M. Oussaïd and K. Nitsch, *J. Raman Spectrosc.*, 2003, **34**, 388-393.
23. P. J. S. Rana, T. Swetha, H. Mandal, A. Saeki, P. R. Bangal and S. P. Singh, *J. Phys. Chem. C*, 2019, **123**, 17026-17034.
24. D. Chen, G. Fang, X. Chen, L. Lei, J. Zhong, Q. Mao, S. Zhou and J. Li, *J. Mater. Chem. C*, 2018, **6**, 8990-8998.
25. R. Ghosh, J. Ghosh, R. Das, L. P. L. Mawlong, K. K. Paul and P. K. Giri, *J. Colloid Interface Sci.*, 2018, **532**, 464-473.

Chapter 6

Plasmonic Hole-Transport-Layer Enabled Self-Powered Hybrid Perovskite Photodetector Using a Modified Perovskite Deposition Method in Ambient Air

In this chapter, we demonstrate an air processed high-performance self-powered hybrid perovskite photodetector with plasmonic silver nanoparticles (Ag NPs) embedded hole-transport-layer (HTL), without the use of any electron-transporting layer (ETL). It is demonstrated that without the incorporation of ETL in the device, the use of Ag NPs embedded in the PEDOT:PSS HTL improves the photodetection performance significantly. In contrast to the conventional deposition method, we used a novel N_2 gas-assisted fast crystallization method for the deposition of perovskite film in ambient condition to form a uniform perovskite layer. At zero bias, the ETL-free hybrid plasmonic device shows enhanced responsivity and faster photoresponse compared to the pristine device. The enhancements in the performance of hybrid photodetector are attributed to plasmon-enhanced high optical absorption, as well as improvement in charge extraction and transport by Ag NPs, which are corroborated by steady-state and time-resolved PL, impedance analysis and KPFM measurements.

6.1. Introduction

The ultrasensitive photodetection is important in a wide range of fields, such as optical communication, environmental monitoring, biomedical imaging, security, fire detection, night-vision, motion detection etc.[1-3] Organic-inorganic hybrid perovskites, especially methylammonium lead iodide ($CH_3NH_3PbI_3$), have drawn remarkable research attention over the past few years for their extraordinary performance in self-powered photodetector (PD). In most of the commercial photodetectors, an external bias voltage is essential to achieve the specified performance, and there are certain other limitations due to the complicated fabrication process, high power consumption, high cost, and bulkiness of the photodetectors.[4, 5] In contrast, the fabrication of perovskite (Pe) based photodetector is much simpler due to its low-cost solution-processable fabrication. Perovskite PD with planar and mesoporous "solar cell structure" has recently been reported, which shows excellent performance.[6, 7] In this type of p-i-n or n-i-p PDs, one hole transporting layer (HTL) and one electron transporting layer (ETL) are used to separate

and transport of photogenerated electrons and holes, while Pe layer acts as a light-absorbing active material. Interestingly, these PDs can operate without any external bias due to built-in potential, though the stability and cost are the principal issues for these devices, as different organic HTL and ETL accelerate the degradation of the device.[8] Another important issue of perovskite photodetector is the poor device performance when fabricated under ambient condition. The perovskite film processed in ambient air is often highly nonuniform and rough, which results in poor device performance. Thus, it is imperative to study Pe photodetectors without any charge transporting layer or an external bias with a modified perovskite deposition method and processed in ambient air.

The use of plasmonic metal NPs in solar cells and optoelectronic devices dramatically improves the device performance. Metal NPs under photon illumination can give rise to localized surface plasmon resonance (LSPR), which induces strong photon scattering and absorption. Thus, the photon absorption of the surrounding material can be improved via both the increase in the plasmonic scattering and the near-field enhancement induced excitation effects.[5, 9] Plasmonic metal NPs can also lead to better charge separation and transport.

In this chapter, we demonstrate the enhanced performance of an ETL-free self-powered Pe photodetector by embedding plasmonic Ag NPs in the HTL layer. Ag NPs were synthesized by well-known citrate reduction method, and different concentrations of Ag NPs dispersed in water were added to PEDOT:PSS HTL and deposited by spin coating on a patterned FTO/glass substrate. For the deposition of the Pe active layer, we used a novel N_2 gas-assisted fast crystallization method to form a uniform Pe layer in ambient air. We investigate the mechanism of improved performance of the hybrid photodetector (with Ag NPs) that shows high responsivity and high detectivity along with faster photoresponse than the pristine (without Ag NPs) device.

6.2. Experimental Details

6.2.1. Sample Preparation and Device Fabrication

6.2.1.1. Synthesis of CH_3NH_3I

CH_3NH_3I was synthesized by the method as described in **Chapter 2, Section 2.2.1.2.**

6.2.1.2. Synthesis of Ag Nanoparticles

Ag NPs were synthesized freshly by chemical reduction method using trisodium citrate solution as a reducing agent. First, a solution of 50 mL of 4 mM $AgNO_3$ in double distilled water was prepared and heated to its boiling point using the hot plate and magnetic stirrer. Next, 10 mL of

2% trisodium citrate was added dropwise to the solution. During this process, the solution was stirred vigorously and heated until its color became yellowish brown. Next, it was removed from the heating element and stirred until it cooled down to room temperature. The NPs were collected by centrifugation at 10000 rpm and redispersed in water via sonicating for 15 min.

6.2.1.3. Device Fabrication

The fluorine-doped tin oxide (FTO) coated glass substrates with a sheet resistance of 7 Ω/sq were patterned by using zinc powder and HCl solution, then cleaned sequentially with deionized water, acetone, isopropanol and ethanol using an ultrasonic cleaner for 20 min each and dried in N_2 gas flow. Next, the FTO substrates were treated by UV ozone cleaner for 15 min. 10, 20, and 30 vol% Ag NPs solutions were added with PEDOT:PSS solution and homogenized by ultrasonication, and these samples are named as Ag10, Ag20, and Ag30, respectively. Note that the bare PEDOT:PSS without Ag NPs was named as Ag0. PEDOT:PSS solution was spin-coated at 4000 rpm for 30 sec on the cleaned patterned FTO glass, followed by annealing at 125 ºC for 25 min. To prepare the Pe precursor solution with concentration 1.35 M, 0.212 g of methylammonium iodide (CH_3NH_3I) and 0.62 g of lead iodide (PbI_2) were dissolved in a solvent of 1 ml DMF and heated for 1 hour to form a yellow color transparent solution. We found that conventionally followed spin coating in the ambient atmosphere produces rough and nonuniform Pe film, and the multiple drop-casting using anti-solvent results in nonuniform Pe layer and poor reproducibility of the device. To form a uniform Pe layer, we used dry N_2 gas flow during the spin coating for the rapid crystallization and uniformity of the film. Perovskite precursor was spin-coated on PEDOT: PSS layer at 3500 rpm for 30 sec. The samples were then dried at 90 °C for 10 min after deposition to produce a dark brown dense $CH_3NH_3PbI_3$ film. For the ETL free devices, finally, 100 nm aluminum (Al) electrodes were deposited by thermal evaporation under a high vacuum. For comparison with a device with ETL, a 20 mg/mL solution of PCBM was prepared in chlorobenzene and deposited via spin coating at 1000 rpm for 30 s. Then Al electrodes were deposited by thermal evaporation. The schematic of the fabrication process and device configuration of the hybrid photodetector is shown in **Fig. 6.1**. All the fabrication process was carried out in an open-air atmosphere with high humidity (60%).

6.2.2. Characterization Techniques

The details of the characterization techniques (FESEM, FETEM, EDX, XRD, UV-vis absorbance, PL, TRPL, etc.) used to study the systems were described in **Chapter 2, Section 2.2.2.** The details

of AFM and KPFM measurements were described in **Chapter 4, Section 4.2.2.** Different characterizations were done immediately after fabrication to avoid the degradation of Pe film. The I-V characteristics and the photoelectric response curves of the photodetector were measured using a homemade setup using a Xenon lamp (Newport, Oriel Instrument) with a monochromator (Newport, Oriel Instrument), chopper (Stanford Research Systems) and a source meter (Keithley 2400).

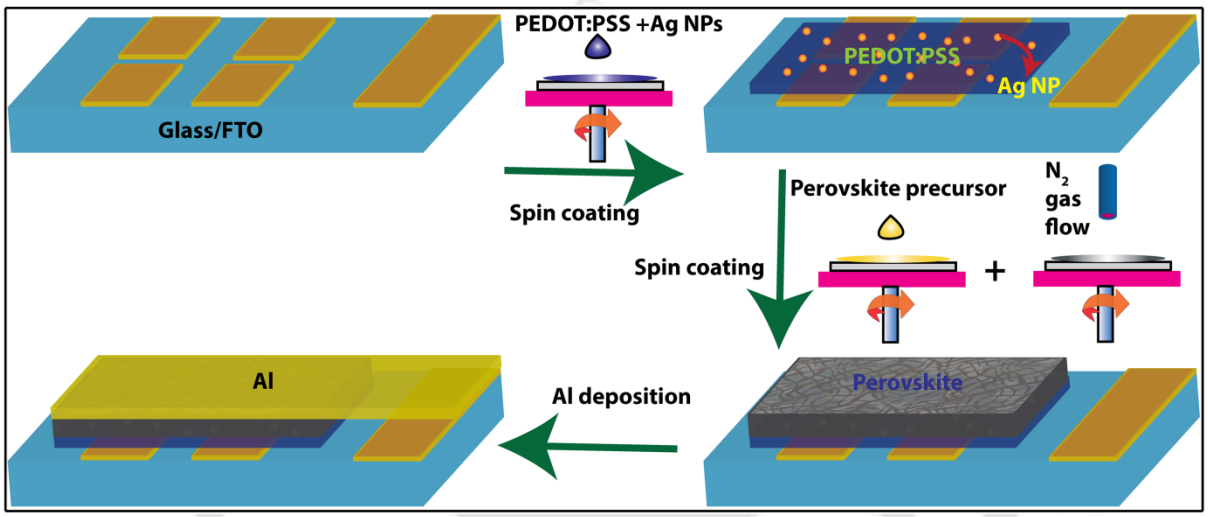

Fig. 6.1: (a) Schematic of the device fabrication steps of plasmonic perovskite photodetector.

6.3. Results and Discussion

6.3.1. Morphology and Structural Analyses

Fig. 6.2(a) depicts the FESEM image of Pe layer fabricated by N_2 gas-assisted crystallization method, which reveals the compact grains and full coverage Pe film on FTO/Ag20. Note that the conventional deposition method in ambient air (with high humidity) results in highly nonuniform and rough film. Due to the pinhole-free compact morphology with large grains of Pe film, better separation of photogenerated carriers and reduced recombination of carriers were observed. Thus highly compact Pe film deposited by N_2 gas-assisted fast crystallization method results in the superior performance of photodetection. **Fig. 6.2(b)** shows the cross-sectional FESEM image of the device. The cross-sectional FESEM image depicts different layers of the PD. The thickness of the Pe active layer is ~590 nm. We also varied the thickness of the Pe active layer by precursor concentration. The superior performance of the ETL-free PD was observed for a device with ~600 nm of Pe active layer. **Fig. 6.2(c)** shows the AFM image of the Pe film, which clearly depicts the large and compact grains in the as-deposited Pe layer. AFM micrograph is consistent with the

FESEM image of Pe film. The root mean square (rms) roughness of the film was observed ~64 nm, and grain sizes are in the range ~a few 100 nm to 2 μm.

Size, morphology, and crystal structure of as-grown Ag NPs were studied using FETEM/ HRTEM lattice imaging. **Fig. 6.2(d)** shows the FETEM image of as-synthesized Ag NPs, while the bottom inset depicts the HRTEM image of a single NP. The lattice spacing of 0.24 nm corresponds to (111) plane of silver, as shown in **Fig. 6.2(d)**.[10] The top inset of **Fig. 6.2(d)** shows the size distribution of Ag NPs. The size of the Ag NPs is in the range 5-14 nm with a mean size of ~11 nm. These Ag NPs helps in efficient photodetection due to the plasmonic effect in the hybrid PD.

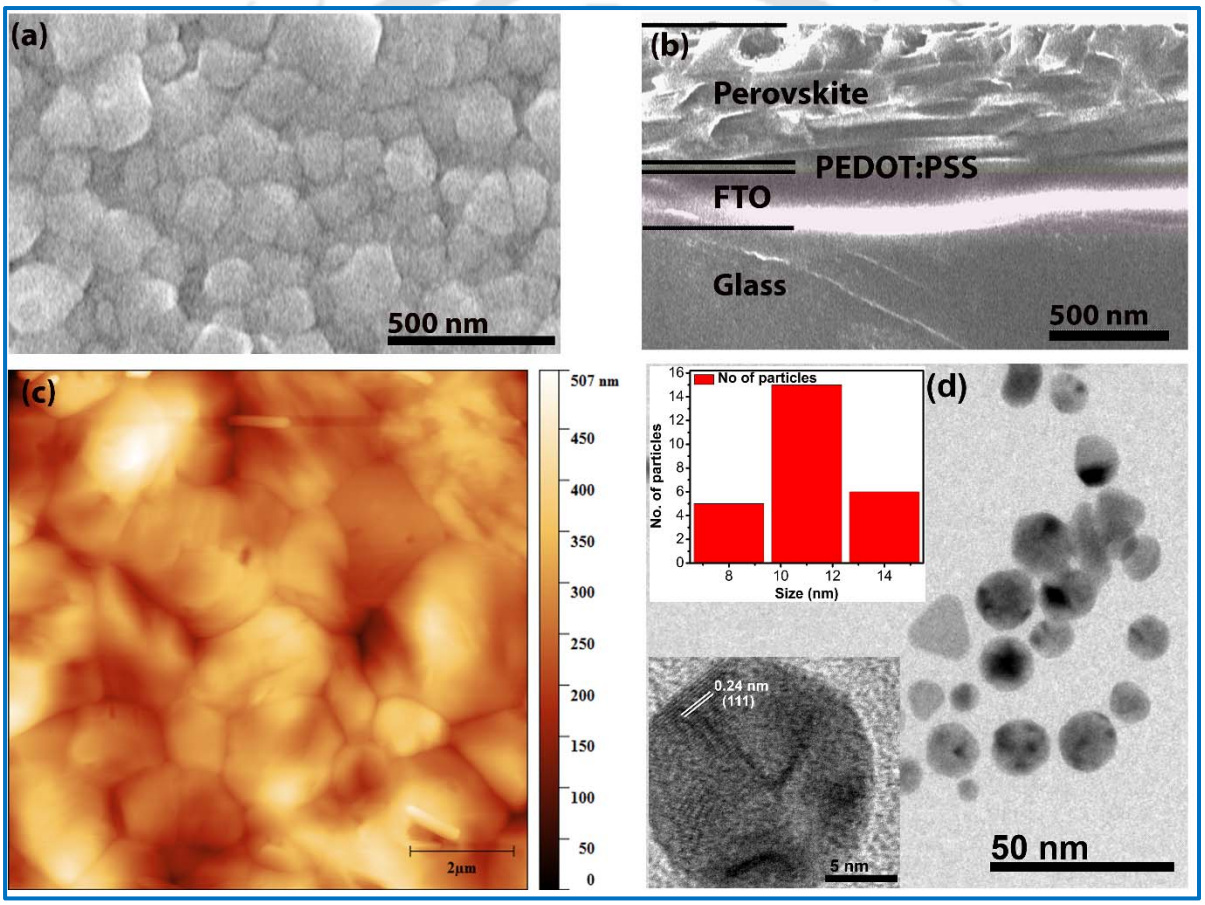

Fig. 6.2: (a) FESEM image of perovskite film on the FTO/Ag_20 layer. (b) Cross-sectional FESEM image of the device showing the thickness of the different layers. (c) AFM image of perovskite film on the FTO/Ag20 layer. (d) The TEM image of Ag NPs. The top inset shows the corresponding size distribution of Ag NPs, and the bottom inset shows the HRTEM lattice fringe of single Ag NP.

The morphology of the undoped and Ag doped PEDOT:PSS films are shown in **Fig. 6.3**. **Fig. 6.3(a,b)** shows the FESEM images of PEDOT:PSS film without and with Ag NPs, respectively,

while **Fig. 6.3**(c,d) shows the EDX spectra of PEDOT:PSS film without and with Ag NPs. C, S, O were observed due to PEDOT:PSS film, while Sn was observed due to the FTO layer. The rest of the elements correspond to the underlying glass substrate. The EDX spectrum confirms the presence of Ag in Ag20 film.

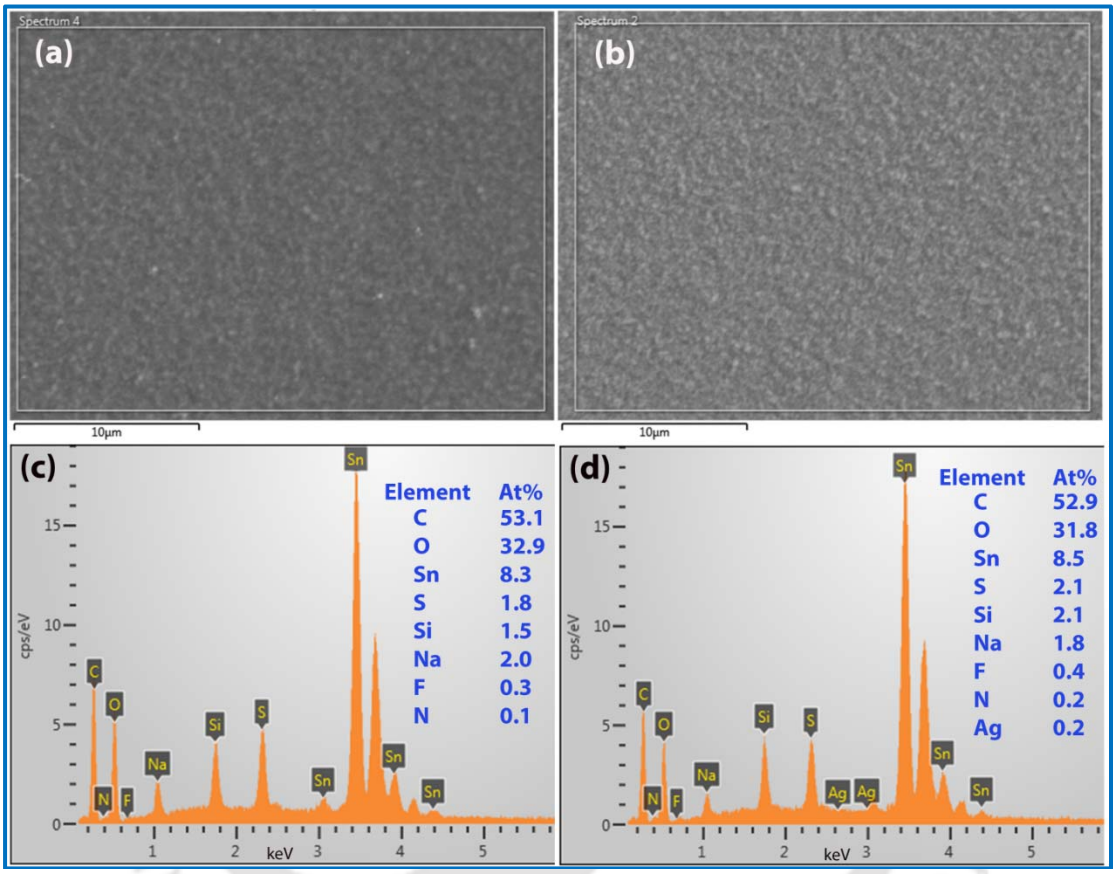

Fig. 6.3: FESEM image of PEDOT:PSS film on FTO glass: (a) without Ag NPs, and (b) with Ag NPs. EDX spectra of PEDOT:PSS film on FTO glass: (c) without Ag NPs and (d) with Ag NPs.

The phase and crystalline quality of Pe film were further confirmed by XRD analysis. XRD patterns of Pe film on glass, FTO/Ag0, and FTO/Ag20 shown in **Fig. 6.4** confirm the crystalline phase of the $CH_3NH_3PbI_3$. The sharp peaks of Pe films are attributed to its highly crystalline nature. All the samples show nearly identical XRD patterns, and it indicates that the structural ordering and preferential orientation of the crystallites relative to the substrate are retained in all the films. The strong diffraction peaks at 2θ equal to 14.16º, 20.04º, 23.55º, 24.57º, 28.50º, 31.92º, 35.04º, 40.56º, 43.11º, and 50.25º can be assigned to (110), (112), (211), (202), (220), (310), (312), (224), (314) and (404) crystal planes, which indicate the tetragonal structure of $CH_3NH_3PbI_3$. The peaks marked with the symbol '♦' are arising from the underlying FTO substrate.

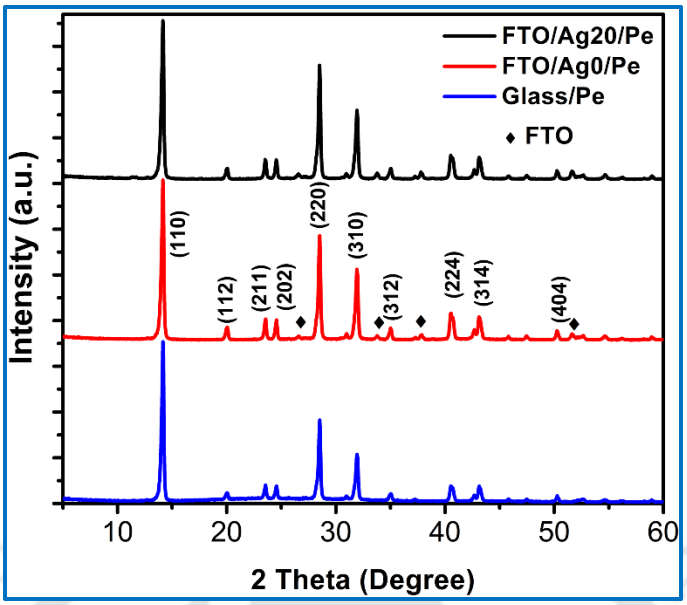

Fig. 6.4: Comparison of XRD patterns of perovskite films on glass, FTO/Ag0, and FTO/Ag20.

6.3.2. Optical Studies

The absorption spectrum of as-grown Ag NPs dispersed in water shows a strong peak at ~432 nm corresponding to the characteristic plasmonics absorption of Ag NPs, as shown in **Fig. 6.5(a).** Thus, the strong absorbance of plasmonic Ag NPs helps in better light-harvesting in the plasmonic Pe device (discussed later). The optical absorption spectra of the $CH_3NH_3PbI_3$ Pe film on Ag0 and Ag20 are shown in **Fig. 6.5(b)**. The Pe film exhibits a wide spectral absorption in the range 400-800 nm with a high absorption value. This gives rise to the high photo-responsivity of the PD over a broad spectral range (discussed later). From the absorption edge of Pe film, the bandgap was obtained as ~1.58 eV. Note that the Pe film on Ag20 shows enhanced absorption in the region 400-550 nm as compared to Pe film on Ag0. This is due to the plasmonic absorption by the Ag NPs, peaked at 432 nm, as shown in **Fig. 6.5(a).** Note that both the bare PEDOT:PSS film and PEDOT:PSS film with Ag NPs show a very low absorbance in the wavelength region 300 nm to 800 nm due to the high transmittance, which is essential to photoexcite the Pe active layer. Interestingly, with the Ag NPs, the absorbance of Ag20 film in the wavelength region 300-600 nm is higher than the Ag0 film. Due to the multiple reflections in the interface of Ag20 and Pe film, the absorbance of the hybrid system was significantly improved.

To study the effect of Ag NPs on dynamics of photoexcited charge carriers, steady-state PL and TRPL measurements were carried out. The comparison of the PL spectra of the Pe film on FTO, Ag0, and Ag20 are shown in **Fig. 6.5(b)**. A PL peak centered at ~ 779 nm for each sample

corresponds to the photoemission peak for $CH_3NH_3PbI_3$ Pe due to the band-to-band transition. Note that for Pe films on Ag0 and Ag20, the PL intensity was quenched to 50.1% and 31.4% of the peak intensity of Pe film on the FTO substrate. The PL emission of the Pe film on PEDOT:PSS layer was quenched due to the transfer of photogenerated charges from Pe to PEDOT:PSS layer, which essentially reduces the radiative recombination of carriers.

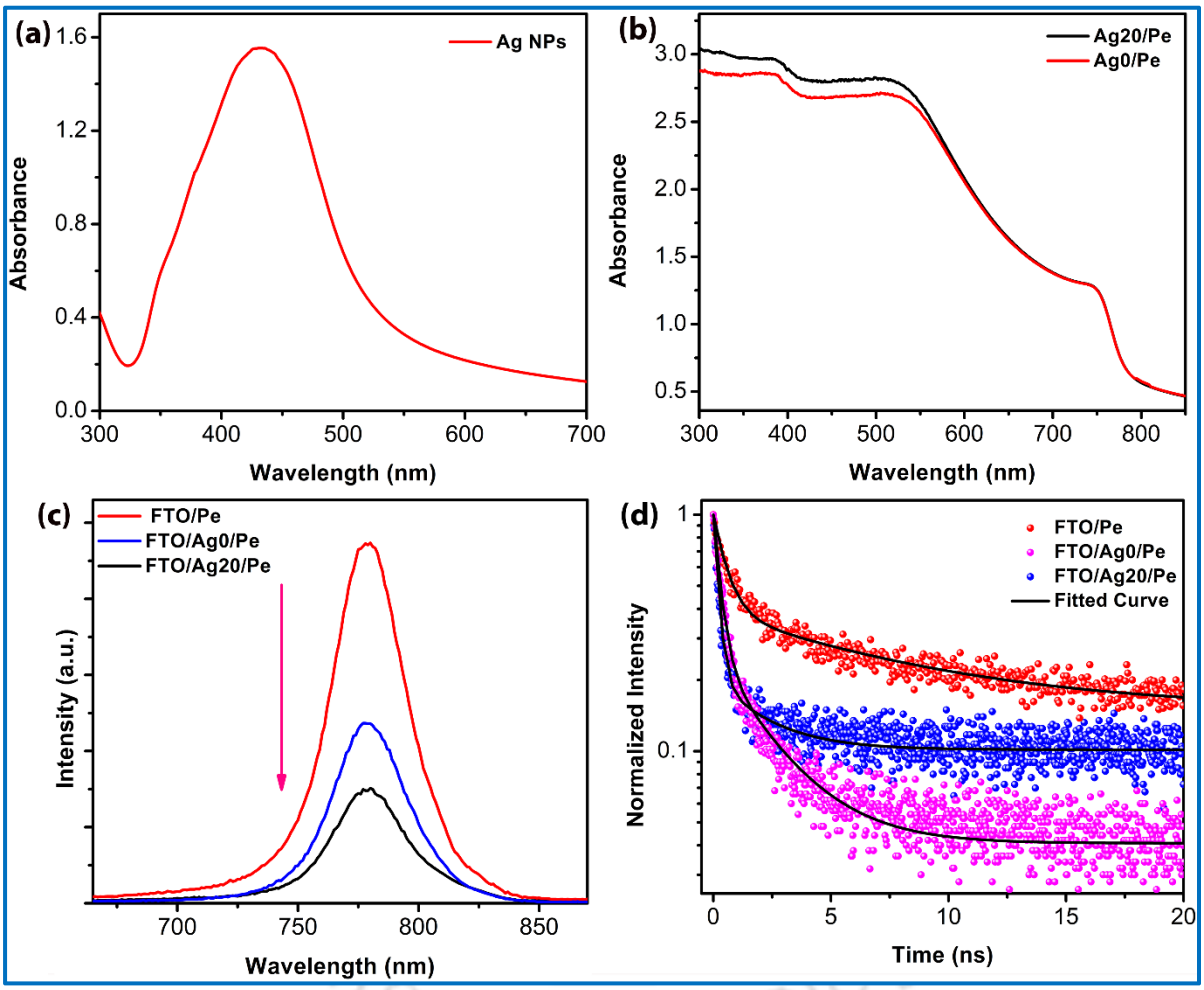

Fig. 6.5: (a) The UV-visible absorption spectrum of bare Ag NPs dispersed in water. (b) Comparison of the absorbance spectra of perovskite film on FTO/Ag0 and FTO/Ag20. (c) Comparison of steady-state PL spectra of perovskite film on FTO, FTO/Ag0, and FTO/ Ag20. (d) Time-resolved PL decay profiles of perovskite film on FTO, FTO/Ag0, and FTO/ Ag20. In each case, symbols represent the experimental data, and solid lines represent the fitted data.

With the introduction of Ag NPs, further quenching of PL emission was observed, indicating that the photo-excited carriers in Pe layer possibly transfer to Ag NPs by reducing the charge recombination, and it is beneficial for the superior photodetection.[5] Due to the efficient

photogenerated carrier separation suppressing the radiative recombination in Pe active layer, a higher photocurrent was observed in the hybrid plasmonic PD.

The charge transfer process is further ascertained from the TRPL analysis. **Fig. 6.5(d)** shows a comparison of the TRPL decay profiles of Pe film on FTO, Ag0, and Ag20 monitored at the corresponding PL peak center. TRPL data in each case was fitted with a bi-exponential decay function.[11] The two time constants are correlated with the radiative electron-trapping and the radiative electron-hole recombination of halide perovskite. The corresponding average lifetime of carriers, τ_{ave}, is found to be 6.84 ns, 1.67 ns, and 1.30 ns for Pe film on FTO, Ag0, and Ag20, respectively. The shortening of time constants in Ag0 indicates a faster charge transfer between the Pe and the PEDOT:PSS layer, resulting in an improved carrier separation from the Pe layer.[5, 12] Note that the TRPL decay lifetime of Pe film on Ag20 is further decreased from than of Ag0, which confirms the better transfer of photogenerated carriers in Ag20.

6.3.3. Performance in Photodetection

To assess the performance of the PDs, we investigated the photocurrent (PC) switching, responsivity, and detectivity of the Pe PDs. It is significant to note that all the measurements were conducted at room temperature under ambient conditions with high relative humidity. The PC response and sustainability of pristine and hybrid devices were measured with repeated on/off switching cycles under illumination intensity of 1.1 mW/cm^2 without any external bias. **Fig. 6.6(a)** shows the time-dependent PC response curves under zero bias with on/off intervals of 5 s with 400 nm incident light pulse. From **Fig. 6.6(a)**, it is clear that with the incorporation of Ag NPs in PEDOT:PSS layer, the PC of the hybrid device increased significantly as compared to that without the Ag NPs. The PCs for the devices with Ag0, Ag10, Ag20, Ag30 were observed to be 7.54, 8.83, 11.13, and 9.68 μA, respectively. Note that the PC first increased with increasing concentration of Ag NP, showed the highest value for the Ag20 case, and then decreased for Ag30. The decrease in PC at high concentration may be due to the structural inhomogeneity of the HTL induced by a high concentration of Ag NPs that decreases the overall carrier transport through the layer by causing charge carrier scattering. Thus, the Ag20 device shows optimum performance. We, therefore, focused on the device with Ag20 for the HTL, and further investigations were made with a comparative analysis of Ag0 and Ag20 devices. We have further quantified the photoresponse speed of growth and decay of the PC of Ag0 and Ag20 devices.[13] **Fig. 6.6(b-c)** shows the enlarged view of a single cycle photoresponse of Ag20 and Ag0 devices, respectively.

The rise time (τ_r) and decay time (τ_d) of PC can be defined as the time to transition between the minimum current to the 90% of the maximum value, and from the maximum current value down to 10%, respectively.[14] The time constant of PC growth is found to be τ_r= 110 ms and 260 ms for Ag20 and Ag0 devices, respectively at zero bias under 400 nm light illuminated at an intensity of 1.1 mW/cm^2. It is clear that the device with Ag NPs responds faster with higher current gain than the pristine one. This is due to the enhanced plasmonic absorbance and better charge transport by the Ag NPs. Similarly, the time constant (τ_d) of the PC decay is found to be 72 ms and 271 ms, respectively, for Ag20 and Ag0 device at zero bias under the same condition.

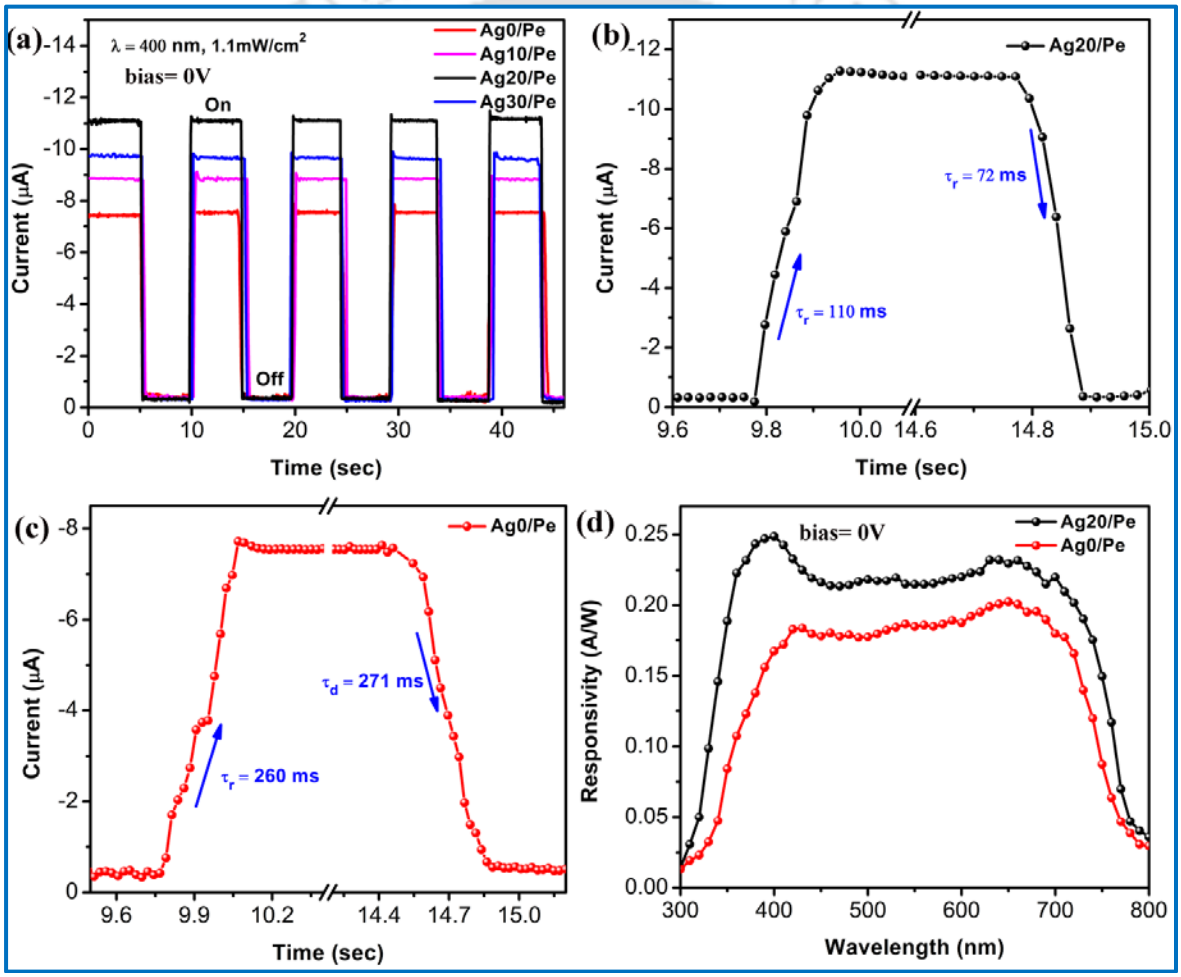

Fig. 6.6: (a) Time-dependent photocurrent response of the perovskite photodetector under zero bias without and with Ag NPs at different concentrations for 400 nm light with intensity 1.1 mW/cm^2. (b) An enlarged view of growth and decay of photocurrent of the device with Ag NPs (Ag20). (c) An enlarged view of growth and decay of photocurrent of the device without Ag NPs (Ag0). (d) The wavelength-dependent photoresponsivity of pristine and hybrid photodetector at zero bias.

The spectral responsivity (R_λ) is an important parameter to estimate the performance of the PD which indicates how efficiently the detector responds to an optical signal. The responsivity of the PD was calculated using **equation 3.6 (Chapter 3)**.[1, 15] **Fig. 6.6(d)** shows the spectral responsivity of the pristine and hybrid PDs without any external bias. The self-biased ETL-free $CH_3NH_3PbI_3$ pristine PD shows the responsivity of 0.18-0.20 AW^{-1} in the region 400-720 nm, which is comparable/higher than the other reported transport layer free self-biased Pe PD.[5, 16, 17] From **Fig. 6.6(d)**, it is clear that the responsivity of the hybrid device increased significantly with the incorporation of plasmonic Ag NPs. The hybrid PD shows improved responsivity of 0.20-0.25 AW^{-1} in the wavelength region 400-720 nm with the highest responsivity 0.25 AW^{-1} at 400 nm. The enhanced responsivity of the hybrid device in the entire visible region is attributed to the improved carrier extraction and transport by the plasmonic Ag NPs. From **Fig. 6.6(d)**, it is evident that the enhancement of responsivity in the near UV region (330-500 nm) in the hybrid device is relatively higher than the visible region. It is believed that the enhanced optical absorption by the Ag NPs causes a higher enhancement in the responsivity in the near UV region, while the enhanced carrier extraction and transport by the plasmonic NPs result in the enhanced responsivity in the entire visible-NIR region. Our plasmonic-perovskite hybrid photodetector shows comparable performance with the reported self-powered perovskite devices. Note that our device is fabricated completely in an ambient atmosphere with a modified perovskite deposition method, without the use of glove box. Thus the measured performance suggests the novelty and versatility of our self-powered PD.

Next, we measure the specific detectivity of the pristine and hybrid PDs. The specific detectivity (D*) of the PD represents the capability of detecting low-level light signals, taking into account the contributions of the photocurrent and dark current. The wavelength dependent detectivity of Ag0 and Ag20 devices is shown in **Fig. 6.7(a)**. The pristine device shows a maximum detectivity of 1.04×10^{11} Jones, while the hybrid device reveals a higher detectivity of 1.53×10^{11} Jones, as shown in **Fig. 6.7(a).** Thus detectivity was significantly improved in the plasmonics Pe PD compared to pristine PD.

Fig. 6.7(b) represents the current density versus voltage (J-V) plot of the pristine and hybrid PD in dark and under light illumination (400 nm light with 1.1 mW cm^{-2}). The dark current of the hybrid device is similar to that of the pristine device because of the large Schottky barrier at the contact between Pe and Al electrode.[5] Under illumination, the hybrid Ag20 PD shows a

significantly higher PC than the Ag0 (pristine). Under reverse bias, band bending in the Pe layer close to the Al electrode reduces the Schottky junction thickness and enables the injection of carriers into the Pe layer, leading to a dramatic increase in the PC in both pristine and hybrid devices. From **Fig. 6.7(b)**, it is clear that even at 0 V, there is a significant PC in both the pristine and hybrid devices. This is owing to the fact that there exists a built-in electric field in the heterojunction device, which can force the photogenerated carriers in the absorber to be separated and collected by different electrodes. Thus, this PD can be self-powered and works at 0 V bias.

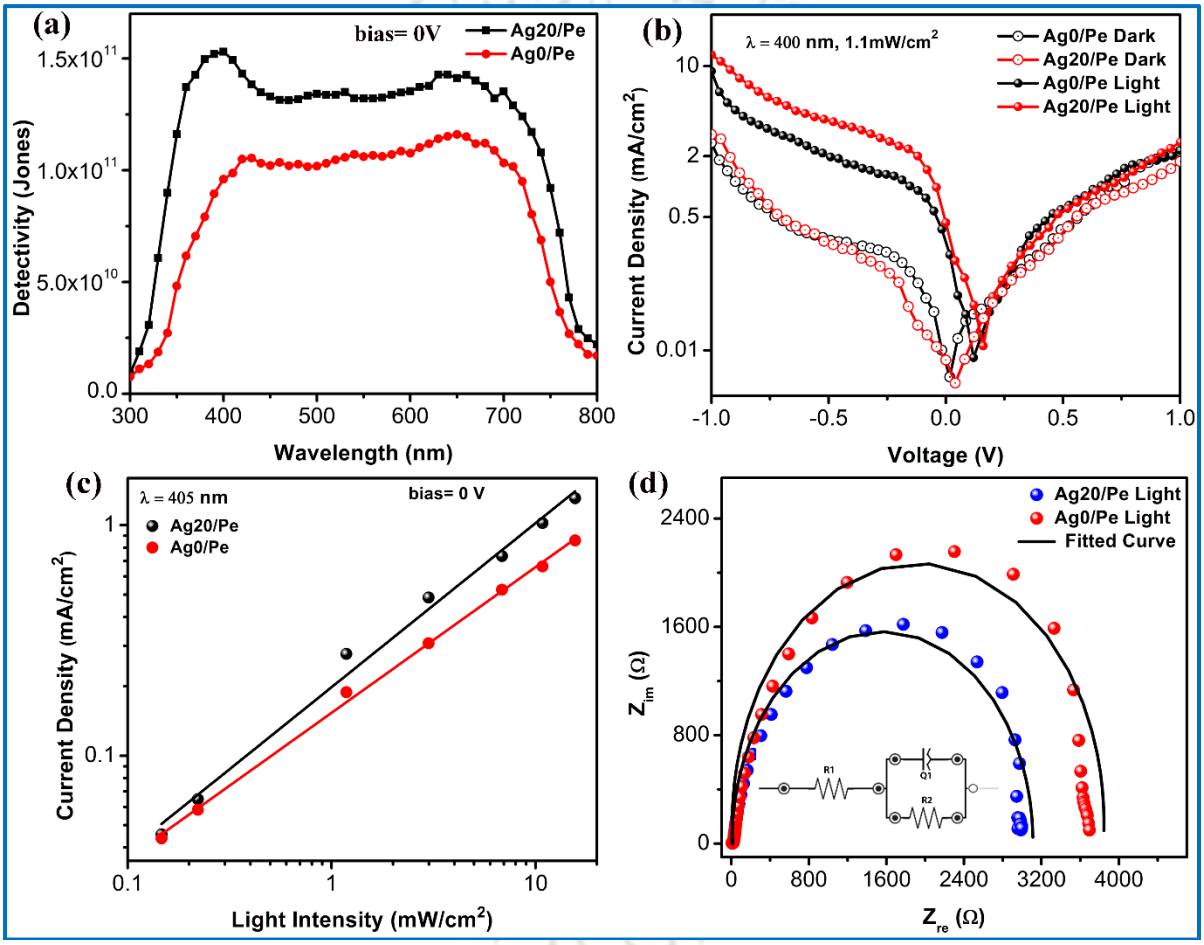

Fig. 6.7: (a) The wavelength-dependent detectivity of pristine and hybrid photodetector at zero bias. (b) The J–V characteristics of the photodetector with and without Ag NPs in the dark and under illumination. (c) Intensity-dependent photocurrents of pure and hybrid photodetectors under zero bias at 405 nm incident light with corresponding linear fitting. (d) Impedance spectra of photodetector without and with Ag NPs under illumination at 400 nm of intensity 1.1 mW/cm^2. The inset shows the equivalent circuit diagram.

The dependence of photocurrent density on the intensity of incident light at 0 V bias is shown in **Fig. 6.7(c)**. A 405 nm laser is used for this measurement. The pristine and hybrid devices show a linear increment in current density with the intensity of incident light in the range of 0.14

to 15.64 mW/cm^2. It is clear that at a higher intensity, the enhancement in PC for the hybrid device is higher than that of the pristine device. This may be due to the enhanced hot electron generation, efficient charge extraction, and transport by the plasmonic Ag NPs at a higher intensity.[5]

To analyze the capacitance and resistance components of the multilayered pristine and hybrid devices, the impedance characteristics were measured under illumination at 400 nm at intensity 1.1 mW/cm^2 by impedance spectroscopy, as shown in **Fig. 6.7(d)**.[18] The electrochemical impedance plots were fitted to a circuit shown in the equivalent circuit diagram in the inset of **Fig. 6.7(d)**, where the series resistance R1 is connected to a parallel R-C circuit.[18] However, the capacitor is modeled by a constant phase element, which is better to reflect the capacitive factors in a thin film photodetector device. The Levenberg-Marquardt method as built into the fitting software PSTrace5 was used for the fitting. Under illumination, series resistance R1 was determined to be 14.32 Ω for the pristine device and 6.19 Ω for the hybrid device. This series resistance denotes the carrier transfer resistance and therefore is inversely proportional to the efficiency of the hole transfer across the heterojunction.[19] Thus, the carrier transfer efficiency is enhanced (doubled) in the presence of Ag NPs in the hybrid device (see **Fig. 6.7(d)**).

In order to evaluate the performance of the PD under very low bias conditions, we further measured the PC response under a reverse bias of 0.5 V. **Fig. 6.8(a)** shows the time-dependent PC response curves under 0.5 V with 400 nm incident light of intensity 1.1 mW/cm^2.

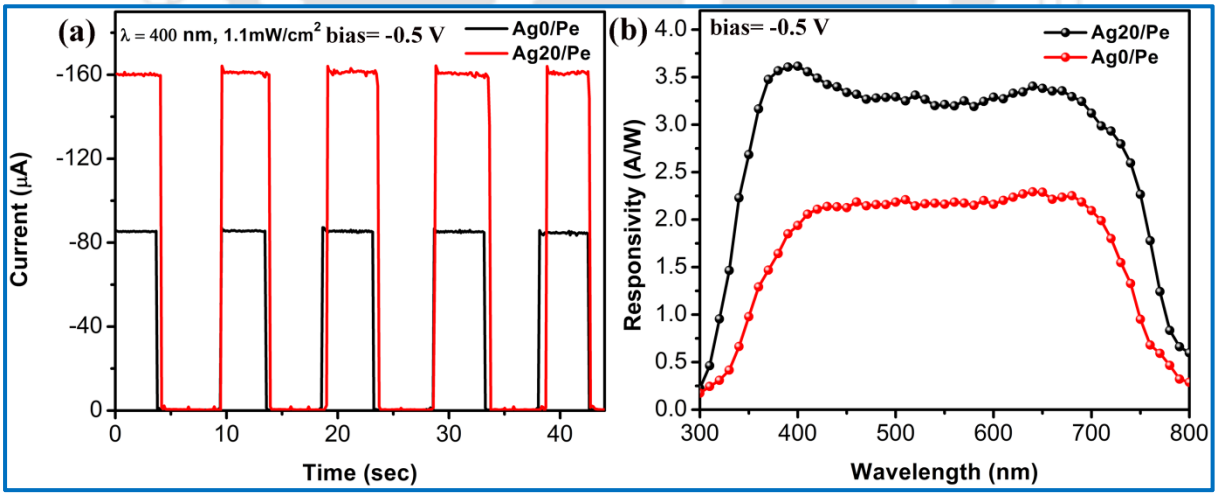

Fig 6.8: (a) Time-dependent photocurrent response of the perovskite photodetector under -0.5 V applied bias without and with Ag NPs (Ag20) using 400 nm light of intensity 1.1 mW/cm^2. (b) The spectral responsivity of pristine and hybrid photodetector at -0.5V applied bias.

Interestingly, the PC increased significantly at such a small reverse bias (0.5V), though the enhancement factor is much higher for the plasmonic photodetector case. Note that the applied reverse bias in the device enables easier transport of photogenerated carriers to the electrodes resulting in superior device performance. **Fig. 6.8(b)** depicts the spectral responsivity of Ag0 and Ag20 devices with 0.5V reverse bias. The hybrid device shows the highest responsivity of 3.61 A/W, while the pristine device shows the highest responsivity of 2.28 A/W at 0.5 V bias. This implies a 58% improvement in the responsivity of the hybrid device made with plasmonic Ag nanoparticles, which is significant.

Note that with the addition of PCBM as ETL, the PC increased for both the pristine and hybrid devices due to higher carrier transport to the electrodes. The time-dependent PC response of Ag0 and Ag20 device with PCBM ETL under zero bias is shown in **Fig. 6.9(a)** with ON/OFF intervals of 5 s with 400 nm incident light.

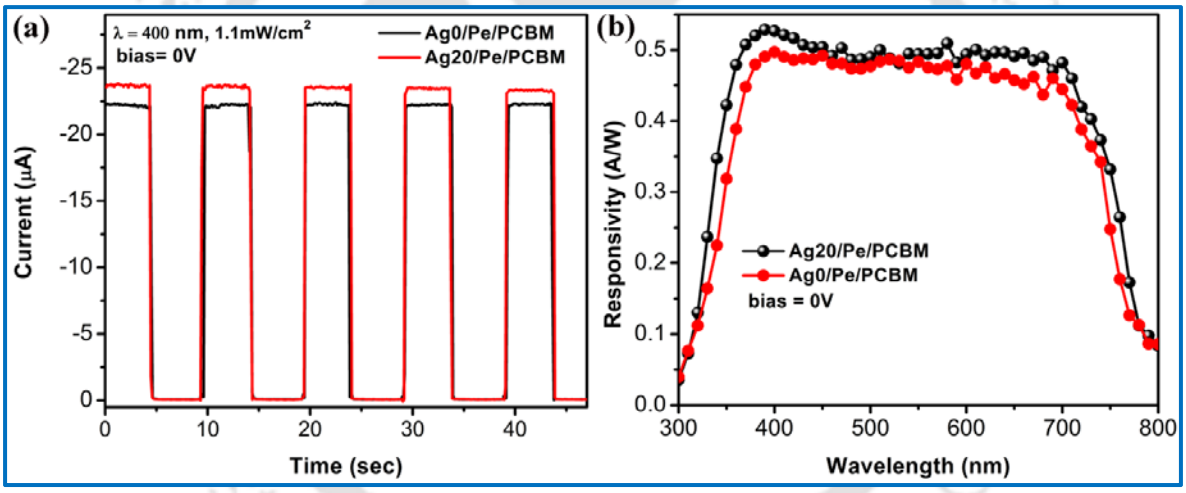

Fig. 6.9: (a) Time-dependent photocurrent response of the pristine and hybrid photodetector under zero bias with 400 nm light of intensity 1.1 mW/cm^2, with PCBM as electron transporting layer. (b) The spectral responsivity of pristine and hybrid photodetector at zero bias with PCBM as the ETL.

Although the devices with organic ETL layer shows higher photocurrent and improved responsivity than the ETL free device, as shown in **Fig. 6.9**, such organic layers are not desirable considering the cost, toxicity, and stability issues.[20] Note that in presence of Ag NPs, the enhancement of the PC of the hybrid device with ETL is much less than the ETL free device. **Fig. 6.9(b)** shows the spectral responsivity of the pristine and hybrid photodetector with the PCBM as ETL. Note that with ETL, the enhancement of responsivity in the hybrid device is much smaller than the pristine device. Thus the plasmonic effect of the Ag NPs is dominant in the device without

ETL and hence it is advantageous to incorporate the plasmonic NPs in the ETL free PDs for improved performance.

Next, we address the issue of stability of the plasmonic-perovskite device. Organometal halide perovskite, especially, $CH_3NH_3PbI_3$ usually shows very poor stability in the ambient atmosphere, and it degrades very fast in the presence of water and oxygen molecules.[20] **Fig. 6.10** shows the normalized photocurrent as a function of the time exposed in ambient air up to 50 hr with humidity ~65%. Note that we have measured our device without any encapsulation or protection. The Ag NPs can also react with organometal halide perovskites. This may be responsible for the fast degradation of the device. We believe that the encapsulation of the device will significantly improve the stability of the device.

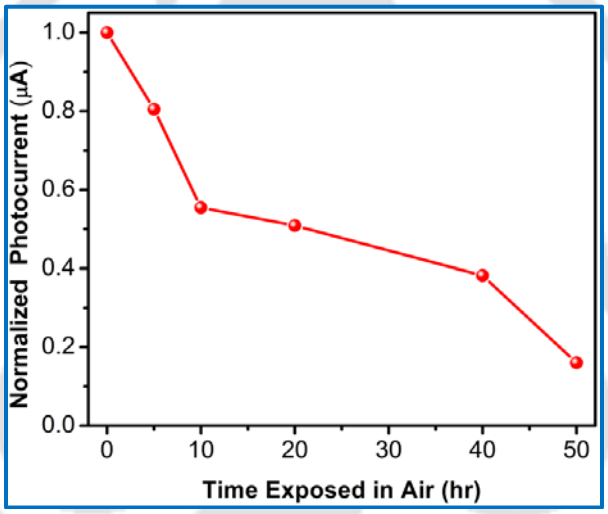

Fig. 6.10: Normalized photocurrent of the plasmonic perovskite photodetector with time exposed in ambient air with humidity ~ 65% after fabrication.

Note that we added Ag NPs dispersion with PEDOT:PSS and sonicated thoroughly to make a homogeneous dispersion. So, we expect that the maximum Ag NPs are embedded in PEDOT:PSS layer or coated with PEDOT:PSS, which are separated from the perovskite interface. Though some NPs may be there in the interface with the Pe layer, which can react and degrade the Pe layer.

6.3.4. Mechanism of Improved Photodetection

To gain a better insight into the change in the electronic structure of PEDOT:PSS with the addition of Ag NPs, we further performed KPFM analysis, as it is sensitive to the surface work function of materials. The comparison of the work function of Ag0 and Ag20 layers was estimated by KPFM. **Fig. 6.11(a) and (c)** shows the AFM topography of the Ag0 and Ag20 layer, while **Fig. 6.11(b)**

and (d) shows the surface potential image of Ag0 and Ag20, respectively. The Ag0 (bare PEDOT:PSS film) shows the surface potential in the range 0 - 0.244 V, while Ag20 shows values in the range 0 - 0.197 V. As the KPFM image indicated a uniform distribution of the surface potential across multiple spots that we imaged, we can assume that the surface potential of pristine and PEDOT:PSS film with Ag NPs is uniform on a macroscopic scale. Thus 0.047 V decrease in surface potential of the Ag20 film corresponds to its higher work function by 47 meV than that of the Ag0 film.[21, 22]

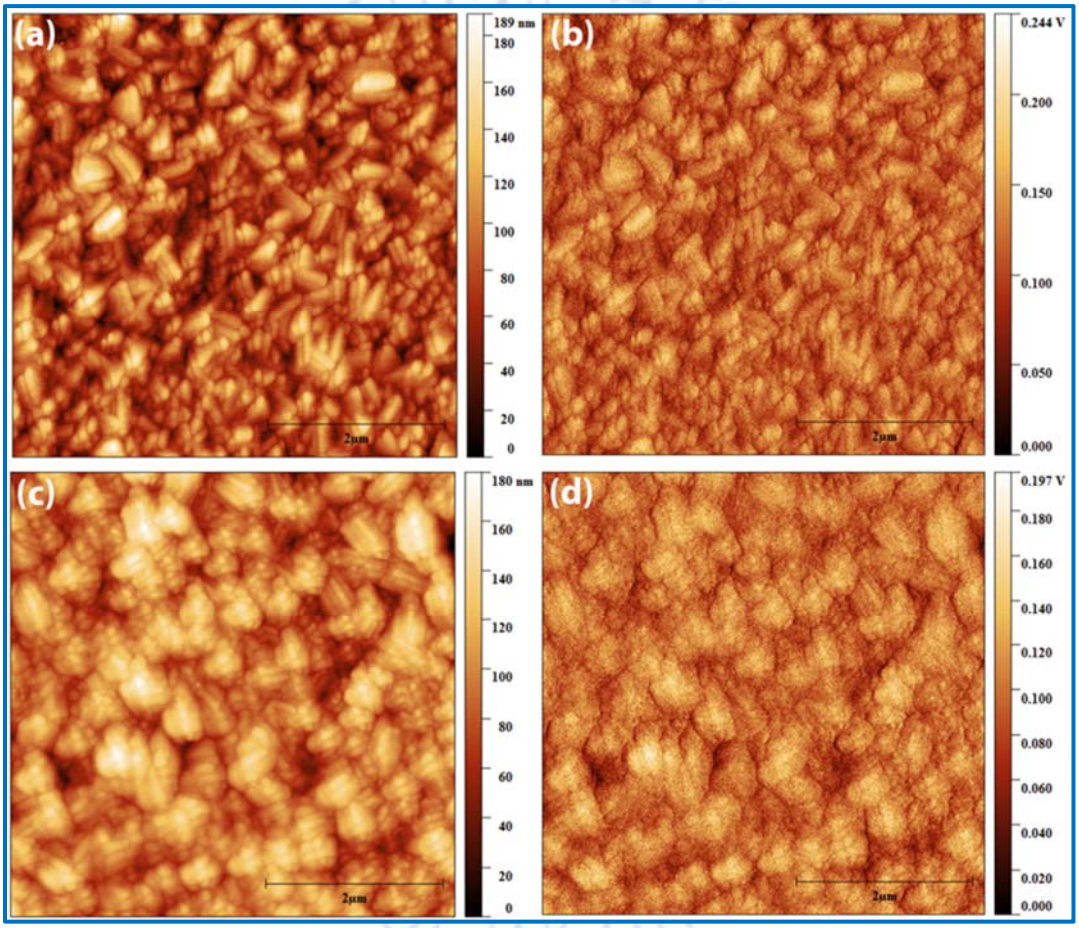

Fig. 6.11: (a, c) AFM surface topography images of FTO/Ag0 and FTO/Ag20 film, respectively. (b, d) The corresponding KPFM surface potential images.

The change of the work function and band alignment of the hybrid device is shown in **Fig. 6.12**.[18 6 23] Under light excitation, electron-hole pairs were generated in Pe active layer. Due to the built-in potential, these holes were transferred to the PEDOT:PSS side and finally reached the FTO electrode, while the electrons were transferred to the Al counter electrode, as shown in **Fig. 6.12.** Thus, we observed substantial photocurrent in the external circuit without external bias. Note that

from the KPFM analysis, we observed a higher work function of Ag20 film than Ag0 film, as shown in **Fig. 6.11**. The dashed line in **Fig. 6.12** for PEDOT:PSS layer shows the work function of Ag0, while the solid line corresponds to the work function of Ag20. Thus, the increase in the work function of Ag20 brings it closer to that of the Pe film, and it helps to reduce the energy barrier between the FTO/Pe interface.[24] This enables a superior carrier transport resulting in improved photodetection performance of Ag20. In presence of light, hot electron can also be generated in the plasmonic Ag NPs, as shown in **Fig. 6.12,** which further increases the PC of the hybrid device compared to the pristine PD.

Therefore, the enhanced performance of the ETL-free hybrid Pe PD is attributed to (a) plasmon-enhanced higher optical absorption and hot electron generation, and (b) improved charge extraction and transport in PEDOT:PSS film with Ag NPs by favorable band alignment. It is quite likely that hot electrons contribute significantly to the improved performance of the ETL-free hybrid PD demonstrated here. Further optimization of the plasmonic layer may lead to more improved device performance.

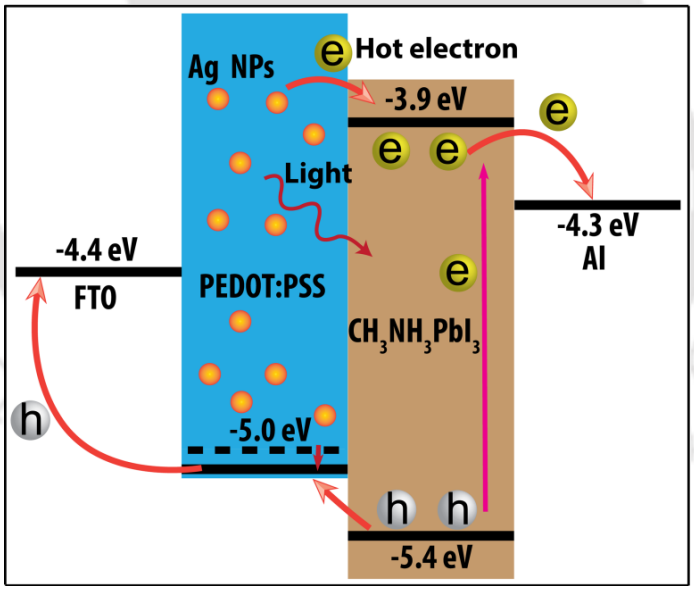

Fig. 6.12: Schematic of the band diagram illustrating the charge separation and transport processes in hybrid photodetector under zero bias.

6.4. Conclusions

In conclusion, we have demonstrated the superior performance of the ETL free self-biased Pe PD by integrating the plasmonic Ag NPs in the HTL layer. A novel N_2 gas-assisted fast crystallization method is used for the Pe active layer deposition to form a uniform Pe layer as compared to the

conventional deposition method in ambient condition. In absence of any external bias, the responsivity of the hybrid device is enhanced by ~45% compared to the pristine device due to the Ag NPs, with a peak responsivity of 0.25 AW^{-1}, while the detectivity is enhanced from 1.04×10^{11} Jones (pristine device) to 1.53×10^{11} Jones (hybrid device). The hybrid device also shows about three times faster photoresponse as compared to the pristine device. Under small reverse bias (0.5V), the hybrid device exhibited a peak responsivity of 3.61 A/W, which is significantly higher than the Si-based commercial PDs. The improved performance of the hybrid PD is attributed to plasmon-enhanced optical absorption, as well as improvement in charge extraction and transport by Ag NPs, which are evidenced by the steady-state and time-resolved PL analysis. Impedance analysis of the devices shows the reduced carrier transfer resistance of the hybrid device, which results in superior transport of photogenerated charge carriers. Kelvin probe force microscopy analysis revealed the change in the work function of PEDOT:PSS film with Ag NPs and suitable band alignment, which enables superior carrier transport resulting in improved photodetection performance for the hybrid device. Our results open up the possibility of fabrication of air processed low-cost plasmonic perovskite photodetectors with high performance without any ETL layer.

References

1. L. Dou, Y. Yang, J. You, Z. Hong, W.-H. Chang, G. Li and Y. Yang, *Nat. Commun.*, 2014, **5**, 5404.
2. X. Wang, M. Li, B. Zhang, H. Wang, Y. Zhao and B. Wang, *Org. Electron*, 2018, **52**, 172-183.
3. H. Wang and D. H. Kim, *Chem. Soc. Rev*, 2017, **46**, 5204-5236.
4. G. Konstantatos and E. H. Sargent, *Nat. Nanotechnol.*, 2010, **5**, 391.
5. H. Wang, J. W. Lim, L. N. Quan, K. Chung, Y. J. Jang, Y. Ma and D. H. Kim, *Adv. Opt. Mater*, 2018, **6**, 1701397.
6. C. Xie and F. Yan, *J. Mater. Chem. C*, 2018, **6**, 1338-1342.
7. C. Bao, W. Zhu, J. Yang, F. Li, S. Gu, Y. Wang, T. Yu, J. Zhu, Y. Zhou and Z. Zou, *ACS Appl. Mater. Interfaces*, 2016, **8**, 23868-23875.
8. K. Mahmood, S. Sarwar and M. T. Mehran, *RSC Adv.*, 2017, **7**, 17044-17062.
9. J. Ghosh and P. K. Giri, *AIP Conf. Proc.*, 2019, **2082**, 050004.
10. R. Ghosh, J. Ghosh, R. Das, L. P. L. Mawlong, K. K. Paul and P. K. Giri, *J. Colloid Interface Sci.*, 2018, **532**, 464-473.
11. J. Li, S. Yuan, G. Tang, G. Li, D. Liu, J. Li, X. Hu, Y. Liu, J. Li, Z. Yang, S. F. Liu, Z. Liu, F. Gao and F. Yan, *ACS Appl. Mater. Interfaces*, 2017, **9**, 42779-42787.
12. J. Ghosh, R. Ghosh and P. K. Giri, *Sens. Actuator B-Chem.*, 2018, **254**, 681-689.
13. A. Sharma, B. Bhattacharyya, A. K. Srivastava, T. D. Senguttuvan and S. Husale, *Sci. Rep.*, 2016, **6**, 19138.
14. S. Tong, H. Wu, C. Zhang, S. Li, C. Wang, J. Shen, S. Xiao, J. He, J. Yang, J. Sun and Y. Gao, *Org. Electron*, 2017, **49**, 347-354.

15. Y. Wang, Q. Song, T. Lin, Y. Fu, X. Sun, B. Chu, F. Jin, H. Zhao, W. Li, Z. Su and Y. Li, *Org. Electron*, 2017, **49**, 355-359.
16. Y. Wang, T. Zhang, P. Zhang, D. Liu, L. Ji, H. Chen, Z. D. Chen, J. Wu and S. Li, *Org. Electron*, 2018, **57**, 263-268.
17. L. Li, C. Wang, C. Wang, S. Tong, Y. Zhao, H. Xia, J. Shi, J. Shen, H. Xie, X. Liu, D. Niu, J. Yang, H. Huang, S. Xiao, J. He and Y. Gao, *Org. Electron*, 2019, **65**, 162-169.
18. C. H. Ji, K. T. Kim and S. Y. Oh, *RSC Adv.*, 2018, **8**, 8302-8309.
19. Z. Liang, P. Zeng, P. Liu, C. Zhao, W. Xie and W. Mai, *ACS Appl. Mater. Interfaces*, 2016, **8**, 19158-19167.
20. Y. Liyan, T. B. Alexander, G. L. David and W. Tao, *Rep. Prog. Phys.*, 2016, **79**, 026501.
21. P. Wang, D. Tanaka, S. Ryuzaki, S. Araki, K. Okamoto and K. Tamada, *Appl. Phys. Lett.*, 2015, **107**, 151601.
22. S. Intu and B. R. Mehta, *Nanotechnology*, 2017, **28**, 445701.
23. P. Chen, Z. Xiong, X. Wu, M. Shao, Y. Meng, Z.-h. Xiong and C. Gao, *J. Phys. Chem. Lett.*, 2017, **8**, 3961-3969.
24. Z. Zhao, Q. Wu, F. Xia, X. Chen, Y. Liu, W. Zhang, J. Zhu, S. Dai and S. Yang, *ACS Appl. Mater. Interfaces*, 2015, **7**, 1439-1448.

भारतीय प्रौद्योगिकी संस्थान गुवाहाटी
Indian Institute of Technology Guwahati

Chapter 7

Vacuum Deposited PbI_2 Film Grown at Elevated Temperature for Improved Efficiency of Planar Perovskite Solar cells

In this chapter, we investigate on the vacuum deposition of lead iodide (PbI_2) film at elevated substrate temperature and its conversion into high-quality $CH_3NH_3PbI_3$ perovskite (Pe) film using two-step vapor-solution deposition process for the fabrication of large-area perovskite solar cells. Our studies revealed that at elevated substrate temperature, the PbI_2 films were very compact and pinhole-free with higher crystallinity. In particular, the Pe films made with PbI_2 layer deposited at 150 ºC possess large grain size and pinhole-free morphology, and they exhibit very high absorption and low radiative recombination as compared to the film deposited at room temperature, which is beneficial for high-performance solar cells. Interestingly, the power conversion efficiency (PCE) was improved by ~66% for PbI_2 layer deposited at 150 ºC of substrate temperature compared to the film grown at room temperature. These devices show enhanced ambient stability as compared to the case of the PbI_2 layer deposited at room temperature. Our results demonstrate that the spin-coating free and toxic solvent-free two-step green vacuum-solution deposition technique is suitable for large-area Pe solar cells with improved efficiency.

7.1. Introduction

Recently, the PCE of Pe solar cells has achieved over 23%.[1, 2] However, most of the studies on Pe solar cells are based on the typical size of approximately only 0.1 cm^2. Generally, for the deposition of Pe layer, single-step spin coating, or sequential two-step spin coating methods are used.[3-5] In a single-step spin-coating method, Pe precursor is directly deposited while in the two-step deposition method, first, the inorganic part (PbI_2) is deposited and then the organic component (CH_3NH_3I) is deposited on top of it for its conversion into Pe layer.[5] Different types of modified spin-coating methods for deposition of Pe layer, such as solvent engineering, anti-solvent assisted crystallization, gas-assisted nucleation, etc. have been already explored to form homogenous Pe films directly from the Pe precursor solution.[6-10] However, the deposition of large-area Pe film for commercial applications by the spin-coating method is still challenging due to the complexity of the processing and reproducibility of the devices. In the case of the spin-coating method, different

toxic and volatile organic solvents such as DMF, DMSO are also used, which is not desirable. Thus, it is imperative to explore alternative green methods for the deposition of Pe film without toxic solvents. Fabrication of large-area pinhole-free Pe films for solar cells by novel alternative methods are still very challenging. Interestingly, several spin-coating free deposition techniques for Pe film, such as dual-source co-evaporation, have also been reported.[11] Liu et al. reported on the fabrication of homogeneous Pe film by using the dual-source co-evaporation with PCE of 15.4%.[12] However, it's very difficult to control the deposition of CH_3NH_3I in the dual-source co-evaporation technique and proper reaction between PbI_2 and CH_3NH_3I to form the final Pe film does not always take place. Thus, one can look for a combined method, such as vapor-solution deposition, to grow high-quality Pe film.

In this present chapter, we have studied the effect of substrate temperatures for the growth vacuum-deposited of PbI_2 layer. These PbI_2 layers were dipped into CH_3NH_3I solution and annealed at 90ºC, which result in the growth of Pe film. The Pe film using PbI_2 film deposited at 150ºC of substrate temperature shows pinhole-free and compact superior morphology. The average PCE of Pe solar cells using PbI_2 film deposited at 30ºC was observed to be 7.9 %, while for the device using PbI_2 film deposited at 150ºC, PCE was found to be 13.1%. Thus 66% increase in PCE is attributed to improved quality Pe film with pinhole-free compact morphology and superior optical absorbance in solar cells using the PbI_2 layer deposited at elevated temperature of 150ºC.

7.2. Experimental Details

7.2.1. Sample Preparation and Device Fabrication

7.2.1.1. Synthesis of CH_3NH_3I

CH_3NH_3I was synthesized by the method described in **Chapter 2, Section 2.2.1.2.**

7.2.1.2. Growth of $CH_3NH_3PbI_3$ film and Fabrication of Solar Cells

First, the fluorine-doped tin oxide (FTO) coated glass substrates with a sheet resistance of 7 Ω/sq were patterned by using zinc powder and HCl solution. Next, the patterned substrates were cleaned sequentially with deionized water, acetone, isopropanol, and ethanol using an ultrasonic cleaner for 10 min each and then dried in N_2 gas flow. Subsequently, the substrates were treated by UV ozone cleaner for 10 min. Next, PEDOT:PSS solution was spin-coated at 4000 rpm for 45 sec on the patterned FTO coated glass substrates, followed by annealing at 125 ºC for 25 min, which acts as a hole transporting layer (HTL). Next, PEDOT:PSS coated substrates were transferred to the

thermal evaporation chamber for the deposition of the PbI_2 layer of thickness of ~ 130 nm at a deposition rate of 5Å/s. For the optimization of the growth, the substrate temperatures (T_s) were varied. The PbI_2 layers deposited at T_s = 30 °C, 50 °C, 100 °C and 150 °C are named as $PbI_2$30, $PbI_2$50, $PbI_2$100 and $PbI_2$150, respectively. After the deposition of the PbI_2 layer, substrates were transferred to N_2 gas-filled glovebox. For the transformation of PbI_2 layers in $CH_3NH_3PbI_3$ Pe film, substrates were then immersed in CH_3NH_3I solution in IPA with a concentration of 10 mg/ml for 5 min. Next, the substrates were immersed in IPA for removal of unreacted residual CH_3NH_3I and subsequently annealed at 90 ºC for 10 min resulting in films transforming into deep brown color. **Fig. 7.1** shows a schematic illustration of the two-step vacuum-solution deposition process for the growth of the $CH_3NH_3PbI_3$ Pe layer.

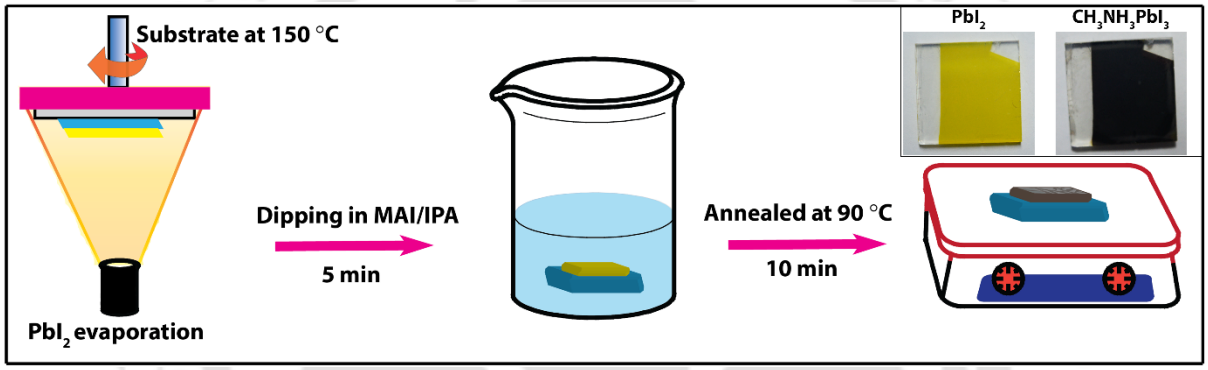

Fig. 7.1: Schematic of the two-step vapor-solution deposition process of hybrid perovskite thin-film at elevated temperature. The inset at the top-right corner shows the photograph of PbI_2 film (yellow) and $CH_3NH_3PbI_3$ perovskite (dark brown) film.

The Pe samples are named as Pe30, Pe50, Pe100, and Pe150, corresponding to films $PbI_2$30, $PbI_2$50, $PbI_2$100, and $PbI_2$150, respectively. A 20 mg/mL solution of the PCBM as an electron transporting layer (ETL) is prepared in chlorobenzene and deposited via spin coating at 1000 rpm for 30 s on perovskite layer. Finally, the Al electrodes of thickness ~100 nm are deposited by thermal evaporation. The Pe solar cells thus made are named as D30, D50, D100 and D150 using the Pe30, Pe50, Pe100, and Pe150 films, respectively. The final device area is 0.5cm × 0.5 cm.

7.2.2. Characterization Techniques

The details of the characterization techniques (FESEM, XRD, UV-vis absorbance, PL, TRPL, etc.) used to study the different samples were described in **Chapter 2, Section 2.2.2.** The details of AFM and XPS measurements were described in **Chapter 4, Section 4.2.2.** Different characterizations were done immediately after the fabrication to avoid the degradation of Pe film

in ambient air. Device characteristics were evaluated in ambient air without any encapsulation under a solar simulator (Newport Oriel), AM 1.5G illumination with an intensity of 100 $mWcm^{-2}$ (1 Sun) calibrated with an NREL-certified Silicon reference cell (Photo Emission Tech, USA). Meanwhile, the current density-voltage (J-V) curves were recorded using a digital source meter (Keithley, Model 2400). The photon-to-current conversion efficiency (EQE) spectra were obtained using a solar cell quantum efficiency measurement system (Holmarc, Model HO-SC-QE) calibrated with the silicon reference cell.

7.3. Results and Discussion

7.3.1. Morphology Analysis

For the development of large-area Pe solar cells for commercialization, it is essential to explore alternative techniques different from the most explored spin coating method for the Pe deposition. Here, the light-absorbing Pe active layer was deposited by a modified two-step vacuum-solution deposition method without the help of the spin coating technique. **Fig. 7.1** shows a schematic illustration of the two-step vacuum-solution deposition process for the growth of the $CH_3NH_3PbI_3$ Pe layer. First, the PbI_2 layer was deposited by vacuum thermal evaporation technique on top of PEDOT:PSS coated FTO substrates. The substrate temperature was varied (30°C, 50°C, 100°C and 150°C) for different samples for the deposition of PbI_2 layer. Note that in thermal evaporation, the thickness of the film and substrate temperature can be controlled precisely, which are very difficult in the spin coating method.[13, 14] After the deposition of the PbI_2 layer, the substrates were dipped into the IPA solution containing CH_3NH_3I (10 mg/ml) for 5 min, as shown in **Fig. 7.1**. Next, the substrates were annealed on a hotplate at 90 °C for 10 min to form the $CH_3NH_3PbI_3$ Pe layer. In the process of dipping, the CH_3NH_3I solution diffuses into the PbI_2 layer and reacts with it through the grain boundaries of PbI_2 crystals, and crystallization occurs during the annealing.[15] The inset of **Fig. 7.1** shows the digital photographs of the PbI_2 and Pe films. After dipping in CH_3NH_3I/IPA solution and annealing, the shining yellow color of vapor-deposited PbI_2 film turns into a shining black color confirming the formation of $CH_3NH_3PbI_3$. Note that in our vapor-solution deposition technique for the Pe film growth, no toxic solvents are used, which is in stark contrast to the spin coating method that involves the use of different toxic organic volatile solvents, such as DMF or DMSO. Thus, we adopted a relatively green approach for the improvement of solar cell performance, and it can be a good alternative for the deposition/fabrication of Pe thin film-based solar cells.

The morphology and structural properties of the vapor-deposited PbI_2 layer can be controlled by varying the substrate temperatures during the deposition. Here, we have deposited PbI_2 layer at T_s = 30°C, 50°C, 100 °C, and 150°C, at a constant deposition rate. These vapor-deposited PbI_2 layers were used for the growth of Pe film used in the fabrication of solar cells. **Fig. 7.2(a)** shows the FESEM image of the PbI_2 layer deposited at T_s =30°C, while **Fig. 7.2(b)** shows the FESEM image of the PbI_2 layer deposited at T_s = 150°C.

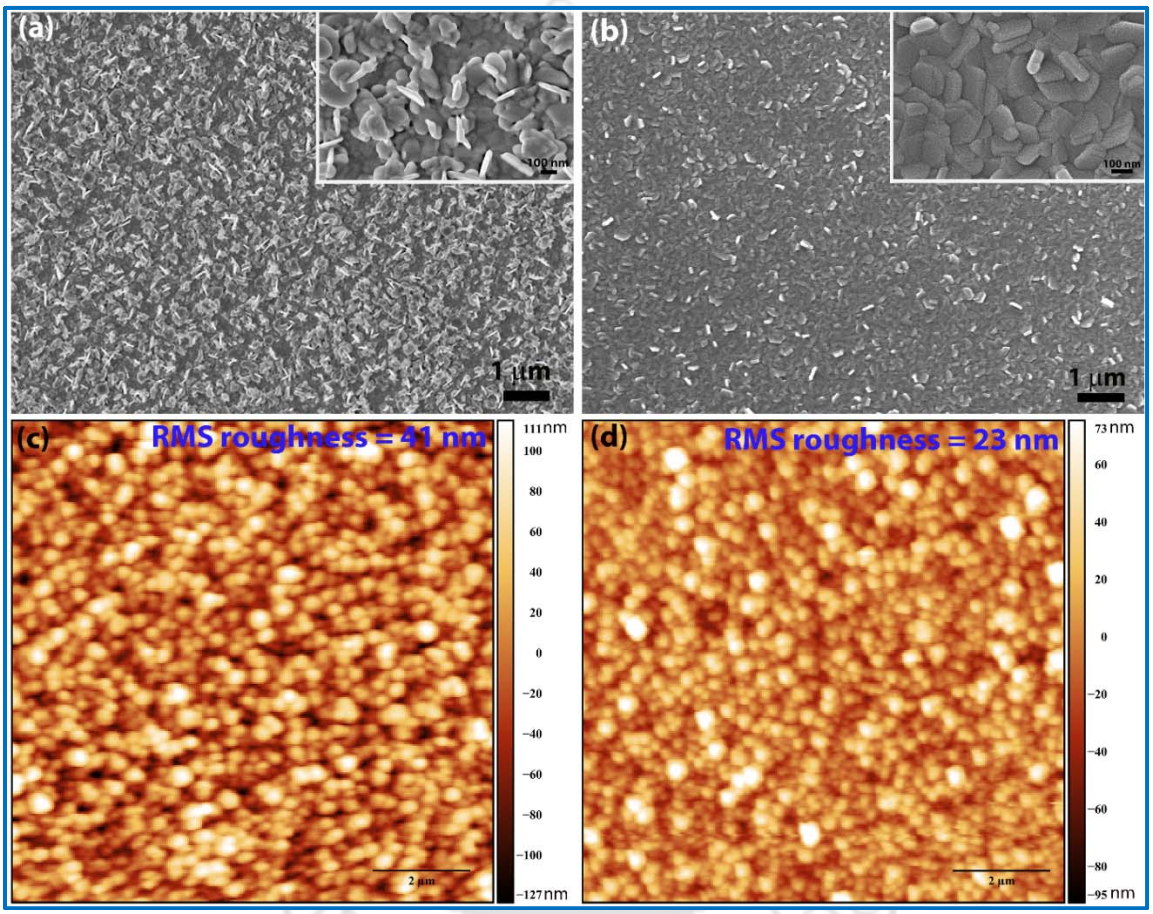

Fig. 7.2: (a) FESEM image of the vapor-deposited PbI_2 layer grown at 30 °C of substrate temperature. The inset shows a higher magnification image of the surface morphology. (b) FESEM image of the vapor-deposited PbI_2 layer grown at 150 °C (substrate temperature). The inset shows a higher magnification image of the surface morphology. (c) AFM micrograph of the $PbI_2$30 film, and (d) AFM micrograph of $PbI_2$150 film. RMS roughness is indicated in each case.

The insets of **Fig. 7.2(a)** and **Fig. 7.2(b)** show the higher magnification image depicting the surface morphology of PbI_2 layers. As shown in **Fig. 7.2(a)**, the morphology of the PbI_2 layer deposited at T_s = 30°C is very rough with pinholes. On the other hand, the PbI_2 layer deposited at T_s = 150°C is smooth, compact, and pinhole-free, as shown in **Fig. 7.2(b)**. It is due to the fact that the higher substrate temperature gives extra thermal energy for oriented crystal growth of PbI_2 molecules,

which result in highly crystalline smooth and pinhole-free compact PbI_2 films and superior device performance.[16-18] In the case of deposition at low substrate temperature, the movement/ alignment of the molecules is minimal due to insufficient thermal energy, and this results in the growth of Pe film with pinholes and finally poor device performance. **Fig. 7.2(c)** and **Fig. 7.2(d)** show the AFM topography images of PbI_2 films deposited at T_s = 30°C and 150°C, respectively. As evident from **Fig. 7.2(c)**, PbI_2 film deposited at T_s = 30°C contains a high density of pinholes with high roughness, while the film deposited at T_s = 150°C is compact and nearly pinhole-free (see **Fig. 7.2(d)**). The corresponding RMS roughness of PbI_2 films is observed to be 41 nm and 23 nm at T_s =30°C and 150°C, respectively. Thus, the RMS roughness is relatively lower for deposition at elevated temperature.

Fig. 7.3(a) and **7.3(b)** show the FESEM image of the morphology of the Pe films Pe30 and Pe150, respectively.

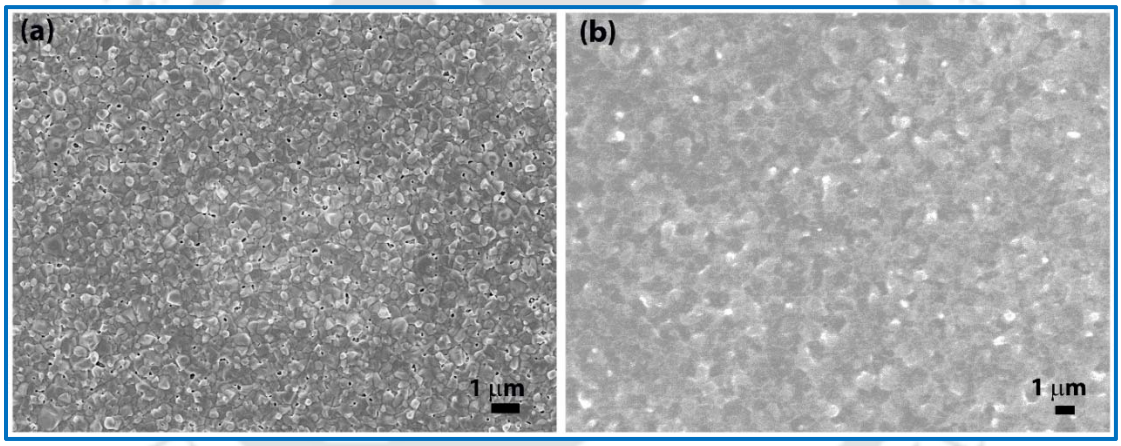

Fig 7.3: (a) FESEM image of $CH_3NH_3PbI_3$ perovskite film using $PbI_2$30 film showing a lot of pinholes. (b) FESEM image of $CH_3NH_3PbI_3$ perovskite film using $PbI_2$150 film showing pinhole-free morphology.

It is evident that the Pe30 sample contains a lot of pinholes, and the surface is very rough compared to that of Pe150. The high roughness along with many pinholes in the Pe30 layer is due to the higher roughness of the corresponding PbI_2 layer deposited at T_s = 30°C. In contrast, the Pe150 is relatively smooth and compact with no visible pinholes due to the nearly pinhole-free PbI_2 layer deposited at T_s = 150°C. This high-quality Pe layer is responsible for the high optical absorbance of the film (discussed later). Due to the smooth and compact nature of the Pe film with large grains, the recombination of photogenerated carriers is reduced (discussed later). Thus, improved separation and transport of carriers in the Pe150 film leads to the superior performance of the corresponding solar cell.

7.3.2. Structural Analysis

The phase, crystalline quality, and microstructure of PbI_2 and Pe films were assessed by XRD analysis. **Fig. 7.4(a)** shows the XRD pattern of PbI_2 film deposited at T_s = 30 °C, 50°C, 100°C and 150°C, respectively.

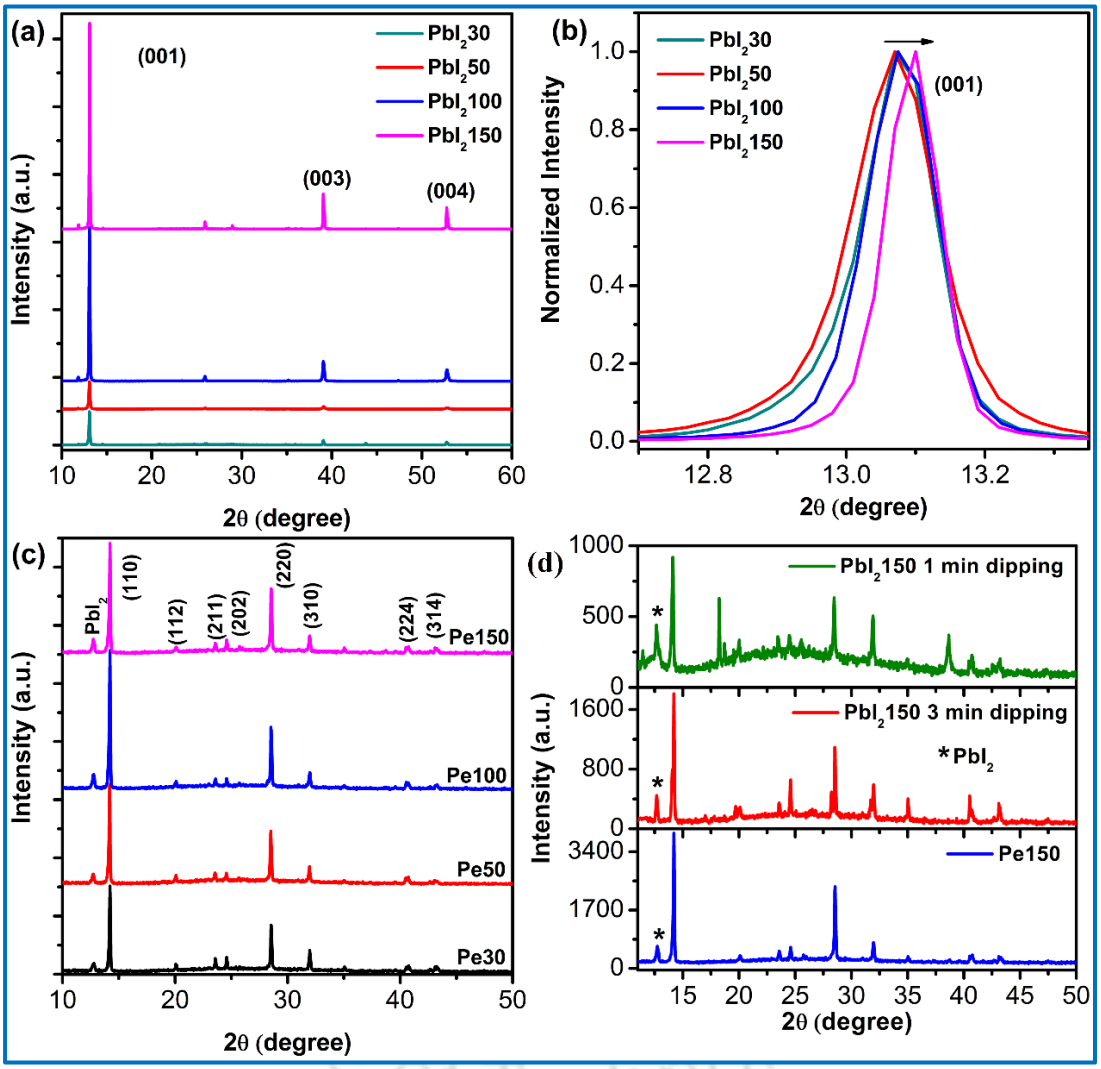

Fig 7.4: (a) Comparison of the XRD pattern of PbI_2 layer deposited at substrate temperatures of 30°C, 50°C, 100°C and 150°C, respectively. (b) Comparison of normalized XRD pattern of PbI_2 corresponding to (001) XRD peak. (c) XRD pattern of Pe30, Pe50, Pe100, and Pe150 perovskite films. (d) Comparison of the XRD pattern of PbI_2 films after 1 min, 3min, and 5 min of dipping into the CH_3NH_3I solution.

In **Fig. 7.4(a)**, the diffraction peaks at 2θ=13.05º, 39.05º, and 52.79º are assigned to (001), (003), and (004) planes of PbI_2, respectively.[19] Considering the XRD intensity pattern in **Fig. 7.4(a)**, all the PbI_2 films show preferred C (001) axis orientation. Interestingly, as the substrate temperature is increased systematically from 30 °C to 150°C, the XRD peak intensity is systematically

increased. Note that the thickness of the PbI_2 layer is almost identical for all the samples. Thus, the higher intensity peak at higher substrate temperature is attributed to the enhanced crystallinity of the respective samples. We believe that the higher substrate temperature provides extra energy to the molecules to form highly crystalline PbI_2 films, which eventually yields high-quality Pe film with enhanced performance in the solar cells. **Fig. 7.4(b)** shows a normalized XRD pattern for (001) peak for different samples. It reveals that with the increase in substrate temperature, the full width at half maxima (FWHM) of (001) XRD peak decreases systematically along with the upshift of the peak for $PbI_2$150. The $PbI_2$150 possesses the smallest FWHM implying that it contains bigger size crystallites, and thus the film is most compact in nature. The crystallite size of different samples was calculated using the Scherer equation (**equation 2.1**) using the FWHM of (001) XRD peak.[20, 21] The calculated crystallite sizes for $PbI_2$30, $PbI_2$50, $PbI_2$100, and $PbI_2$150 are ~64 nm, 56 nm, 70 nm, and 93 nm, respectively. Thus, crystallite size is the largest for the PbI_2 film deposited at T_s = 150 °C. Note that the calculated values of crystallite sizes are smaller than the corresponding grain sizes observed from the FESEM images.

For the transformation of PbI_2 films to $CH_3NH_3PbI_3$ perovskite layer, PbI_2 films are dipped in CH_3NH_3I/IPA solution and subsequently annealed at 90 °C. The XRD pattern of different Pe films grown with PbI_2 films grown at different substrate temperatures is shown in **Fig. 7.4(c)**. XRD peaks at 14.21°, 20.09°, 23.57°, 24.59°, 28.55°, 31.97°, 40.61°, and 43.28° can be assigned to (110), (112), (211), (202), (220), (310), (224), and (314) crystal planes of $CH_3NH_3PbI_3$, respectively. These peaks imply the tetragonal structure of the $CH_3NH_3PbI_3$ film. Besides the standard peaks for Pe, all the samples have an extra peak at ~12.9°, which may be due to the unreacted residue of PbI_2 (001). Interestingly, it has been reported that the Pe film with some residue of PbI_2 shows better performance in solar cells.[15, 22] Note that the penetration depth of CH_3NH_3I into a compact PbI_2 layer is of the order of a few tens of nm from the surface. Interestingly, though the vapor-deposited PbI_2 layer is very compact, it consists of submicrometer size PbI_2 grains, as revealed from **Fig. 7.2**. Thus, during its dipping into the CH_3NH_3I solution, CH_3NH_3I diffuses through the grain boundaries of the PbI_2 layer and finally forms compact Pe film.[15] For optimization purposes, we have also varied the dipping time into the CH_3NH_3I solution and observed a higher amount of unreacted PbI_2 for lower dipping time. We find that 5 min of dipping time allows most of the PbI_2 to convert to $CH_3NH_3PbI_3$, as shown in **Fig. 7.4(d)**. Thus, the highly compact pinhole-free large area Pe film could be obtained using a two-step vapor-solution

deposition method. Our method allows the growth of large-area Pe film for commercial Pe solar cells without the use of the convention spin coating method.

To investigate the chemical state and transformation of PbI_2 film into Pe, XPS analysis was performed.

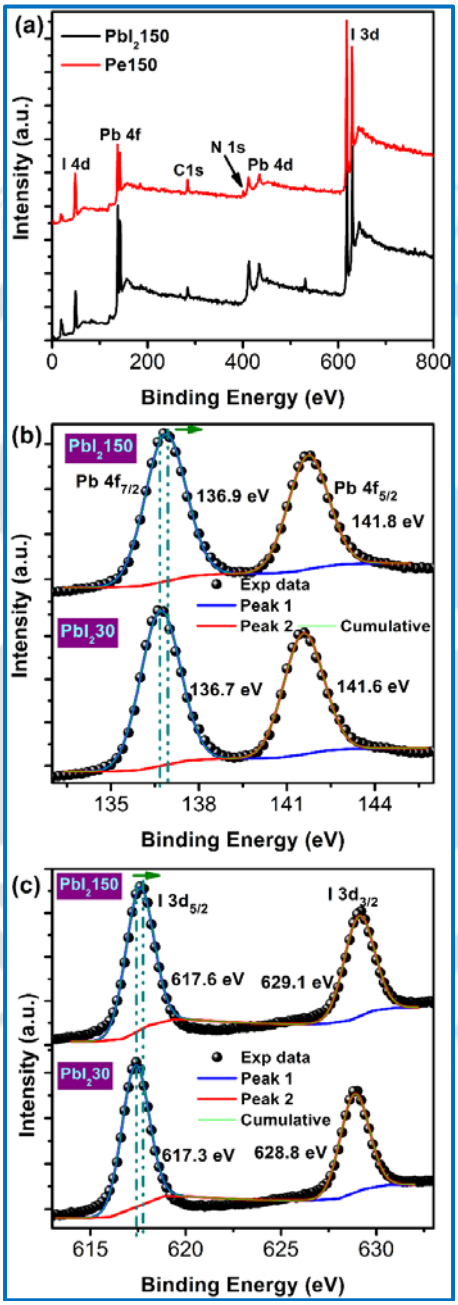

Fig 7.5: (a) (a) XPS survey scan spectra of $PbI_2$150 and Pe150. The peak associated with N at 401 eV in Pe150 confirms the formation of the perovskite phase. (b) Comparison of Pb 4f core-level XPS spectra of $PbI_2$30 and $PbI_2$150 with Gaussian fittings. (c) Comparison of I 3d core-level XPS spectra of $PbI_2$30 and $PbI_2$150 with Gaussian fittings.

Fig. 7.5(a) represents the survey scan XPS spectra for bare PbI_2 film and the Pe film in the range 0-800 eV. The presence of Pb and I is evident from the spectrum of the PbI_2 film. The presence of low-intensity carbon peak is due to the contamination/adsorption from the ambient air. In the case of Pe film, an additional peak associated with N at 401 eV was observed, which confirms the transformation of PbI_2 into Pe. Note that the intensity of the carbon 1s peak is relatively higher in the Pe film, as expected. **Fig. 7.5(b)** shows the high-resolution XPS spectra associated with Pb 4f of PbI_2 film deposited at T_s = 30°C and 150°C. In $PbI_2$30, the peaks at 136.7 eV and 141.6 eV correspond to Pb $4f_{7/2}$ and $4f_{5/2}$, respectively, while for $PbI_2$150, the corresponding peaks were observed at a binding energy of 136.9 eV and 141.8 eV, as shown in **Fig. 7.5(b)**. **Fig. 7.5(c)** depicts the high-resolution XPS spectra associated with I 3d of PbI_2 film deposited at T_s = 30°C and 150°C. The peaks at ~617.3 eV and 628.8 eV for $PbI_2$30 represent I $3d_{5/2}$ and $3d_{3/2}$, respectively, while for $PbI_2$150, the peaks were observed at ~617.6 eV and 629.1 eV, respectively. Thus, the XPS peaks in $PbI_2$150 shifted slightly to higher binding energy, which may be attributed to the rearrangement of crystal structure due to the substrate heating during deposition. Note that a carbon peak with higher intensity is also observed in the Pe film.

7.3.3. Optical Studies

Optical absorption spectra of Pe film in the UV-visible range using the PbI_2 layer deposited at different substrate temperatures are shown in **Fig. 7.6(a)**. All the films exhibit a broad spectral absorption in the range of 380-780 nm with high absorbance. Interestingly, the absorbance of the Pe films was found to be higher for the PbI_2 film deposited at higher substrate temperatures. This is attributed to the improved crystal structure and pinhole-free compact Pe film obtained from the PbI_2 layer deposited at higher substrate temperatures. Note that in the vacuum-solution deposition process, the thickness of the Pe layer can be controlled precisely, which is difficult to control in the spin coating method. It will be shown below that due to the high optical absorbance, solar cell performance is superior for Pe100 and Pe150 film. We have further estimated the bandgap of each sample using the Tauc plot considering the direct bandgap nature of the Pe film. **Fig. 7.6(b)** shows the Tauc plot for different samples. From the Tauc plot, bandgaps were found to be 1.6, 1.59, 1.57, and 1.56 eV for Pe30, Pe50, Pe100, and Pe150, respectively. Thus, the bandgap was found to decrease marginally with the increase in the substrate temperature of PbI_2 deposition, which may be associated with reduced lattice strain for higher temperature deposition. However, the higher

absorbance of the films grown with higher substrate temperatures is most beneficial for the solar cell application.

To study the photo-induced charge carriers and their relaxation dynamics, steady-state PL and TRPL measurements were carried out on Pe films. **Fig. 7.6(c)** shows the comparison of PL spectra for Pe30, Pe50, Pe100, and Pe150 on PEDOT:PSS/FTO glass. The PL peak with center at ~774 nm was observed for each sample, which is attributed to the excitonic recombination of $CH_3NH_3PbI_3$. Interestingly, the intensity of the PL peak is much lower for the Pe films grown at higher substrate temperature, as shown in **Fig. 7.6(c)**, though the absorbance of the corresponding films is higher. Thus, despite higher absorption, the systematic quenching of the PL peaks for Pe150 is attributed to the less radiative recombination and higher separation of excitons in the film.

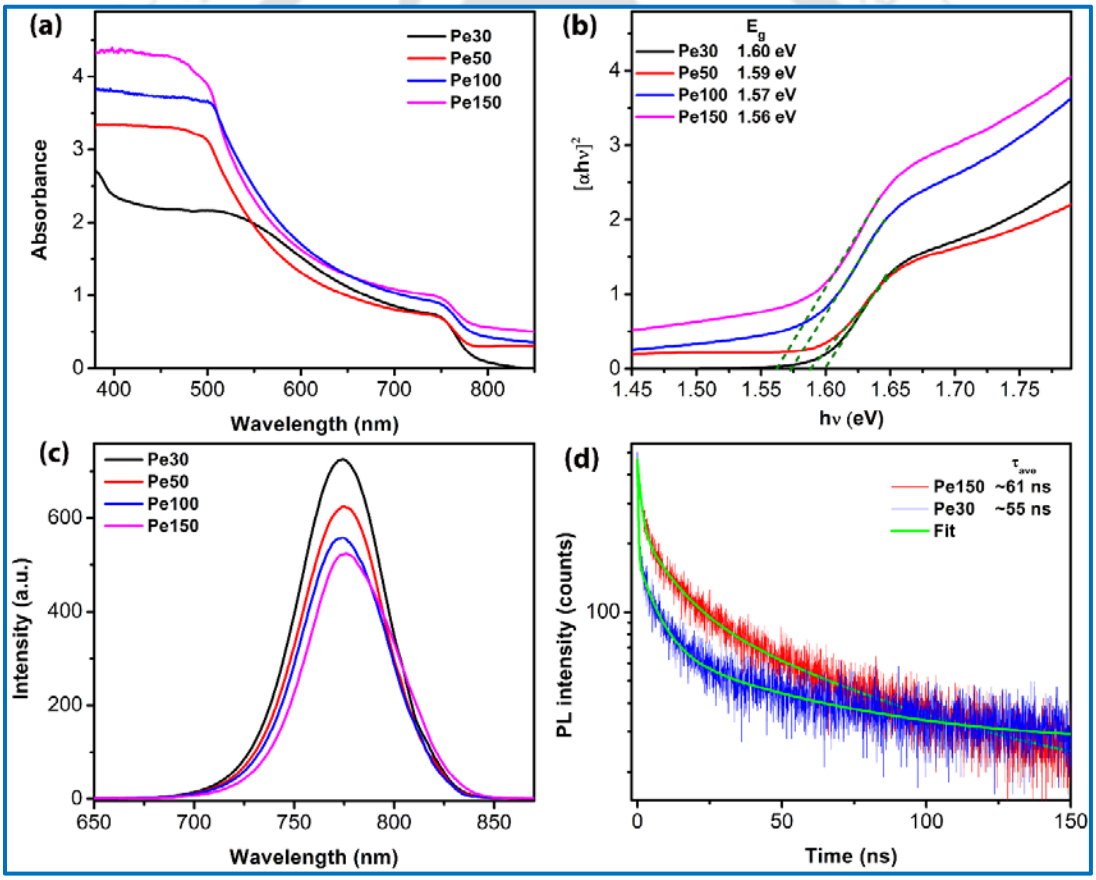

Fig 7.6: (a) Comparison of absorbance spectra of Pe30, Pe50, Pe100, and Pe150 film. (b) Tauc plot for different perovskite samples. Bandgap (Eg) is calculated from the intercept of the extrapolated line (dashed). (b) Comparison of PL spectra of Pe30, Pe50, Pe100, and Pe150 film. (c) Variation of TRPL decay profile of Pe30 and Pe150 with corresponding bi-exponential fitting.

We believe that due to the pinhole-free compact film, the grain boundaries are reduced, and thus the recombination of photogenerated carrier is less in Pe150 as compared to the rough Pe30 film

containing pinholes. The enhanced carrier separation and transport in Pe150 film result in the enhanced photovoltaic performance. The charge carrier dynamics are further studied by TRPL measurement. **Fig. 7.6(d)** shows a comparison of the TRPL decay profiles of Pe150 and Pe30 film on PEDOT:PSS coated FTO substrate monitored at the corresponding PL peak positions. TRPL decay profiles in each case were fitted with a bi-exponential decay function. The two time constants are correlated with the radiative electron-trapping and the radiative electron-hole recombination of halide perovskite. The corresponding average lifetime (τ_{ave}) is found to be 61 ns and 55 ns for Pe150 and Pe30 film, respectively. An increase in the carrier lifetime in Pe150 as compared to Pe30 implies reduced recombination and carrier separation, which is highly beneficial for the solar cell application. The improved carrier lifetime is attributed to the compact pinhole-free perovskite film with a large grain size in Pe150.

7.3.4. Performance of Perovskite Solar cells

The PbI_2 films deposited at different substrate temperatures were finally used for the fabrication of planar Pe solar cells with a structure of glass/FTO/PEDOT:PSS/perovskite/PCBM/Al. Devices were termed as D30, D50, D100, and D150 using Pe30, Pe50, Pe100, and Pe150, respectively. Except for the PbI_2 vapor deposition at different substrate temperatures, other conditions of the device fabrication process were identical for all the cells. **Fig. 7.7(a)** depicts the cross-sectional FESEM image of a Pe solar cell, which shows the different layers.

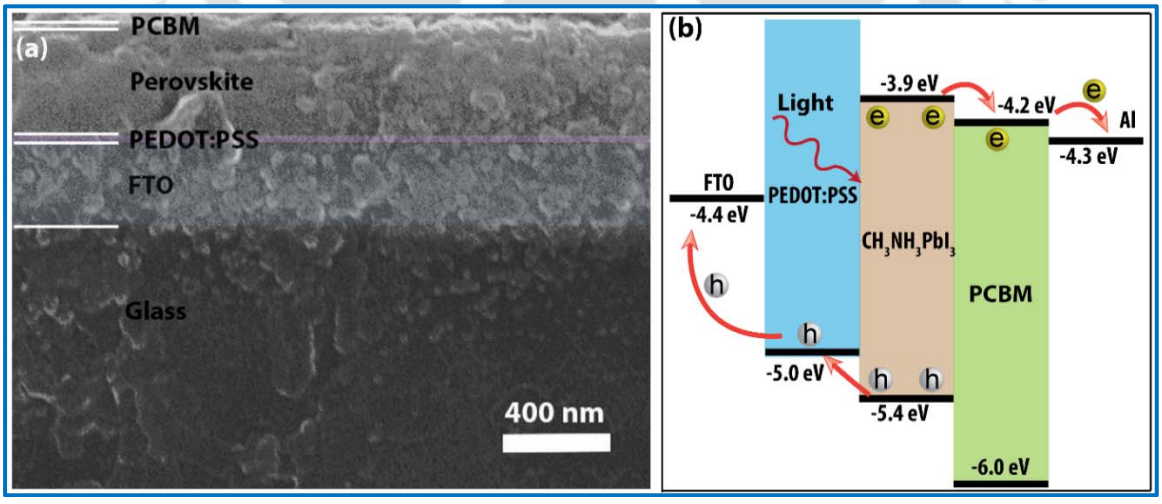

Fig. 7.7: (a) Cross-sectional FESEM image of the perovskite solar cell. (b) Schematic of the energy band diagram illustrating the charge separation and transport processes in perovskite solar cells.

The thickness of the Pe active layer is about ~330 nm. **Fig. 7.7(b)** shows a schematic of the energy band diagram of the Pe solar cell. With light illumination, electron-hole pairs are generated in the Pe active layer. The holes are captured by PEDOT:PSS HTL and transported to the FTO electrode, while the electrons are captured by PCBM ETL and transported in the Al counter electrode.

The photovoltaic performance of the Pe solar cells using PbI_2 films deposited at different substrate temperatures is shown in **Fig. 7.8(a-f)**.

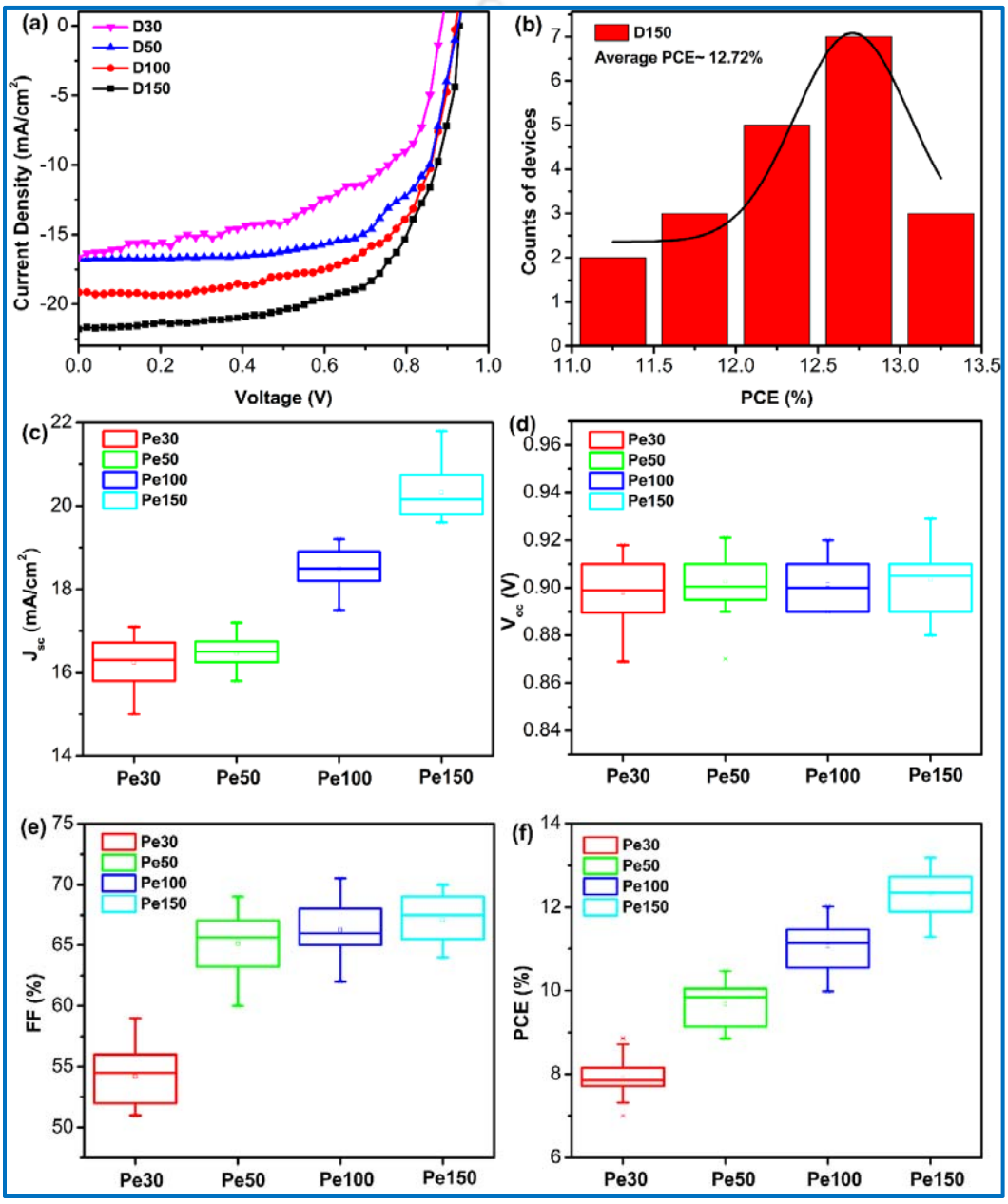

Fig 7.8: (a) Current density-voltage curves of different perovskite solar cells measured under AM 1.5 G illumination at 100 mW cm^{-2}. (b) Histogram of PCE of D150 perovskite solar cell. Statistical distributions of (c) J_{sc}, (d) V_{oc}, (e) FF, and (d) the corresponding PCE of the different groups of perovskite solar cells. Each group consists of 20 cells.

Fig. 7.8(a) shows the J-V characteristics of D30, D50, D100, and D150 Pe solar cells under AM 1.5 G (100 mW/cm^2) light illumination. Note that our device area is 0.25 cm^2, which is significantly higher than the commonly reported cells. Interestingly, with the increase in the substrate temperature (for PbI_2 deposition), the photovoltaic performance of the corresponding devices was improved significantly, as shown in **Fig. 7.8(a)**. The corresponding photovoltaic parameters of different devices are summarized in **Table 7.1**. For the device D30, the power conversion efficiency (PCE) is observed to be 7.9%, whereas PCE for D150 is found to 13.1%, which corresponds to an improvement of PCE by ~66%. Thus, we observed a substantial increase in PCE for D150 as compared to that of D30, which is significant, considering the large area of the solar cells. The improved performance is attributed primarily to the pinhole-free compact, high-quality Pe film with high absorbance in the D150 device.

Table 7.1: *The photovoltaic parameters of different perovskite solar cells.*

Device code	Substrate temperature for vapor deposition PbI_2 (°C)	J_{sc} (mA/cm^2)	V_{oc} (V)	Fill factor (%)	PCE (%)
D30	30	16.6	0.898	53.0	7.9
D50	50	16.8	0.918	67.7	10.4
D100	100	19.2	0.918	65.4	11.5
D150	150	21.8	0.929	64.6	13.1

Fig. 7.8(b) shows a histogram of the device counts with PCE for D150 solar cells. The average PCE of the D150 device was observed to be ~12.7%, while the highest PCE was measured to be 13.1% with device area 0.25 cm^2. Note that al the measurements were performed in ambient air without encapsulation of the device. **Fig. 7.8(c-f)** shows the variation of short circuit current density (J_{sc}), open-circuit voltage (V_{oc}), fill factor (FF), and PCE for different perovskite solar cells. Each of the groups contains 20 numbers of solar cells. As shown in **Fig. 7.8(c)**, J_{sc} was increased in the cell with PbI_2 deposited higher substrate temperatures. Note that the J_{sc} of solar cells is mainly dependent on the absorbance of the active material in the solar cells. As shown in **Fig. 7.6(a)**, the absorbance of Pe films was increased with the increase in substrate temperatures

of PbI_2 film deposition. Thus, the increased absorption of Pe film results in a higher value of J_{sc} for D100 and D150 devices. Further, due to the pinhole-free compact film, the separation and transport of photogenerated carriers are very efficient in D150, which results in the increase in J_{sc} value. The variation of V_{oc} for different cells is nearly similar, as shown in **Fig. 7.8(d)**, though the V_{oc} is slightly higher for D150. Typically, the V_{oc} of the solar cell is determined by the energy difference between the LUMO of the ETL (PCBM layer) and HOMO of the HTL (PEDOT:PSS layer). **Fig. 7.8(e)** shows the variation of fill factors of D30, D50, D100, and D150 devices. The fill factor is increased for the devices with the PbI_2 layer deposited at higher substrate temperatures. Note that the Pe30 film is rough with pinholes and contains more grain boundaries, which increase the series resistance of the device, resulting in the poor fill factor of the corresponding solar cell. **Fig. 7.8(f)** shows the comparison of PCE for different devices, which clearly reveals a systematic increase in the PCE for the devices with the PbI_2 layer deposited at higher substrate temperatures. We have also fabricated solar cells using the PbI_2 layer deposited at above 150°C and observed a reduction in PCE. This may be attributed to the degradation of underlying PEDOT:PSS HTL at higher substrate temperature. Further investigation by optimizing different layers and interfaces maybe lead to high-performance Pe solar cells made by our vapor-solution process.

To address the stability issue, we next studied the storage stability of D30 and D150 devices. The devices were stored in N_2 gas-filled glovebox without encapsulation, and after different storage times, the devices were taken outside the glovebox for PCE measurement. PCE was measured in ambient condition with relative humidity ~55% and without any encapsulation. The change of normalized PCE of D30 and D150 device is shown in **Fig. 7.9(a)**.

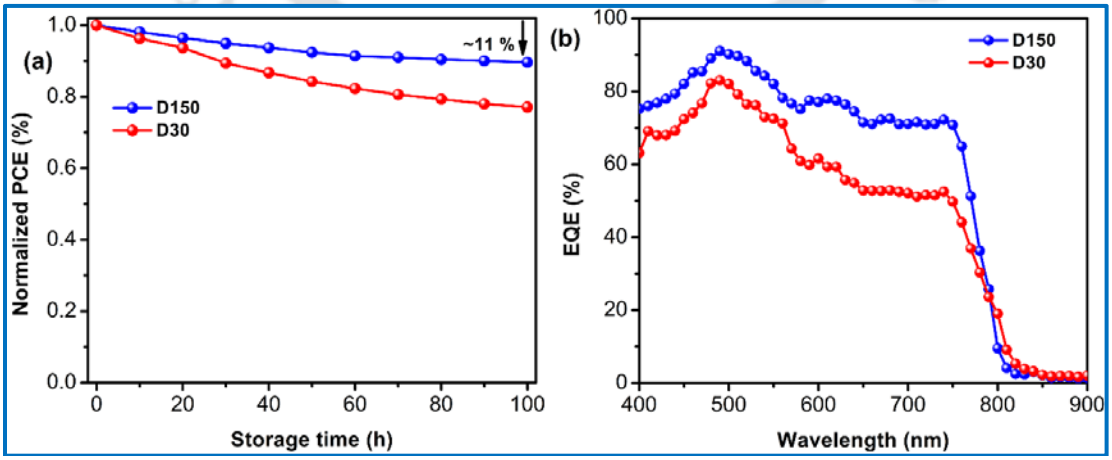

Fig 7.9: (a) Variation of average PCE of D30 and D150 solar cells with storage time. (b) EQE spectra for D30 and D150 solar cells.

Average data were taken over each of the ten devices. Interestingly, the PCE of D30 decreases by ~23% after 100 h of storage, while that of the D150 device shows a decrease of only ~11%. Thus, the solar cells using the PbI_2 layer deposited at 150°C show much higher ambient stability. It is well known that organometal halide Pe material starts degrading upon exposure to water and oxygen molecules, which results in a decrease in PCE of solar cells. Generally, water and oxygen molecules interact near the grain boundaries of Pe and diffuse into it, resulting in faster degradation. In the present case, the Pe150 film is pinhole-free and highly compact as compared to the Pe30 film. Thus, diffusion of water and oxygen molecules is more probable in the Pe30 film due to the high density of pinholes, and this results in the faster degradation of the cells, as shown in **Fig. 7.9(a)**. Interestingly, in our case, some residue of unreacted PbI_2 may be present in the perovskite films, as seen from the XRD analysis. The presence of a small amount of residual PbI_2 is reported in many of the high-efficiency devices. This residual PbI_2 may affect grain boundary passivation and hole-blocking into the devices.[23] In our case, this residue of unreacted PbI_2 may have helped in the improved ambient stability of the devices.

The incident photon-to-current conversion efficiency or external quantum efficiency (EQE) spectra of D30 and D150 devices are shown in **Fig. 7.9(b)** in the wavelength region of 400-900 nm. As shown in **Fig. 7.9(b)**, the EQE value starts increasing at 800 nm, in agreement with the bandgap of the $CH_3NH_3PbI_3$, and reaches peak values around 500 nm. As shown in **Fig. 7.9(b)**, the EQE value of D150 is higher that of D30 devices, which matches well with the PCE results.

7.4. Conclusions

We elucidated the effect of substrate temperatures in the growth of vapor-deposited PbI_2 film and its conversion into high-quality $CH_3NH_3PbI_3$ Pe film using a two-step vapor-solution deposition process for the fabrication of large-area Pe solar cell. With the increase in substrate temperatures, the PbI_2 films were observed to be very compact and pinhole-free along with higher crystallinity. The vacuum-deposited PbI_2 films were transformed into the $CH_3NH_3PbI_3$ Pe film by dipping in the CH_3NH_3I solution, followed by annealing at 90 ºC. The Pe films made using PbI_2 films deposited with higher substrate temperatures (150 ºC) are again very compact with large grains and pinhole-free morphology, and they show very high broad-band absorption and low radiative recombination compared to the Pe film grown using PbI_2 film deposited at 30 ºC, which is highly beneficial for the solar cell application. We further fabricated FTO/PEDOT:PSS/$CH_3NH_3PbI_3$/PCBM/Al planar Pe solar cell using PbI_2 layers deposited at

different substrate temperatures, by keeping the fabrication process identical for all the solar cells. The average power conversion efficiency was observed to be 12.7%, and champion efficiency was found to be 13.1 % with a device area of 5 mm × 5 mm for solar cells using PbI_2 layers deposited at 150 ºC, which is ~66% higher than the device made using PbI_2 layers deposited at 30 ºC. The improved performance is attributed to the reduced recombination and efficient transport of carriers in pinhole-free crystalline film grown at higher substrate temperatures. The devices made using the PbI_2 layer deposited at 150 ºC also show enhanced ambient stability compared to the device made using the PbI_2 layer deposited at 30 ºC. Thus, pinhole-free compact Pe film helps in enhanced stability of the device. Our results demonstrate an effective strategy to develop Pe solar cells without the use of a conventional spin-coating technique. Our results may stimulate further investigations for the vapor-solution process technique for high-efficiency Pe solar cells with high reproducibility.

References

1. Y. Zhou, X. Yin, Q. Zhang, N. Wang, A. Yamamoto, K. Koumoto, H. Shen and H. Lin, *Mater. Today Energy*, 2019, **12**, 363-370.
2. P. Wang, R. Li, B. Chen, F. Hou, J. Zhang, Y. Zhao and X. Zhang, *Adv. Mater.*, **n/a**, 1905766.
3. J.-H. Im, H.-S. Kim and N.-G. Park, *APL Mater.*, 2014, **2**, 081510.
4. N. Yantara, D. Sabba, F. Yanan, J. M. Kadro, T. Moehl, P. P. Boix, S. Mhaisalkar, M. Grätzel and C. Grätzel, *ChemComm*, 2015, **51**, 4603-4606.
5. T. Zhang, N. Guo, G. Li, X. Qian, L. Li and Y. Zhao, *J. Mater. Chem. A*, 2016, **4**, 3245-3248.
6. N. J. Jeon, J. H. Noh, Y. C. Kim, W. S. Yang, S. Ryu and S. I. Seok, *Nat. Mater.*, 2014, **13**, 897-903.
7. J. Zhang, L. Zhang, X. Li, X. Zhu, J. Yu and K. Fan, *ACS Sustain. Chem. Eng.*, 2019, **7**, 3487-3495.
8. M. M. Tavakoli, P. Yadav, D. Prochowicz, M. Sponseller, A. Osherov, V. Bulović and J. Kong, *Adv. Energy Mater.*, 2019, **9**, 1803587.
9. D. Prochowicz, M. M. Tavakoli, A. Solanki, T. W. Goh, K. Pandey, T. C. Sum, M. Saliba and P. Yadav, *J. Mater. Chem. A*, 2018, **6**, 14307-14314.
10. J. Ghosh and P. K. Giri, *AIP Conf. Proc.*, 2019, **2082**, 050004.
11. J. Ávila, C. Momblona, P. P. Boix, M. Sessolo and H. J. Bolink, *Joule*, 2017, **1**, 431-442.
12. M. Liu, M. B. Johnston and H. J. Snaith, *Nature*, 2013, **501**, 395-398.
13. D. Pérez-del-Rey, P. P. Boix, M. Sessolo, A. Hadipour and H. J. Bolink, *J. Phys. Chem. Lett.*, 2018, **9**, 1041-1046.
14. J. Ávila, C. Momblona, P. Boix, M. Sessolo, M. Anaya, G. Lozano, K. Vandewal, H. Míguez and H. J. Bolink, *Energy Environ. Sci.*, 2018, **11**, 3292-3297.
15. K. Li, J. Xiao, X. Yu, T. Li, D. Xiao, J. He, P. Zhou, Y. Zhang, W. Li, Z. Ku, J. Zhong, F. Huang, Y. Peng and Y. Cheng, *Sci. Rep.*, 2018, **8**, 442.
16. R. A. Ismail, A. M. Mousa and S. S. Shaker, *Mater Sci Semicond Process.*, 2019, **99**, 165-174.
17. M. Schieber, N. Zamoshchik, O. Khakhan and A. Zuck, *J. Cryst. Growth*, 2008, **310**, 3168-3173.
18. A. Ioakeimidis, C. Christodoulou, M. Lux-Steiner and K. Fostiropoulos, *J. Solid State Chem.*, 2016, **244**, 20-24.

19. H. Zhang, M. Tao, B. Gao, W. Chen, Q. Li, Q. Xu and S. Dong, *Sci. Rep.*, 2017, **7**, 8458.
20. J. Ghosh, R. Ghosh and P. K. Giri, *Sens. Actuators B Chem*, 2018, **254**, 681-689.
21. J. Ghosh, R. Ghosh and P. K. Giri, *ACS Appl. Nano Mater.*, 2018, **1**, 1551-1562.
22. T. J. Jacobsson, J.-P. Correa-Baena, E. Halvani Anaraki, B. Philippe, S. D. Stranks, M. E. F. Bouduban, W. Tress, K. Schenk, J. Teuscher, J.-E. Moser, H. Rensmo and A. Hagfeldt, *J. Am. Chem. Soc.*, 2016, **138**, 10331-10343.
23. B. Shi, X. Yao, F. Hou, S. Guo, Y. Li, C. Wei, Y. Ding, Y. Li, Y. Zhao and X. Zhang, *J. Phys. Chem. C*, 2018, **122**, 21269-21276.

Chapter 8

Summary and Outlooks

The highlights of the major contributions of the thesis and important conclusions of the work are presented in this chapter. New findings on the controlled growth of perovskite nanoparticles (NPs) embedded in mesoporous Si nanowires (NWs) template for different optoelectronic applications are summarized. New findings on the solid-state synthesis of all-inorganic perovskite nanocrystals (NCs) and manganese (Mn) doping in the NCs for different optoelectronic applications are summarized. New methodologies of fabrication of high-quality perovskite films for self-powered photodetector (PD) and solar cells are also summarized.

The scope for the future works is discussed at the end.

8.1. Summary and Highlights of the Thesis Contribution

In this dissertation, at first, we have presented the controlled fabrication of $CH_3NH_3PbI_3$ perovskite NPs on a mesoporous Si NW template and the mechanism of its high photoluminescence quantum yield (PL QY) (Chapter 2). Next, we have investigated the origin of strong cathodoluminescence (CL), PL of $CH_3NH_3PbBr_3$ perovskite NPs embedded in mesoporous Si NWs with high ambient stability. Further, we have demonstrated the superior performance of $CH_3NH_3PbBr_3$ NPs/Si NWs heterojunction photodetector (PD) (Chapter 3). Next, we have presented a facile room-temperature, bulk scale solid-state synthesis of highly luminescent color-tunable $CsPbX_3$ nanocrystals (NCs) with superior optoelectronic performance and exceptional ambient stability. We have further integrated the $CsPbBr_3$ NCs on direct CVD grown large-area monolayer (1-L) MoS_2 on Si/SiO_2 substrates and fabricated a vertical type-II heterojunction PD. We have systematically investigated the mechanism of high-performance photodetection of the 1-L MoS_2/ $CsPbBr_3$ NCs PD (Chapter 4). Next, we have demonstrated the solid-state synthesis of highly stable and highly luminescent Mn-doped $CsPbCl_3$ NCs with high Mn substitution, and investigated the origin and tunability of its dual-color emission. Further, we have fabricated white light-emitting diodes (WLEDs) by employing blue-emitting $CsPbCl_{1.5}Br_{1.5}$ NCs, green-emitting $CsPbBr_3$ NCs and orange-red emitting 10% Mn-doped $CsPbCl_3$ NCs (Chapter 5). Next, we have fabricated an air processed high-performance self-powered hybrid perovskite PD with plasmonic silver nanoparticles (Ag NPs) embedded hole-transport-layer (HTL), without the use of any electron-

transporting layer (ETL) and systematically elucidated the mechanism of the superior performance of the broadband hybrid plasmonic perovskite PD (Chapter 6). Finally, the effect of substrate temperatures in the growth of vaccum-deposited lead iodide (PbI_2) film and its conversion into high-quality $CH_3NH_3PbI_3$ perovskite film using a two-step, vapor-solution deposition process for large-area perovskite solar cells were studied. We demonstrated ~66% improvement in power conversion efficiency (PCE) of perovskite solar cells with the PbI_2 film deposited at elevated temperature (150 °C). The perovskite solar cells using perovskite film grown by the vapor-solution deposition technique exhibit PCE of 13.1% with a device area of 5 mm × 5 mm (Chapter 7).

The major contributions of the present thesis work are summarized below.

A. Controlled Fabrication of $CH_3NH_3PbI_3$ NPs with High PL QY using a Mesoporous Si NW Template

We have developed an easy and cost-effective fabrication technique of $CH_3NH_3PbI_3$ perovskite NPs confined in mesoporous Si NWs array template, for the first time. Highly crystalline perovskite NPs with controlled sizes were synthesized by spin-coating of perovskite precursor on the surface of MACE grown mesoporous Si NWs. Our results demonstrate that the porous sites of the Si NWs act as the nucleation centers for the growth of the perovskite NPs with high crystallinity. We have tuned the size (diameter 3-30 nm) and PL properties of the $CH_3NH_3PbI_3$ NPs by controlling the porosity of the mesoporous Si NWs and perovskite precursor concentrations. It is demonstrated that the ultra-small size and the quantum confinement effect in the perovskite NPs are primarily responsible for the enhanced PL intensity and the blue-shift of the PL peak compared to the bulk perovskite. The reabsorption of photons by perovskite NPs from the highly luminescent mesoporous Si NWs followed by the re-emission by the perovskite NPs (photon recycling), partly contributes to the PL intensity enhancement of perovskite NPs. We have achieved a PL QY of 9.82 % for the perovskite NPs grown on the Si NW template under the normal ambient condition, which is significant. *This work has been published in "ACS Appl. Nano Mater., 1, 1551-1562, (2018)".*

B. On the Origin of Strong Cathodoluminescence and Fast Photoresponse from Embedded $CH_3NH_3PbBr_3$ NPs

We have demonstrated the superior optoelectronic properties of $CH_3NH_3PbBr_3$ NPs grown on a mesoporous Si NW template by means of their strong cathodoluminescence (CL), stable PL, and fast photoresponse characteristics. The FESEM, FETEM, XRD, and EDX analyses confirm the uniform decoration of crystalline perovskite NPs over the entire surface of the mesoporous Si NWs. For the first time, we have shown that the perovskite NPs confined in Si NWs show enhanced CL emission with a marked blue shift as compared to the bare perovskite film, which is fully consistent with the PL spectra of perovskite NPs. A systematic study reveals that the quantum confinement effect and ultralow defects in $CH_3NH_3PbBr_3$ NPs are mainly responsible for their enhanced CL and PL emissions. Our study revealed a direct correlation between the CL and PL emissions from the perovskite NPs, for the first time. Low-temperature PL and time-resolved PL analyses confirm the high radiative recombination in perovskite NPs. High exciton binding energy for $CH_3NH_3PbBr_3$ NPs (113 meV) as compared to the bulk film (70 meV) is fully consistent with the quantum confinement of carrier in perovskite NPs. We have obtained a high PL QY of 40.5% for the perovskite NPs film embedded in Si NWs, while it is only 2.8% for the bulk perovskite film. The embedded perovskite NPs show higher ambient air stability than the bare film due to the protection provided by the dense Si NWs array as the dense Si NWs array can slow down the lateral diffusion of oxygen and water molecules in perovskite NPs. We have further fabricated $CH_3NH_3PbBr_3$ NP/Si NWs heterojunction PD. The PD exhibited superior visible light photodetection with a responsivity of 0.223 A/W and a response speed of ~0.28 s at a low bias voltage (2 V), which is significant. *This work has been published in "ACS Appl. Mater. Interfaces, 11, 14917-14931, (2019)".*

C. Solid-State Synthesis of Highly Stable Perovskite Nanocrystals and Mechanism of High-Performance Photodetection in a Monolayer $MoS_2/CsPbBr_3$ Vertical Heterojunction Photodetector

We have developed a facile, room-temperature, nearly solvent-free, and bulk scale solid-state synthesis strategy for highly stable and color-tunable $CsPbX_3$ (where X= Cl, Br and I) NCs. A minute amount of surfactant-assisted two-step ball milling process results in perovskite NCs, which exhibit incredibly high PL QY (up to 95%) and color-tunable PL emission over the entire visible region with excellent ambient stability up to several months. These highly luminescent perovskite NCs were utilized in color-tunable down-converted light-emitting devices by employing NCs composite films with PMMA on commercial UV LED chips with superior

operational stability >100 hr, without any encapsulation. We have further integrated the as-synthesized $CsPbBr_3$ NCs with direct CVD grown monolayer MoS_2 (1L-MoS_2) on SiO_2 substrates and fabricate a vertical heterojunction PD. Our 1L-MoS_2/$CsPbBr_3$ NCs heterojunction PD can operate at a very low applied bias (0.1V), while the photo responsivity of the device is obtained to be 24.34 A/W at 400 nm, which is about one order of magnitude higher than that of bare 1L-MoS_2. The temporal response of the PD is found to be ~5.48 μs, which is much faster than the reported values. The performance of the heterojunction PD is much superior to that of the pristine 1L-MoS_2 based PD. The enhanced performance of the heterojunction PD is attributed to the efficient transfer of photogenerated electrons from $CsPbBr_3$ NCs to 1L-MoS_2, which is probed by steady-state and time-resolved PL and Raman analyses. Direct evidence for charge transfer in the heterojunction is obtained from the Kelvin probe force microscopy (KPFM) that shows a type-II heterojunction formation and a suitable band bending at the 1L-MoS_2/$CsPbBr_3$ interface. These conclusions are supported by density functional theory (DFT) calculations showing the distinct change in the density of states in the heterostructure, thus providing clear evidence for charge transfer from perovskite NCs to the MoS_2 layer. *This work has been published in "J. Mater. Chem. C, 8, 8917-8934 (2020)".*

D. Origin and Tunability of Dual Color Emission in Solid-State Synthesized High Mn Doped $CsPbCl_3$

We have developed a facile, low-cost, nearly solvent-free, bulk scale, room-temperature mechano-synthesis process for highly luminescent Mn-doped $CsPbCl_3$ NCs with high Mn substitution (up to 40%). A two-steps physical milling process with a very low amount of surfactant results in undoped and Mn-doped perovskite NCs in the size range 9-14 nm, which exhibit superior optical properties. The Mn-doped $CsPbCl_3$ NCs exhibit distinct excitonic PL emission in the UV region and Mn related PL emission in the orange-red region with high PL QY (up to 35%). We have demonstrated the tunability of the Mn-related orange-red PL emission intensity by controlling the doping concentration, excitation intensity, and measurement temperature. Importantly, it was shown that Mn-doped $CsPbCl_3$ NCs synthesized by the physical milling method exhibit better emission stability over a long time due to the high Mn doping efficiencies achieved through the high pressure-mediated synthesis conditions in physical milling. Deconvolution of the PL spectra revealed the contribution of the defect-related emission, besides the excitonic emission and Mn

related emission in the overall PL spectra. Further, white light-emitting diode (WLED) was demonstrated by employing blue-emitting $CsPbCl_{1.5}Br_{1.5}$ NCs, green-emitting $CsPbBr_3$ NCs and orange-red emitting 10% Mn-doped $CsPbCl_3$ NCs composite films with PMMA. The coupled $CsPbCl_{1.5}Br_{1.5}$/ $CsPbBr_3$/ 10% Mn-doped $CsPbCl_3$ film with UV chip yields blue-green-orange tri-color emissions leading to bright pure white light emission with corresponding CIE color coordinates of (0.31, 0.34). *This work has been published in "J. Colloids & Interface Sci., 564, 357–370, (2020)".*

E. Efficient Plasmonic Hole-Transport-Layer Enabled Self-Powered Hybrid Perovskite PD

We have fabricated a self-biased $CH_3NH_3PbI_3$ perovskite PD by integrating Ag NPs in the PEDOT:PSS hole-transport-layer (HTL) and without the use of any electron-transport-layer (ETL). We have deposited the perovskite active layer by a novel N_2 gas-assisted fast crystallization method to form a uniform perovskite film compared to the conventional deposition method in ambient condition, for the first time. Without any external bias, the responsivity of the hybrid device (with Ag NPs) is enhanced by ~45% compared to the pristine device (without Ag NPs), with a peak responsivity of 0.25 AW^{-1}, while the detectivity is enhanced from 1.04×10^{11} Jones (pristine device) to 1.53×10^{11} Jones (hybrid device). The hybrid device also shows about three times faster photoresponse as compared to the pristine device. Under small reverse bias (0.5V), the hybrid device exhibited a peak responsivity of 3.61 A/W, which is significantly higher than the Si-based commercial PDs. The improved performance of the hybrid PD is attributed to plasmon-enhanced optical absorption, as well as improvement in charge extraction and transport by Ag NPs, which are evidenced by the steady-state and time-resolved PL analysis. Impedance analysis of the devices shows the reduced carrier transfer resistance of the hybrid device, which results in superior transport of photogenerated charge carriers. KPFM analysis revealed the change in the work function of PEDOT:PSS film with Ag NPs and suitable band alignment, which enables superior carrier transport resulting in improved photodetection performance for the hybrid device. *This work has been published in "Organic Electronics, 71, 175–184 (2019)".*

F. Vacuum Deposited PbI_2 Film Grown at Elevated Temperature for Efficient Planar Perovskite Solar Cells

We have developed a spin-coating-free two-step vacuum-solution deposition technique for the growth of large-area perovskite film for solar cell application. First, the PbI_2 layer was deposited by vacuum thermal evaporation, and subsequently these films were dipped into CH_3NH_3I solution for the formation of $CH_3NH_3PbI_3$ perovskite film. We have demonstrated the effect of substrate temperatures in the growth of vapor-deposited PbI_2 film and its conversion into high-quality perovskite film. With the increase in substrate temperatures of deposition, the PbI_2 films were observed to be very compact and pinhole-free with higher crystallinity. Perovskite films using PbI_2 films deposited at higher substrate temperatures (150 ºC) are very compact with large grains and pinhole-free morphology with superior optical properties. The power conversion efficiency (PCE) for solar cells using PbI_2 layers deposited at 150 ºC was observed to be 13.1 % with a device area of 5 mm × 5 mm, while PCE of the cell using PbI_2 layers deposited at 30 ºC of substrate temperature was found to 7.9%. Thus, the performance of solar cells using the PbI_2 layer deposited at 150 ºC of substrate temperature was increased by ~66% due to the excellent perovskite film obtained from it. The devices using the PbI_2 layer deposited at 150 ºC also show enhanced ambient stability compared to the device using the PbI_2 layer deposited at 30 ºC. Thus, the pinhole-free compact perovskite film helps in enhanced stability of the device. *This work has been submitted for publication, and it is under review.*

8.2. Scope of Future Work

The present thesis has focused on the growth of embedded perovskite NPs, solid-state synthesis of undoped and doped perovskite NCs followed by new strategy of fabrication of perovskite films for different light emission, photodetection, and solar cell applications. There is a vast scope to extend the present work for a broad range of applications, as described below:

1. Fabrication of perovskite NPs in cost-effective alternative mesoporous inorganic templates, for various optoelectronic applications. These inorganic stable mesoporous matrix can encapsulate perovskite NPs from the ambient condition, which may result in better ambient stability.

2. Fabrication and optimization of high-performance light-emitting diodes with better ambient stability using perovskite NCs/QDs synthesized by the novel solid-state method.

3. Effective doping of different main group metal cations, transition metal cations, and rare earth metal cations in perovskite NCs by pressure mediated solid-state synthesis and investigation of its photophysical properties.

4. Perovskite NCs/films can be combined with different 2D materials such as WS_2, WSe_2, $MoSe_2$, Bi_2O_2Se, MXenes for high-performance heterojunction PDs with ultrafast photoresponse.

5. Investigation of the carrier trapping and charge transfer dynamics in perovskite/ 2D material heterostructure for future improvement in the optical and electrical properties, which may be useful for various optoelectronic applications.

6. Fabrication of transport layer free high-performance and low-cost self-powered perovskite PDs for real-life applications.

7. Interface engineering and fabrication of high-performance plasmonic-perovskite solar cells for commercial applications.

8. Improvement of the efficiency and stability of large area perovskite solar cell deposited by vapor-solution technique by optimizing different layers of the devices and interface engineering for commercial applications.

9. Partial and complete substitution of toxic lead in halide perovskite for different optoelectronic applications.